

**FUNCTIONALITY AND DIMENSIONALITY EFFECT ON VARIATION  
OF CO<sub>2</sub> UPTAKE AND PROTON CONDUCTION IN METAL  
ORGANIC FRAMEWORKS (MOFs)**

*Thesis Submitted to*

**Academy of Scientific and  
Innovative Research (AcSIR) for  
the Degree of Doctor of  
Philosophy in Chemical Sciences**



**By**

**TAMAS KUMAR PANDA**

**Registration Number: 10CC11J26027**

**Under the guidance of  
Dr. Rahul Banerjee**

**Physical and Material Chemistry Division  
CSIR National Chemical Laboratory  
Pune-411008, India**

**May 2014**

---

*Dedicated to*

*My Parents*

---



राष्ट्रीय रासायनिक प्रयोगशाला

(वैज्ञानिक तथा औद्योगिक अनुसंधान परिषद)

डॉ. होमी भाभा रोड, पुणे - 411 008. भारत

**NATIONAL CHEMICAL LABORATORY**

(Council of Scientific & Industrial Research)

Dr. Homi Bhabha Road, Pune - 411008. India



## CERTIFICATE

Certified that the work “**Functionality and Dimensionality Effect on Variation of CO<sub>2</sub> Uptake and Proton Conduction in Metal Organic Frameworks (MOFs)**” submitted to Academy of Scientific & Innovative Research (AcSIR) was carried out by **Tamas Kumar Panda**, at the CSIR-National Chemical Laboratory Pune, under my supervision. Such material has not been submitted elsewhere for a degree.

*Rahul Banerjee*

**Dr. Rahul Banerjee,**

(Thesis Supervisor),

Physical and Materials Chemistry Division,

CSIR-National Chemical Laboratory,

Pune-411008.

**Date: 04/06/2014**



## STATEMENT

I hereby declare that the matter embodied in this thesis entitled “**Functionality and Dimensionality Effect on Variation of CO<sub>2</sub> Uptake and Proton Conduction in Metal Organic Frameworks (MOFs)**” is the result of investigations carried out by me in Physical and Materials chemistry Division, National Chemical Laboratory, Pune under the supervision of Dr. Rahul Banerjee.

In keeping with the general practice of reporting scientific observations due acknowledgements have been made wherever the work described is based on the findings of other investigators.

Pune

May 2014



**Tamas Kumar Panda**



## ACKNOWLEDGEMENT

I am extremely grateful to my supervisor Dr. **Rahul Banerjee** for his constant guidance, support and encouragement throughout my Ph.D. tenure. I am very much thankful to him for introducing me to this fascinating multi-faceted field of research. I warmly thank him for his valuable advice, constructive criticism and his extensive discussions around my work. I would like to thank my DAC committee members Dr. Sayam Sengupta, Dr. Kumar Vanka and Dr. Guruswamy Kumaraswamy for their constructive and innovative suggestion.

Most of the results described in this thesis would not have been obtained without a close collaboration with few laboratories. I would like to acknowledge the assistance of Dr. Vedavati G Puranik for giving us the opportunity to use single crystal instrument. I am also thankful to Dr. Jianwen Jiang, NUS Singapore for his help in theoretical calculations in few projects. I owe a great deal of appreciation and gratitude to Dr. Sreekumar Kurungot for proton conductivity measurements and studies on MOF crystals.

I am grateful to CSIR, New Delhi for fellowship support. I thank all the non-teaching staff of CSIR NCL for their assistance on various occasions. I wish to thank all my friendly and cooperative labmates *Pradip, Chandan, Arijit, Subhadeep, Tanay, Sharath, Bishnu, Suman, Bikash, Harshitha, Subhash, Jayshri, Gobinda and Digambar* for creating a cheerful and enjoyable working atmosphere in the lab. They were extremely supportive as well as helpful during my tenure. I thank project students particularly Mayur, Nitya, Neha, Arun, Sredipta, Arya and Suman who helped me in various projects.

My stay on this campus has been pleasant with the association of all the research scholars at CSIR NCL. I am thankful to Parthada, Mrinmoy, Achintya, Arpan, Kanak, Susanta, Anjan, Saikat, Pravat, Jayasis, Patida, Krisanu, Animesh, Shyamda, Sajalda, Shymboda, Aryya, Himadri, Munmun, Subha, Tanaya, Anupamda, Abhik, Souvik, Doss, Prithvi, Sujitda, Sumantrada, Debasisda, Garaida, Basabda, Prathit, Binoyda, Chandan (Chudhory), Debarati, Amrita, Swagata, Chakadola, Chinmay, Sekhar, Nagesh, Vishal, Jitu, Rajashri, Manik, Satej, Kaushalendra, Bahusaheb and Sushma.

I would also like to thankful to my all juniors Anup, Soumen (Das), Saibal, Sudip, Shantanu, Prasenjit, Jhumur, Atanu, Prabhu, Santu, Somen (Dey), Atreyee, Arunava, Shantigopal, Hridayesh, Monalisa, Chayanika, Sujit, Manik, Soumyojyoti, Tapas, Tamal, Manoj, Subhrasis, Bappa, Saikat, Rupa and Piyali.

I offer my sincere regards to people, teachers who have inspired me directly or indirectly in research carrier.

I am grateful to CSIR, New Delhi, for awarding the research fellowship and Dr. Pal, Director, and Dr. Sivaram, former director, CSIR-National Chemical Laboratory to carry out my research works, extending all infrastructural facilities and to submit this work in the form of a thesis for the award of Ph. D degree. I am also thankful to Academy of Scientific & Innovative Research (AcSIR) for giving me a chance to complete one the dream in my life.

I thank my brother (Manas) and sister-in-law (Papun) for their constant support and encouragement. I thank the entire members in my family for their constant care and wishes. I also extend my thanks to my Mama and Masi for their encouragement. Last but not least, I would like to pay high regards to my parents for their sincere encouragement and inspiration throughout my research work and lifting me uphill this phase of life. I owe everything to them. Dedicating this thesis to them is a minor recognition for their invaluable support and encouragement.

**Tamas Kumar Panda**

## PREFACE

The capture and storage of CO<sub>2</sub> emitted from industrial processes become a global challenge. At present, the separation of CO<sub>2</sub> from such a low pressure stream of gases is performed by amine sorbents through chemisorptions. However, researchers are exploring alternative approaches as amine regeneration requires significant heating and has high operational cost. These limitations have prompted investigations on porous materials relying on reversible physisorption of CO<sub>2</sub>, because it requires less energy for regeneration than materials relying on chemisorptions. On the other hand, increasing environmental pollution and energy shortages, clean energy has become the main challenges for the 21st century. The usefulness of proton-exchange membrane fuel cells (PEMFCs) which generate electricity appears to be an attractive option as an alternative clean energy. In principal, membrane materials which can efficiently transport protons from anode to cathode will be the heart of the fuel-cell technology. Commercially, sulfonated fluoropolymers (nafion) are used as membrane materials, shows proton conductivities of up to 1 Scm<sup>-1</sup>. However, requirement to keep these materials hydrated limits their operating temperature and efficiency in PEMFCs. The work presented in this thesis is an attempt to design a series of MOFs for addressing the issues like high CO<sub>2</sub> storage capacity as well as efficient proton conductivity. Chapter 1 gives an overview on porous metal organic frameworks including their synthesis, structure and applications. It also discusses about literature review and various strategies for high CO<sub>2</sub> uptake as well as high proton conduction in MOF architectures.

Chapter 2 will address the role of different functionality (-NH<sub>2</sub>, -NO<sub>2</sub>, -Cl, -Br ) on CO<sub>2</sub> uptake in zeolitic metal organic frameworks. Initially, we choose -NH<sub>2</sub> functionalized organic linker (5-amino tetrazole) for the synthesis of MOF (ZTF-1) as such functional group has strong potential to interact with CO<sub>2</sub>. The structure, thermal stability and CO<sub>2</sub> storage capability of ZTF-1 was investigated. The experimentally determined CO<sub>2</sub> storage capability and isosteric heat of adsorption (Q<sub>st</sub>) of ZTF-1 also verified with computational results. In order to understand the role of functionality in ZIFs we have also investigate the study on three new Co-ZIFs [Co-ZIF-68, -69, -81]. They have same GME topology like structure but different functionality, composed of one common nitroimidazolate (nIM), and one substituted benzimidazolate [C<sub>6</sub>H<sub>6</sub>, -C<sub>6</sub>H<sub>5</sub>Cl, -C<sub>6</sub>H<sub>5</sub>Br]. The polarity of these functional groups on CO<sub>2</sub> storage capacities in these Co-ZIFs will be discussed. Moreover, the experimental resulted CO<sub>2</sub> adsorptions were further contrasted with computational results. (*Chem. Commun.*, 2011, **47**, 2011 and *CrystEng Comm*, 2014, **16**, 4677).

In Chapter 3, synthesis and characterization of three new metal organic framework isomers (Mn-MOFs) will be presented. The effect of triazole functionality on CO<sub>2</sub> uptake in these MOFs will be discussed. We will also address the role of size dependent template on structural conversions from non-porous to porous MOFs. The periodic increased porosity in Mn-MOFs depending on the size of the template used has been expected to confirm by the CO<sub>2</sub> adsorption isotherms. (*Chem. Commun.*, 2011, **47**, 7674)

In Chapter 4, the synthesis, structure and proton conduction characteristics of two isostructural metal organic nanotubes will be discussed. Both these structures functionalize with triazole moieties and neutralized by the trapped dimethyl ammonium cations. The triazole decorated pores along with dimethyl ammonium cation and metal bound carboxylate moiety expectedly provide an unique pathway for proton conduction under humid condition. This chapter will also address the mechanisms and theories of inherent proton conduction in metal organic nanotubular architectures. (*Chem. Commun.*, 2012, **48**, 5464)

Chapter 5 deals with effects of dimensionality on hydrous and anhydrous proton conduction in In (III) isophthalic acid based frameworks will be discussed. It was anticipated that, the presence of dimethyl ammonium cations as well as trapped solvent molecules inside these structures are expected to show hydrous as well as anhydrous proton conduction. The detailed proton conduction mechanism is also addressed in this chapter. (*Chem. Commun.*, 2013, **49**, 6197)

Finally chapter 6 will describe the conclusion of the overall work presented in this thesis. The future direction and schemes of this thesis also presented in this chapter.

An extended Appendix describes crystallographic information of all these MOF crystals reported in this thesis.

**Tamas Kumar Panda**

## CONTENTS

Certificate	ii
Statement	iii
Acknowledgement	iv
Preface	vi

### CHAPTER 1

#### **INTRODUCTION OF POROUS METAL ORGANIC FRAMEWORKS (MOFs): SYNTHESIS, STRUCTURE AND APPLICATIONS 1-39**

1.1	Background of porous materials	1
1.2	Synthesis of MOFs	3
1.3	Structure of MOFs	5
1.4	Properties and Applications of MOFs	6
1.5	CO <sub>2</sub> adsorption in MOFs	10
1.5.1	CO <sub>2</sub> adsorption in MOFs at high pressures	12
1.5.2	CO <sub>2</sub> adsorption in MOFs at low pressures	16
1.6	Key strategies to enhance CO <sub>2</sub> adsorption	18
1.6.1	Open metal site	19
1.6.2	Metal doping inside the pores of the MOF	20
1.6.3	Framework cavity functionalized by nitrogen basic sites	21
1.7	Proton Conduction in MOFs	27
1.7.1	Challenges of proton conductivity in MOFs	29
1.7.2	Water assisted proton conductivity in MOF	29
1.7.3	Anhydrous proton conductivity in MOF	36

### CHAPTER 2

#### **FUNCTIONALIZED ZEOLITIC IMIDAZOLATE AND TETRAZOLATE FRAMEWORKS FOR HIGH CARBON DIOXIDE STORAGE CAPACITY 40-73**

2.1	Introduction	40
2.2	Result and Discussion	42
2.2.1	Structural analysis of ZTF-1	42
2.2.2	Structural analysis of Co-ZIF-68, -69 and -81	45
2.2.3	Thermal properties and X-ray powder diffraction analysis	48
2.2.4	Gas adsorption Properties	50
2.2.5	Computational Studies for ZTF-1 and Co-ZIFs	56
2.3	Conclusion	62

2.4	Experimental Procedures	63
2.4.1	Materials	63
2.4.2	Synthesis of N,N-Dimethylformamide Azine Dihydrochloride	63
2.4.3	Synthesis of ZTF-1	63
2.4.4	Synthesis procedure of Co-ZIFs	65
2.4.5	General methods for characterization	67
2.4.6	X-ray Crystallography	68

### **CHAPTER 3**

#### **ENHANCEMENT OF POROSITY IN TRIAZOLE FUNCTIONALIZED ISOMERIC MOFs BY INDUCING SIZE DEPENDENT TEMPLATE** **74-88**

3.1	Introduction	74
3.2	Result and Discussion	76
3.2.1	Structural analysis of Mn-MOFs	76
3.2.2	Thermal properties and X-ray powder diffraction analysis	79
3.2.3	Gas adsorption Properties of Mn-MOFs	80
3.3	Conclusion	82
3.4	Experimental Procedures	83
3.4.1	Materials	83
3.4.2	Synthesis procedure of Mn-MOFs	83
3.4.3	General methods for characterization	84
3.4.4	X-ray Crystallography	85

### **CHAPTER 4**

#### **SELF ASSEMBLED ONE DIMENSIONAL FUNCTIONALIZED METAL ORGANIC NANOTUBES (MONTs) FOR HYDROUS PROTON CONDUCTION** **89-113**

4.1	Introduction	89
4.2	Result and discussion	91
4.2.1	Structural analysis of In-IA, In-5TIA and Cd-5TIA	91
4.2.2	Thermal properties and X-ray powder diffraction analysis	95
4.2.3	Proton Conductivity Measurement	96
4.3	Conclusion	105
4.4	Experimental Procedures	106
4.4.1	Materials	106
4.4.2	Synthesis of 5-triazole isophthalic acid	106
4.4.3	Synthesis of In-5TIA and Cd-5TIA	107
4.4.4	General methods for characterization	108
4.4.5	X-ray Crystallography	109

## **CHAPTER 5**

### **STRUCTURAL ISOMERISM LEADING TO ANHYDROUS PROTON CONDUCTIVITY IN INDIUM (III) ISOPHTHALIC ACID BASED FRAMEWORKS 114-138**

5.1	Introduction	114
5.2	Result and Discussion	115
5.2.1	Structural analysis of In-IA-2D-1 and In-IA-2D-2	115
5.2.2	Thermal properties and X-ray powder diffraction analysis	117
5.2.3	Proton Conductivity	120
5.3	Conclusions	132
5.4	Experimental Procedures	132
5.4.1	Materials	132
5.4.2	Synthesis of In-IA-2D-1 and In-IA-2D-2	133
5.4.3	General methods for characterization	134
5.4.4	X-ray Crystallography	134

## **CHAPTER 6**

### **CONCLUSION OF ALL CHAPTERS AND FUTURE DIRECTION 139-145**

6.1	Conclusion	139
6.2	Future direction	141

### **REFERENCES 146-162**

Appendix 1 (MOF Crystallographic Details)	163
About the Author	166
List of Publications	167

## List of Figures, Tables and Schemes

### Figures

1.1	Schematic representations of the types of microporous solids (polymers for porous organic solids, zeolites for porous inorganic solids and MOFs for porous organic inorganic hybrid solids).	1
1.2	Model representation of 1D, 2D and 3D MOF constructed from organic linkers, metal salt and solvent molecules.	2
1.3	Model representation of three dimensional functionalized MOF.	3
1.4	Scheme of various synthetic approaches and conditions used for the preparation of MOFs.	4
1.5	Model representation for the construction of 3D network generated from the connector and linker (top). Similarly 3D MOF synthesized by assembling secondary building units (SBUs) and organic linker, which dictate the final topology of a framework.	5
1.6	Various applications of MOFs such as gas storage, separation, catalysis, drug delivery, magnetism, proton conductivity, non linear optics, light harvesting, photoluminescence, explosive sensing, charge carrier mobility etc.	7
1.7	Model representation of MOFs and their most promising applications on high CO <sub>2</sub> uptake (environmental related) and high proton conduction (energy related).	10
1.8	CO <sub>2</sub> capture process in coal fire power plant by using mono ethanolamine and the disadvantages of the process	11
1.9	Comparison of gravimetric CO <sub>2</sub> capacities for all MOFs compare with activated carbon at ambient temperature and pressures up to 42 bar.	12
1.10	Zn <sub>4</sub> O(CO <sub>2</sub> ) <sub>6</sub> SBU unit (middle) is connected with various types of organic linkers to form MOFs with high surface area and CO <sub>2</sub> uptake.	13
1.11	Single crystal structure of M <sub>2</sub> (DOBDC) {M= Mg, Co, Ni and Zn}, formed by reaction of the 2, 5 dihydroxy terephthalic acid linker with different M(NO <sub>3</sub> ) <sub>2</sub> ·6H <sub>2</sub> O. The structure consists of 1D hexagonal channel with open metal sites inside the pore after strong evacuation.	15
1.12	Schematic representation of CO <sub>2</sub> uptake in selected MOFs at 0.15 bar pressures.	16
1.13	Schematic representation of zero-coverage isosteric heat of CO <sub>2</sub> adsorption (Q <sub>st</sub> ) in MOFs.	17
1.14	Generation of open metal sites by removal of coordinated solvents from MOF architecture (model representation).	19
1.15	Synthesis of Mg-MOF-74 and HKUST-1. Open metal site is generated (for high CO <sub>2</sub> adsorption) after proper evacuation of these MOFs at high temperature and pressure.	20
1.16	Systematic enhancement of CO <sub>2</sub> uptake from IRMOF-1 to IRMOF-3 by incorporating –NH <sub>2</sub> functionalization in organic linker.	22



1.17	Single-crystal structure of $Zn_2(atz)_2(ox)$ loaded with $CO_2$ after proper evacuation. It has been observed that $CO_2$ molecules trapped closely to the $-NH_2$ groups inside the framework which also proved by single crystallographically. Green, gray, blue and red spheres represent Zn, C, N, and O atoms respectively; H atoms are omitted for clarity. Inset version shows distance between the amine group and the $CO_2$ molecule.	23
1.18	Post synthetic modification of Cu-BTTri framework through the binding ethylene diamine (en) to the open metal coordination sites. The free amine groups of en lined inside the framework pores facilitate to interact with $CO_2$ molecules for higher adsorption.	24
1.19	Synthesis of Bio-MOF-11 starting from adenine and Co(II) salt. Extended structure of Bio MOF-11 contains several amine groups dangled inside the pore which enhances the $CO_2$ uptake.	25
1.20	Structural similarity between zeolite and ZIF.	26
1.21	Model representation of proton exchange membrane fuel cell (PEMFCs).	27
1.22	(a) Mechanism of Grotthuss proton hopping through the H bonded network of water (b) Vehicle proton hopping mechanism through the network. The arrow indicates the movement of protons.	28
1.23	(a) Schematic view of the one dimensional MOF channel impregnated with protonated water molecules. The arrows indicate the possible movement of protons through the channel in water assisted proton conduction.	30
1.24	(a) Three dimensional arrangement of ferrous oxalate based coordination polymer. (b) Three dimensional packing of 2, 5-dihydroxy- 1,4-benzoquinone (Dhbq) and Fe (II) based MOF. The protons transport through the coordinated water of 1D chain structure under hydrous condition. Fe yellow, O red, C gray and Zn green.	31
1.25	Structure of (a) 1, 3, 5 benzene trisulphonic acid and (b) 1, 3, 5 benzene triphosphonic acid (c) Structure of PCMOF-3, showing two layers (top and bottom) and forming 1- D water filled channels which enhances the proton conductivity. Colour code: Zn green, O red, C gray and P yellow.	32
1.26	Representation of D and L valline based MOF with Zn(II) metal center. Close proximity of water molecules inside the framework is responsible for proton conduction.	33
1.27	Honeycomb layer structure of Zinc oxalate framework $(NH_4)_2(adp)-[Zn_2(ox)_3] \cdot 3H_2O$ . inside the interlayer spaces of 2D network ammonium cation, water molecule as well as adipic acid (adp) is arranged by H bonds. Color code: Zn green, O red, C gray and N blue.	34
1.28	Schematic representation of MOF channel which is filled by imidazole/ triazole /pyrazole etc. molecules for anhydrous proton conduction.	36

1.29	Structure of Al based MOF (a) imidazoles loaded Al-NDC based framework [1@ Im]. (b) imidazoles loaded Al-BDC based framework [2@ Im], (c) structure of Al-NDC based MOF loaded with histamines for anhydrous proton conduction. Colour code: Al Yellow, O red, C gray and Imidazole green pentagone	37
1.30	(a) Structure of $\beta$ PCMOF-2, constructed from 1, 3, 5 benzene trisulphonic acid and Na metal. 1, 2, 4 Triazole molecule incorporated inside the pore of $\beta$ -PCMOF-2 for anhydrous proton conduction. (b) Packing structure of $[\text{Zn}(\text{H}_2\text{PO}_4)_2(\text{TzH})_2]_n$ coordinated triazolate linker forms 2D sheets where phosphates are dangled along the channel and creates proton conduction pathway. Color code: Na cyan, Zn green, P yellow, O red, N blue, C grey and 1, 2, 4 triazole-light blue pentagon respectively. H atoms have been omitted for clarity.	38
2.1	Synthesis of ZTF-1 from 5-amino tetrazole and Zn(II) salt in presence of structure directing agent DMAz.	42
2.2	Crystal structure of ZTF-1. (a) The Zn-TET-Zn bridging angle in ZTF-1 resembles with Si-O-Si structure in zeolites. (b) The framework adopts a dia topology. The structure is shown as an exploded tiling of adamantane (brown) with all the tetrahedral Zn(II) atoms (green) are linked. (c) Zn(II) and 5-amino tetrazolate clusters are bridged together to generate an extended 3D porous structure(d) 3D packing diagram of ZTF-1. [Zn(II) blue, C black, N green]	43
2.3	Angular distribution for the M-X-M angles. X axis represent the angle range and Y axis represent the number of hits. It should be noted that, we have assigned total number of hits for every case in order to separate each type from others.	45
2.4	Reaction of 2nIM with different imidazole based linkers (bIM, Cl-bIM and Br-bIM) construct the <b>GME</b> topology. Blue and pink polyhedral indicates Zn and Co metal center respectively. H atoms are omitted for clarity. At right side, the schematic representation of <i>hpr</i> , <i>gme</i> , and <i>kno</i> cages, which construct the <b>GME</b> topology.	46
2.5	(a) Pictorial definition of pore aperture ( $d_a$ ) and pore diameter ( $d_p$ ) of Zn and Co based GME ZIFs. (b) pore diameter ( $d_p$ ) vs surface area for Co and Zn based GME ZIFs. (c) Pore diameter ( $d_p$ ) vs CO <sub>2</sub> uptake for Co and Zn based GME ZIFs at 273K and (d) 298K. It is clearly indicate that Co based GME ZIFs analogue have much higher CO <sub>2</sub> uptake than Zn based GME ZIFs.	47
2.6	PXRD patterns of (a) Co-ZIF-68 (b) Co-ZIF-69 and (c) Co-ZIF-81 performed during stability test in water. The framework structure of all Co-ZIFs were unchanged after 5 days and matches well with simulated PXRD. (d) Thermo gravimetric analysis (TGA) of Co-ZIF-68, -69, and -81.	49

2.7	Gas adsorption isotherms of ZTF-1, (a) Nitrogen adsorption isotherm (77) K. (b) Adsorption isotherms for CO <sub>2</sub> and N <sub>2</sub> at 273 K and 298 K. (c) Hydrogen adsorption isotherms at 77K. The filled and open circles represent adsorption and desorption, respectively. (d) Overlay of TGA traces of as-synthesized (black), solvent-exchanged (red) and activated (blue) samples of ZTF-1.	50
2.8	Volumetric Gas adsorption isotherms of ZIF-68, 69 and 81. (a) Nitrogen adsorption isotherm at 77K. Comparison of CO <sub>2</sub> adsorption isotherms (273K and 298K) of (b) Zn and Co-ZIF-68 (c) Zn and Co-ZIF-69 (d) Zn and Co-ZIF-81. The filled and open circles represent adsorption and desorption, respectively. Zn ZIF-68, 69 and 81 ( <i>J. Am. Chem. Soc.</i> , 2009, <b>131</b> , 3875) isotherm have been reproduced (with permission from ACS).	53
2.9	Selectivity of CO <sub>2</sub> uptake in compare with its N <sub>2</sub> uptake at 273K of (a) Co-ZIF-68, (b) Co-ZIF-69 and (c) Co-ZIF-81.(d) H <sub>2</sub> adsorption isotherms of Co-ZIF-68, -69 and -81 taken at 77 K (red). Filled and open symbols represent adsorption and desorption branches.	54
2.10	(a) Pore morphology and (b) diameter along the X axis in ZTF-1. (c) Atomic labels of ZTF-1. (d) The Qst value for the CO <sub>2</sub> adsorption of ZTF-1.	56
2.11	(a) Isotherm and (b) isosteric heat for CO <sub>2</sub> adsorption in ZTF-1 at 273 K. The open symbols are from simulation and the filled symbols are from experiment. (c) Distances between CO <sub>2</sub> molecule and different N atoms and (d) radial distribution functions of CO <sub>2</sub> around N6, N7, N3 and Zn atoms in ZTF-1 at 273 K.	58
2.12	Density distributions of adsorbed CO <sub>2</sub> molecules on (a) YZ and (b) XY planes in ZTF-1 at 273 K and 100 kPa.	59
2.13	Calculated distances of carbon dioxide (CO <sub>2</sub> ) from (a) ZTF-1 (b) ZTF-1 analogue without free tetrazole nitrogen (c) ZTF-1 analogue without amino functionality.	60
2.14	(a) Zn-ZIF-68 (b) Co-ZIF-68 clusters. The clusters are terminated by Li atoms (yellow); H atoms are omitted for clarity. (c) and (d) optimized CO <sub>2</sub> positions around Zn-ZIF-68 and Co-ZIF-68 clusters respectively.	61
2.15	Comparison of the experimental PXRD pattern of as-synthesized (top) with the simulated from its single crystal structure (bottom) of (a) ZTF-1 (b) Co-ZIF-68 (c) Co-ZIF-69 and (d) Co-ZIF-81.	66
2.16	Asymmetric unit ORTEP diagram (50% probability) of (a) ZTF-1 (b) Co-ZIF-68 (c) Co-ZIF-69 and (d) Co-ZIF-81.	70
3.1	Synthesis of three isomeric Mn-MOFs starting from 5TIA, Mn(II) salt and DMF, shows enhancement of porosity depending on the size of templates used during synthesis. Color code: Mn (green), N (blue), O (red), C (black), H (white).	76

3.2	(a) Structural differences between Mn-5TIA-2 and -3. In Mn-5TIA-2 the N2 nitrogen of triazole ring is connected with Mn(II) but in Mn-5TIA-3 the N3 nitrogen of triazole ring is connected with Mn(II) resulting into the increase in MZC angle (Mn-centroid of benzene ring in 5-TIA-carboxylate carbon of 5-TIA) for Mn-5TIA-3 (129°) than Mn-5TIA-2 (109°). Color code: Mn (green), N (blue), O (red), C (black), H (light pink).	77
3.3	Coordination of 5TIA with metal SBU (left), ball and stick three dimensional packing (middle) and metal connections (right) of (a) Mn-5TIA-1 (b) Mn-5TIA-2 and (c) Mn-5TIA-3. Solvent molecules are omitted for clarity. Color code: Mn (green), N (blue), O (red), C (black), H (light pink).	78
3.4	Comparison of the simulated (bottom) and experimental (top) PXRD patterns of (a) Mn-5TIA-1 (b) Mn-5TIA-2 and (c) Mn-5TIA-3. The framework structures of all Mn-MOFs were matches well with simulated PXRD. (d) Thermo gravimetric analysis (TGA) of Mn-5TIA-1, -2, and -3.	80
3.5	Gas adsorption isotherms of Mn-5TIA-1, -2 and -3, (a) CO <sub>2</sub> adsorption isotherms for all Mn-MOFs, showing increase in CO <sub>2</sub> uptake from Mn-5TIA-1 to Mn-5TIA-3. (b) H <sub>2</sub> adsorption isotherms of Mn-MOFs at 77 K. (c) and (d) Comparison of CO <sub>2</sub> and CH <sub>4</sub> gas-adsorption isotherms for Mn-5TIA-2 and -3 measured at 298 K respectively. Open and filled symbol represents adsorption and desorption, respectively.	82
3.6	Asymmetric unit ORTEP diagrams (50% probability) of Mn-5TIA-1, -2 and -3.	87
4.1	Structures of In-IA and In-5TIA MONTs: a) Schematic view IA ligand, showing the angle 118° between two carboxylic acid moiety and forms three centered MONT with In(III). (b) and (c) Schematic view of functionalized 5-TIA ligand, showing the angle 115° between two carboxylic acid moiety and forms four centered MONT with In(III) and Cd(II) respectively. Color code: In (green), Cd (light blue), N (blue), O (red), C (gray) and H (white).	92
4.2	(a) The cross sectional view of In-5TIA MONTs. (b) Self assembled MONTs are arranged in three dimensional manners. (c) Simplified view of a eight-connected Indium center, yellow stick indicates each $\mu_1$ -CO <sub>2</sub> <sup>-</sup> carboxyl group connected with octahedral In(III) node (d) Side view of the simplified nanotube structure (e) packing view of three different self assembled MONTs.	93
4.3	Thermal gravimetric analysis (TGA) data of (a) In-5TIA and (b) Cd-5TIA. Variable temperature powder Xray diffraction VTPXRD data of (c) In-5TIA and (d) Cd-5TIA comparison with the simulated one clearly indicates its high crystallinity as well as thermal stability at broad temperature range (25 °C to 150 °C).	95
4.4	Equivalent circuit model representation of the Nyquist plot.	96
4.5	Nyquist plots of (a) In-5TIA MONT (b) Cd-5TIA MONT and (c) In-IA MONT at 31 °C under 98% RH (b) Arrhenius plots of activation energy for In-5TIA, Cd-5TIA and In-IA MONTs.	97

4.6	Proton conductivity vs humidity plot of (a) In-5TIA and (b) Cd-5TIA, shows that at lesser humidity decrease in proton conductivity values. Proton conductivity plots of (c) In-5TIA and (b) Cd-5TIA, at 60% RH shows decrease in proton conductivity values.	98
4.7	Water vapour adsorption plot at 298K and 1 bar pressure for (a) In-5TIA and (b) Cd-5TIA. Filled circle represents adsorption and empty circle represents desorption.	99
4.8	Proton conductivity plots of (a) In-5TIA at lower temperature, (b) In-5TIA at elevated temperature, (c) Cd-5TIA at lower temperature, (d) Cd-5TIA at elevated temperature, (e) In-IA at lower temperature and (f) In-IA at elevated temperature.	103
4.9	Schematic view of stacking triazole incorporated in the one dimensional nanotube which is the key factor for proton conduction.	104
4.10	Possible scheme of Grotthuss proton hopping mechanism of In and Cd-5TIA.	104
4.11	Proton conductivity vs temperature plot of (a) In-5TIA and (b) Cd-5TIA with increasing temperature.	105
4.12	Comparison of the experimental PXRD pattern of as-synthesized (a) In-5TIA(top) and (b) Cd-5TIA (top) with the one simulated from its single crystal structure (bottom).	108
4.13	ORTEP diagram of the asymmetric unit of (a) In-5TIA and (b) Cd-5TIA.	113
5.1	Schematic representation of isophthalic acid (IA) moiety and In(III)(CO <sub>2</sub> <sup>-</sup> ) <sub>4</sub> SBU. Two dimensional (2D) structure of In-IA-2D-1 and -2, indicating [(CH <sub>3</sub> ) <sub>2</sub> NH <sub>2</sub> ] <sup>+</sup> cations inside In-IA-2D-1 framework, and [(CH <sub>3</sub> ) <sub>2</sub> NH <sub>2</sub> ] <sup>+</sup> cations as well as DMF molecules inside the In-IA-2D-2 framework. (Note: Zoomed in figures have been rotated 90° for clarity).	116
5.2	Three dimensional packing orientations of (a) In-IA-2D-1 and (b) In-IA-2D-2 MOFs. Each 2D layer clarified by different color. (c) and (d) structural difference of In-IA-2D-1 and -2.	117
5.3	Variable temperature powder Xray diffraction (VTPXRD) data of (a) In-IA-2D-1 and (b) In-IA-2D-2 comparison with the simulated one clearly indicates its high crystallinity as well as thermal stability at broad temperature range (25 °C to 200 °C). (c) PXRD analysis of as synthesized (Expt), humidified (under 98% RH for 3 days) and preheated at 350 °C of In-IA-2D-1 in comparison with the simulated (d) Thermal gravimetric analysis (TGA) data of In-IA-2D-1 and In-IA-2D-2.	118
5.4	Powder X-ray diffraction analysis of (a) as synthesized (Expt) and pre heated (200 °C and 350 °C) samples of In-IA-2D-2 in comparison with the simulated one and (b) In-IA-2D-2 as synthesized (Expt), 98% Relative humidified condition and 98% RH then heated to 90 °C and 120 °C of In-IA-2D-2 . All these case it is clearly indicates its high crystallinity, purity as well as stability at long time humidified condition.	119

5.5	Equivalent circuit model representation of the Nyquist plot.	120
5.6	(a) Nyquist plot of In-IA-2D-1 at 27 °C in 98% RH (b) Nyquist plot of In-IA-2D-2 at 27 °C in 98% RH.	121
5.7	Proton conductivity plots at lesser humidity (60% RH) of (a) In-IA-2D-1 showing decrease in proton conductivity values $2.4 \times 10^{-5} \text{ Scm}^{-1}$ and (b) In-IA-2D-2 showing decrease in proton conductivity values $6.2 \times 10^{-5} \text{ Scm}^{-1}$ . Proton conductivity vs. temperature plots of (c) In-IA-2D-1 and (d) In-IA-2D-2 under 98% RH.	122
5.8	Proton conductivity plots of In-IA-2D-1 at (a) lower temperature and (b) higher temperature under 98% RH showing decrease in proton conductivity. Proton conductivity plots of In-IA-2D-2 at (c) lower temperatures and (d) elevated temperatures under 98% RH.	124
5.9	Arrhenius plot of activation energy (under 98% RH) for In-IA-2D-1 and -2 MOFs.	125
5.10	Water vapor adsorption of In-IA-2D-1 at STP	126
5.11	Schematic representation of increasing hydrophilicity of In-IA-2D-2 via DMF removal at 90 °C, confirmed by water vapor adsorption experiment at STP.	127
5.12	In situ variable temperature single crystal XRD structures and anhydrous proton conductivity plot of In-IA-2D-2 at 25, 90 and 95 °C. Electron density of DMF resides in the cavity dispersed considerably at temperatures beyond 90 °C.	128
5.13	Anhydrous proton conductivity plots of In-IA-2D-2 at different temperatures (40, 55, 65 85 °C) for 1, 2 and 4 hrs respectively.	130
5.14	Intermolecular distance between proton hopping sites in the crystal structure of In-IA-2D-2.	131
5.15	Schematic representation and possible proton hopping mechanism of In-IA-2D-2 MOF under anhydrous condition. The arrows indicate the possible movement of the $\text{H}^+$ ion.	132
5.16	Comparison of the experimental PXRD pattern of (a) as-synthesized In-IA-2D-1 (top) with the simulated one from its single crystal structure (bottom) and (b) as-synthesized In-IA-2D-1 (top) with the simulated one from its single crystal structure (bottom).	133
5.17	ORTEP diagram (50% probability) of the asymmetric unit of In-IA-2D-1.	136
5.18	ORTEP diagram (50% probability) of the asymmetric unit of In-IA-2D-2 MOF.	137
5.19	ORTEP diagrams (50% probability) of In-IA-2D-2 single crystal X-ray data at variable temperature (35, 55, 75 and 95 °C).	138
6.1	RHO topology of 5-amino tetrazole with Zn(II) and Co(II) metal could be the suitable candidates for high $\text{CO}_2$ uptake.	141
6.2	Induction of polar functionality in ZTF (a) 5-nitro tetrazole based zeolitic MOF (b) and (c) Incorporation of polar functional group $-\text{F}$ and $-\text{Cl}$ in 5 position of tetrazole moiety could enhance the high	142
6.3	Scheme of synthesis and proposed proton conduction mechanism in phosphoric acid doped benzimidazole based covalent organic frameworks	143

6.4	Scheme of synthesis and structures of stable COFs loaded with n-tetrabutylammonium hydroxide (NBu <sub>4</sub> OH) salts inside the pore surface. Hydrophobic interaction between NBu <sub>4</sub> <sup>+</sup> cations and COF frameworks leaves OH <sup>-</sup> ions free for conduction.	145
-----	---	-----

**Table**

1.1	The advantages and disadvantages of various synthetic techniques of MOFs	4
1.2	Recent reports of MOF based catalysts used for different catalysis reaction.	8
1.3	Advantages and disadvantages of zeolites and porous carbons.	12
1.4	High-Pressure CO <sub>2</sub> Adsorption Capacities in MOFs	14
1.5	Low-Pressure CO <sub>2</sub> Adsorption Capacities in MOFs.	17
1.6	Proton-conducting MOFs under hydrous condition reported in literature.	35
2.1	Types of ZIFs (including the number of times) reported in the literature and the M-X-M bond angle range.	44
2.2	Pore volume, surface area and CO <sub>2</sub> uptake of all Co and Zn-ZIFs	52
2.3	Ranking of low pressure (1 bar) CO <sub>2</sub> Adsorption Capacities in Metal Organic Frameworks at 273K and 298K	54
2.4	Atomic charges in ZTF-1 with the atomic labels indicated in Figure 2.18c	57
2.5	Types of structure directing agents used for the synthesis of ZTF-1	64
4.1	Comparison of Proton Conductivity Values of Cd-5TIA and In-5TIA with other proton conducting MOF.	99
4.2	Low temperatures Proton Conductivities of In-5TIA and Cd-5TIA	101
4.3	High temperature Proton Conductivities of In-5TIA and Cd-5TIA	102
5.1	Low temperatures proton conductivities of In-IA-2D-1 and -2.	123
5.2	High temperatures proton conductivities of In-IA-2D-1 and -2	123
5.3	Comparison of hydrous proton conductivity values of In-IA-2D-1 and In-IA-2D-2 with other proton conducting MOFs.	125
5.4	Anhydrous proton conductivity values of In-IA-2D-2 at different temperatures.	129
5.5	Comparison of anhydrous proton conductivity values of In-IA-2D-2 with other proton conducting MOFs.	129

## CHAPTER 1

# INTRODUCTION OF POROUS METAL ORGANIC FRAMEWORKS (MOFs): SYNTHESIS, STRUCTURE AND APPLICATIONS

### 1.1 Background of porous materials:

Porous materials are solid-state materials possessing permanent pores or voids that are accessible for gases or solvents [1.1]. They are useful in gas storage, separation, shape/size selective catalysis etc [1.1]. Depending on the size of the pores, porous materials are classified mainly in three different categories. (a)

#### **Microporous materials**

[pore size 0.2-2 nm e.g., zeolites and metal organic frameworks] (b)

#### **Mesoporous materials**

[pore size 2-50 nm e.g., silica and alumina]. (c)

#### **Macroporous materials**

[pore size 50-1000 nm e.g., Inverse opals and foams]

[1.2]. The most common organic porous material having high surface area

and high adsorption capacities is activated carbon which is synthesized by the pyrolysis of carbon-rich materials. Despite the lack of periodicity in the structure, porous carbons have been extensively used for gas storage, separation, purification of water, solvent removal, etc. However, low surface area, poor selectivity and lack of crystallinity limit their use in large scale applications and investigation.

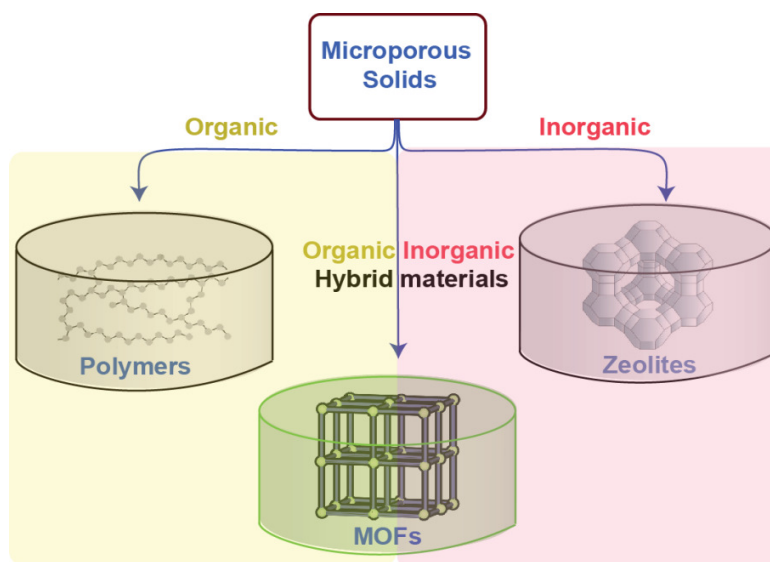


**Figure 1.1:** Schematic representations of the types of microporous solids (polymers for porous organic solids, zeolites for porous inorganic solids and MOFs for porous organic inorganic hybrid solids).



On the other hand, inorganic porous materials such as zeolites, although possess highly ordered three dimensional structure and higher surface area than organic materials, suffer from structural instability during the isolation process. Hence, the necessity of developing a stable, rigid and crystalline porous material capable of efficient gas adsorption and storage, and gas separations, remains a big challenge till today. Metal

organic frameworks (MOF's), a hybrid porous crystalline materials, principally comprised of coordination bonds between metal nodes (SBU's) and organic linkers (Figure 1.1 and 1.2), have emerged as most promising candidate for sorbent applications [1.3]. MOFs have much higher surface area for gas adsorption than traditional materials (zeolites, carbon etc). The greatest advantages of crystallinity in MOF materials provide the unique opportunity to determine the high resolution

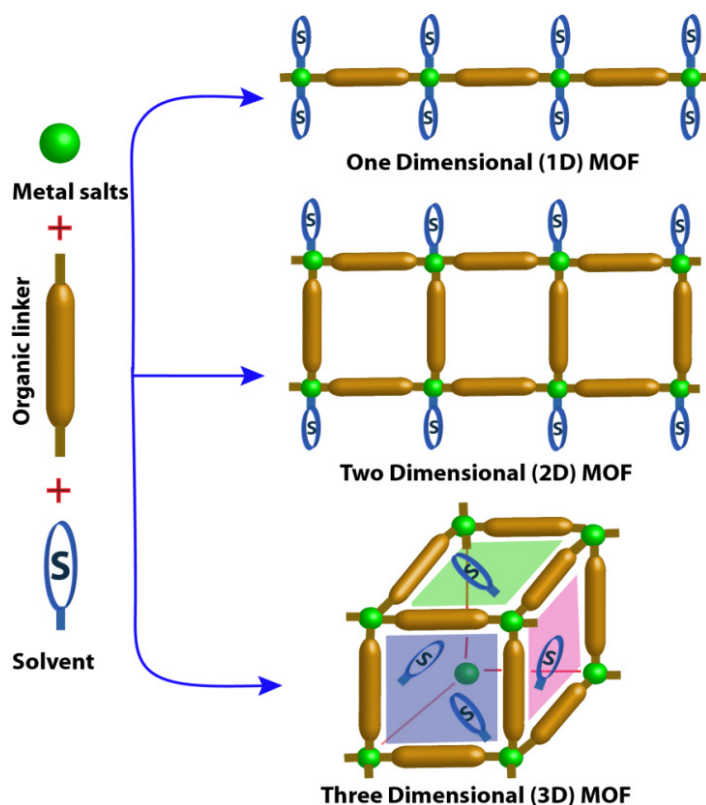


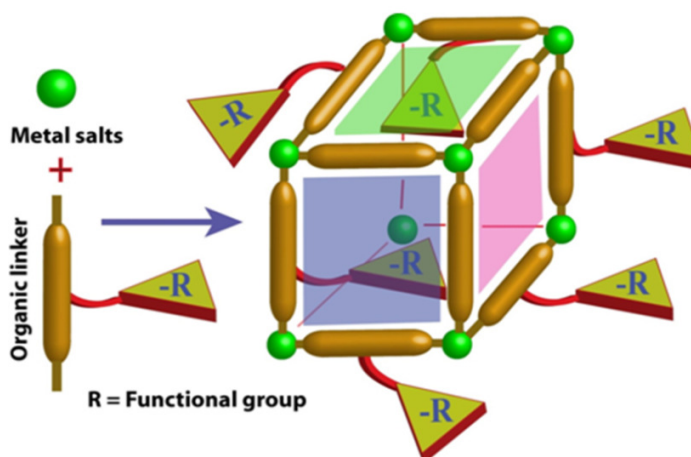
**Figure 1.2:** Model representation of 1D, 2D and 3D MOF constructed from organic linkers, metal salt and solvent molecules.

crystal structure and accurate pore size/dimension of the MOF channel. This in turn, provides better insight into the structural parameters that facilitates rational design of MOF architectures (Figure 1.3). In addition, various reaction sites of the organic linkers inside MOF channels facilitate post-synthetic modification, a unique advantage, which is beyond the scope of organic or inorganic adsorbent materials. The porosity of MOF materials have been utilized for traditional applications that includes gas adsorption and storage, gas separation etc. [1.3]. However, in recent years, focus has been shifted to other interesting applications such as proton conduction, charge carrier motion, oxygen reduction catalysis, light harvesting etc. [1.4]. These applications are particularly interesting in terms of

renewable energy research involving MOF materials. In the following parts of this chapter, we shall focus on a brief overview of synthesis, structural and different applications of MOF's.

## 1.2. Synthesis of MOFs:

The synthesis of metal-organic frameworks (MOFs) has been focused mainly due to the possibility in obtaining undiscoverable structures which could be of great interest for various applications. Generally, MOFs are synthesized by liquid phase synthesis method where metal salts and ligand solutions are mixed together

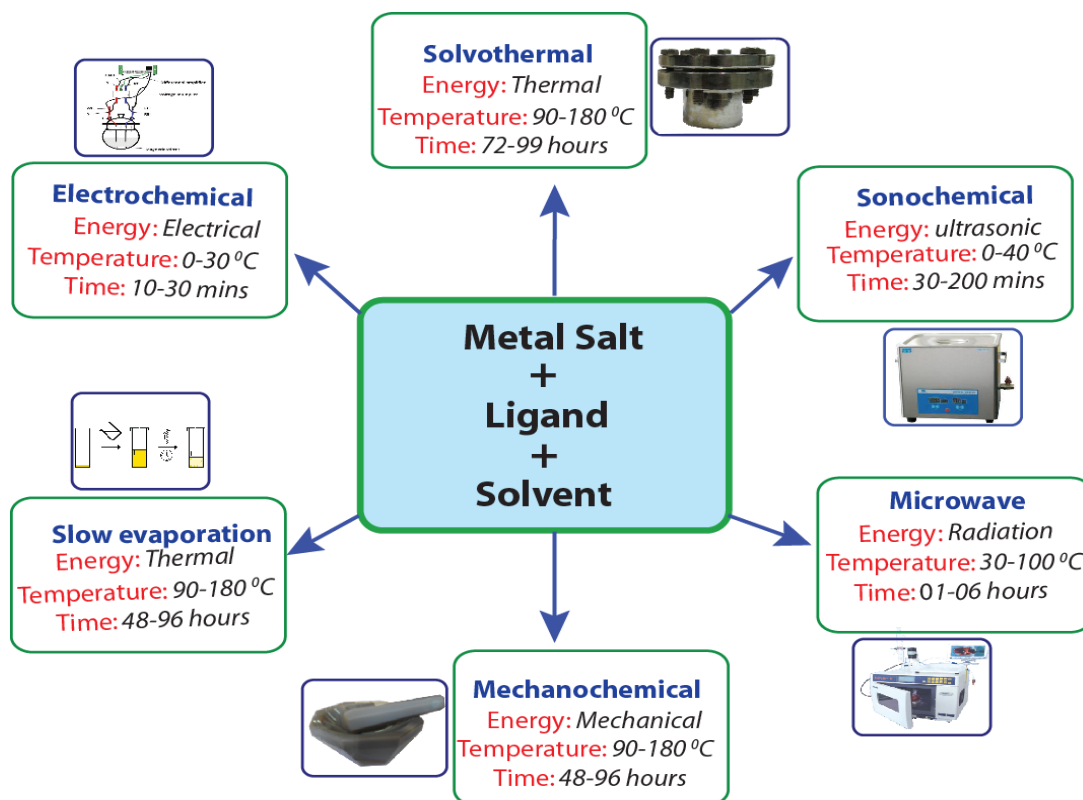


**Figure 1.3:** Model representation of three dimensional functionalized MOF.

or solvent is added to the mixture of solid salt and ligand in culture tube and heated it at higher temperature (100-180 °C). Solvent is the most important factor of a particular reaction which determines the thermodynamic control as well as activation energy of the system and also enhance the crystallinity at higher extent. Generally, for high temperature solvothermal reactions, high boiling solvents like DMF, DEF, NMP etc. have been used. To enhance the rate of synthesis in solvothermal process, researchers have discovered high-throughput methods for higher scale production of MOF. Solid phase reactions were also attempted for the synthesis of MOFs due to its easier, quicker, and solvent free synthesis despite the poor crystallinity of the product. One of the examples of solid phase reaction is the mechano-chemical synthesis where MOFs have been synthesized using the internal activation energy created by mechanochemical force. Additional synthetic techniques like electrochemical synthesis, microwave-assisted synthesis, slow evaporation synthesis, sono-chemical synthesis etc have been attempted for synthesis of MOFs. Although, it is worth mentioning that solvothermal process have been used routinely for the synthesis of high crystalline 3D metal organic frameworks (Figure 1.4 and Table 1.1) illustrated the condition used, advantages and disadvantages for all these synthetic techniques.

**Table 1.1:** The advantages and disadvantages of various synthetic techniques of MOFs

Synthetic techniques	Advantages	Disadvantages	Ref
<b>Solvothermal</b>	(a) High crystallinity and Purity in large scale. (b) Possibility to get the 3D structure.	(a) Need of expensive autoclaves. (b) The impossibility of observing the crystal as it grows.	1.5
<b>Sonochemical</b>	(a) Rapid reaction rate. (b) High purity, narrow size distributions, controllable reaction conditions.	(a) Low crystallinity. (b) Evaporation of volatile solvent during the reaction.	1.5
<b>Microwave</b>	(a) Quick synthesis of MOF. (b) High crystallinity and purity.	(a) For less polar reactants and solvents microwave assisted reactions are extremely slow. (b) Low possibility to get the desired product.	1.5
<b>Mechanochemical</b>	(a) Quick synthesis of MOF. (b) Solvent free synthesis.	(a) Low crystallinity and purity. (b) Low surface area and poor gas adsorption uptake.	1.5
<b>Slow evaporation</b>	(a) Small amounts of substrates give good crystals. (b) Parameters are easy to control	(a) Needs a lot of material, starts with saturated solution. (b) Air sensitive starting materials are not suitable for reaction.	1.5

**Figure 1.4:** Scheme of various synthetic approaches and conditions used for the preparation of MOFs.

### 1.3 Structure of MOFs:

Solid state materials like zeolites and activated carbons have no control over the structural integrity because the starting materials do not maintain their arrangement [1.6]. However, MOF maintain their structural integrity during the synthesis because of their rigid molecular building blocks and reaction condition. While considering the structure of MOFs, it is helpful to recognize the reticular synthesis, the process of assembling judicious primary building blocks and secondary building units (SBUs), which dictate the final topology of a framework (Figure 1.5).

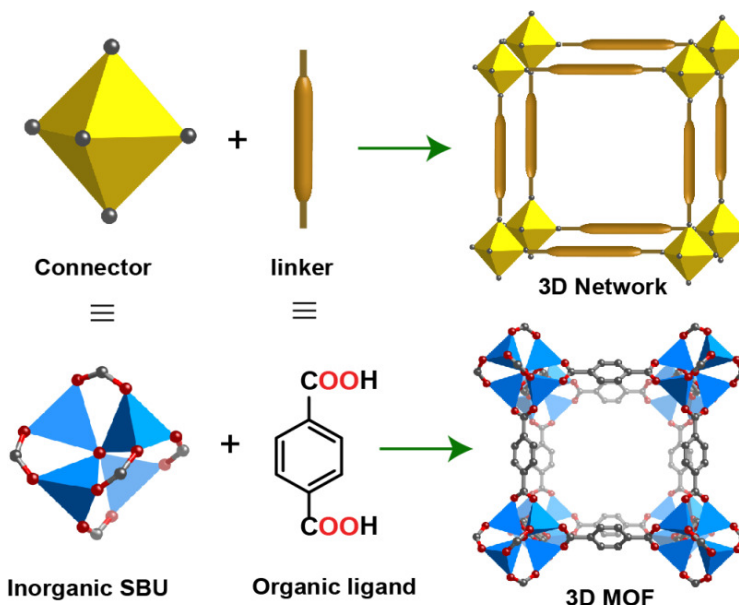


**Figure 1.5:** Model representation for the construction of 3D network generated from the connector and linker (top). Similarly 3D MOF [redrawn the structure from the cif file of MOF 5 (1.8)] synthesized by assembling secondary building units (SBUs) and organic linker, which dictate the final topology of a framework.

The SBUs which predetermine ordered structures held together by strong coordination bonds and expected to result into the formation of different geometric shapes. Generally, MOF synthesis was performed by reacting two types of primary building units. One is the multitopic organic linker and another one is polytopic metal centre or metal cluster. During the synthesis, two primary building units get assembled and connects to form secondary building units (SBUs) which finally self assembled at higher dimension and construct different (1D, 2D and 3D) MOF architectures. Reticular chemistry [1.7] defines the three dimensional architecture when metal clusters are abstracted as shape such as triangle, square, tetrahedra, and octahedra and joined into a periodic fashion. All types of network structures (organic, inorganic or organic-inorganic hybrid materials) possess inherent nets, and the interest of researchers is the topological construction of MOF networks based on

rational assembly of building units in different dimensions [1.7a]. The detailed investigation of the structure of MOF-5 which consists of tetrahedral  $ZnO_4$  SBU connected with organic linker terephthalic acid and builds a three dimensional cubic network structure with interconnected pores of 8 Å apertures and 12 Å pore diameter [1.8]. In contrast, by changing the metal building block from  $Zn_4O$  to  $Cr_3O$  keeping terephthalic acid intact generate totally different structure called MIL-101 which have diverse pore aperture and diameter (3nm) compared to MOF-5.

#### 1.4 Properties and Applications of MOFs:

Since, the application of MOF covered diverse area (Figure 1.6). Hence, in order to convey the enormous potential of MOFs, we highlighted the selected applications of MOF which are extensively studied in the literature.

**Gas storage in MOFs:** In the past two decades, much attention has been paid to increase the storage of fuel gases such as hydrogen and methane under practical conditions. Hydrogen possess enormous amount of energy and considered as an attractive fuel due to its high gravimetric energy density and heat of combustion. However, due to its very small volumetric density,  $0.0899 \text{ kg/m}^3$  at STP, storing hydrogen at ambient temperature and pressure is very difficult [1.9]. Even in the liquid state, the volumetric density of hydrogen  $70.8 \text{ kg/m}^3$  is very low compare to gasoline. As a result, serious difficulties need to be faced during the  $H_2$  filling at lower temperature (20.27 K). From the last decades, MOFs have been used for the  $H_2$  storage materials due to its permanent porosity and high surface area [1.10]. The first study of hydrogen adsorption was reported in 2003 for MOF-5 which shows high BET surface area ( $3800 \text{ m}^2\text{g}^{-1}$ ) and 7.1 wt%  $H_2$  uptake at 40 bar and 77 K [1.11a]. After that, more than 300 MOFs have been tested till now for their  $H_2$  uptake capacity. The highest  $H_2$  uptake in NOTT-112 reaches up to 10 wt% at 77 bar and 77 K [1.11b]. On the other hand, NU-100 and MOF-210 [1.11c and d] exhibit hydrogen adsorption as high as 7.9 to 9.0 wt% at 56 bar for both MOFs and 15 wt% at 80 bar for MOF-210. In general, the functionality of organic linkers has little influence on hydrogen adsorption, whereas increasing the pore volume and surface area of MOFs markedly enhances the gravimetric hydrogen uptake at 77 K under high pressure [1.10]. However, for volumetric hydrogen capture, adsorption enthalpy of hydrogen ( $Q_{st}$ ) plays the role rather

than surface area. In this condition, unsaturated open metal sites are the effective tool to enhance the hydrogen uptake capacity in MOF architecture.

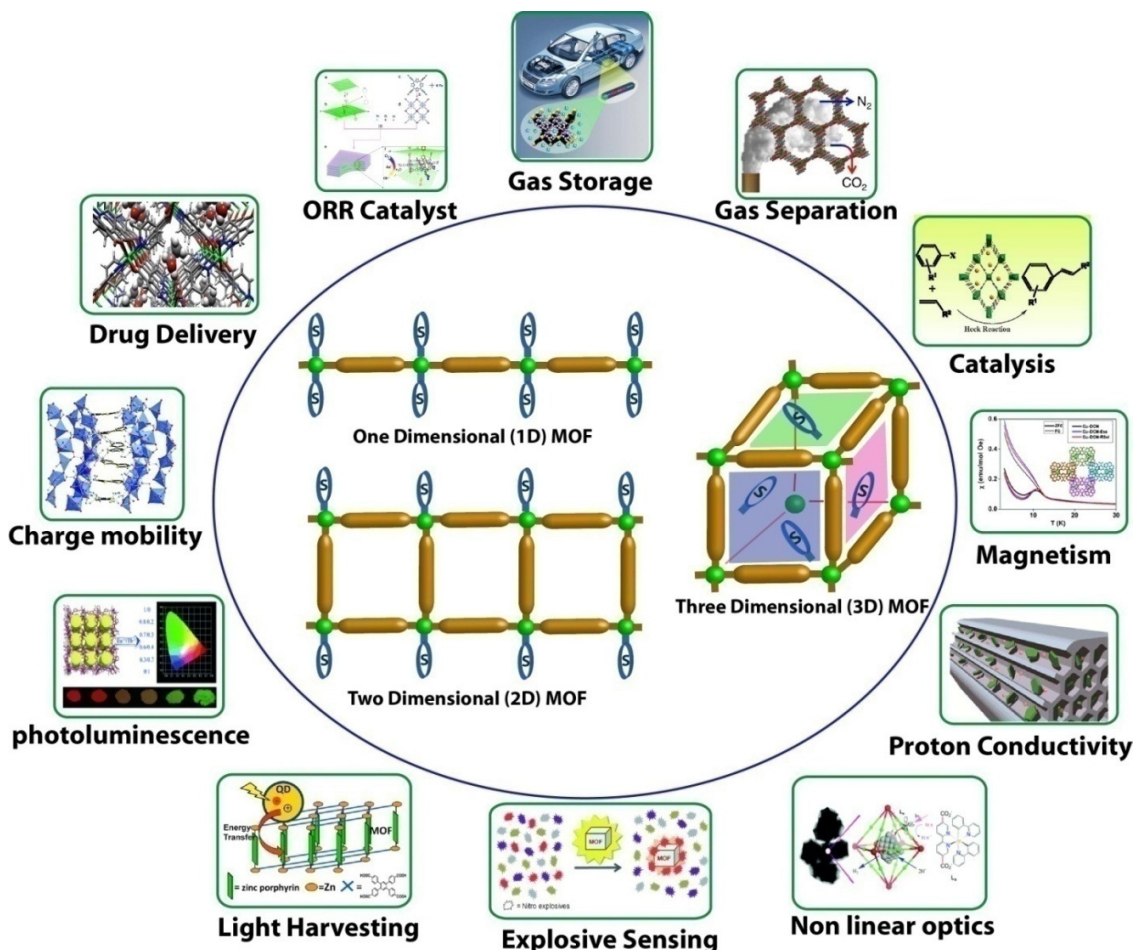


**Figure 1.6:** Various applications of MOFs such as gas storage, separation, catalysis, drug delivery, magnetism, proton conductivity, non linear optics, light harvesting, photoluminescence, explosive sensing, charge carrier mobility etc.

Natural gas is another good candidate for on-board fuel. The main component of natural gas is methane, which is an alternative high-density fuel source compare to hydrogen and gasoline. The first report of high-pressure methane adsorption in an extended metal-organic structure  $[\text{CuSiF}_6(\text{BPy})_2]$ , which demonstrated an uptake capacity of 104 mg/g at 36 atm and 298 K [1.12]. It is believed that, two competing factor such as high surface area and open metal sites are responsible for high methane uptake. Afterward, methane uptake measurement was reported for MOF-177, MOF-200 and MOF-210 are 345  $\text{mg g}^{-1}$ , 446  $\text{mg g}^{-1}$ , and 476  $\text{mg g}^{-1}$ , respectively, at 80 bar and 298 K [1.13 and 1.11d]. The



increased surface area is the main factor for enhancement of methane uptake at high pressure. Apart from H<sub>2</sub> and CH<sub>4</sub>, MOFs also offer reversible carbon dioxide adsorption and are promising materials for the selective capture of carbon from the atmosphere and flue gas. The detailed description of CO<sub>2</sub> storage in MOFs is discussed in the section 1.5

**Catalysis in MOFs:** The high surface areas, uniform pore size and high density of active sites within the open structures of MOFs offer their use in catalysis [1.14]. MOFs can be used to support homogeneous catalyst, short-lived catalysts, molecular catalysts, and encapsulate catalysts within their inner space. The first example of catalysis in MOF, reported in 1994, involved the cyanosilylation of aldehydes by a 2D MOF (layered square grids) of formula [Cd(BPy)<sub>2</sub>(NO<sub>3</sub>)<sub>2</sub>; BPy=4,4'-bipyridine]. This investigation centered mainly on size and shape selective clathration. The majority of the known catalytic MOFs, together with descriptions of the specific catalyzed are tabulated in Table 1.2.

**Table 1.2:** Recent reports of MOF based catalysts used for different catalysis reaction.

Chemical formula	Name of the MOF	Substrate used	Reactions for catalysis	Conv (%)	Ref
Cd(BTAPA) <sub>2</sub> (NO <sub>3</sub> ) <sub>2</sub>		Benzaldehyde and malononitrile	Knoevenagel condensation	98	1.15a
Zn <sub>4</sub> O(BDC-NH <sub>2</sub> ) <sub>3</sub>	IRMOF-3	Benzaldehyde and ethyl cyanoacetate	Knoevenagel condensation	99	1.15b
Cr <sub>3</sub> O(H <sub>2</sub> O) <sub>2</sub> F(BDC) <sub>3</sub>	MIL-101(Cr)	Benzaldehyde and ethyl cyanoacetate	Knoevenagel condensation	98	1.15c
Fe <sub>3</sub> O(H <sub>2</sub> O) <sub>3</sub> F(BTC) <sub>2</sub>	MIL-100(Fe)	4-Nitrobenzaldehyde and ethyl 2 cyano acetate	Aerobic oxidation of thiophenol	>99	1.15d
Zr <sub>3</sub> O <sub>2</sub> (OH) <sub>2</sub> (BDC-X) <sub>3</sub>	UiO-66-X (X = NH <sub>2</sub> , Cl, Br, NO <sub>2</sub> )	(+)-Citronellal	Cyclization of citronellal	15-100	1.15e
Zn <sub>2</sub> Sn(IV)(TPyP)(HCOO) <sub>2</sub> (H <sub>2</sub> O) <sub>4</sub>		Xe light	Photo-oxygenation of 1,5- dihydroxy naphthalene	>99.8	1.15f
Cd(BPy) <sub>2</sub> (NO <sub>3</sub> ) <sub>2</sub>		Benzaldehyde and cyanotrimethylsilane	Cyanosilylation of aldehyde	77	1.15g
Ce(MDIP)(H <sub>2</sub> O)	Ce-MDIP1	2-Naphthaldehyde and cyanotrimethylsilane	Cyanosilylation of aldehyde	>98	1.15h
[(iPrO)TiCl] <sub>2</sub> (L2)		Acrolein and 1,3-cyclohexadiene	Diels-Alder reaction	100	1.15i
Cd(BTB)(L-IP)(H <sub>2</sub> O) <sub>4</sub>	Cd-TBT	4-Nitrobenzaldehyde and cyclohexanone	Aldol reactions	97	1.15j
Zn <sub>4</sub> O(BDC) <sub>3</sub>	MOF-5	Toluene and benzyl	Friedel-Crafts	>99	1.15k

		bromide	alkylation reactions		
$Zn_2(L3)(BPY)_2$	NU-601	<i>N</i> -methylpyrrole and ( <i>E</i> )-1-nitroprop-1-ene	Friedel Crafts reactions between pyrroles and nitroalkenes	98	1.15l
$Pd-Al(OH)(BDC-NH_2)$	$Pd/MIL-53(Al)-NH_2$	Bromobenzene and phenylboronic acid	Suzuki-Miyaura coupling	29-97	1.15m
$Cu(PdCl_2BPY)$		Phenyl halides and arylboronic acid	Suzuki-Miyaura coupling	75-99	1.15n
$Cu(Ac)_2(PBBM)(CH_3OH)$		2,6-Dimethylphenol	Oxidative coupling of dimethylphenol	90	1.15o
$(Zn_4O)_3(BDC-C_8H_5O_4NIn)_3(BTB)_4$	UMCM-1-	2-Phenylloxirane and aniline	Epoxide ring-opening reactions	99	1.15p
$Ln(OH)(1,5-NDS)$	$LnPF-1$	Linalool	Epoxidation of olefin	76-100	1.15q
$Pt-Zn_4O(BTB)_2$	$Pt@MOF-177$	2-Chlorobenzyl alcohol	Oxidation of alcohol	99	1.15r
$Au-Zn(2Me-Im)_2$	$Au@ZIF-8$	CO and O <sub>2</sub>	Oxidation of CO	100	1.15s
$Ni(BPy)(HBTC)$		NH <sub>3</sub> BH <sub>3</sub>	H <sub>2</sub> generation	100	1.15t
$Ni + Tb_{16}(TATB)_{16}$	$Ni-MesMOF-1$	Nitrobenzene, NaBH <sub>4</sub>	Hydrogenolysis of nitrobenzene	>99	1.15u
$In_2(OH)_3(BDC)_{1.5}$		Nitrobenzene and 2-methyl-1-	Reduction of nitroaromatic	100	1.15v

Apart from these applications, several other applications (viz, gas separation, drug delivery, magnetism, proton conductivity, non linear optics, light harvesting, photoluminescence, explosive sensing, charge carrier mobility, ORR catalyst *etc.*) are also documented in MOF chemistry. The detailed applications of MOFs are pictorially assembled and clarified in Figure 1.6. However, in this thesis special emphasis are given to the applications of MOFs as platform of two major aspects (1) MOFs for high CO<sub>2</sub> uptake and (2) MOFs for high proton conduction (Figure 1.7). Since, the application of CO<sub>2</sub> storage and proton conduction is connected with the green environment and clean energy related issues that motivated us to choose these applications for MOF materials. As all of us know that, the coal fire power plant produced CO<sub>2</sub> releases into the atmosphere which causes global warming (so-called greenhouse effect) [1.16]. However, the current technologies used (chemisorptions by monoethanol amines) for capturing CO<sub>2</sub> has several disadvantages [1.17]. Porous MOFs are promising materials to achieve such separations from flue gases and proposed as proficient materials to replace current technologies. On the other hand, Energy resources (coal, gas, oil and uranium) are not homogeneously distributed across the world. Many resources are at risk of becoming depleted and it is a threatening sustainability of humankind to consume more amounts of resources.



Hence, extensive research is ongoing to replace fossil fuels economy with the more sustainable energy economy. Proton exchange membrane fuel cell (PEMFC) is the device which converts chemical energy to electrical energy by combining hydrogen with oxygen produces water and heat. Faster the proton transports from cathode to anode, the efficiency of PEMFC as well electricity increases to higher extent. Recently, MOFs have been used for proton-conductivity studies and show their conduction ability almost similar to the nafion, a commercially used proton

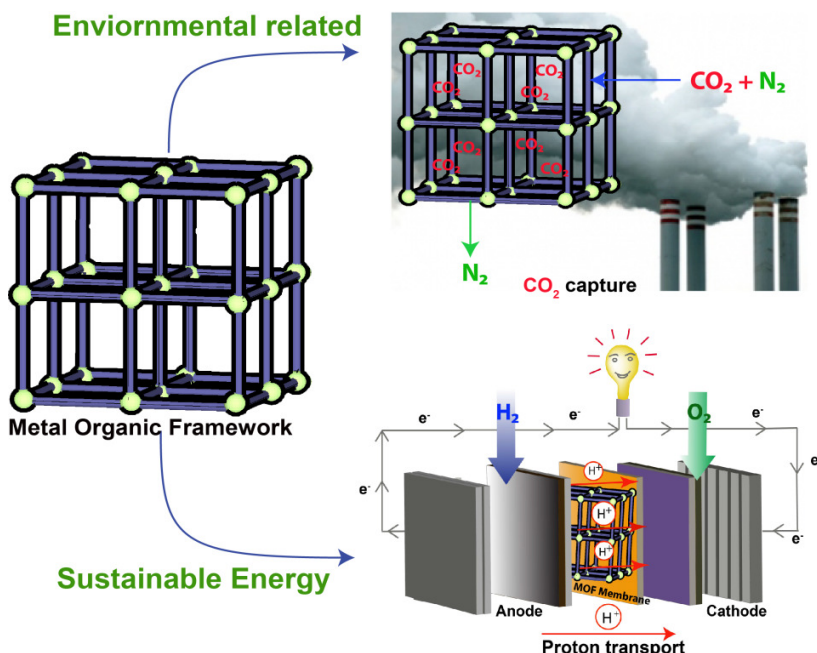


**Figure 1.7:** Model representation of MOFs and their most promising applications on high CO<sub>2</sub> uptake (environmental related) and high proton conduction (energy related).

conductor in fuel cell. In this thesis, chapter 2 and 3 will describe about the MOFs ability for high CO<sub>2</sub> uptake. On the other hand, chapter 3 and 4 will showcase the proton conducting measurement of newly synthesized MOFs and their conducting performance at variable temperatures. In the following section we will address detailed description and key aspects of MOFs for high CO<sub>2</sub> uptake as well as for high proton conduction.

### 1.5 CO<sub>2</sub> adsorption in MOFs:

Selective CO<sub>2</sub> capture from coal-fired power plant is a critical issue, as these plants produce post-combustion flue gases with ~15% CO<sub>2</sub> concentration [1.18]. At present, the separation of CO<sub>2</sub> from such a low pressure stream of gases is performed by amine sorbents through chemisorptions [1.19]. However, researchers are exploring alternative approaches as amine regeneration requires significant heating and has high operational cost. These limitations have prompted investigations on porous materials relying on reversible physisorption of

CO<sub>2</sub>, because it requires less energy for regeneration than materials relying on chemisorption (Figure 1.8) [1.20]. One such kind of porous material is Zeolite which is used as commercial adsorbents due to its low cost, robust nature and well-developed structural topology. Adsorbents like Zeolite 13X has been reported to provide uptake of

~4.7 mmol CO<sub>2</sub>/g sorbent

via physisorption [1.21].

Activated carbons also have attracted much interest as CO<sub>2</sub> adsorbents. The lower enthalpy of adsorption for CO<sub>2</sub>, promoted this material for high pressure gas adsorption

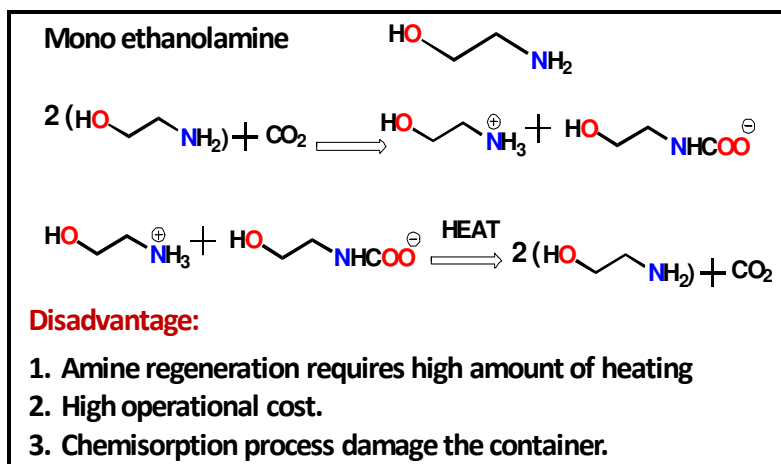


**Figure-1.8:** CO<sub>2</sub> capture process in coal fire power plant by using mono ethanolamine and the disadvantages of the process.

and separation applications. However, the common deficits of these traditional adsorbents (zeolite and activated carbons) have either difficult to regeneration processes or low capacities for CO<sub>2</sub> at low pressures [Table 1.3]. Recently, MOFs have attracted intense research interest as novel functional materials due to their superior surface areas relative to those of traditional adsorbents such as activated carbon and zeolites. Most of MOFs have porous three dimensional structures with well-defined periodicity as determined from single crystal XRD analysis. In these MOFs, solvents molecules get trapped inside the pores. However, removal of these solvents generates the open pores or channels inside the MOF architecture that are useful for other guest adsorption or loading for further application. The permanent porosity, high surface area and tailorble pore size have facilitated MOFs as suitable candidates for CO<sub>2</sub> capture. In certain circumstances, ultra-high surface area of MOFs have capacity to store nearly ten times more CO<sub>2</sub> at particular pressure than a normal empty cylinder. In this chapter, first, research on high pressure CO<sub>2</sub> storage in MOFs will be reviewed. Then, the CO<sub>2</sub> adsorption at sub-atmospheric pressure and selective CO<sub>2</sub> adsorption in MOFs will be presented and analyzed.

**Table 1.3:** Advantages and disadvantages of zeolites and porous carbons.

Physisorptive materials	Advantages	Disadvantages	Ref
<b>Zeolites (porous aluminosilicate materials)</b>	(a) High chemical and thermal stability. (b) High surface area, micro pore volume and large variety of structures. (c) Rapid adsorption of CO <sub>2</sub> and lower energy penalty for the process. (d) Some zeolites contain charge balancing metal cations within the pores, which enhances CO <sub>2</sub> uptake.	(a) Zeolites get saturated with the water vapor present in the flue gas stream; as a result the CO <sub>2</sub> adsorption capacity is consequently reduced. (b) The large enthalpy of adsorption of CO <sub>2</sub> leads to relatively high CO <sub>2</sub> desorption temperatures (135 °C-150 °C).	1.22a
<b>Activated Carbons (amorphous porous forms of carbon)</b>	(a) Higher surface areas than zeolites lead to greater adsorption capacities at high pressures. (b) Hydrophobic nature hindered the decomposition or decreased capacities under hydrated conditions. (c) Lower heat of adsorption for CO <sub>2</sub> , results lower temperature for regeneration compared with zeolites.	(a) Lower enthalpy of adsorption for CO <sub>2</sub> , and hence lower capacities for CO <sub>2</sub> compared with zeolites at lower pressures. (b) Limited only for high-pressure gas adsorption and separation applications.	1.22b

### 1.5.1 CO<sub>2</sub> adsorption in MOFs at high pressures

Reminiscent of porous materials, CO<sub>2</sub> adsorption capacities in MOFs mainly depends on the surface area at high pressures. Till now, some MOFs reported in the literature have high surface area and high CO<sub>2</sub> uptake capacity than other well known adsorbents such as MAXSORB carbons and zeolite 13X.

First demonstration of CO<sub>2</sub> adsorption has been studied in MOF-5 [Zn<sub>4</sub>O(BDC)<sub>3</sub>] [1.23] which consists of tetrahedral [Zn<sub>4</sub>O]<sup>6+</sup> clusters connected by BDC (1, 4 benzene dicarboxylic acid) linkers to form

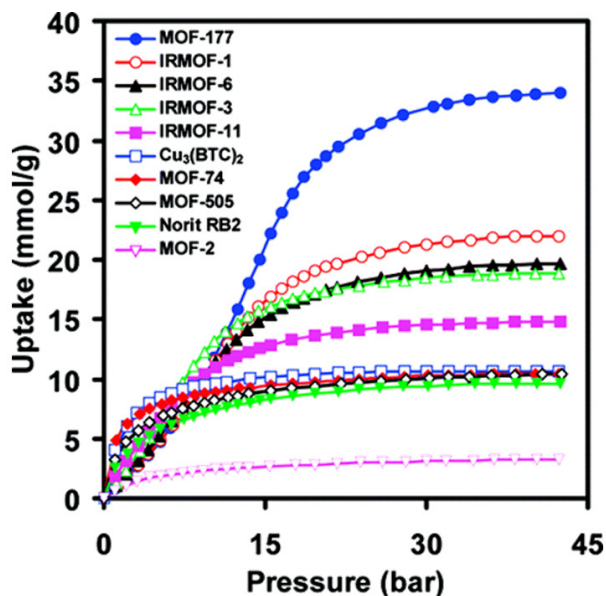


**Figure 1.9:** Comparison of gravimetric CO<sub>2</sub> capacities for all MOFs compare with activated carbon at ambient temperature and pressures up to 42 bar. Reprinted with permission, 2009 American Chemical Society.

a cubic, three-dimensional network. Afterwards, the investigation has been attempted on a series of MOFs to explore the relationship between surface area and CO<sub>2</sub> capacity. Reports of nine MOFs were examined for surface area as well as porosity to evaluate the CO<sub>2</sub> uptake capacities (Figure 1.9). All these MOFs have different structure for example, MOF-2 have square shaped channel, MOF-505 and Cu-BTC have open metal sites inside the pores, MOF-74 contains hexagonal channels, IRMOF-11 have interpenetrated structure and IRMOFs-3 and -6 have amino and alkyl-functionalized pores. Among these MOFs, the IRMOF-1 and MOF-177 consists highly porous framework. The high surface area of MOF-177 has highest CO<sub>2</sub> uptake at high pressure (60 wt% at 35 bar) among these materials. The detailed studies of surface area versus CO<sub>2</sub> uptake capacity of these MOFs at high pressure are assembled in Table 1.4.

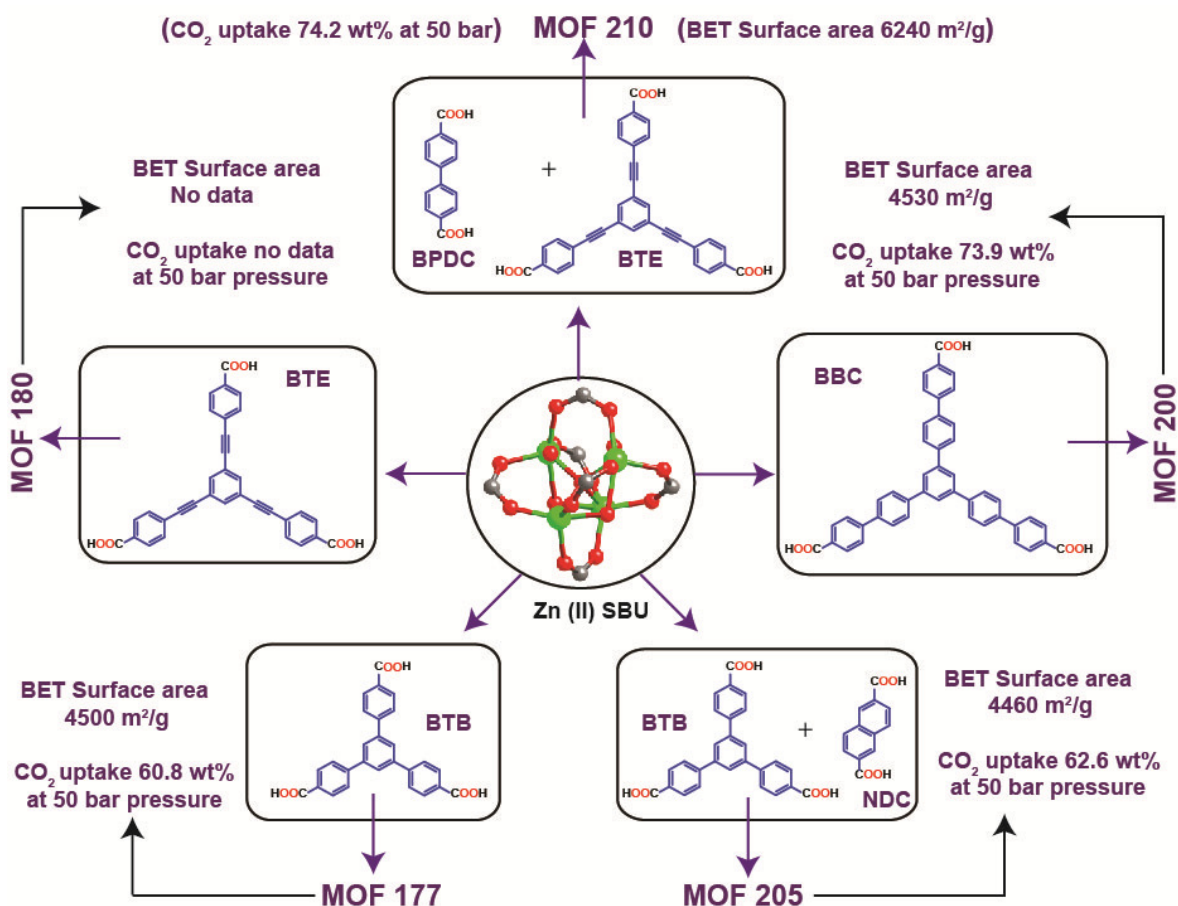


**Figure 1.10:** Zn<sub>4</sub>O(CO<sub>2</sub>)<sub>6</sub> SBU unit (middle) is connected with various types of organic linkers to form MOFs [1.11d] with high surface area and CO<sub>2</sub> uptake.

**Table 1.4: High-Pressure CO<sub>2</sub> Adsorption Capacities in MOFs**

Chemical formula	Name of the MOF	Surface area (m <sup>2</sup> g <sup>-1</sup> )		Pressure (bar)	Uptake (wt%)	Temp (K)	Ref
		Langmuir	BET				
Zn <sub>4</sub> O(BTE) <sub>4/3</sub> (BPDC)	MOF-210	10400	6240	50	74.2	298	1.11d
Zn <sub>4</sub> O(BBC) <sub>2</sub> (H <sub>2</sub> O) <sub>3</sub>	MOF-200	10400	4530	50	73.9	298	1.11d
Cu <sub>3</sub> (TCEPEB)	NU 100		6143	40	69.8	298	1.11c
Zn <sub>4</sub> O(FMA) <sub>3</sub>		1618	1120	28	69.0	300	1.24a
Mg-DOBDC	Mg-MOF-74		1542	36	68.9	278	1.24b
		2060	1800	40	39.8	313	1.24c
Zn <sub>3.16</sub> Co <sub>0.84</sub> O(BDC) <sub>3</sub>	Co21-MOF-5	2900		10	65.0	273	1.24d
Be <sub>12</sub> (OH) <sub>12</sub> (BTB) <sub>4</sub>	Be-BTB	4400	4030	40	58.5	313	1.24c
Zn <sub>4</sub> O(BDC) <sub>3</sub>	MOF-5, IRMOF-1	2900		10	58.0	273	1.24d
		3008		40	45.1	298	1.24e
Zn <sub>4</sub> O(BTB) <sub>4/3</sub> (NDC)	MOF-205	6170	4460	50	62.6	298	1.11d
Ni <sub>5</sub> O <sub>2</sub> (BTB) <sub>2</sub>	DUT-9			47	62.1	298	1.24f
Zn <sub>4</sub> O(BTB) <sub>2</sub>	MOF-177	5340	4500	50	60.8	298	1.11d
		5400	4690	40	60.6	313	1.24c
		6210	4898	30	56.8	298	1.24g
[Cu <sub>3</sub> (H <sub>2</sub> O)] <sub>3</sub> (ptei)	PCN-68	6033	5109	35	57.2	298	1.24h
Cr <sub>3</sub> O(H <sub>2</sub> O) <sub>2</sub> F(BDC) <sub>3</sub>	MIL-101(Cr)		4230	50	56.9	304	1.24i
		4792	3360	30	50.2	298	1.24j
Ni <sub>2</sub> (dobdc)	Ni-MOF-74, CPO-27-Ni		1218	22	54.2	278	1.24k
[Cu(H <sub>2</sub> O)] <sub>3</sub> (ntei)	PCN-66	4600	4000	35	53.6	298	1.24h
Zn <sub>4</sub> O(BDC)(BTB) <sub>4/3</sub>	UMCM-1	6500	4100	24	52.7	298	1.24l
[Cu(H <sub>2</sub> O)] <sub>3</sub> (btei)	PCN-61	3500	3000	35	50.8	298	1.24h
Cu <sub>4</sub> (TDCPTM)	NOTT-140		2620	20	46.2	293	1.2m
Tb <sub>16</sub> (TATB) <sub>16</sub> (DMA) <sub>24</sub>		3855	1783	43	44.2	298	1.2n
Cr <sub>3</sub> O(H <sub>2</sub> O) <sub>3</sub> F(BTC) <sub>2</sub>	MIL-100(Cr)		1900	50	44.2	304	1.24i
Cu <sub>3</sub> (BTC) <sub>2</sub>	HKUST-1		1270	300	42.8	313	1.24o
			2211	40	40.1	303	1.24p
			1571	15	35.9	298	1.24q, 1.24r
H <sub>3</sub> [(Cu <sub>4</sub> Cl) <sub>3</sub> (BTTri) <sub>8</sub> ]	Cu-BTTri	2050	1750	40	42.8	313	1.24c
Co(BDP)	Co-BDP	2780	2030	40	41.3	313	1.24c
Zn <sub>2</sub> (BDC) <sub>2</sub> (DABCO)				15	37.6	298	1.24s
Zn(MeIm) <sub>2</sub>	nanoZif-8		1264	30	35.0	298	1.24t
Al(OH)(BDC)	MIL-53(Al)			25	30.6	304	1.24u
Al(OH)(BDC-NH <sub>2</sub> )	amino-MIL-53(Al)			30	30.0	303	1.24v
Zn <sub>2</sub> (BPnDC) <sub>2</sub> (bpy)	SNU-9	1030		30	29.9	298	1.24w
Al(OH)(ndc)	DUT-4	1996	1308	10	26.4	303	1.24x
Cr <sub>3</sub> O(H <sub>2</sub> O) <sub>2</sub> F(BDC) <sub>3</sub>	MIL-101(Cr)			5.3	26.0	283	1.24y
Zn(F-pymo) <sub>2</sub>	β-Zn(F-pymo)			28	26.0	273	1.24z



In order to investigate the relationship between high surface area and CO<sub>2</sub> uptake in MOF networks, a series of ultrahigh porous MOFs were reported [1.11d], constructed from Zn<sub>4</sub>O(CO<sub>2</sub>)<sub>6</sub> building unit with single or multiple organic linkers (Figure 1.10).

These are MOF-210, -205 and -200 and compared their surface area as well as CO<sub>2</sub> uptake with MOF-177, MOF-180. It has been observed that, MOF-210 (pore volume 3.60 cm<sup>3</sup>g<sup>-1</sup>) having highest BET and Langmuir surface area (6240 and

10400 m<sup>2</sup>g<sup>-1</sup> respectively), showed 74.2% of CO<sub>2</sub> uptake at 50 bar pressure. The ultrahigh porosity of MOF achieved by increasing length of organic linker from BTB to BTE and BBC to form highly porous MOF-180 and MOF-200. The Langmuir and BET surface area of MOF-200 are 10400 and 4340 m<sup>2</sup>g<sup>-1</sup> respectively. The CO<sub>2</sub> uptake of MOF-200 at 50 bar pressure and 298 K is ~74wt%. Thus, from the above discussion it is clear that CO<sub>2</sub> capacities at high pressures depend on surface areas and pore volumes of the MOFs similar like other porous materials. However, it should be noted that, materials which adsorb CO<sub>2</sub> gas at high pressure region have less importance in coal fire power plants. They emit N<sub>2</sub> and other gases such as H<sub>2</sub>O, O<sub>2</sub>, CO, NO<sub>x</sub>, SO<sub>x</sub> etc. The gas stream contains all these components released at 1 bar total pressure (approximately). Hence, for CO<sub>2</sub> capture,

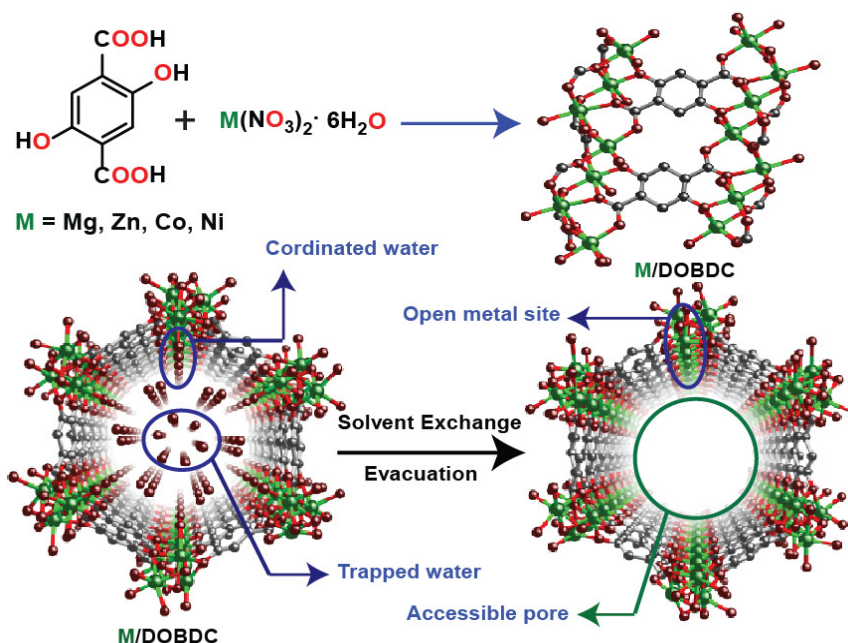


**Figure 1.11:** Single crystal structure of M<sub>2</sub>(DOBDC) {M= Mg, Co, Ni and Zn}, formed by reaction of the 2, 5 dihydroxy terephthalic acid linker with different M(NO<sub>3</sub>)<sub>2</sub>·6H<sub>2</sub>O. The structure consists of 1D hexagonal channel with open metal sites inside the pore after strong evacuation. Redrawn the structure from the cif file of Mg/DOBDC (1.26d).

materials which can adsorb at low pressure (specially at 1 bar) region and room temperature are most important for industrial carbon capture [1.25].

### 1.5.2 CO<sub>2</sub> adsorption in MOFs at low pressures

At low pressures, high CO<sub>2</sub> capture capability predominantly depends on the open metal sites and chemical functionalization of the pore surface. In coal fire power plant, the pressure of the flue gas (~1 bar) and the low partial pressure of CO<sub>2</sub> (~0.15 bar) indicates to the area of interest for the CO<sub>2</sub> adsorption isotherm at lower-pressure region. Thus, special focus on the adsorption capacities around 0.15 bar would be expected from new materials with enhanced performance for post-combustion CO<sub>2</sub> capture. Till now, Mg/DOBDC (Figure 1.11) has the highest CO<sub>2</sub> capacity at 0.1 bar as well as at 1 bar, which is 20.6 and 35.2 wt% respectively at 298 K. The very high uptake of Mg/DOBDC at low pressures attributed to the presence of light weight open metal sites located towards the pore (Figure 1.11). The low pressures (0.15 bar and 1 bar) adsorption capacities for MOFs are tabulated according to their uptake capacities in figure 1.12 and table 1.5 respectively.

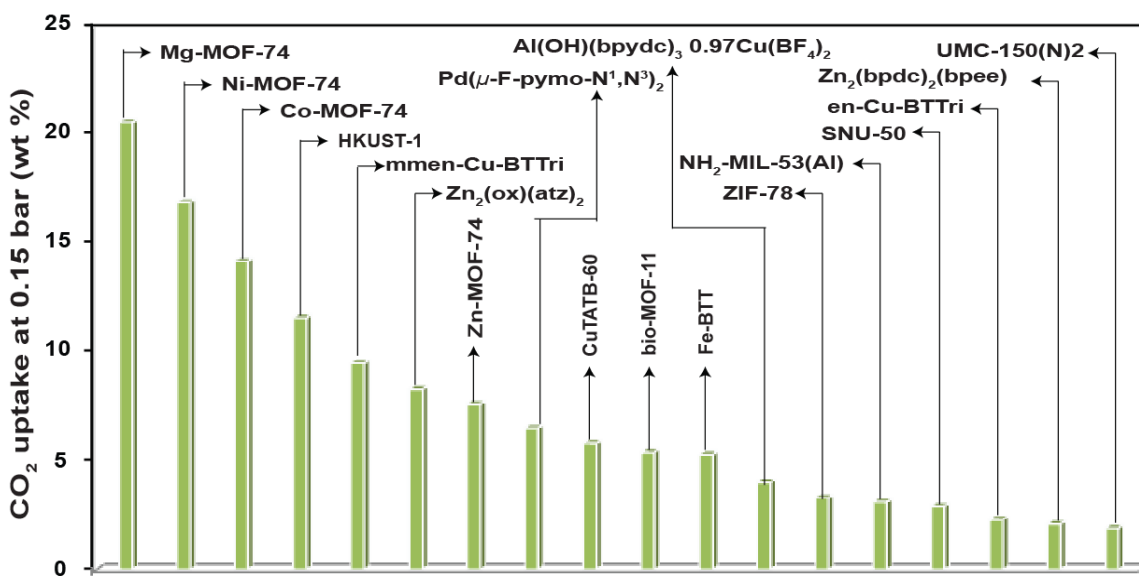


**Figure 1.12:** Schematic representation of CO<sub>2</sub> uptake in selected MOFs at 0.15 bar pressures.

Note that, high CO<sub>2</sub> uptake at 1 bar pressure does not depend on the high surface area or pore size of the material. However, it depends on the heat of adsorption ( $Q_{st}$ ), a parameter which measures the CO<sub>2</sub> adsorption capacities in MOFs at low pressures. The magnitude of the  $Q_{st}$  dictates the affinity of the pore surface toward CO<sub>2</sub>, which in turn plays a crucial

role in determining the adsorptive selectivity and the energy required to release the CO<sub>2</sub> molecules during regeneration. By increasing Q<sub>st</sub>, although the CO<sub>2</sub> binding with the framework increases, however, the regeneration cost will also becomes high due to large quantity of energy required in order to break the framework CO<sub>2</sub> interactions. One further parameter of interest for evaluating the strength of CO<sub>2</sub> binding, particularly at the lowest CO<sub>2</sub> pressures, is the zero-coverage Q<sub>st</sub>. This parameter provides the information of the strength of the strongest binding sites within the framework. In figure 1.13 the summary of zero-coverage Q<sub>st</sub> value of selected MOF are listed pictorially.

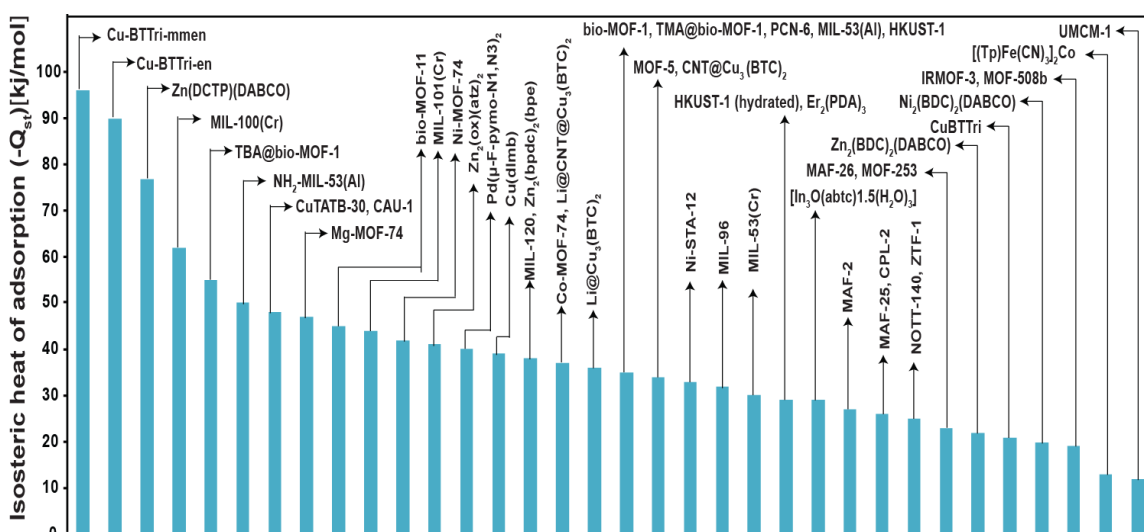


**Figure 1.13:** Schematic representation of zero-coverage isosteric heat of CO<sub>2</sub> adsorption (Q<sub>st</sub>) in MOFs.

**Table 1.5: Low-Pressure CO<sub>2</sub> Adsorption Capacities in MOFs**

Chemical formula	Name of the MOF	Surface area (m <sup>2</sup> g <sup>-1</sup> )		Pressure (bar)	Uptake (wt %)	Temp (K)	Ref
		Langmuir	BET				
Mg <sub>2</sub> (dobdc)	Mg-MOF-74,	1733	1174	1	27.5	298	1.26a
				1	27.2	298	1.26b
		2060	1800	1	26.7	298	1.26c
				1.1	26	298	1.26d
		1905	1495	1	26	296	1.26e
Cu <sub>3</sub> (BTC) <sub>2</sub> (H <sub>2</sub> O) <sub>1.5</sub>	HKUST-1, 4 wt% H <sub>2</sub> O			1	27	298	1.26f
Co <sub>2</sub> (dobdc)	Co-MOF-74,CPO-27-Co	1388	957	1	24.9	298	1.26b
			1080	1	23.4	296	1.26e
Ni <sub>2</sub> (dobdc)	Ni-MOF-74/CPO-27-Ni	1356	936	1	23.9	298	1.26b



			639	1	22.7	298	1.26g
		1312	1083	1	22.6	303	1.26h
			1070	1	20.4	296	1.26e
<b>Zn<sub>2</sub>(dobdc)</b>	Zn-MOF-74/CPO-27-Zn			1	19.8	296	1.26b
				1	19.6	296	1.26e
			816	1.1	17.6	298	1.23
<b>Cu<sub>3</sub>(BTC)<sub>2</sub></b>	HKUST-1		1400	1	19.8	293	1.26i
		1492		1	18.4	298	1.26f
				1	18.3	295	1.26b
			1781	1	15.2	298	1.23
			1482	1	15	298	1.26j
				0.8	10.6	298	1.26k
				1	6.2	313	1.26l
			857	1	6.2	295	1.26j
<b>Cu<sub>3</sub>(BTC)<sub>3</sub>(H<sub>2</sub>O)<sub>3</sub></b>	HKUST-1,(8 wt% H <sub>2</sub> O)			1	17.4	298	1.26f
<b>Cu<sub>3</sub>(TATB)<sub>2</sub></b>	CuTATB-60, PCN-6	4436	3811	1	15.9	298	1.26m
<b>H<sub>3</sub>[(Cu<sub>4</sub>Cl)<sub>3</sub>(BTTri)<sub>8</sub>(mmen)<sub>12</sub>]</b>	mmen-Cu-BTTri		870	1	15.4	298	1.26n
<b>Co<sub>2</sub>(adenine)<sub>2</sub>(CO<sub>2</sub>C H<sub>3</sub>)<sub>2</sub></b>	bio-MOF-11		1040	1	15.2	298	1.26o
<b>H<sub>3</sub>[(Cu<sub>4</sub>Cl)<sub>3</sub>(BTTri)<sub>8</sub>]</b>	Cu-BTTri	1900	1770	1	14.3	298	1.26p
<b>Zn<sub>2</sub>(ox)(atz)<sub>2</sub></b>			782	1.2	14.3	293	1.26q
<b>Ni<sub>2</sub>(2-amino-BDC)<sub>2</sub>(DABCO)</b>	USO-2-Ni-A		1530	1	14	298	1.26r
<b>Cu<sub>2</sub>(bdcppi)(DMF)<sub>2</sub></b>	SNU-50	2450	2300	1	13.7	298	1.26s
<b>Fe<sub>3</sub>[(Fe<sub>4</sub>Cl)<sub>3</sub>(BTT)<sub>8</sub>(MeOH)<sub>4</sub>]<sub>2</sub></b>	Fe-BTT		2010	1	13.5	298	1.26t
<b>Cu<sub>3</sub>(TATB)<sub>2</sub></b>	Cu-TATB-30	3065	2665	1	13.4	298	1.26u
<b>Cu(bpy)<sub>2</sub>(BF<sub>4</sub>)<sub>2</sub></b>	ELM-11			1	12.7	298	1.26v
<b>Cu<sub>2</sub>(bptc)(H<sub>2</sub>O)<sub>2</sub>(DMF)<sub>3</sub></b>	MOF-505		1547	1.1	12.6	298	12.3
<b>Al(OH)(2-amino-BDC)</b>	NH <sub>2</sub> -MIL-53(Al),	816	960	1	12	298	1.26r

### 1.6 Key strategies to enhance CO<sub>2</sub> adsorption

Various strategies have been addressed to enhance the CO<sub>2</sub> adsorption capacities of MOFs at low pressure (1 bar) and ambient temperature (273K). However, three approaches have been proven to be particularly effective for high CO<sub>2</sub> uptake in MOFs. These are (1) Open metal site inside the framework backbone, (2) Metal doping inside the pore of the MOF, (3) Framework cavity functionalized by nitrogen basic sites.

### 1.6.1 Open metal site

The open metal sites are usually generated by removal of coordinated solvent molecules from metal centers of MOF architecture (Figure 1.14). The unsaturated open metal sites have high-affinity binding sites to interact with CO<sub>2</sub> molecules. The earliest studies of MOFs possessing open metal sites were performed predominantly on the structures of M<sub>2</sub>(DOBDC) (M = Mg, Co, Ni, Zn and DOBDC = 2, 5 dihydroxy terephthalic acid) [1.27, 1.26d and e] and HKUST-1 [1.28].

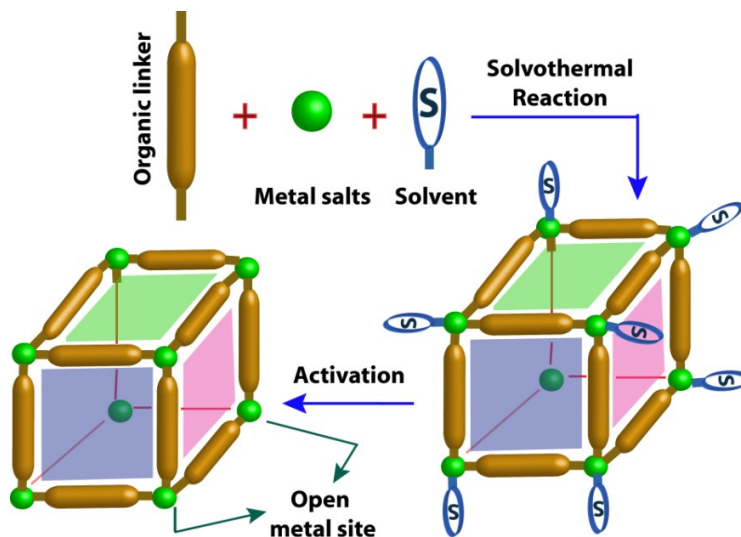


**Figure 1.14:** Generation of open metal sites by removal of coordinated solvents from MOF architecture (model representation)

one-dimensional pores of

M<sub>2</sub>(DOBDC) with high adsorption capacities for CO<sub>2</sub> at 1 bar and 296 K, ranging from 19.8 to 26.0 wt% within Zn<sub>2</sub>(dobdc) and Mg<sub>2</sub>(dobdc), respectively. In fact, the value for Mg<sub>2</sub>(dobdc) represents the highest low-pressure gravimetric and volumetric adsorption capacity for CO<sub>2</sub> in a MOF, despite its relatively low surface area (BET= 1495 m<sup>2</sup>g<sup>-1</sup>), which indicates the importance of decorating the pores with a large numbers of high-affinity binding sites (Figure 1.15). The zero-coverage isosteric heat of CO<sub>2</sub> adsorption of Mg<sub>2</sub>(dobdc) was noted the strongest affinity ( $Q_{st} = -42$  kJmol<sup>-1</sup>), whereas Zn<sub>2</sub>(dobdc) exhibited the weakest interactions ( $Q_{st} = -26$  kJmol<sup>-1</sup>) among the M<sub>2</sub>(DOBDC) series. Note that, the higher ionic character of the Mg-O bonds in Mg<sub>2</sub>(DOBDC) [compare with other M<sub>2</sub>(DOBDC) series] leading to a higher partial positive charge on the Mg<sup>2+</sup> metal centers, which eventually facilitate a greater degree of polarization on the adsorbed CO<sub>2</sub> molecules as well as difference in the isosteric heat of adsorption. Similar kind of example is Cu<sub>3</sub>(BTC)<sub>2</sub> (HKUST-1) MOF, where exposed open metal sites generated by the removal of

H<sub>2</sub>O molecules originally bound to the metal centre (Figure 1.15) [1.28]. As expected CO<sub>2</sub> interact more strongly due to the high charge density of the Cu<sup>2+</sup> cations, resulting in a zero-coverage isosteric heat of adsorption ( $Q_{st}$ ) of  $-29.2 \text{ kJmol}^{-1}$ . Hence, large amounts of CO<sub>2</sub> have been adsorbed through small cage window and shows higher uptake at low pressure region. A number of independent research have investigated on the adsorption isotherms of this compound, among them HKUST-1, (4 wt% H<sub>2</sub>O) shows better performance at 1 bar pressure and 298 K temperature (Table 1.5).

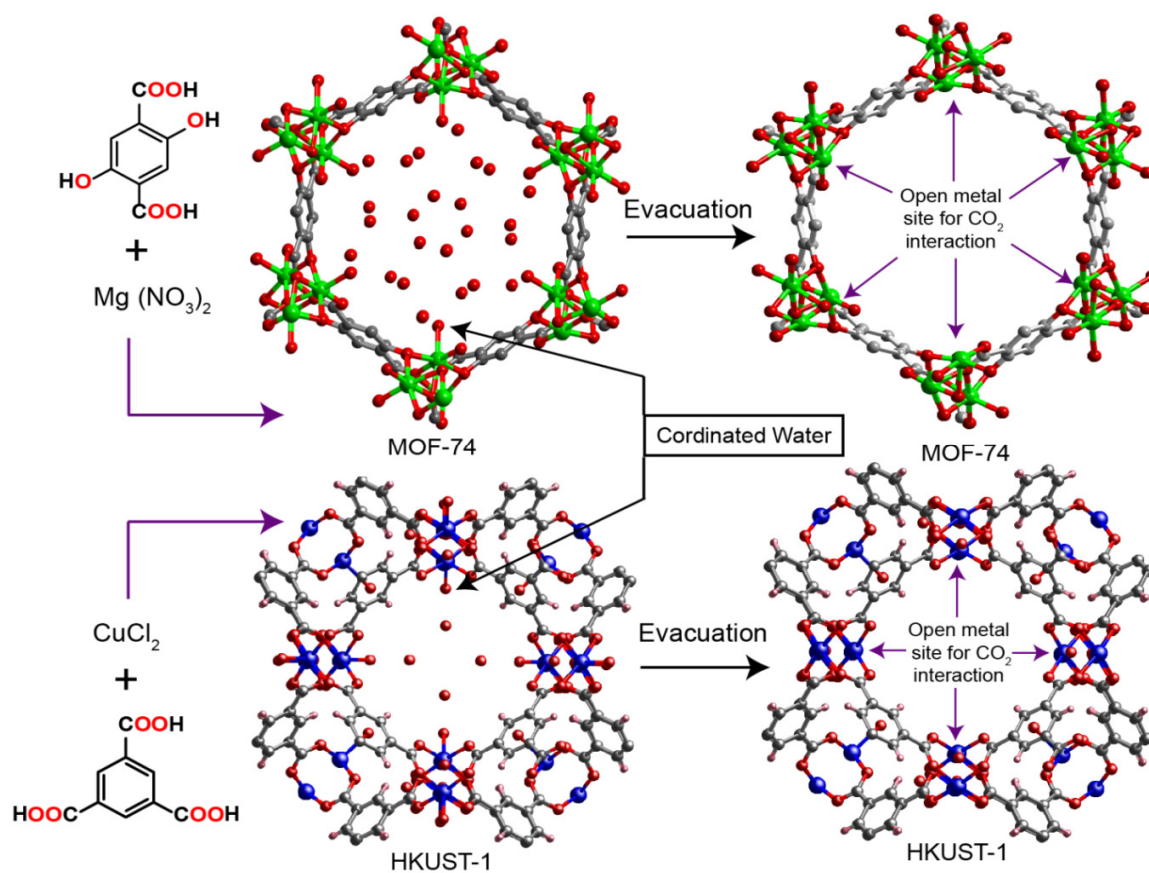


**Figure 1.15:** Synthesis of Mg-MOF-74 and HKUST-1. Open metal site is generated (for high CO<sub>2</sub> adsorption) after proper evacuation of these MOFs at high temperature and pressure. Redrawn these structures from the cif files of Mg/DOBDC [1.26d] and HKUST-1 [1.28].

### 1.6.2 Metal doping inside the pores of the MOF

It has been observed that, incorporation of light weight metal (Li, Al, Na, etc) inside the MOF architecture can enhance the CO<sub>2</sub> uptake noticeably [1.29]. Recent report predicted that Li doping can greatly improve the CO<sub>2</sub>/CH<sub>4</sub> selectivity in MOF-5 [1.30]. Higher

uptake arises due to increased dipole–quadrupolar interactions between the reduced Li ion and CO<sub>2</sub> molecules, but there is little effect on the binding of non-polar CH<sub>4</sub>. It is evident that the chemically reduced nature of the material leads to the drastic increase in selectivity of polar CO<sub>2</sub> over non polar CH<sub>4</sub>. First experimental approach [1.31] was the incorporation of Li<sup>+</sup> ions inside the cationic MOF for enhancement of CO<sub>2</sub> selectivity by the cation exchange strategy. Three Zn based mixed-ligand MOFs are investigated for this purpose. Two of them have same two-fold catenated structure {Zn<sub>2</sub>(2,6-NDC)<sub>2</sub>(diPyNI)} [where 2,6-NDC = 2,6-naphthalenedicarboxylate and diPyNI = N,N-di-(4-pyridyl)-1,4,5,8-naphthalenetetra carboxy diimide] but are synthesized in different route. The structure of third MOF is a non-catenated with hydroxyl groups [Zn<sub>2</sub>(TCPB)(DPG)]; TCPB = 1,2,4,5-tetrakis(4-carboxy-phenyl) benzene and DPG = meso-1,2-bis(4-pyridyl)-1,2-ethane diol). Each MOF was reacted with a lithium suspension for 10 min and rinsed with THF to remove any unreacted lithium. All these cases, the Li incorporation can significantly enhance the CO<sub>2</sub>/CH<sub>4</sub> selectivity. The increase in CO<sub>2</sub>/CH<sub>4</sub> selectivity in Li incorporated MOFs were attributed to the favourable displacement of catenated frameworks and pore-volume reduction. Moreover, the adsorption of CO<sub>2</sub> also enhanced in Li<sup>+</sup> exchanged MOFs due to the interaction between desolvated Li<sup>+</sup> (charge) and CO<sub>2</sub> (quadrupole). Similar strategy studied on diamide based porous polymer [1.31] as well for selective capture of CO<sub>2</sub> in presence lithium metal incorporation. The other inorganic materials such as boron nitride BNH<sub>x</sub> ( $x \leq 1$ ) also incorporated into the void space of MIL-53 based MOF to improve their performance on CO<sub>2</sub> capture. After loading 1.3 wt% and 1.7 wt% of BNH<sub>x</sub>, CO<sub>2</sub> capacity increases with higher boron content from the original 13.7 wt% to 15.9 wt% and 16.8 wt% respectively at 780 mmHg and 273 K temperature.

### 1.6.3 Framework cavity functionalized by nitrogen basic sites

It has been noticed that, MOF functionalized with amine or basic nitrogen containing organic groups shows promising CO<sub>2</sub> interaction with the framework entity. The electrostatic force generated due to the interaction of the quadrupole moment of CO<sub>2</sub> with localized dipoles produced by heteroatom incorporation is paving way to enhance the CO<sub>2</sub> adsorption. For some cases, interactions of acidic CO<sub>2</sub> and basic lone pair of nitrogen have been observed as well. As already mentioned, functional groups have major contribution for the enhancement of CO<sub>2</sub> storage capacity in MOF architectures. Therefore, depending on

the nature, four major classes of nitrogen-functionalized MOF have been categorized (a) amine functionalized MOF (b) alkylamine (*i.e.*, ethylenediamine) bearing frameworks (c) MOFs with heterocycle derivatives and (d) polar organic functional groups bearing MOFs/ZIFs.

#### (a) Amine functionalized MOF

The potential of amine groups to interact with CO<sub>2</sub> molecules is now well understood in the literature [1.32]. It is interesting to know that, less basic amines interact with CO<sub>2</sub> via physisorption over chemisorptions and greatly reduce the energy of regeneration.

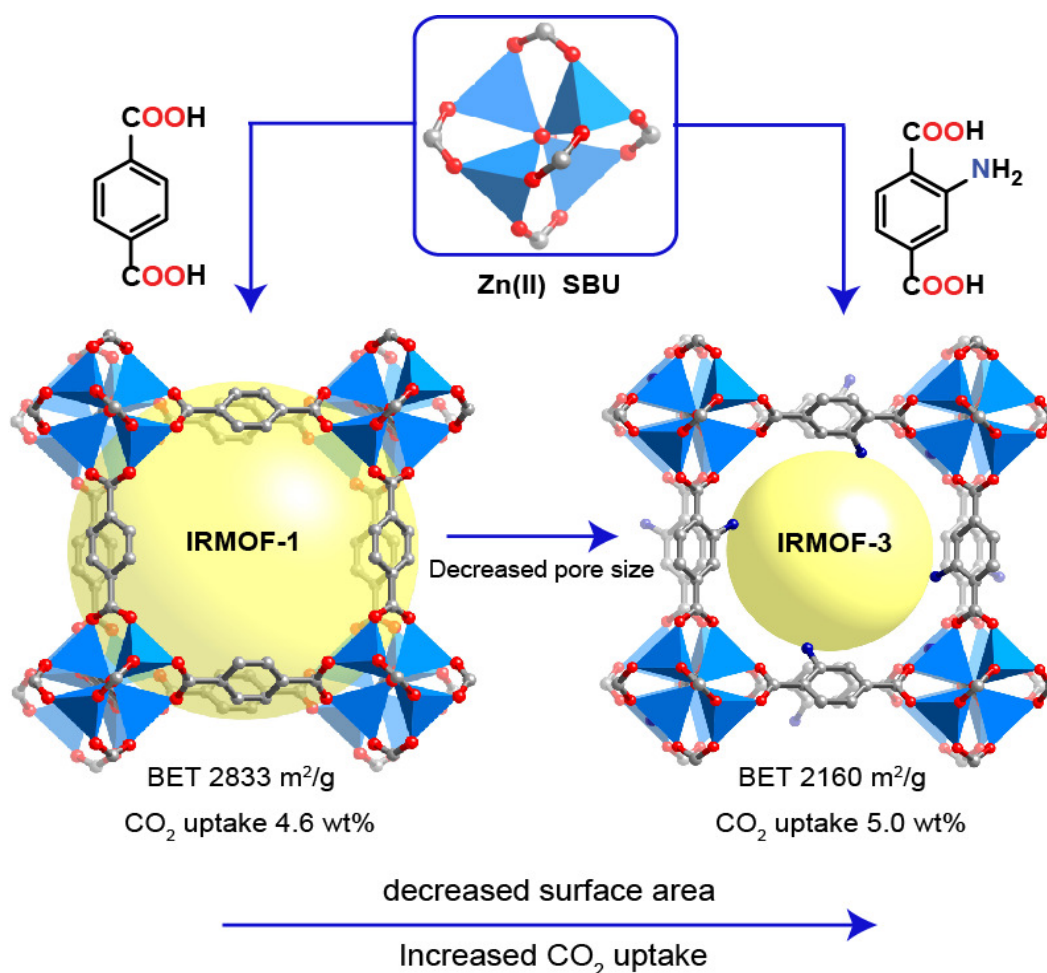


**Figure 1.16:** Systematic enhancement of CO<sub>2</sub> uptake from IRMOF-1 to IRMOF-3 by incorporating -NH<sub>2</sub> functionalization in organic linker. Redrawn these figures from the cif files of reference 1.23.

The aromatic amine containing linkers [1.23], specially 2-aminoterephthalic acid (NH<sub>2</sub>-BDC) build amine-functionalized variant Zn<sub>4</sub>O(NH<sub>2</sub>-BDC)<sub>3</sub> [IRMOF-3] with Zn(II) SBU,

isostructural with well known IRMOF-1 or MOF-5 [ $\text{Zn}_4\text{O}(\text{BDC})_3$ ]. Characterization shows that, at 298 K and 1.1 bar, IRMOF-1 adsorbs approximately 4.6 wt%  $\text{CO}_2$ , while the IRMOF-3 adsorbs 5.0 wt%  $\text{CO}_2$ , despite a decrease in the BET surface area from 2833 to 2160  $\text{m}^2\text{g}^{-1}$  (Figure 1.16). High  $\text{CO}_2$  uptake at low pressure in IRMOF-3 is due to the presence of free  $-\text{NH}_2$  groups inside the pore which interacts with acidic  $\text{CO}_2$ .

To observe the interaction of MOF framework with  $\text{CO}_2$  gas molecules, single-crystal X ray diffraction study on zinc-based MOF  $\text{Zn}_2(\text{atz})_2(\text{ox})$  loaded with  $\text{CO}_2$  have been investigated [1.33]. The structure of  $\text{Zn}_2(\text{atz})_2(\text{ox})$  consist  $\text{Zn}^{2+}$  ions coordinated by amine functionalized triazolate ligands and pillared by oxalate ligands.  $\text{Zn}_2(\text{atz})_2(\text{ox})$  shows rapid uptake of  $\text{CO}_2$  (8.3 wt% at 0.15 bar and 14.3 wt% at 1.2 bar ) at low pressure with high enthalpy of adsorption ( $Q_{\text{st}} = -41 \text{ kJmol}^{-1}$ ).

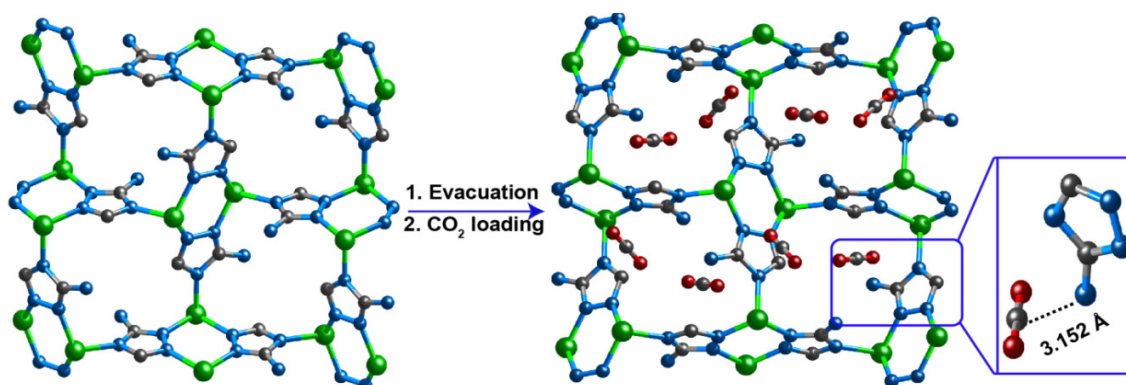


**Figure 1.17:** Single-crystal structure of  $\text{Zn}_2(\text{atz})_2(\text{ox})$  loaded with  $\text{CO}_2$  after proper evacuation. It has been observed that  $\text{CO}_2$  molecules trapped closely to the  $-\text{NH}_2$  groups inside the framework which also proved by single crystallographically. Green, gray, blue and red spheres represent Zn, C, N, and O atoms respectively; H atoms are omitted for clarity. Inset version shows distance between the amine group and the  $\text{CO}_2$  molecule. Redrawn the structure from the cif file of  $\text{Zn}_2(\text{atz})_2(\text{ox})$  [1.33]

The  $\text{CO}_2$  binding sites of  $\text{Zn}_2(\text{atz})_2(\text{ox})$  are crystallographically identified at different temperatures (123, 173, 195 and 293 K) from the SCXRD data (Figure 1.17). Note that, located  $\text{CO}_2$  molecules were refined properly within framework at 173 K [R factor = 2.7%, weighted R factor  $R_w = 6.5\%$ ] as well as at 293 K, where the disorder could be modelled. The location of  $\text{CO}_2$  molecules were also modelled with high accuracy via a combination of classical grand canonical Monte Carlo (GCMC) simulations, molecular dynamics (MD) simulations, and periodic density functional theory (DFT) calculations. Figure 1.17 shows



the primary binding site for CO<sub>2</sub>, in which the carbon atom of the CO<sub>2</sub> molecules and the nitrogen of the amine groups are in close contact (3.152 Å) with the primary binding site for CO<sub>2</sub>.

### (b) Alkyl amine (ethylenediamine) bearing frameworks

In order to improve the affinity and selectivity of CO<sub>2</sub>, more basic amine species need to be incorporated onto the pore surfaces of MOFs. Strong adsorption of CO<sub>2</sub> has been shown via incorporation of alkylamines into MOF pores.

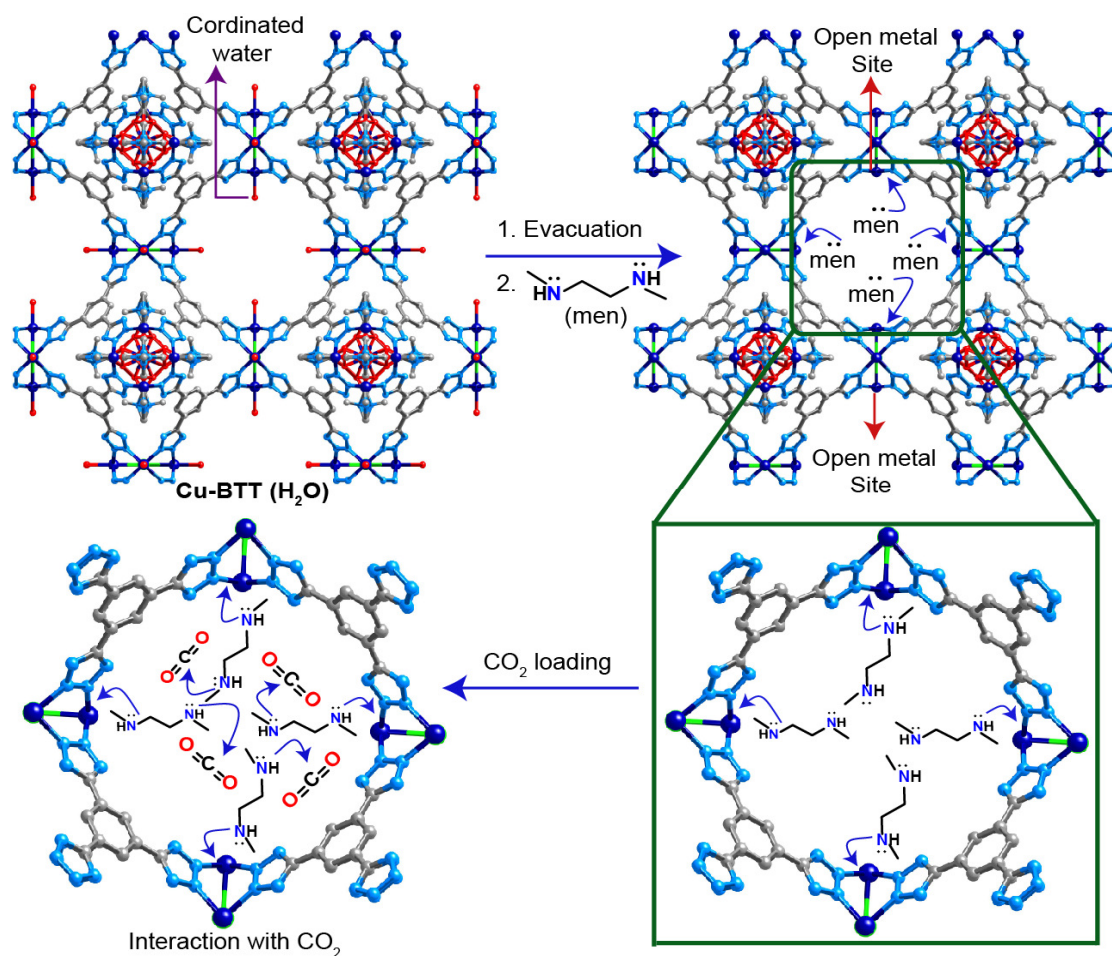


**Figure 1.18:** Post synthetic modification of Cu-BTtri framework through the binding methyl ethylene diamine (men) to the open metal coordination sites. The free amine groups of en lined inside the framework pores facilitate to interact with CO<sub>2</sub> molecules for higher adsorption. Redrawn the crystal structure from the cif file of 1.26n.

There is a report [1.26n and p] of Cu based MOF, HCu[(Cu<sub>4</sub>Cl)<sub>3</sub>(BTtri)<sub>8</sub>] (Cu-BTtri) with open metal sites created by the removal of solvent molecules originally bound to the metal

centers. N, N'-dimethylethylenediamine (mmen) was incorporated inside the open metal site of Cu-BTTRI post synthetically to get mmen-functionalized Cu-BTTRI (mmen-Cu-BTTRI) as shown in Figure 1.18. It is noteworthy that, although surface area of Cu-BTTRI decreased after post synthetic modification with mmen however, mmen-Cu-BTTRI shows higher CO<sub>2</sub> uptake at very low pressure associated with high heat of adsorption ( $-Q_{st} = 96 \text{ kJmol}^{-1}$ ) compare to the parent Cu-BTTRI MOF ( $Q_{st} = -23 \text{ kJmol}^{-1}$ ). It was assumed that, one amine group of en first coordinated to the unsaturated metal center and another one is free to interact with adsorbed CO<sub>2</sub> molecules (Figure 1.18). Post synthetic incorporation of ethylene diamine (en) inside the void space of MOF-74 also has been investigated [1.34]. As expected, MOF-74@en shows high heat of adsorption ( $Q_{st} = -71 \text{ kJmol}^{-1}$ ) with exceptional capacity [2.0 mmol/g (8.1 wt%) at 0.39 mbar and 25 °C] for CO<sub>2</sub> adsorption at low pressure.

### (c) MOFs with Heterocyclic derivatives:

There are several MOFs reported in literature, where organic bridging units derived from nitrogen-containing heterocycles, have been studied for CO<sub>2</sub> capture [1.35b-e]. It is expected that, the ratio of heteroatoms to carbon atoms in these frameworks can be quite large, results significant surface polarization inside the pore surfaces of MOFs. Till now the best performing heterocycle for high CO<sub>2</sub> are adenine based bio-MOF-11, [1.35a] among all others heterocycle MOFs. The bio-MOF-11, synthesized via a solvothermal

reaction and the structure contains one cobalt metal coordinated with-four adenines and two acetates (Figure 1.19). The CO<sub>2</sub> uptake of bio MOF-11 is 5.8 wt% at 298 K and 0.15 bar pressure, associated with  $-45 \text{ kJmol}^{-1}$  isosteric heat of adsorption at zero-coverage. The

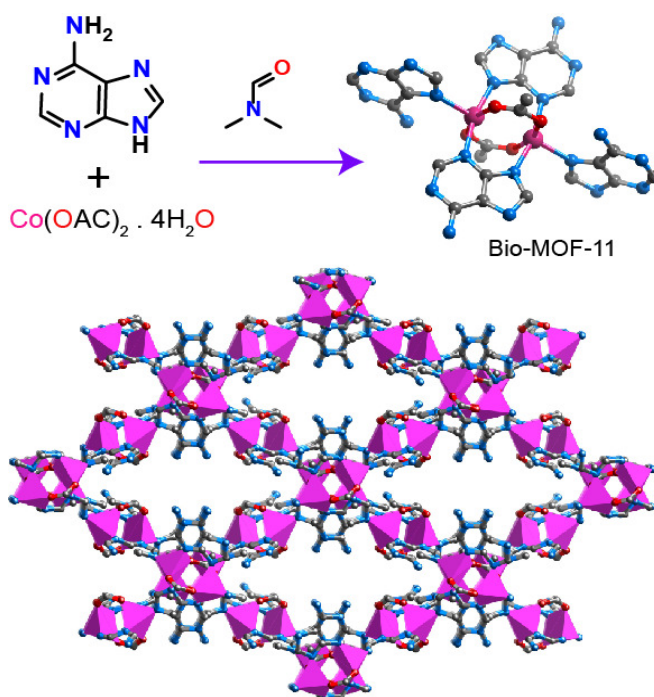


**Figure 1.19:** Synthesis of Bio-MOF-11 starting from adenine and Co(II) salt. Extended structure of Bio MOF-11 contains several amine groups dangled inside the pore which enhances the CO<sub>2</sub> uptake. Redrawn the structure from the cif file of bio-MOF-11, [1.35a]



higher CO<sub>2</sub> uptake and isosteric heat of adsorption were attributed due to the presence of enormous surface polarization generated from uncoordinated nitrogen and free amine of adenine inside the small pore of bio-MOF-11. Since, the CO<sub>2</sub> capacity of bio-MOF-11 exceeds than other aromatic amine functionalized MOF reported to date at 1 bar pressure. Hence, the effects of the nitrogen heterocycle in bio-MOF-11 are noteworthy for high capacity of CO<sub>2</sub> uptake despite its low surface area (BET 1040 m<sup>2</sup>g<sup>-1</sup>).

#### (d) Polar organic functional groups bearing MOFs/ZIFs

It is interesting to know that, despite amine and other nitrogen-based functionalities discussed in earlier paragraph, organic linkers with strongly polar functional groups also have much contribution on the CO<sub>2</sub> capture in MOFs. These polar functional groups are – NO<sub>2</sub>, –OH, –CN, –Cl, and –Br groups. It has been sought that, by increasing polarizing strength of the functional group, CO<sub>2</sub> uptake capability enhances. A systematic study of functionality and polarization strength is best observed in zeolitic imidazolate frameworks (ZIFs), another class of metal organic frameworks with zeolite type structure (Figure

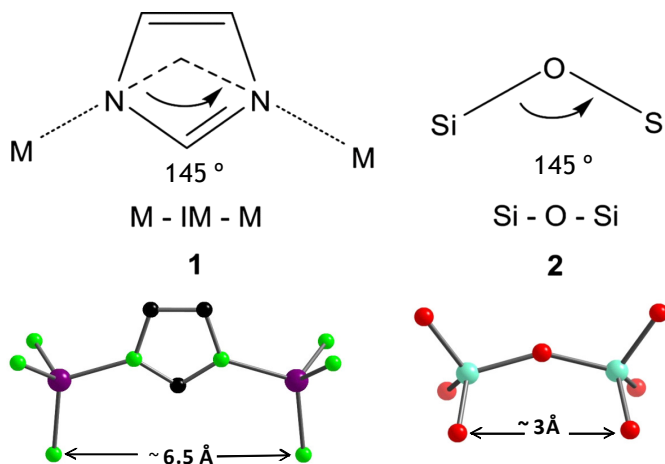


**Figure 1.20:** Structural similarity between zeolite and ZIF. (Permission taken *Proc. Natl. Acad. Sci. U.S.A.*, 2006.)

1.20). Due to their large and modifiable pores ZIFs have received considerable attention for storage of CO<sub>2</sub> and H<sub>2</sub> gases [1.36]. ZIF frameworks composed by imidazolate based organic linkers and tetrahedral metal center (Zn<sup>2+</sup>, Co<sup>2+</sup> and Cd<sup>2+</sup>) with various structural topologies. Hence, by changing the functionality in imidazolate linker a wide number of isostructural compounds could be generated with different functional groups. A series of mixed imidazolate linker frameworks of the GME topology were examined for CO<sub>2</sub> adsorption by changing functional group and pore size effect [1.37]. The size of the functional groups in organic linkers attributes a series of isostructural frameworks with different pore sizes varied between 7.1 and 15.9 Å. The framework of Zn(nbIm)(nIm) (ZIF-78) exhibits the largest volumetric capacity due to the presence of polarizing nitro group in

both imidazolate and benzimidazolate linker. On the other hand, ZIF synthesized from cyano- and nitro-functionality (ZIF-82), chloro and nitro-functionalized (ZIF-69), as well as bromo and nitro-functionalized (ZIF-81) imidazolate linkers adsorbed almost similar amount of  $\text{CO}_2$  uptake but slightly less than ZIF-78. Conversely, same topological frameworks functionalized with alkyl groups adsorbed very less amount of volumetric  $\text{CO}_2$  due to its non polar nature. Therefore, it is understandable that, by increasing the surface polarization induced by the functional groups enhances the  $\text{CO}_2$  capture in ZIFs at low pressure.

### 1.7 Proton Conduction in MOFs:

The projection of world marketed energy consumption increasing by 50 % from 2012 to 2030 due to various factors such as rapid urbanization, increasing number of industry and population growth [1.38]. Hence, there are growing pressures to progress from a fossil fuel based economy to an alternative renewable energy economy [1.39]. Fuel cell technology is one of them which have attracted considerable attention as a renewable energy source [1.40]. Fuel cell is the devices which convert chemical energy to electrical energy by combining hydrogen from fuel with oxygen from the air and produces by product water and heat [1.40].

The basic set up of fuel cell consist a negative side anode, a cathode (positive side) and an electrolyte that allows charges to move between the two sides of the fuel cell. Several different fuel cell systems have been developed over the years, among which the polymer electrolyte membrane fuel cells (PEMFCs) [1.41] (Figure 1.21) are important. In PEMFCs, the basic principle relies on the movement of protons from anode to cathode pass through proton-exchange membrane inside the cell, while the electrons generated at anode through external circuit towards cathode and thereby generate electricity [1.41]. Although, several proton conducting

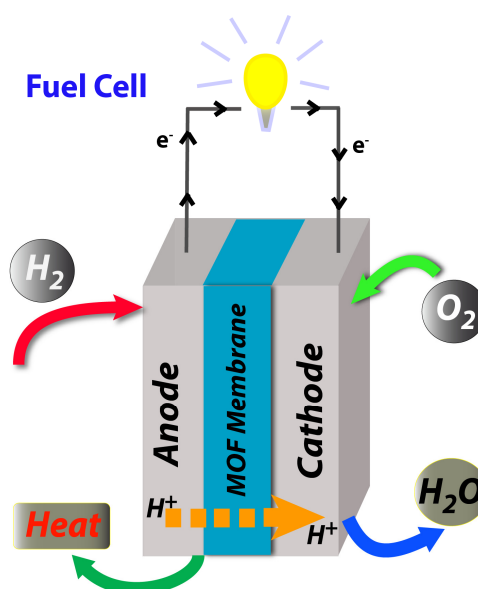


**Figure 1.21:** Model representation of proton exchange membrane fuel cell (PEMFCs).

materials have been reported in literature, till date only one product based on sulfonated fluoropolymer (nafion) [1.42] has been successfully commercialized as proton exchange membrane in PEMFCs primarily because of its high proton conductivity up to  $0.1 \text{ Scm}^{-1}$ . However, humidified condition is required to achieve high proton conductivity of nafion which lacks its conducting efficiency. Moreover, there is also a need to power the humidifiers. Such a need also limits the use of nafion in terms of operating temperatures which has several

cautions: potential for CO poisoning of Pt catalysts at temperatures less than  $100 \text{ }^\circ\text{C}$  (CO from steam reforming to produce  $\text{H}_2$ ) and sluggish reaction kinetics. Hence, there is an urgent need of materials that can perform proton conduction with similar or higher efficiency than nafion at lower

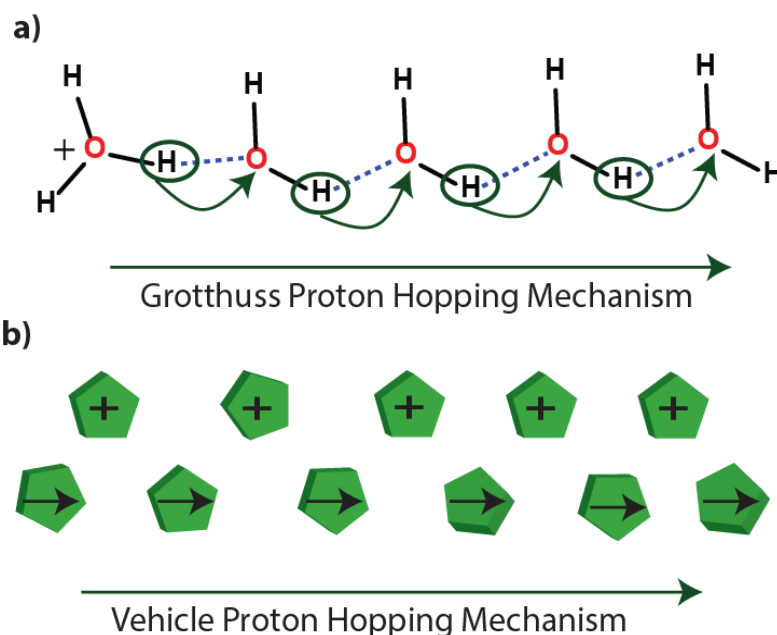


**Figure 1.22:** (a) Mechanism of Grotthuss proton hopping through the H bonded network of water (b) Vehicle proton hopping mechanism through the network. The arrow indicates the movement of protons.

temperatures ( $< 90 \text{ }^\circ\text{C}$ ). In addition, conduction at high temperature ( $100 \text{ }^\circ\text{C} - 300 \text{ }^\circ\text{C}$ ) as well as under anhydrous condition is also highly desirable for this purpose. During last few years metal-organic frameworks (MOFs), have been utilized as efficient proton conductors due to their permanent porosity, thermal stability which could be exploited for the development of proton-conducting membranes. Generally, two types of proton conductivity mechanisms have been sought in MOFs (1) Grotthuss mechanism (2) Vehicle mechanism [1.43]. In Grotthuss mechanism proton transport occurs through the hydrogen bonded  $\text{H}_2\text{O}$  molecule chain along the MOF channels. The overall mechanism performs well under hydrous condition as well as at lower temperature ( $< 80 \text{ }^\circ\text{C}$ ). On the other hand, vehicle

mechanism occurs by the movement of guest molecules (imidazole, triazole etc.) through the MOF architecture to conduct protons (Figure 1.22). Based on the above discussion the proton conductivity in MOFs is divided mainly in two ways (a) water mediated (hydrous) proton conductivity [1.44] (b) Anhydrous proton conductivity [1.45].

### 1.7.1 Challenges of proton conductivity in MOFs

Solid state ionic conduction occurs by facile movement of proton through conducting channel path that have least energy barriers. The overall conduction process going through the arrangement of protonation and deprotonation mechanism where donor and acceptor sites of proton must have high accessible space for facile movement pathway. In general, the improvement of materials is facilitated when changes in properties can be directly related to changes in structure. Unlike polymers, MOFs are crystalline, and Sxrd provide atomic level structural information. The crystallinity of MOFs, coupled with the many options for structural modification, enables molecular level design and hence structural optimization. Moreover, the porosity of MOF which facilitate unwanted fuel crossover in a PEMFC, can be used to advantage by filling pores with water or a nonvolatile proton carrier. At current situation two main targets of MOF for PEMFC operation have emerged, (1) to synthesize better proton conducting materials that can perform efficiently under humid conditions (below 100 °C) and should be cheaper than well known proton conducting material nafion. (2) Development of efficient anhydrous proton conductors that should operate at higher temperature (more than 100 °C) as well as anhydrous condition.

#### 1.7.2 Water assisted proton conductivity in MOF:

Hydrous proton conductivity in MOF generally happens in presence of water vapour. Here, proton conduction process occurs through the hydrogen bonded network of water molecules by the formation and cleavage of covalent bonds (Figure 1.23) at temperature range below 100 °C (Grotthuss mechanism). To synthesize proton conducting PCP/MOFs under humid conditions, the framework should retain a large number of water molecules, and the accommodated water should have high mobility. Based on the framework architecture, conduction process in MOFs under hydrous condition have been categorized in two different sections (1) inherent water assisted proton conduction (2) ion assisted proton conduction.

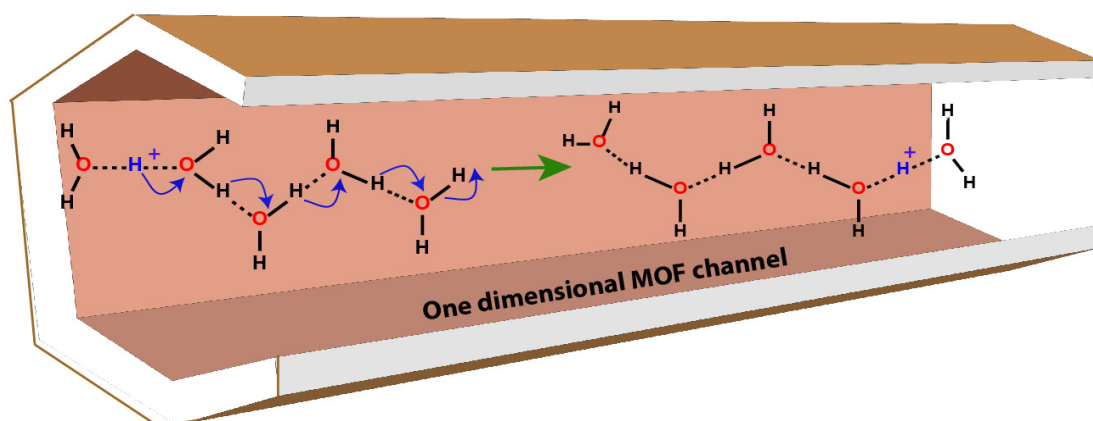


**Figure 1.23:** (a) Schematic view of the one dimensional MOF channel impregnated with protonated water molecules. The arrows indicate the possible movement of protons through the channel in water assisted proton conduction.

### 1.7.2.1 Inherent Water assisted proton conduction:

Efficient proton conduction needs the facile movement of protons through the channels of the framework. Inherent water molecules inside the MOF backbone can enhance the conduction efficiency by several folds. There are two types of prospect (1) water molecules coordinated to the metal center of the MOF moieties or (2) water molecules trapped inside the pore of MOF structure. However, proton conduction phenomena enhances for these two prospects in presence of hydrous atmosphere.

Proton conducting ability have been investigated on 1-dimensional chain systems based MOFs with oxalate bridging moieties [1.44c]. The first system examined was ferrous oxalate dihydrate which consists of octahedral  $\text{Fe}^{2+}$  metal centers linked with bidentate oxalate ligands and axially coordinated water molecules to form one-dimensional (1D) chain polymer (Figure 1.24a). The proton conductivity showed by this material is  $1.3 \times 10^{-3} \text{ Scm}^{-1}$  at  $25^\circ\text{C}$  under 98% RH with activation energy of 0.37 eV. Lewis acidic ferrous ion ( $\text{Fe}^{2+}$ ) have tendency to subtract proton from coordinated water molecules. Hence, periodic arrangement of coordinated water molecules have been built inside the structure to facilitate the pathway for proton hopping under hydrous environment that could be the possible reason for high proton conduction. Similar kind of study also been performed on 2,5-dihydroxy- 1,4-benzoquinone (Dhbq) [structurally modified from oxalate] based

coordination polymers [1.44h and i] with various divalent metal center (Co, Mg, Mn, Ni and Zn) (Figure 1.24b). However, the proton conductivity of these

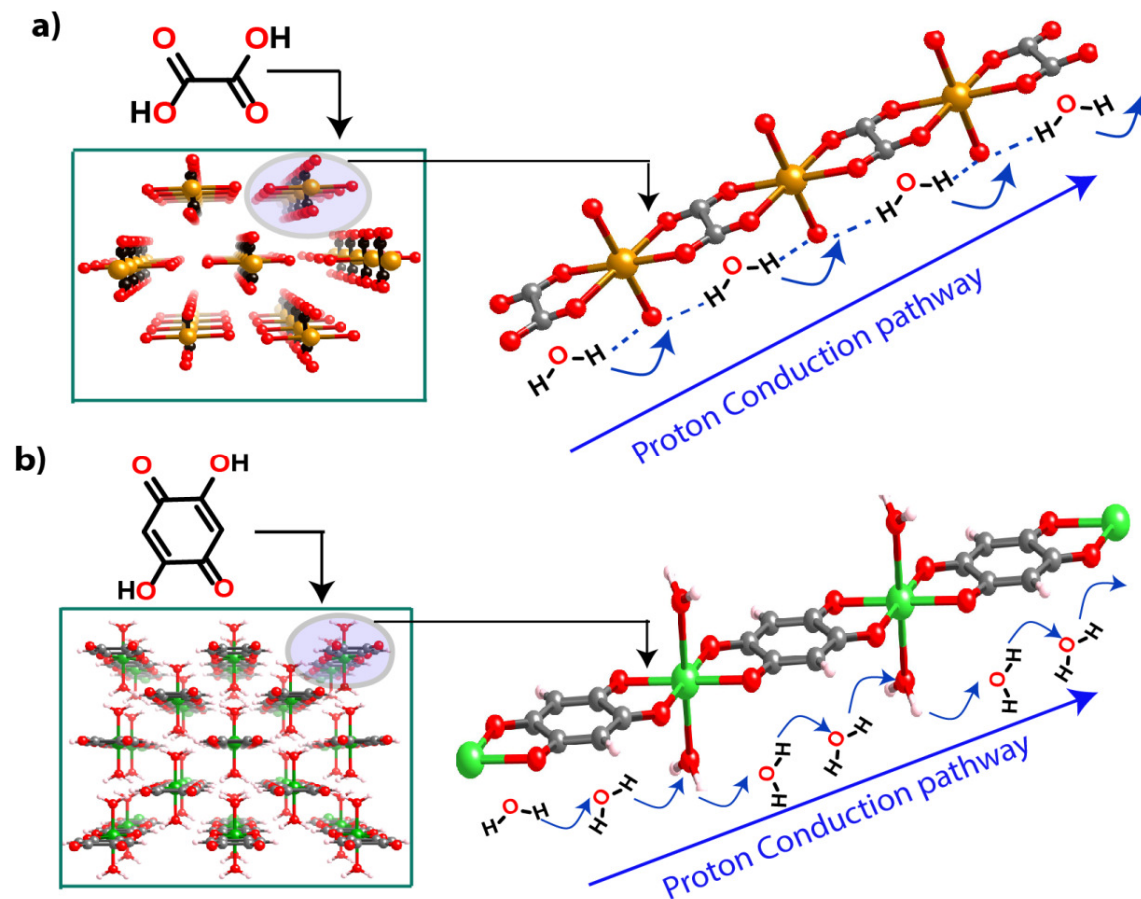


**Figure 1.24:** (a) Three dimensional arrangement of ferrous oxalate based coordination polymer. (b) Three dimensional packing of 2, 5-dihydroxy- 1,4-benzoquinone (Dhbq) and Fe (II) based MOF. The protons transport through the coordinated water of 1D chain structure under hydrous condition. Fe yellow, O red, C gray and Zn green. [Redrawn the structures from the cif files of 1.44c and h]

materials are low [ $4 \times 10^{-5} \text{ Scm}^{-1}$ ] in hydrous condition. Both ferrous oxalate and Dhbq based MOF do not show proton conductivity in absence of coordinated water molecules which indicate that the coordinated water molecules play an important role for high proton conduction at humidified condition.

Proton conductivity studies also have been investigated on MOFs where water molecules are trapped inside the void spaces of MOF architecture. A phosphonate-based two dimensional coordination polymer has been reported [1.44b] for hydrous proton conduction. The MOF ( $\text{Zn}_3\text{Btp/PCMOF3}$ ) has been synthesized from the 1,3,5



benzenetriphosphonate with  $\text{Zn}(\text{NO}_3)_2$  under hydrothermal condition. The framework has been assembled in 2D layer fashion where each layer is stacked through alternating sets of zinc metal centers layers. Water molecules reside

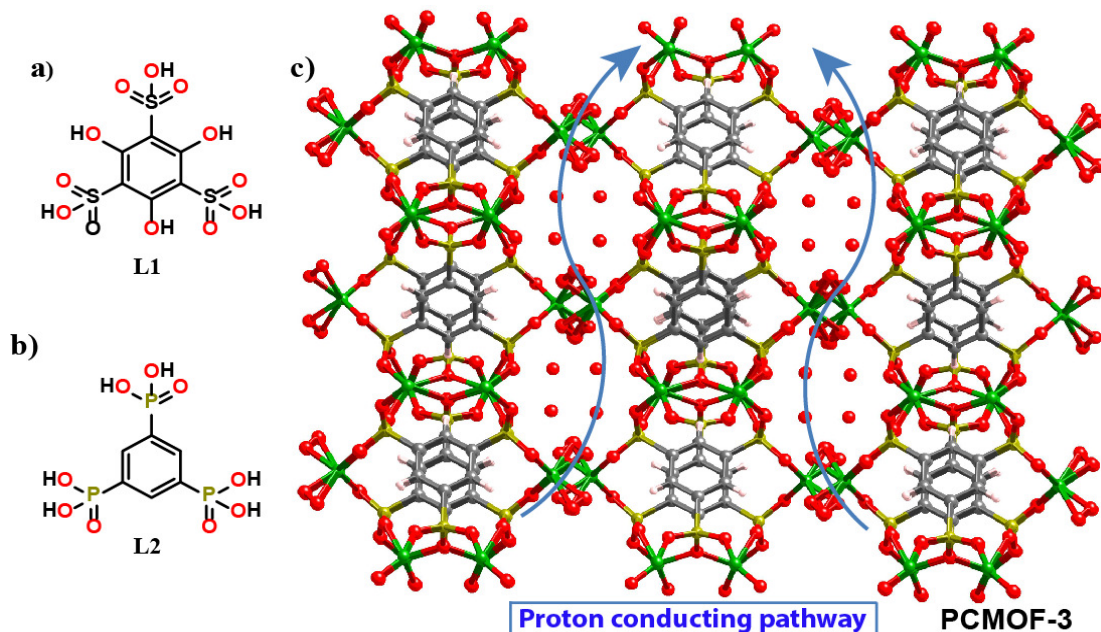


**Figure 1.25:** Structure of (a) 1, 3, 5 benzene trisulphonic acid and (b) 1, 3, 5 benzene triphosphonic acid (c) Structure of PCMOF-3, showing two layers (top and bottom) and forming 1-D water filled channels which enhances the proton conductivity. Colour code: Zn green, O red, C gray and P yellow. Redrawn the structure from the cif file of PCMOF-3, [1.44b]

in order fashion among the layers and create strong hydrogen bonded network which promotes the proton conduction pathway (Figure 1.25c). PCMOF3 showcased decent proton conductivity value  $3.5 \times 10^{-5} \text{ Scm}^{-1}$  at  $25^\circ\text{C}$  and 98% RH. However, under anhydrous condition the conductivity is extremely low which indicates that PCMOF3 is highly humidity-dependent proton conducting material. Along the same line, another report in 2012, where a phosphonate based MOF (PCMOF3) can perform better proton conduction than previous analogue (PCMOF2). The structure of PCMOF2 [trisodium salt of 2,4,6-trihydroxy-1,3,5-benzenetrisulfonate (L1)] contains pores lined with sulfonate oxygen atoms and exhibit poor proton conducting efficiency. In order to improve the proton conductivity in PCMOF2 structure, replacement of the (L1) linkers with 1,3,5 benzenetriphosphonate (L2) linkers (Figure 1.25b) by keeping the hybrid nature of both PCMOF2 and PCMOF3 [1.44j]. The resulting material named as PCMOF2<sup>1/2</sup> has very high

proton conductivity  $2.1 \times 10^{-2} \text{ Scm}^{-1}$  at 90% RH and 85 °C. The PCMOF2<sup>1/2</sup> also showed highly humidity dependent proton conductivity. At 50% RH, the conductivity of PCMOF2<sup>1/2</sup> decreases to  $2.4 \times 10^{-5} \text{ Scm}^{-1}$ . The activation energy ( $E_a$ ) measured 0.21 eV, is indicative of Grotthuss hopping mechanism for high proton conduction.

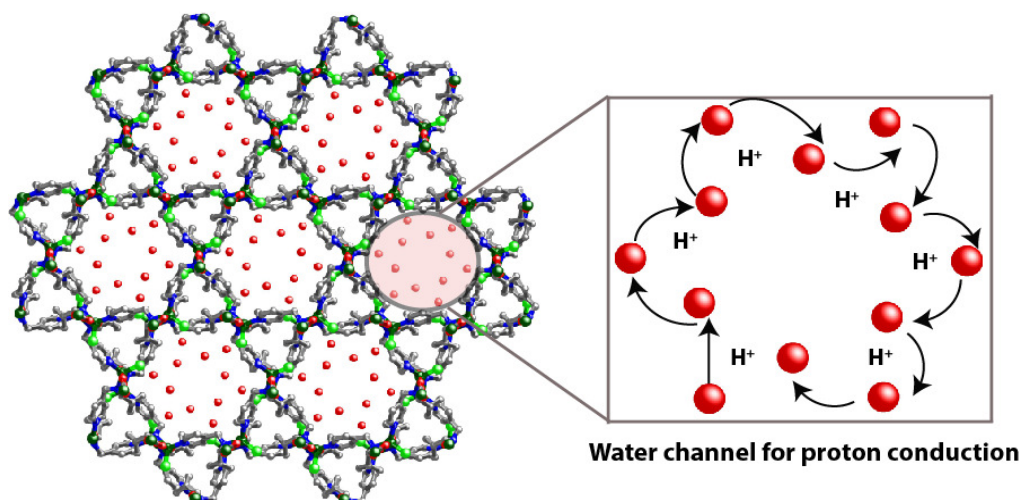


**Figure 1.26:** Representation of D and L valine based MOF with Zn(II) metal center. Close proximity of water molecules inside the framework is responsible for proton conduction. [Redrawn the structure from the cif file of 1.45k].

Similar kind of water channel resides in close proximity inside the MOF void space has been examined for hydrous proton conduction. A series of MOF isomers, [Zn(l-LCl)(Cl)](H<sub>2</sub>O)<sub>2</sub> (**1**), [Zn(l-LBr)(Br)](H<sub>2</sub>O)<sub>2</sub> (**2**) [Zn(d-LCl)(Cl)](H<sub>2</sub>O)<sub>2</sub> (**3**), and [Zn(d-LBr)(Br)](H<sub>2</sub>O)<sub>2</sub> (**4**) with unprecedented *unh* topology was reported [1.45k]. All these MOFs contain helical water chains inside the structure, have explored for proton conduction. **1** and **3** have continuous water chains which promotes proton conduction ( $4.45 \times 10^{-5}$  and  $4.42 \times 10^{-5} \text{ Scm}^{-1}$  respectively at ambient temperature under 98% RH) through the channels (Figure 1.26). On the other hand, **2** and **4** do not show any conductivity due to absence of discrete water assembly inside the cavity, confirmed by VT-SCXRD experiments. Sometimes two different solvents occupied the void spaces of MOF architectures also play the role for hydrous proton conduction. A report of a three dimensional MOF [ $\{(Zn_{0.25})_8(O)\}Zn_6(L)_{12}(H_2O)_{29}(DMF)_{69}(NO_3)_2\}_n$ ] has been synthesized from 1,3 bis (4carboxy phenyl) imidazolium and Zn<sub>8</sub>O clusters [1.45i]. The inner cavities of this framework are occupied by the large numbers of DMF and water molecules. The



imidazolium groups of the organic linkers aligned in the channels and interact with DMF and water to facilitate the hydrous proton conductivity. The proton conductivity increases with an increase of humidity and reaches  $2.3 \times 10^{-3} \text{ Scm}^{-1}$ .

### 1.7.1.2 Ion assisted proton conduction:

There are several MOFs reported where metal coordination creates anionic framework. Hence, to neutralize the anionic framework various cationic molecules [ $\text{NH}_4^+$ ,  $(\text{CH}_3)_2\text{NH}_2^+$ ,  $(\text{C}_2\text{H}_5)_2\text{NH}_2^+$  etc.] gets trapped inside the framework. It has been observed that, cation trapped MOFs could be used as proton transfer

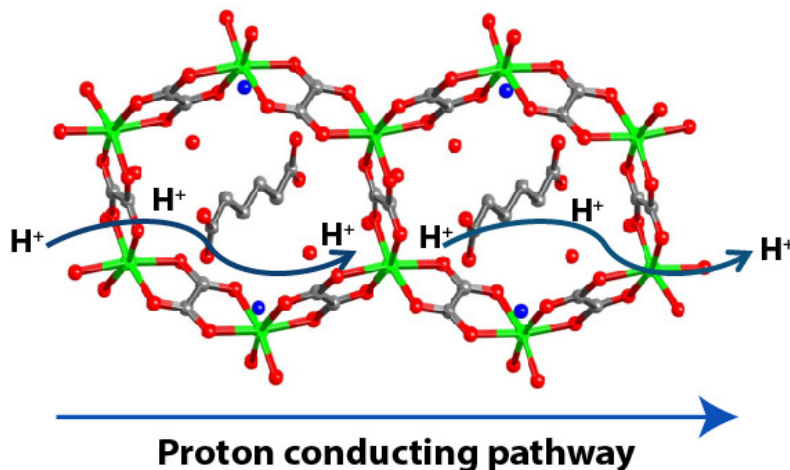


**Figure 1.27:** Honeycomb layer structure of Zinc oxalate framework  $(\text{NH}_4)_2(\text{adp})\text{-}[\text{Zn}_2(\text{ox})_3]\cdot 3\text{H}_2\text{O}$ . Inside the interlayer spaces of 2D network ammonium cation, water molecule as well as adipic acid (adp) is arranged by H bonds. Color code: Zn green, O red, C gray and N blue. [Redrawn the structure from the cif file of 1.44e]

sites and can initiate the conduction process under hydrous condition. Such kind of cationic MOFs also have been examined for proton conduction. There is a report in 2009, [1.44e] where zinc oxalate based framework  $(\text{NH}_4)_2(\text{adp})\text{-}[\text{Zn}_2(\text{ox})_3]\cdot 3\text{H}_2\text{O}$ , consist ammonium cations, water molecules and adipic acids (adp) inside the interlayer spaces of 2D network (Figure 1.27). The proton conductivity of this MOF was found to be  $8 \times 10^{-3} \text{ Scm}^{-1}$  at  $25^\circ\text{C}$  under 98% RH, which is comparable to the proton conductivity of nafion. The higher proton conductivity at hydrous condition is due to the extended hydrogen-bonded network that is generated from the strong hydrogen bonding between ammonium cations, adipic acids and water molecules inside the 2D architecture. The proton conductivity of similar kind oxalate-bridged bimetallic complexes  $\text{NH}(\text{prol})_3$   $[\text{M}^{\text{II}}\text{Cr}^{\text{III}}(\text{ox})_3]$  ( $\text{M}^{\text{II}} = \text{Mn}^{\text{II}}, \text{Fe}^{\text{II}}, \text{Co}^{\text{II}}$ ) also have been examined, [1.44n] where the hydrophilic tri(3-hydroxy propyl) ammonium  $[\text{NH}(\text{prol})_3]^+$  cations inside the crystal structure promote hydrous proton conductivity. They reveal lower proton conductivity ( $\sim 1$

$\times 10^{-4} \text{ Scm}^{-1}$ ) and show performance only under the humidified condition only. The proton conductivities of the complexes significantly decrease to  $4.4 \times 10^{-10} \text{ Scm}^{-1}$  under 40% RH.

**Table 1.6:** Proton-conducting MOFs under hydrous condition reported in literature.

SL.No	MOFs and CPs	Proton conductivity ( $\text{Scm}^{-1}$ )	Ea (eV)	Conditions	Reference
1	$(\text{NH}_4)_2(\text{adp})[\text{Zn}_2(\text{ox})_3] \cdot 3\text{H}_2\text{O}$	$8 \times 10^{-3}$	0.63	25 °C and 98% RH	1.4e
2	1D Ferrous Oxalate Dihydrate	$1.3 \times 10^{-3}$	0.37	25 °C and 98% RH	1.44c
3	$(\text{NH}_4)_4[\text{MnCr}_2(\text{ox})_6]_3 \cdot 4\text{H}_2\text{O}$	$1.1 \times 10^{-3}$	0.23	25 °C and 98% RH	1.44o
4	Cucurbit[6]uril (CB[6])	$1.1 \times 10^{-3}$	0.39	25 °C and 98% RH	1.44d
6	$\{\beta\text{-PCMOF2}(\text{Tz})_{0.45}\}$	$5 \times 10^{-4}$	0.51	150 °C	1.45b
7	$\text{Mg}_2(\text{dobdc})_3 \cdot 0.35\text{LiO}i\text{Pr}_3 \cdot 0.25\text{LiBF}_4 \cdot \text{EC}3 \cdot \text{DEC}$	$3.1 \times 10^{-4}$	0.14	27 °C	1.44p
8	$\{\text{NH}(\text{pro})_3\}[\text{MIICrIII}(\text{ox})_3]$ (MII) = MnII, FeII, CoII	$1 \times 10^{-4}$		25 °C and 75% RH	1.44n
9	$(\text{H}_3\text{C}_2)_2(\text{dtoa}) \text{Cu}$	$1 \times 10^{-4}$		25 °C and 80% RH	1.44i
11	$[\text{Zn}(\text{I-L}_{\text{Cl}})(\text{Cl})](\text{H}_2\text{O})_2$	$4.45 \times 10^{-5}$	0.34	28 °C and 98% RH	1.44l
12	PCMOF-3	$3.5 \times 10^{-5}$	0.17	25 °C and 98% RH	1.44b
13	$[\text{MIL-53}(\text{Fe})-(\text{COOH})_2]$	$2.0 \times 10^{-6}$	0.21	25 °C and 98% RH	1.44a

Proton conduction of related bimetallic oxalate-based MOFs  $[\text{N}(\text{R})_3(\text{CH}_2\text{COOH})][\text{FeCr}(\text{ox})_3]$  also have been investigated [1.44q] replacing  $\text{NH}(\text{pro})_3$  cations by  $\text{N}(\text{R})_3(\text{CH}_2\text{COOH})$  cations where R=Me (methyl), Et (ethyl) or Bu (n-butyl). Since, the cationic component consist carboxyl group that will be fruitful for proton carrier under hydrous condition. The hydrophilicity of the cationic ion was tuned by the  $\text{NR}_3$  residue. Generally, hydrophilicity decreases with increasing the size of the R group of the residue:  $[\text{NMe}_3(\text{CH}_2\text{COOH})]^+ > [\text{NEt}_3(\text{CH}_2\text{COOH})]^+ > [\text{NBu}_3(\text{CH}_2\text{COOH})]^+$ . The hydrophilicity of  $[\text{N}(\text{Me})_3(\text{CH}_2\text{COOH})][\text{FeCr}(\text{ox})_3]$  is very high compare to others which is reflected in high water vapour adsorption as well as high proton conductivity of  $\sim 10^{-4} \text{ Scm}^{-1}$  under 65% relative humidity (RH).

### 1.7.3 Anhydrous proton conductivity in MOF:

As already discussed in earlier section, developing proton-conducting materials that are capable of operating above 80 °C temperature have been a great challenge and could be fruitful for practical applications in fuel cell [1.46]. Extensive amount of research is being carried out to find suitable proton conductive materials that can function at high temperatures (80 °C to 250 °C) as well as under anhydrous condition for the commercialization of fuel cell. Along this goal, MOFs proved to be the promising candidate due to their high thermal stability, crystallinity and porosity which can be used as a platform for solid support. Moreover, by tuning the functionality inside MOF network, one can tailor their property as

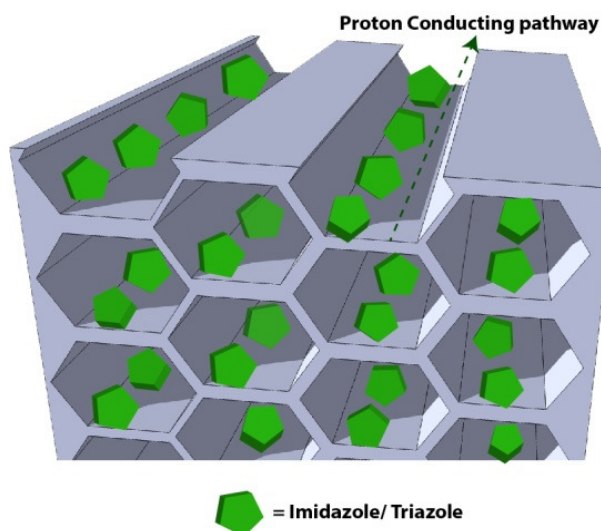


**Figure 1.28:** Schematic representation of MOF channel which is filled by imidazole/ triazole /pyrazole etc. molecules for anhydrous proton conduction. Redrawn with permission of 1.45a

well as efficiency for specific applications. It has been observed that imidazole, pyrazole and triazole type organic molecules can conduct proton through the discrete channels at higher temperature (Figure 1.28) [1.47]. However, several proton conducting MOFs are reported in literature, where water molecules inside 1D or 2D channels are responsible for the proton conduction [1.48]. Based on above idea, replacement of water molecules by imidazole or triazole molecules inside the porous channels of MOF should logically improve the proton conducting efficiency at high temperature. In fact, same approach was first demonstrated in 2009, by encapsulating proton conducting imidazole guest inside the MOF channels. Two porous MOFs  $[Al(\mu_2-OH)(1, 4-NDC)_n]$  (**1**) and  $[Al(\mu_2-OH)(1, 4-BDC)_n]$  (**2**) {1,4-NDC =1,4-naphthalene dicarboxylate and 1,4-BDC = 1,4-benzene dicarboxylate} have been chosen for encapsulation of guest imidazoles inside the frameworks. Both these MOFs [1.49a and b] have the pore dimension  $\sim 8 \text{ \AA}$  as a result, imidazole ( $4.3 \times 3.7 \text{ \AA}^2$ ) molecules easily get incorporated inside the pores (Figure 1.29a and 1.29b). The anhydrous proton conductivities measured for **1@Im** and **2@Im** at room

temperature were found to be in the range of  $10^{-8}$  to  $10^{-10}$   $\text{Scm}^{-1}$  [1.45a]. However, the anhydrous proton conductivity measured at 120 °C have increased drastically [ $2.2 \times 10^{-5}$   $\text{Scm}^{-1}$  for **1@Im** and  $1.0 \times 10^{-7}$   $\text{Scm}^{-1}$  for **2@Im**]. The activation energy of **1@Im** and **2@Im** were found to be 0.6 eV and 0.9 eV respectively, indicating that the proton conduction via vehicle mechanism. The difference in conductivity was due to the polar channels in the BDC framework interfering with the free rotation of the imidazole molecules that result lowering the conductivity of **2@Im**. On the other hand, NDC framework channels have more hydrophobic nature which interact weakly with polar imidazoles and allow the guest molecules to move freely in the channels. It should also be noted that, the conductivity is still lower than pure imidazole under the similar conditions, showing that the non-polar ndc framework is lowering the conduction abilities of imidazoles.

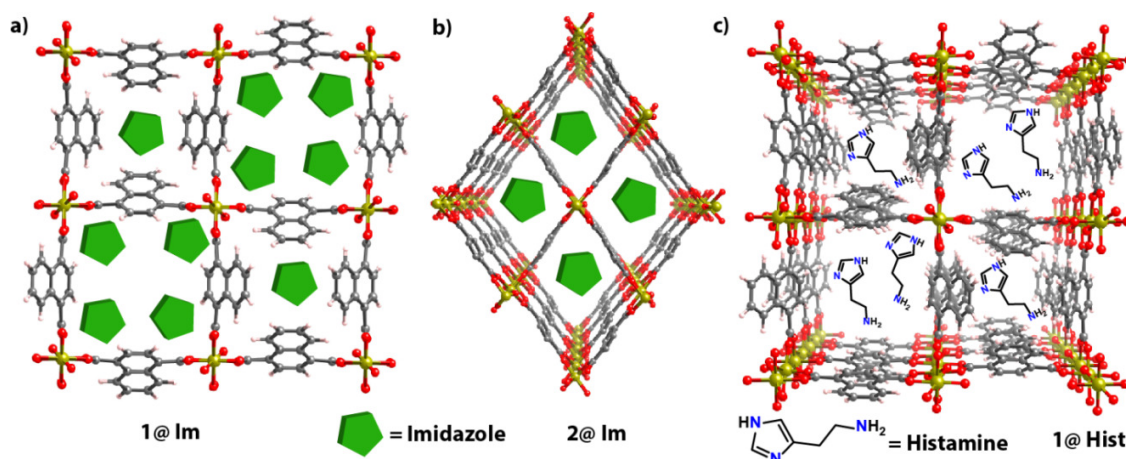


**Figure 1.29.** Structure of Al based MOF (a) imidazoles loaded Al-NDC based framework [**1@Im**], (b) imidazoles loaded Al-BDC based framework [**2@Im**], (c) structure of Al-NDC based MOF loaded with histamines for anhydrous proton conduction. Colour code: Al Yellow, O red, C gray and Imidazole green pentagon. [Redrawn the structures from the cif files of 1.45a and 1.49a]

Similar kind of idea further extended by incorporating histamine molecules inside the cavity of  $[\text{Al}(\mu_2\text{-OH})(1,4\text{-ndc})_n]$  (**1**). As already mentioned the compound (**1**) possess pore diameter of  $7.7 \times 7.7$  Å with one-dimensional channel networks [1.49a] thus, histamine molecules can be incorporated inside the cavity (Figure 1.29c). The proton conductivity of **1@Hist** was found to be  $3.0 \times 10^{-5}$   $\text{Scm}^{-1}$  at room temperature, which increases to  $1.7 \times 10^{-3}$   $\text{Scm}^{-1}$  at higher temperature (150 °C). The reason for increased conductivity of **1@Hist** than **1@Imd** at elevated temperatures is due to higher concentration and dense packing of

histamine molecules compared to imidazole molecules. The activation energy of **1@Hist** was calculated to be 0.25 eV.

In 2009, sulfonates based MOF loaded with triazoles (used as a protic organic guest) have characterized for proton conduction, extensively [1.45b]. The structure of 2,4,6-trihydroxy-1,3,5-benzene trisulfonate hemihydrates [ $\beta$ -PCMOF ( $\text{H}_2\text{O}$ )<sub>2</sub>] reveals 2D sheet in honeycomb like arrangement, which is cross linked in three dimension with sodium ion. The space between the 1D channels is occupied by sodium, hydroxyl and sulfonate polar groups. The conductivity measurement of [ $\beta$ -PCMOF ( $\text{H}_2\text{O}$ )<sub>2</sub>] was found to be  $5.0 \times 10^{-6} \text{ Scm}^{-1}$  at 30 °C under anhydrous condition is mainly due to trapped water molecules inside the crystal structure. Heating the sample up to 80 °C under anhydrous condition results the reduction in conductivity ( $5.0 \times 10^{-6} \text{ Scm}^{-1}$ ) due to dehydration. In next step,  $\text{H}_2\text{O}$  molecules inside the channels of  $\beta$ -PCMOF were replaced by incorporating triazole molecules to produce [ $\beta$ -PCMOF (Tz)<sub>x</sub>, x=0.3, 0.45 and 0.6] (Figure 1.30a). No proton conductivity was observed at low temperatures and under anhydrous condition. However, at higher temperatures, the conductivity reached a maximum ( $5 \times 10^{-4} \text{ Scm}^{-1}$  at 150 °C when x = 0.45) under anhydrous condition, indicating the replacement of water molecules by triazole moieties.

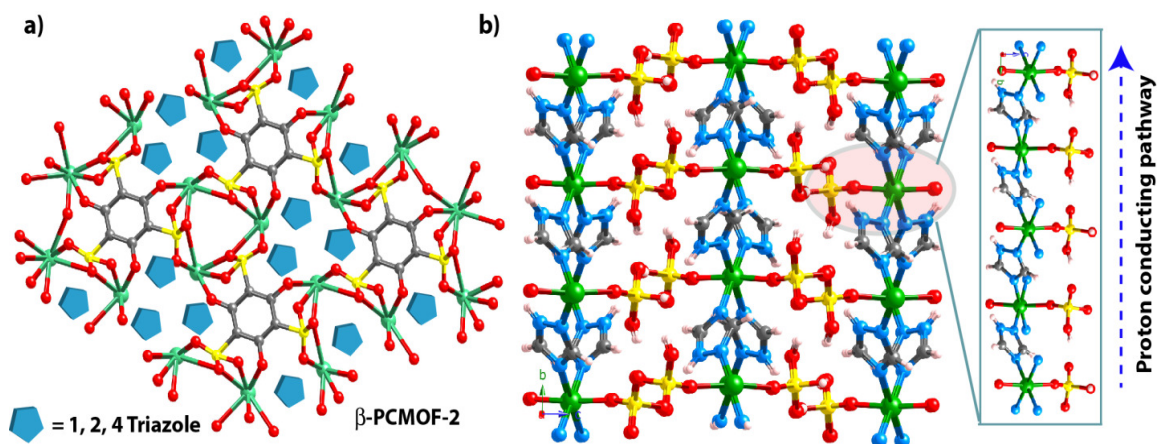


**Figure 1.30.** (a) Structure of  $\beta$ PCMOF-2, constructed from 1, 3, 5 benzene tri-sulphonic acid and Na metal. 1, 2, 4 Triazole molecule incorporated inside the pore of  $\beta$ -PCMOF-2 for anhydrous proton conduction. (b) Packing structure of [ $\text{Zn}(\text{H}_2\text{PO}_4)_2(\text{TzH})_2$ ]<sub>n</sub> coordinated triazolate linker forms 2D sheets where phosphates are dangled along the channel and creates proton conduction pathway. Color code: Na cyan, Zn green, P yellow, O red, N blue, C grey and 1, 2, 4 triazole- light blue pentagon respectively. H atoms have been omitted for clarity. [Redrawn the structures from the cif files of 1.45b and e]

Sometime, MOF shows intrinsic proton conduction without any help of guest molecules. One report of such MOF is  $[\text{Zn}(\text{H}_2\text{PO}_4)_2(\text{TzH})_2]_n$  [1.45e] composed by octahedral  $\text{Zn}^{2+}$  coordinated with orthophosphates as well as bridging TzH units. These sheets are stacked together in the crystallographic  $c$  direction, forming hydrogen bonds between triazoles and orthophosphates and create network for proton conduction through the channels (Figure 1.30b). The conductivity measured by  $[\text{Zn}(\text{H}_2\text{PO}_4)_2(\text{TzH})_2]_n$  at lower temperatures is within the range of  $10^{-6}$  to  $10^{-7}$  due to bulk phase grain boundary. However, higher temperature (150 °C) conductivity increased to  $1.2 \times 10^{-4} \text{ Scm}^{-1}$  with activation energy of 0.6 eV without support of any other guest proton-conducting materials. This was the first proposed example of inherent proton conduction in MOF without any loading of guest molecules.

Recently, high proton conductivity in MOFs has been achieved by the inclusion of inorganic acids into MIL-101 framework. Highly stable and porous chromium terephthalate (MIL-101) were loaded with sulfuric acid and phosphoric acid [1.44u]. The acid loaded MOFs called  $\text{H}_2\text{SO}_4@\text{MIL-101}$  and  $\text{H}_3\text{PO}_4@\text{MIL-101}$  have very high conductivity values,  $1 \times 10^{-2}$  and  $3 \times 10^{-3} \text{ Scm}^{-1}$  respectively at 150 °C and very low humidity (0.15% RH). Higher acidity of the guest acids contributed to the proton-conducting property of these hybrid materials while MOF is just used a vessel for these acids.



## CHAPTER 2

---

# FUNCTIONALIZED ZEOLITIC IMIDAZOLATE AND TETRAZOLATE FRAMEWORKS FOR HIGH CARBON DIOXIDE STORAGE CAPACITY

---

### 2.1 Introduction:

As discussed in section 1.6.3, porous MOFs with  $-NH_2$  functional groups exposed into the pores showed high physisorptive  $CO_2$  adsorption enthalpy resulting in the enhancement of the  $CO_2$  adsorption properties. On the same line, some reports suggest that MOFs with heterocycle derivatives specially adenine based bio-MOF-11 where several  $sp^2$  nitrogen atoms have promoted towards high  $CO_2$  adsorption [1.35a]. Taking these advantages in consideration we anticipate that, presence of both  $-NH_2$  functionality and heterocycle derivatives in single domain would logically improve the heat of  $CO_2$  adsorption. In these regards, in order to study the high  $CO_2$  adsorption behaviors in functionalized MOFs, we started working on the synthesis and  $CO_2$  gas adsorptions of MOFs synthesized from 5-amino tetrazole (5-AT) as linker with Zn (II) metal center. During the synthesis, firstly we have utilized 5-AT as an organic linker not only due to the presence of  $-NH_2$  group into its backbone, but it also holds following advantages:

- (a) Tetrazolate rings have four  $sp^2$  nitrogen atoms which generates polarity inside the MOF architecture suitable for high  $CO_2$  uptake.
- (b) Its geometry can induce the formation of several zeolitic topologies with tunable pore sizes framework which eventually applied for many characteristics such as selective gas adsorption, gas storage and catalysis.
- (c) Moreover the combination of polar amino group bonded with carbon atom in this ligand results in significant surface polarization which enhances the interaction of MOF with  $CO_2$  molecules.

In this chapter, we report of a three dimensional amino functionalized Zeolitic Tetrazolate Framework (ZTF-1) starting from 5-AT and Zn(II) metal salts, where only N1 and N4 are coordinated to metal centers ( $Zn-5AT-Zn$  angle is close to  $145^\circ$ , coincident

with the Si–O–Si angle) and adopt a tetrahedral framework reminiscent of those found in zeolites (Figure 2.1). Note that, previously, there is only one report of ZIF with  $\text{-NH}_2$  functionality due to the difficulty in synthesis as well as  $\text{-NH}_2$  group has affinity to coordinate with metal center that can annihilate the zeolitic topological structure. However, ZTF-1 is the one and only report of  $\text{-NH}_2$  functionalized three dimensional zeolitic metal tetrazolate framework with uncoordinated tetrazolate nitrogen as well as free  $\text{-NH}_2$  functionality. The framework of ZTF-1 adopts zeolitic *dia* topology with a pore size of 4.5 Å in diameter. Moreover, it shows high  $\text{CO}_2$  uptake (120 cc/g at 273 K and 1 bar pressure) due to the presence of free  $\text{-NH}_2$  group and uncoordinated tetrazolate nitrogens which has been verified both experimentally as well as computationally.

Since, the polar functional groups have significant contribution on the  $\text{CO}_2$  capture in MOFs (section 1.6.3). Hence, as a part of our investigation, we have also attempted to synthesize a series of ZIFs with large pore diameter and aperture [1.37]. Specifically, the synthesis of GME topology [1.37c and d] based ZIFs which are exceptional due to their large pore aperture and diameter. GME ZIFs typically synthesized by using equimolar amounts of 2-nitro imidazole (nIm) and a second substituted imidazole [1.37d]. The second link is the key to achieving a wide range of pore diameters and functionalities. Since the polar functional groups such as  $\text{-NO}_2$ ,  $\text{-OH}$ ,  $\text{-CN}$ ,  $\text{-Cl}$ , and  $\text{-Br}$  have been used for the synthesis of GME ZIFs hence, depending on polarizing strength enhancement of  $\text{CO}_2$  uptake capability will change [1.37d]. Here, we report the synthesis and characterizations of three cobalt (Co) based ZIFs, Co-ZIF-68, -69 and -81 that have the GME topology. These ZIFs resemble three previously reported zinc (Zn) based ZIFs (ZIF-68, -69 and -81; hereafter will be mentioned as Zn-ZIF-68, -69 and -81) [1.37c and d] with same GME topology and similar tunable pore apertures,  $d_a$ , (7.7, 4.6 and 4.2 Å) and diameter,  $d_p$  (10.4, 7.9 and 7.6 Å) respectively. These ZIFs are composed of two different imidazolate links (double-links) and the pores are functionalized with  $\text{-NO}_2$  and  $\text{-C}_6\text{H}_6$  (Co-ZIF-68) or  $\text{-C}_6\text{H}_5\text{Cl}$  (Co-ZIF-69) or  $\text{-C}_6\text{H}_5\text{Br}$  (Co-ZIF-81) functionalities (Figure 2.4). Our motivation was to check whether these functionalities in GME ZIF architectures have any role on  $\text{CO}_2$  capture by replacement of metal center. However, similar efforts on iso-structural MOFs containing different metal coordination sites are limited to only handful of systems, such as CPO-27-M, [1.27b] or M/DOBDC [M= Zn, Co, Ni, Mg] [1.26e] with open metal sites



inside the framework. Hence, extensive study on large number of systems is needed to completely understand the effects of metal replacement on  $H_2$ ,  $CO_2$ ,  $CH_4$  and other gas adsorption properties in MOF. This aspect motivated us to attempt for this metal replacement among these Co/Zn-ZIFs, with same crystal structures, so that we can understand the role of metals on  $CO_2$  binding. As mentioned before, this type of metal replacement has been demonstrated in MOFs containing open metal sites, [1.26e] but similar study in MOFs/ZIFs which devoid of any open metal sites have not been attempted so far.

## 2.2 Result and Discussion

### 2.2.1 Structural analysis of ZTF-1

The crystal structure of ZTF-1 was found to be related to the diamond (**dia**) topology [2.1]. The tetrahedral (T) atoms are Zn and the linkers are 5-AT bonding to Zn via the N atoms of the five-membered tetrazolate ring (Figure 2.2a). The Zn...Zn distance ( $\sim 5.9 \text{ \AA}$ ) in ZTF-1 like ZIFs is extended by replacing oxide ions with tetrazolate linkers (the corresponding Si...Si distance in aluminosilicates is about  $3.0 \text{ \AA}$ ) [2.2]. This leads to an expanded metal tetrazolate with voids (Figure 2.2c) and an extended 3D ZTF structure with a pore size of  $4.5 \text{ \AA}$  in diameter (Figure 2.2c). The **dia**

framework of the ZTF-1 is illustrated in figure 2.2b, which shows only the vertices (T atoms), edges (links between the T atoms) and the network topological connectivity (ball-stick). [2.3] It is simply made up of four coordinated  $[6^4]$  tiling with a transitivity of 1111 (vertex, edge, face, tile). A monoclinic unit cell of ZTF-1 which contains 4 zinc ions within

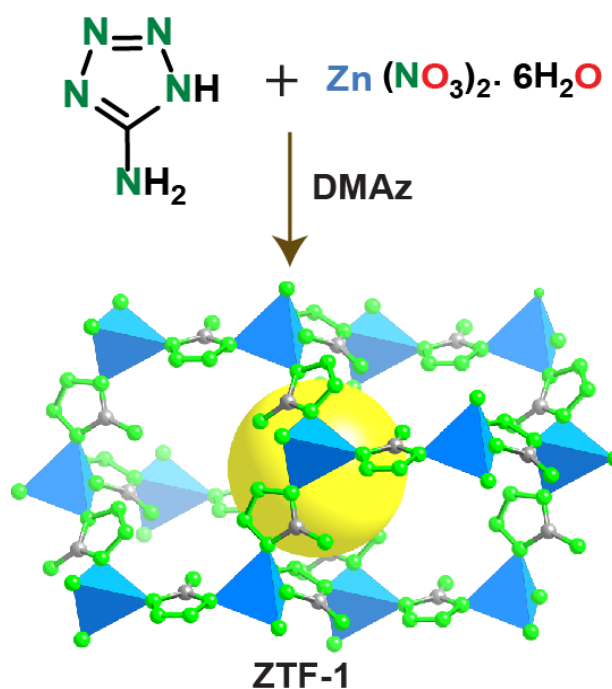


**Figure 2.1:** Synthesis of ZTF-1 from 5-amino tetrazole and Zn(II) salt in presence of structure directing agent DMAz.

a unit cell volume of  $1349.7(5) \text{ \AA}^3$ . The density ( $T/V$ ) of metal atoms per unit volume is  $2.09 \text{ nm}^{-3}$ , which is comparable to ZIFs ( $2.08 - 3.7 \text{ nm}^{-3}$ ) and much less than that of zeolites ( $12 - 20 \text{ nm}^{-3}$ ). Figure 2.2c shows the separate adamantane type cage in the structure of ZTF-1. The adamantane cage consists of 10 Zn (II) ions and 12 5-AT and each cage is surrounded by 6 similar cages (Figure 2.2d). Note that, because of the way the 5-AT linkers are oriented, there are six 5-AT links pointing inwards each cage while six are pointing outwards. Apart from the  $-\text{NH}_2$  functionality, uncoordinated N2 and N3 nitrogen are exposed to the pore. As shown in figure 2.2c, the largest 6-membered ring has a pore aperture of  $4.3 \text{ \AA}$ . The reason for ZTF-1 adopting the **dia** topology (Figure 2.2c) is not very clear to us.

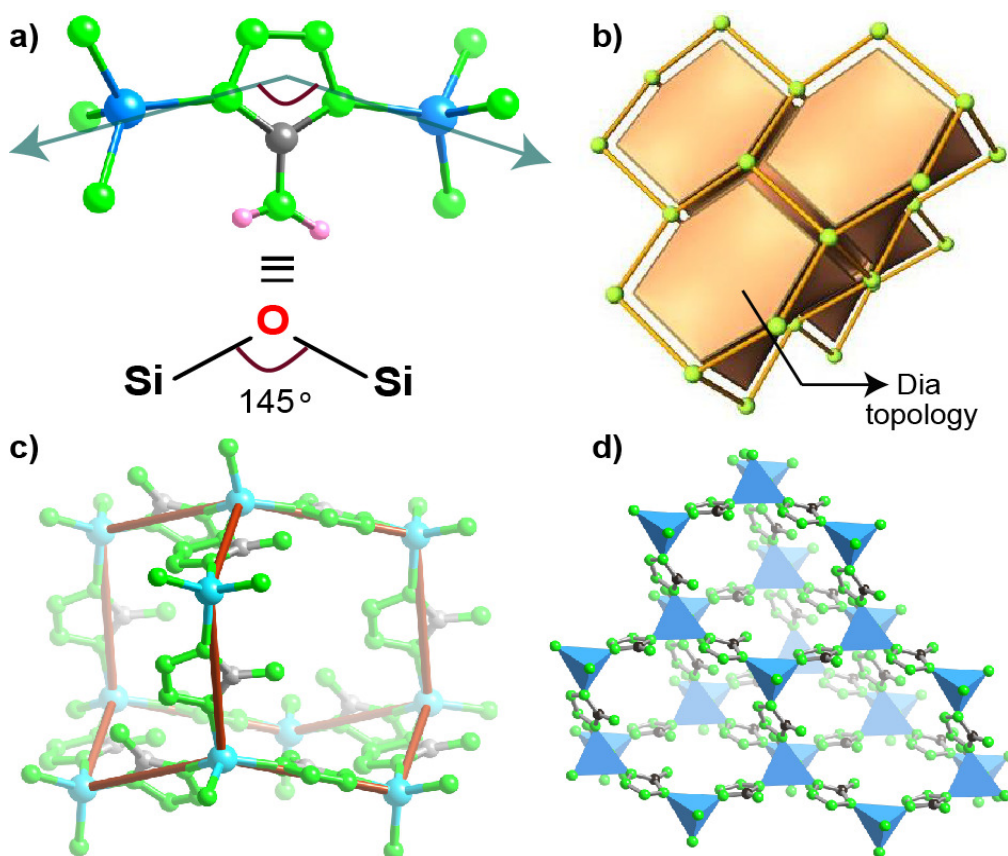


**Figure 2.2:** Crystal structure of ZTF-1. (a) The Zn-TET-Zn bridging angle in ZTF-1 resembles with Si-O-Si structure in zeolites. (b) The framework adopts a dia topology. The structure is shown as an exploded tiling of adamantane (brown) with all the tetrahedral Zn(II) atoms (green) are linked. (c) Zn(II) and 5-amino tetrazolate clusters are bridged together to generate an extended 3D porous structure (d) 3D packing diagram of ZTF-1. [Zn(II) blue, C black, N green]

We calculated the M–L–M angle of all ZIFs reported so far (Table 2.1 and Figure 2.3) to elucidate the reason for the formation of the **dia** topology with 5-AT rather than the **sod** topology (obtained with 2-methylimidazolate and 2-nitroimidazolate). The **dia** topology is found to withstand a wide variation of the M–L–M angle (from 135° to 149°) compared to any other topology reported (**sod** withstands a variation of 141° to 147°) [2.4].

**Table 2.1:** Types of ZIFs (including the number of times) reported in the literature and the M-X-M bond angle range.

SL. No	Type	Number of Hits	Angle Range
1	sod	12	143.32 to 147.78
2	dia	10	140.2 to 149.4
3	crb	7	142.44 to 149.62
4	gis	6	142.34 to 149.05
5	rho	5	141.88 to 151.39
6	cag	5	140.84 to 143.31
7	zni	5	142.76 to 146.38
8	mog	4	141.87 to 146.25
9	ita	4	141.43 to 142.22
10	gme	3	144.26 to 146.13
11	neb	3	140.88 to 145.14
12	nog	3	138.28 to 145.88
13	frl	2	144.81 to 149.25
14	dft	2	143.71 to 145.22
15	coi	2	144.46 to 144.49
16	mer	2	144.81 to 145.03
17	zec	1	142.23
18	zeb	1	140.18
19	fes	1	146.81
20	ana	1	144.88
21	srs-c-b	1	144.16

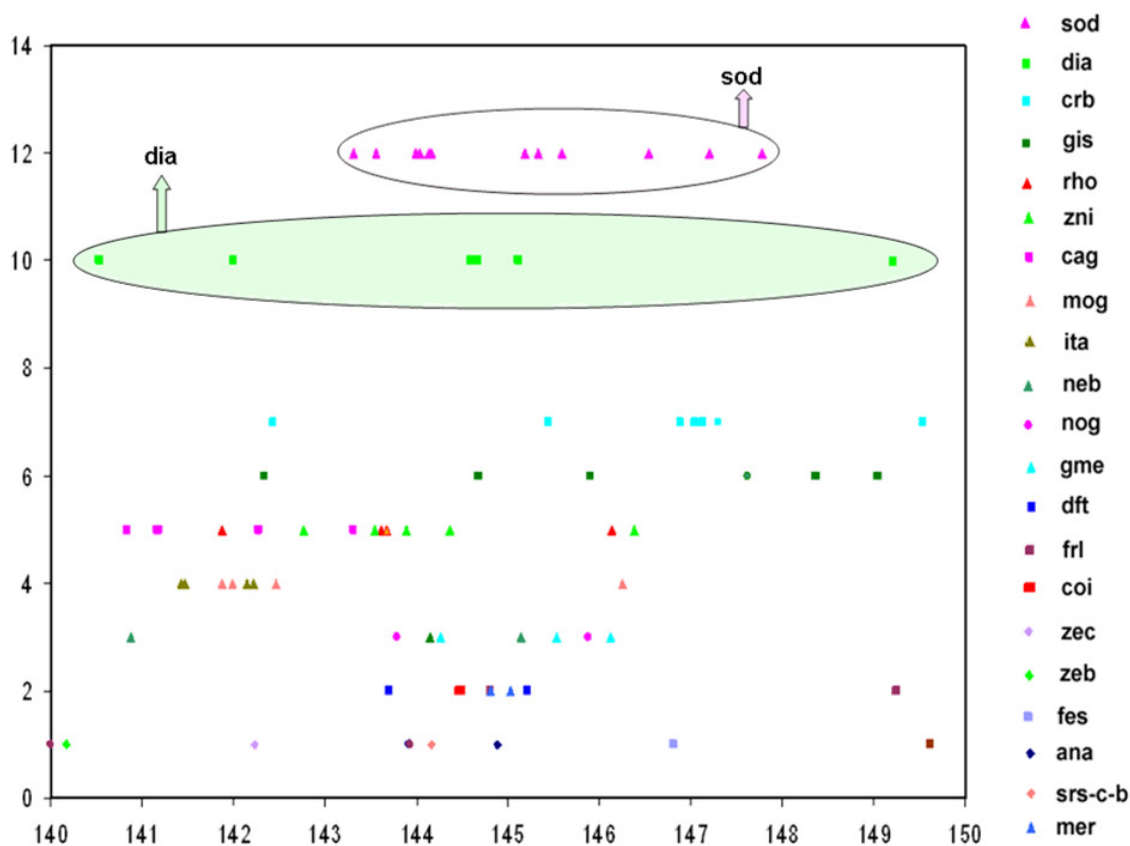


**Figure 2.3:** Angular distribution for the M-X-M angles. X axis represent the angle range and Y axis represent the number of hits. It should be noted that, we have assigned total number of hits for every case in order to separate each type from others.

### 2.2.2 Structural analysis of Co-ZIF-68, -69 and -81

In general the transition metal atoms, Zn or Co, replace the T atoms (e.g. Si, Al and P) of zeolites and imidazolates (IMs) replace the bridging oxide ions in ZIF structures. Moreover, by reacting metals with IM-type links one can rapidly obtain tetrahedral, porous ZIF structures and access topologies previously unrealized in zeolite materials. Furthermore, it has been demonstrated that one can synthesize ZIFs containing two chemically different imidazolate links. This usage of double-links introduces a new level of complexity to the pore composition and structure. Among several double-linked ZIFs reported in literature, we identified three Zn-ZIFs (Zn-ZIF-68, -69 and -81) with the GME topology, composed of one common nitroimidazolate (nIM), and one substituted benzimidazolate [ $C_6H_6$ ,  $-C_6H_5Cl$ ,  $-C_6H_5Br$ ] (Figure 2.4).

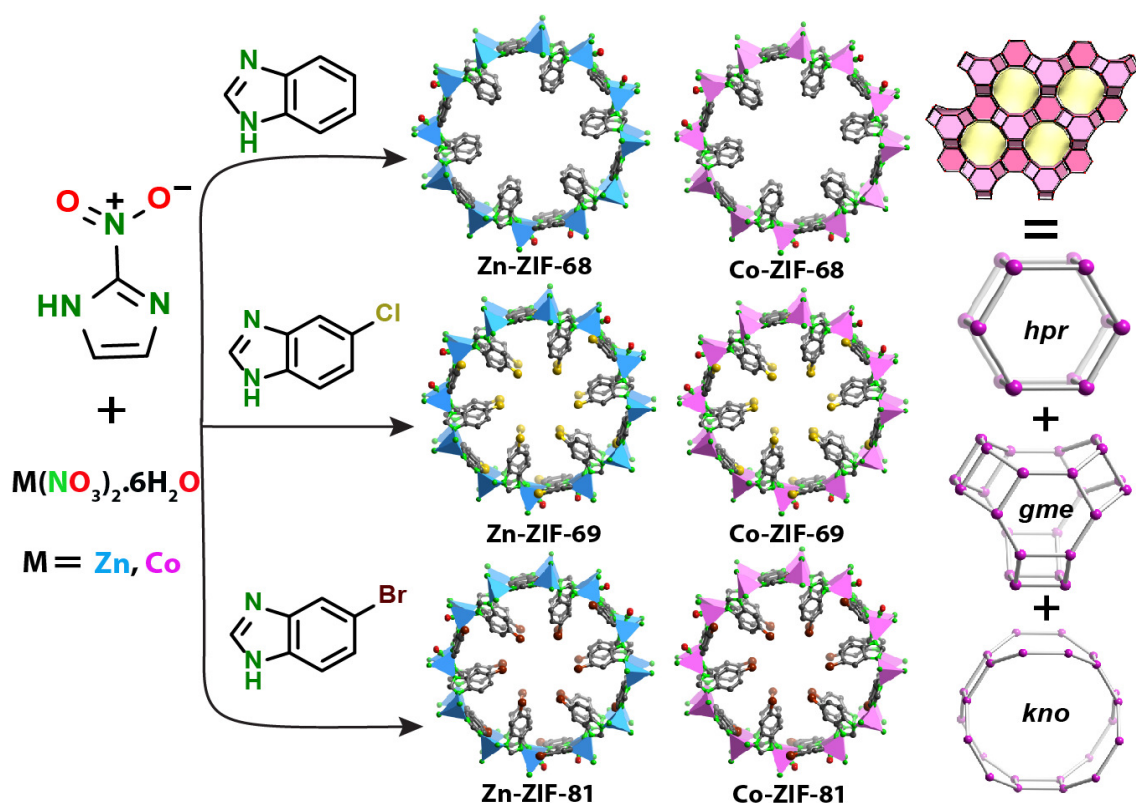


**Figure 2.4:** Reaction of 2nIM with different imidazole based linkers (bIM, Cl-bIM and Br-bIM) construct the **GME** topology. Blue and pink polyhedral indicates Zn and Co metal center respectively. H atoms are omitted for clarity. At right side, the schematic representation of *hpr*, *gme*, and *kno* cages, which construct the **GME** topology.

These links consistently occupy specific positions in the framework of these three Zn-ZIFs. Here, we report an excellent example of metal substitution [from Zn to Co] on these Zn-ZIFs to synthesize three new Co-ZIFs [Co-ZIF-68, -69, -81], which feature the same GME topology as well as a range of functionality and finely varied pore metrics (Figure 2.4). As expected, all these Co-ZIFs crystallize in the same hexagonal space group ( $P6_3/mmc$ ) and have very similar unit cell dimensions ( $a = b \sim 26 \text{ \AA}$ ,  $c \sim 19 \text{ \AA}$ ;  $V \sim 11500 \text{ \AA}^3$ ). The unit cell of these Co-ZIFs contains 24 Co ions. However, they differ in the nature of the functional groups decorating the pores and in the metrics of their pore structure.

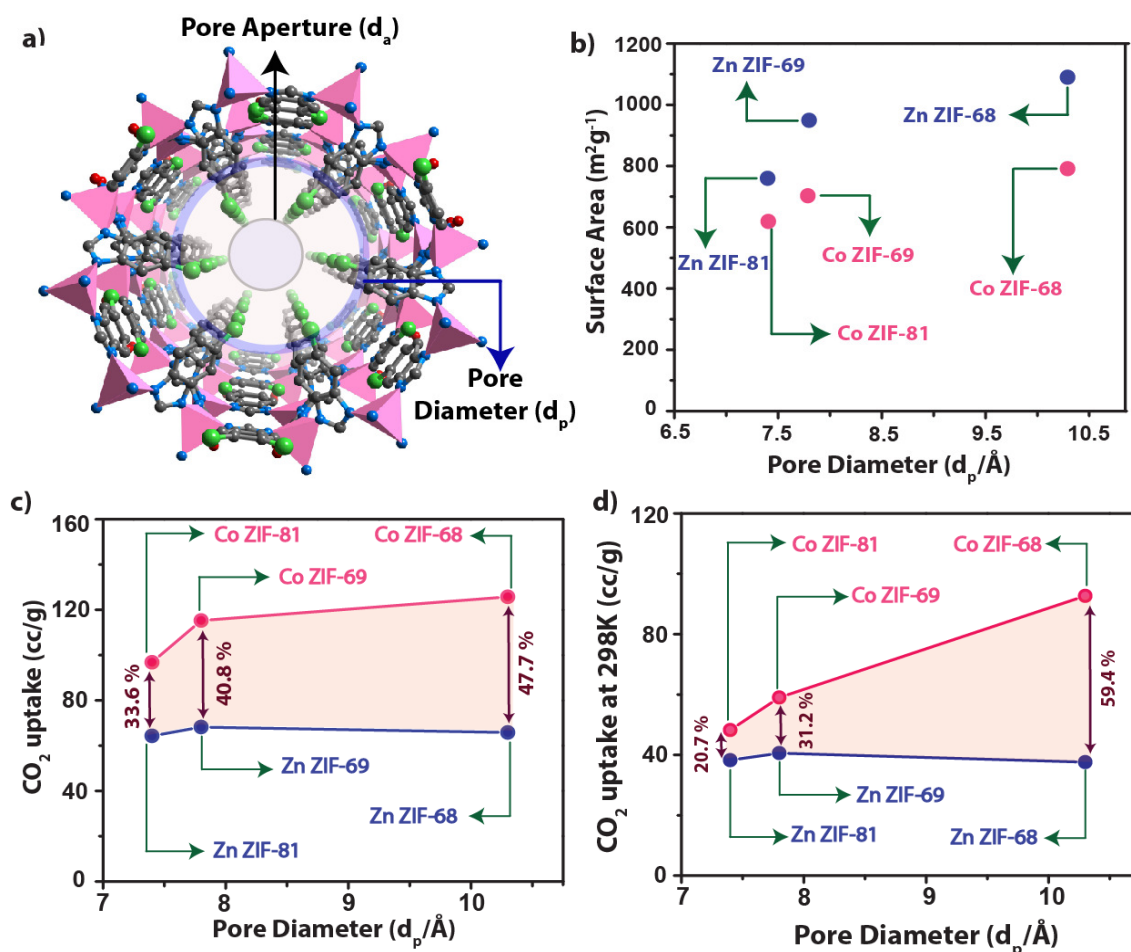


**Figure 2.5:** (a) Pictorial definition of pore aperture ( $d_a$ ) and pore diameter ( $d_p$ ) of Zn and Co based GME ZIFs. (b) pore diameter ( $d_p$ ) vs surface area for Co and Zn based GME ZIFs. (c) Pore diameter ( $d_p$ ) vs  $\text{CO}_2$  uptake for Co and Zn based GME ZIFs at 273 K and (d) 298 K. It is clearly indicate that Co based GME ZIFs analogue have much higher  $\text{CO}_2$  uptake than Zn based GME ZIFs.

The GME topology is illustrated in Figure 2.5, only the vertices (T atoms) and edges (links between T atoms) are shown [2.5]. The structures of Co-ZIF-68, -69 and -81 can be described as being built from three types of cages, namely *kno*, *gme* and *hpr* cages in the ratio 1:1:1. These *kno* cages (24 Co ions), form a 12 membered channel parallel to the *c*-axis. nIM links in the *hpr* cages are oriented in such a way that, there exist a number of weak C–H $\cdots$ O interactions {D, 3.212 (2)  $\text{\AA}$ ; *d*, 2.654(4)  $\text{\AA}$ ;  $\theta$ , 114.2 (3) $^\circ$ } [2.6] between a substituted benzimidazole hydrogen and two oxygen atoms from adjacent nIM links. These interactions appear to favor the formation of *hpr* cage. The  $-\text{NO}_2$  functionalities between two adjacent nIMs are separated [O $\cdots$ O 3.73 (2)  $\text{\AA}$  and 4.16 (4)  $\text{\AA}$ ] in such a way that steric

repulsion is minimal. The *gme* cages are also supported by a number of weak C–H...O interactions [ $\sim$ D, 3.101(6) Å;  $d$ , 2.948(3) Å;  $\theta$ , 110. 1(2)°] similar to those in the *hpr* cages (see supporting information for detailed description). The  $d_a$  and  $d_p$  (Figure 2.5) values of each *gme* cage (4.1 and 6.2 Å) and *hpr* cage (3.1 and 5.4 Å) remain essentially unaltered, as the main constituents of these cages is the common link, nIM, that occupies the same crystallographic positions in all these Co-ZIF structures. The GME topology is known to withstand a wide variation of the T–X–T angle (from 137° to 144°). [1.37c and d] The Co–IM–Co angle in these Co-ZIFs ranges from 137° to 144° whereas ZIFs bearing SOD (143° to 144°), RHO (136° to 140°), LTA (135° to 141°) or other topologies have much narrower range of angular flexibility. This added angular flexibility of the GME ZIFs allows for free variation of the functionality on the imidazolate link. This flexibility makes these ZIFs highly attractive for study, as the topology remains unaltered while one important structural variable such as metal substitution are modulated at will.

### 2.2.3 Thermal properties and X-ray powder diffraction analysis

As-synthesized ZTF-1 consists of 23.5 wt% of DMF, as quantified from XRD crystal structure, corroborated by thermo gravimetric analysis (TGA) (Figure 2.7d). The activated sample was prepared by exchanging the trapped solvent in as-synthesized ZTF-1 with dry methanol, followed by evacuation at room temperature. The methanol-exchanged and activated compounds were characterized by TGA measurements to assure full activation. In order to confirm the phase purity and consistency of the bulk materials, powder X-ray diffraction (PXRD) experiment was carried out on as synthesized ZTF-1 (Figure 2.15a). All major peaks of experimental PXRD of ZTF-1 well matched with simulated PXRD, indicating reasonably good crystalline as well as phase purity.

Thermal gravimetric analysis (TGA), performed on as-synthesized, solvent-exchanged and activated samples of Co-ZIF-68, -69 and -81 (Figure 2.6d), reveals a thermal stability range up to 250 °C, similar to the Zn based ZIFs (Zn-ZIF-68, -69 and -81) [1.37d]. The TGA trace for these as-synthesized and solvent exchanged Co-ZIFs showed a long plateau in the temperature range 100–390 °C, indicating thermal stability in the absence of guest molecules. In order to confirm the phase purity of the bulk materials, PXRD experiments were carried out on Co-ZIF-68, -69 and -81 (Figure 2.15b, c and d). All major peaks of



experimental PXRD of Co-ZIF-68, -69 and -81 are well matched with simulated PXRD, indicating reasonably good crystalline phase purity.

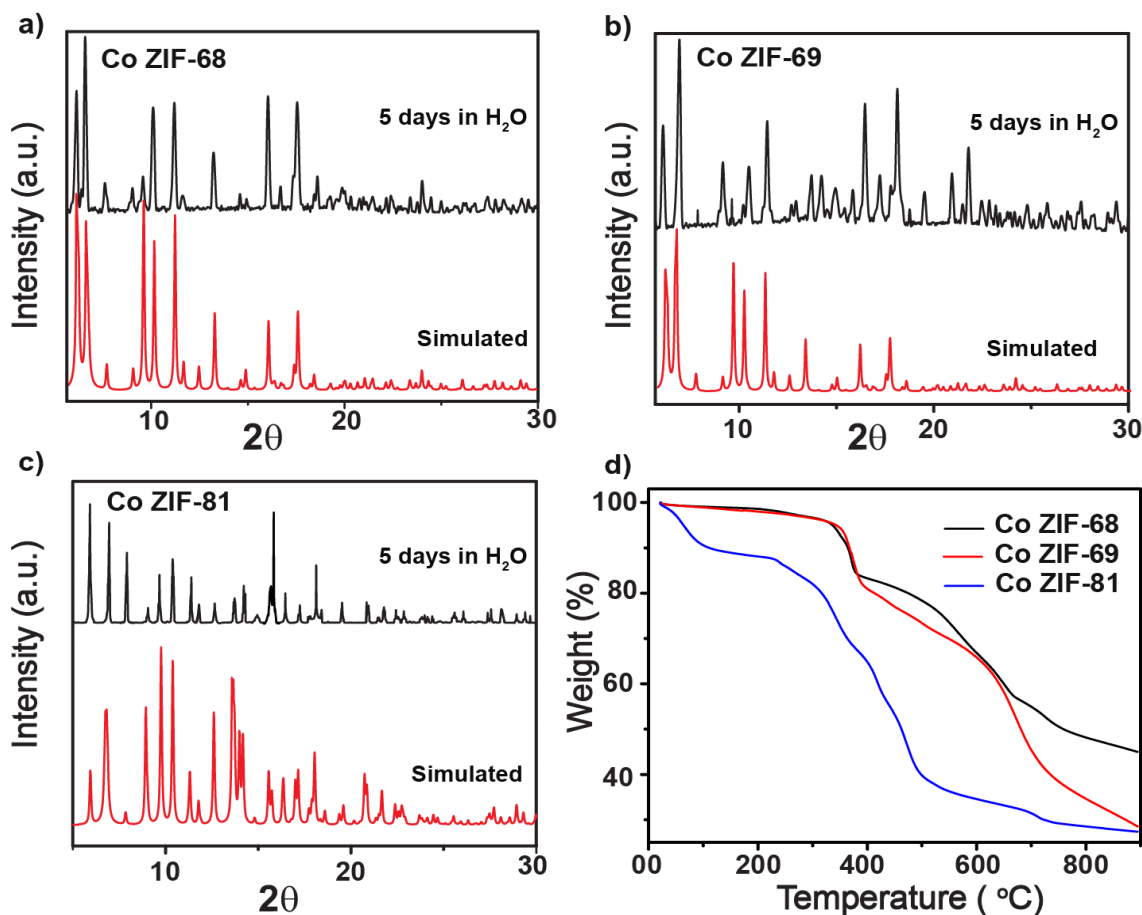


**Figure 2.6:** PXRD patterns of (a) Co-ZIF-68 (b) Co-ZIF-69 and (c) Co-ZIF-81 performed during stability test in water. The framework structure of all Co-ZIFs were unchanged after 5 days and matches well with simulated PXRD. (d) Thermo gravimetric analysis (TGA) of Co-ZIF-68, -69, and -81.

We also note that, the guests in Co-ZIF-68, -69 and -81 were released without damaging the frameworks as evidenced by the coincidence of the powder X-ray diffraction (PXRD) patterns with patterns simulated from the single crystal structures after heating to 300 °C in N<sub>2</sub> atmosphere. Examination of chemical stability was performed by heating the as-synthesized samples in water for 5 days. Remarkably, all retained their structures under this condition as evidenced by the sharp unshifted diffraction lines in their PXRD patterns (Figure 2.6).



## 2.2.4 Gas adsorption Properties

### 2.2.4.1 Gas adsorption study of ZTF-1

The architectural stability and permanent porosity of ZTF-1 were also confirmed by measuring the N<sub>2</sub> gas adsorption of the guest-free material (Figure 2.7a). The BET and Langmuir surface area were calculated to be 355.3 and 443.8 m<sup>2</sup>g<sup>-1</sup>. Recently researchers have shown that MOFs

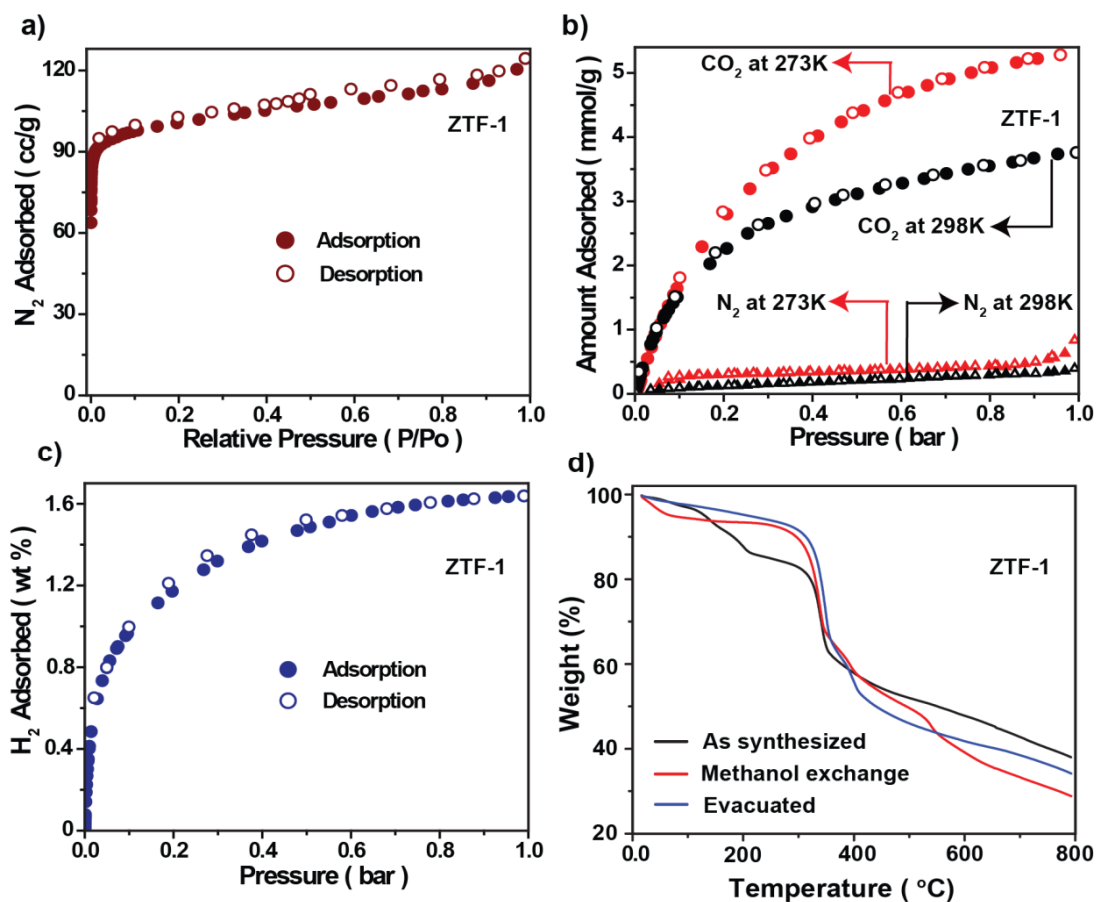


**Figure 2.7:** Gas adsorption isotherms of ZTF-1, (a) Nitrogen adsorption isotherm at 77 K. (b) Adsorption isotherms for CO<sub>2</sub> and N<sub>2</sub> at 273 K and 298 K. (c) Hydrogen adsorption isotherms at 77 K. The filled and open circles represent adsorption and desorption, respectively. (d) Overlay of TGA traces of as-synthesized (black), solvent-exchanged (red) and activated (blue) samples of ZTF-1.

and ZIFs can hold large amounts of carbon dioxide and have demonstrated that ZIFs can capture CO<sub>2</sub> selectively from CO and CH<sub>4</sub> (Table 2.3 for a detailed list of MOFs with high CO<sub>2</sub> uptake) [1.37]. Figure 2.7b shows the CO<sub>2</sub> adsorption isotherms for ZTF-1, which

shows high capacity for CO<sub>2</sub> than N<sub>2</sub> at 273 K. The CO<sub>2</sub> uptake at 760 torr for ZTF-1 is 10 times higher than N<sub>2</sub> at 273 K. Although ZTF-1 has lower CO<sub>2</sub> uptake (5.6 mmol/g at 273 K) than the Mg-MOF-74 (8.08 mmol/g at 298 K) but the CO<sub>2</sub> uptake of ZTF-1 compares well with the recently reported bio-MOF-11 (6 mmol/g at 273 K) and outperforms other ZIFs. Recently, Yaghi and Shimizu reported free -NH<sub>2</sub> functionalised zeolitic MOF, ZIF-96 and Zn-aminotriazolato-oxalate [1.24v, 1.26p, 1.26q, 1.33a and 2.7]. However, ZTF-1 contains both free tetrazole nitrogen and free -NH<sub>2</sub> functionality to interact strongly with CO<sub>2</sub>. As a result in terms of CO<sub>2</sub> uptake ZTF-1 out performs ZIF-96 (2.16 mmol/g at 298 K) and Zn-aminotriazolato-oxalate (4.3 mmol/g at 273 K). Since ZTF-1 has small pores and exposed -NH<sub>2</sub> functionality like the bio-MOF-11, which has a high (1.5 wt% at 77 K) H<sub>2</sub> uptake, we decided to collect H<sub>2</sub> adsorption isotherms for ZTF-1 at 77 K (Figure 2.7c). It should be noted that the repeatability of the H<sub>2</sub> adsorption behaviour was confirmed by reproducing the same isotherm three times at 77 K. The uptake at 760 torr at 77 K is 1.6 wt%, which is comparable to bio-MOF-11 and higher than those for ZIF-11 (1.4 wt%), ZIF-8 (1.3 wt%) and ZIF-20 (1.1 wt%). The initial uptake of ZTF-1, is also higher than that of ZIF-8 (1.3 wt%) and ZIF-11 (1.4 wt%). This suggests that a relatively strong interaction between the ZTF-1 framework and H<sub>2</sub> exists and small pores of ZTF-1 at low pressure and low temperature. A recent theoretical study suggests that nitrogen atoms on aromatic rings in a framework can enhance the adsorption energy of H<sub>2</sub> [2.8]. In ZTF-1, two tetrazole nitrogen and amino nitrogen are available to bind H<sub>2</sub> and thereby possibly enhancing the H<sub>2</sub> uptake compared to other ZIFs.

#### 2.2.4.2 Gas adsorption measurements of Co-ZIFs

The architectural stability and porosity of Co-ZIFs reported in this paper were also confirmed by measuring the N<sub>2</sub> gas adsorption of the guest-free material (Figure 2.8a). N<sub>2</sub> adsorption isotherms for Co-ZIFs exhibit the typical Type I isotherm, which is indicative of microporous materials. Co-ZIF-68, -69 and -81 showcases BET surface area of 792, 700 and 661 m<sup>2</sup>g<sup>-1</sup> respectively. We used CO<sub>2</sub> as a probe to characterize the effect of the change in chemical environment created via metal substitution inside the cages. These ZIFs have a disproportionately higher affinity and capacity for CO<sub>2</sub> than for other gases (Figure 2.9). The CO<sub>2</sub> uptake at 1 bar pressure for Co-ZIF-68, -69 and -81 is eight to ten times higher than the uptake for N<sub>2</sub> at 298 K.

**Table 2.2:** Pore volume, surface area and CO<sub>2</sub> uptake of all Co and Zn-ZIFs:

S.N	Zn and Co ZIFs	Pore diameter (d <sub>p</sub> )	Pore Aperture (d <sub>a</sub> )	Pore Volume	Surface Area (m <sup>2</sup> g <sup>-1</sup> )	CO <sub>2</sub> uptake (cc/g)	
						273 K	298 K
1	Zn-ZIF-68	10.3 Å	7.5 Å	571.8	1090	65.8	37.5
2	Co-ZIF-68	10.5 Å	7.7 Å	605.8	792	125.7	92.6
3	Zn-ZIF-69	7.8 Å	4.4 Å	248.3	950	68.1	40.0
4	Co-ZIF-69	8.0 Å	4.6 Å	267.9	700	115.2	59.0
5	Zn-ZIF-81	7.4 Å	3.9 Å	212.0	760	64.2	38.0
6	Co-ZIF-81	7.7 Å	4.1 Å	238.9	661	96.8	48.2

As shown in figure 2.8b, c and d, CO<sub>2</sub> uptake at 1 bar pressure is 33-48% higher for Co-ZIF-68, -69 and -81 compared to their Zn-ZIF counterparts at 273 K. Interestingly, this difference decreases for Co-ZIF-69 and -81 when we elevate the temperature at 298 K, but for Co-ZIF-68 this difference increases to 60% (Figure 2.5). We believe, this enhancement of CO-ZIFs CO<sub>2</sub> uptake of these ZIFs follow a sequence of Co-ZIF-68 (-C<sub>6</sub>H<sub>6</sub>)> -69(-C<sub>6</sub>H<sub>5</sub>Cl) > -81(-C<sub>6</sub>H<sub>5</sub>Br) > Zn-ZIF-69 (-C<sub>6</sub>H<sub>5</sub>Cl)> -68 (-C<sub>6</sub>H<sub>6</sub>) > -81(-C<sub>6</sub>H<sub>5</sub>Br).

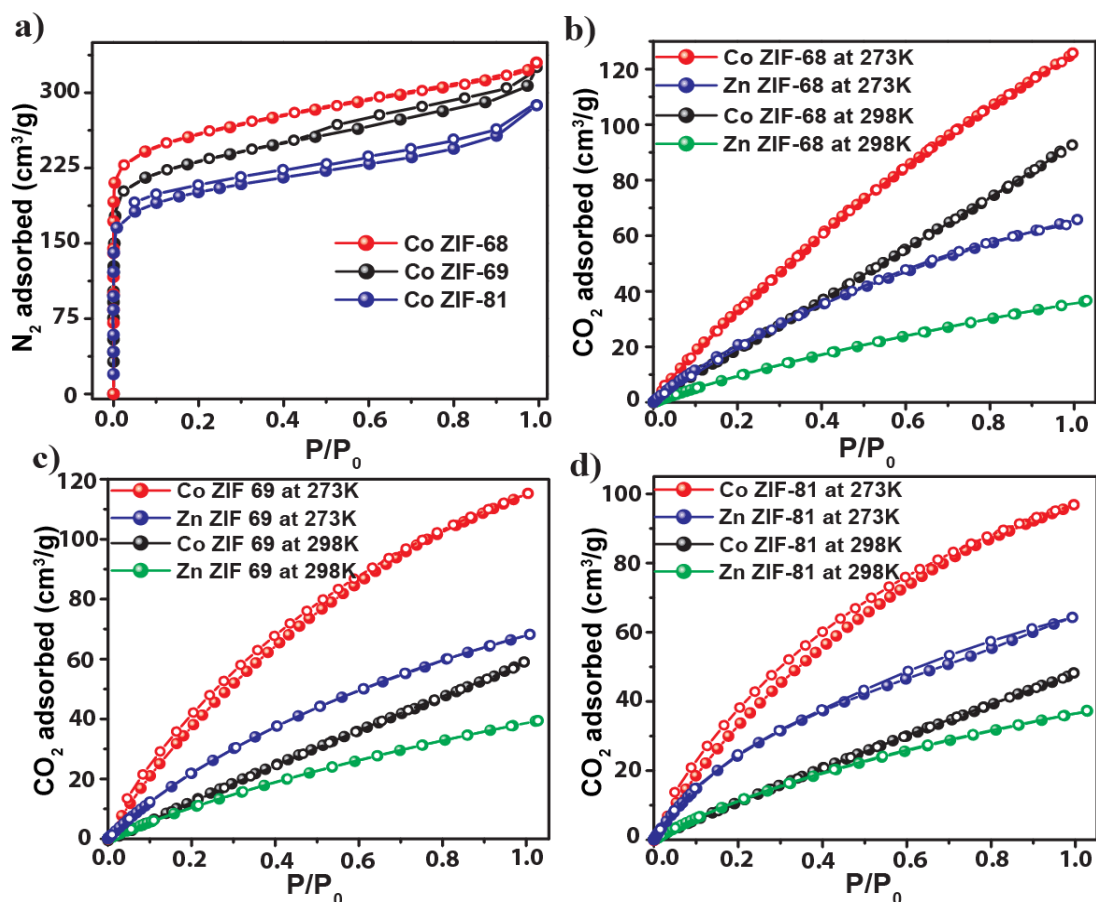


**Figure 2.8:** Volumetric Gas adsorption isotherms of ZIF-68, 69 and 81. (a) Nitrogen adsorption isotherm at 77 K. Comparison of CO<sub>2</sub> adsorption isotherms (273 K and 298 K) of (b) Zn and Co-ZIF-68 (c) Zn and Co-ZIF-69 (d) Zn and Co-ZIF-81. The filled and open circles represent adsorption and desorption, respectively. Zn ZIF-68, 69 and 81 (*J. Am. Chem. Soc.*, 2009, **131**, 3875) isotherm have been reproduced (with permission from ACS).

More importantly, figure 2.5b demonstrates a near linear relationship between pore aperture and surface area for Zn-ZIF-68, -69 and -81 and Co-ZIF-68, -69 and -81, which shows the usefulness of fine tuning of the pore structures along with the Zn/Co metal substitution. It should be noted that, although ZIFs does not have open metal sites like M/DOBDC but it follows the same trend of enhancement of CO<sub>2</sub> uptake upon metal replacement. We believe, the interaction with CO<sub>2</sub> presumably increases inside the Co based ZIFs compare to their Zn based analogues due to decreased ionic radius [Zn<sup>+2</sup> (0.68 Å) and Co<sup>+2</sup> (0.67 Å)] and M-O bond length [Zn-O (2.083 Å) and Co-O (2.031 Å)] in the framework. Moreover, low density of Co-ZIF-68, -69 and -81 frameworks compare to their isostructural Zn based analogue (Zn-ZIF-68, -69 and -81) could possibly enhance the CO<sub>2</sub> uptake as well.

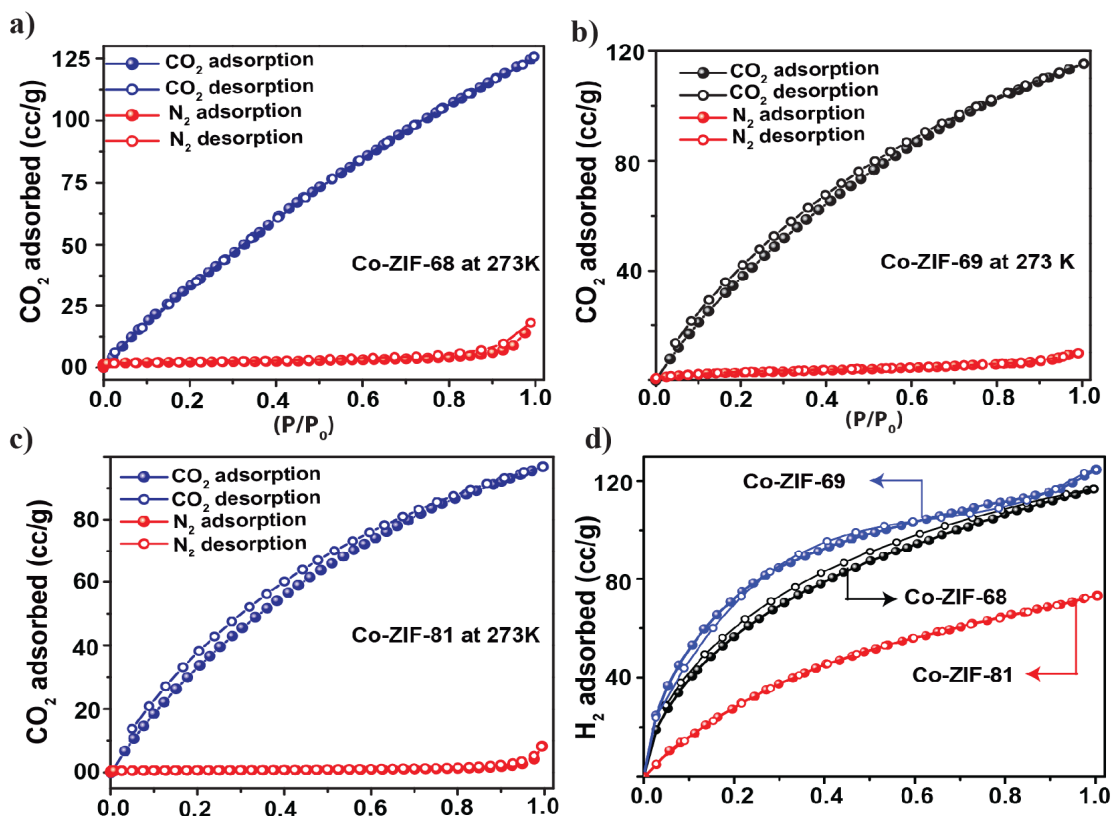


**Figure 2.9:** Selectivity of CO<sub>2</sub> uptake in compare with its N<sub>2</sub> uptake at 273 K of (a) Co-ZIF-68, (b) Co-ZIF-69 and (c) Co-ZIF-81. (d) H<sub>2</sub> adsorption isotherms of Co-ZIF-68, -69 and -81 taken at 77 K (red). Filled and open symbols represent adsorption and desorption branches.

**Table 2.3:** Ranking of low pressure (1 bar) CO<sub>2</sub> Adsorption Capacities in Metal Organic Frameworks at 273 K and 298 K:

SL No	MOFs	CO <sub>2</sub> uptake Gravimetrically (mmol/g at 1 bar)		CO <sub>2</sub> uptake Volumetrically (cc/g at 1 bar)		Ref
		273 K	298 K	273 K	298 K	
1	Mg\DOBDC	NA	8.0		180.9	1.26e
2	Co\DOBDC	NA	7.1		159.2	1.26e
3	Ni\DOBDC	NA	5.8		129.9	1.26e
4	Zn\DOBDC	NA	5.51		123.4	1.26e
5	HKUST-1	NA	4.7		105.7	1.26i
6	Zn + 4,4' bipy + (BTA-TBA)	NA	4.1		91.8	1.26w

7	Bio-MOF-11	6.0	4.0	134.4	89.8	1.26o
8	$[\text{Zn}_2(1)(\text{DMF})_2]_n(\text{DMF})_m$ [MOF(4)]	5.8	NA	129.9		1.26x
9	$[\text{Zn}_3(\text{OH})(p\text{-CDC})_{2.5}]_n$	NA	4.0		89.6	1.26y
10	Co-ZIF-68	5.6	4.1	125.6	91.8	This report
11	ZTF-1	5.3	3.7	119.8	84.8	This report
12	Co-ZIF-69	5.1	2.6	115.1	58.9	This report
13	Cd-ANIC-1	4.7	3.8	105.7	86.0	1.3k
14	Co-ZIF-81	4.3	2.1	96.7	48.1	This report
15	$\text{Zn}_2(\text{C}_2\text{O}_4)(\text{C}_2\text{N}_4\text{H}_3)_2 \cdot (\text{H}_2\text{O})_{0.5}$	4.3	3.7	96.3	84.6	1.26q
16	Co-ANIC-1	4.2	3.4	94.5	77.9	1.3k
17	CUK-1	NA	3.4	NA	77.9	1.3l
18	YO-MOF	NA	3.3	NA	75.9	1.3m
19	SNU-M10	NA	3.3	NA	73.9	1.3n
20	MOF-505	NA	3.2	NA	73.2	3.3f
21	$\text{H}_3[(\text{Cu}_4\text{Cl})_3\text{-}(\text{BTri})_8]$	NA	3.2	NA	72.8	1.26p
22	$(\text{In}_3\text{O})(\text{OH})(\text{ADC})_2(\text{NH}_2\text{IN})_2 \cdot 2.67 \text{H}_2\text{O}$	NA	3.2	NA	71.9	1.3o
23	CPM-6	4.76	2.9	106.62	64.9	1.3p
24	TMA@ Bio-MOF-1,	4.5	NA	100.8	NA	1.3q
25	TEA@ Bio-MOF-1	4.2	NA	94.08	NA	1.3q
26	TBA@ Bio-MOF-1	3.5	NA	78.4	NA	1.3q
27	UMCM-150	NA	2.8	NA	67.7	1.3r
28	$\text{Zn}_2(\text{BDC})_2$ (DABCO)	NA	2.7	NA	60.7	1.3s
29	CPM-5	3.62	2.4	81.08	54.4	1.3p
30	ZIF-78	3.348	2.2	75	49.9	1.37d
31	ZIF-96	NA	2.1	NA	48.3	2.7
32	IRMOF-3	NA	2.1	NA	47.9	1.35d
33	$(\text{In}_3\text{O})(\text{OH})(\text{ADC})_2(\text{IN})_2 \cdot$	NA	2.0	NA	46.5	1.3o

	4.67 H <sub>2</sub> O					
35	MOF-177	NA	1.7	NA	38.5	1.3s
36	Zn-ZIF-69	3.03	1.6	67.87	37.8	1.37d
37	MOF-5	NA	0.9	NA	20.6	1.3t

## 2.2.5 Computational Studies for ZTF-1 and Co-ZIFs:

### 2.2.5.1 GCMC simulation for ZTF-1

#### Simulation Model and Method

Next we wish to investigate the adsorption sites inside the gas-loaded crystal structure of ZTF-1. Grand canonical Monte Carlo (GCMC) simulations were employed to investigate CO<sub>2</sub> adsorption in de-solvated ZTF-1 to further confirm the adsorption mechanism (Figure 2.10a and b).

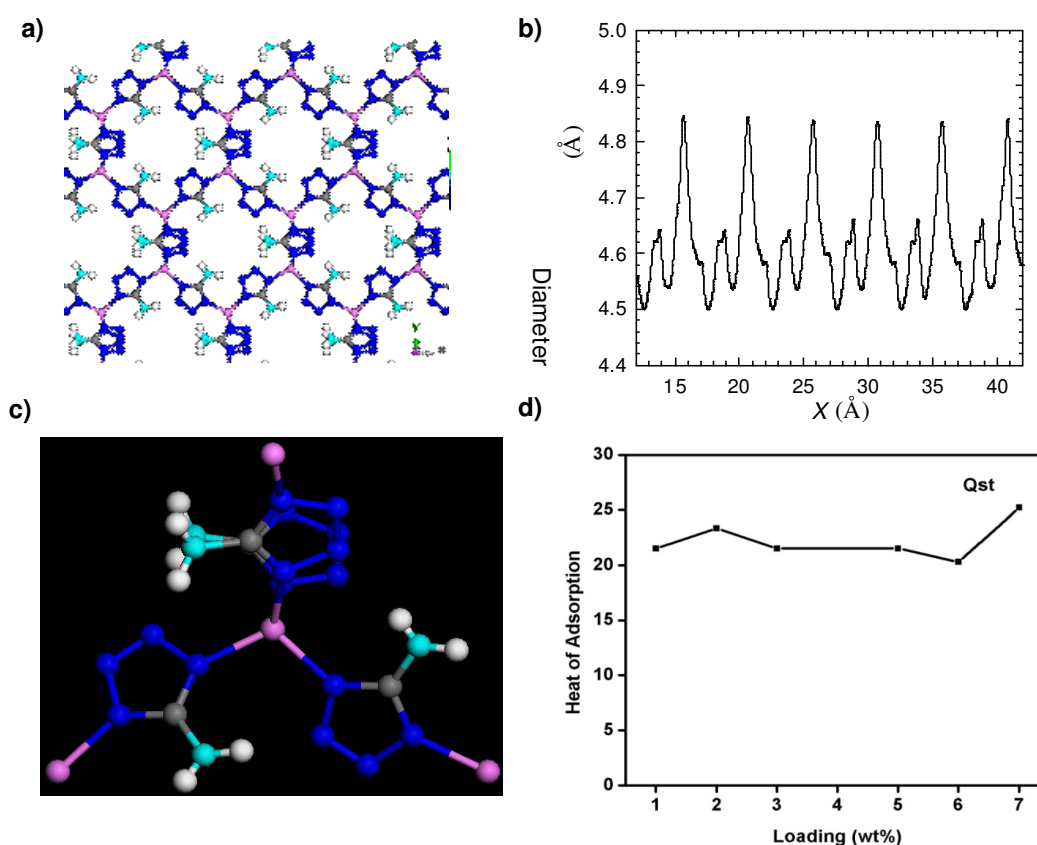


**Figure 2.10:** (a) Pore morphology and (b) diameter along the X axis in ZTF-1. (c) Atomic labels of ZTF-1. (d) The  $Q_{st}$  value for the CO<sub>2</sub> adsorption of ZTF-1.

The crystal structure of ZTF-1 measured from experiment was used in simulation. Figure 2.10a and b shows the morphology and diameter of the pore along the  $X$  direction calculated using HOLE program [2.9]. The pore diameter ranges from 4.50 to 4.85 Å. The porosity of ZTF-1 is 0.626, evaluated using Materials Studio [2.10] with a Connolly probe radius equal to zero. The atomic charges of the framework atoms in a unit cell of ZTF-1 were calculated from density functional theory (DFT) in Materials Studio [2.10]. The DFT calculation used the Becke exchange plus Lee-Yang-Parr correlation functional and the all-electron core potentials. The double- $\xi$  numerical polarization (DNP) basis set was adopted, which is comparable to the 6-31G(d,p) Gaussian-type basis set. Mulliken population analysis was used to estimate the atomic charges as in Table 2.4

**Table 2.4:** Atomic charges in ZTF-1 with the atomic labels indicated in Figure 2.10c.

<b>Atom type</b>	N1	N2	N3	N6	N8	C1	H3(A, B)	Zn
<b>Charge</b>	-0.478	-0.074	0.001	-0.058	-0.458	0.466	0.039, 0.142	0.969
<b>Atom type</b>	N4	N5	N10	N7	N9	C2	H10(A, B)	
<b>Charge</b>	-0.459	-0.121	-0.130	-0.109	-0.435	0.479	0.101, 0.118	

CO<sub>2</sub> was represented as a three-site rigid molecule and its intrinsic quadrupole moment was described by a partial-charge model [2.11]. The partial charges on C and O atoms were  $q_C = 0.576e$  and  $q_O = -0.288e$  ( $e = 1.6022 \times 10^{-19}$  is the elementary charge). The C–O bond length was 1.18 Å and the bond angle O–C–O was 180°. The LJ parameters for CO<sub>2</sub> were  $\sigma_C = 2.789$  Å,  $\epsilon_C = 29.66K$ ,  $\sigma_O = 3.011$  Å,  $\epsilon_O = 82.96K$ . The dispersion interactions of the framework atoms in ZTF-1 were modeled by the Universal Force Field (UFF) [2.12]. The Lorentz-Berthelot combining rules were used to calculate the cross LJ interaction parameters. A number of simulation studies have shown that UFF can accurately predict gas adsorption in various MOFs [2.13- 2.16].

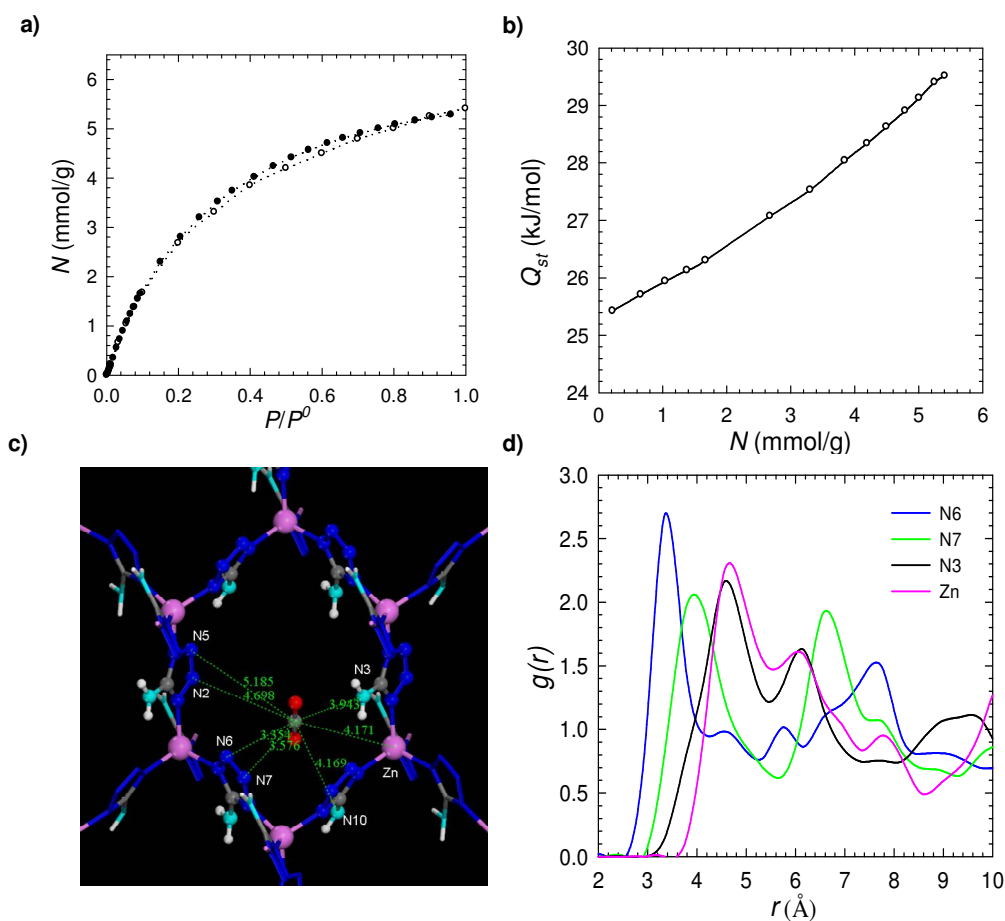
The interactions between CO<sub>2</sub> molecules and framework were represented by electrostatic and Lennard-Jones (LJ) potentials. The atomic charges in ZTF-1 framework were estimated by density functional theory and the LJ potential parameters were adopted from the Universal Force Field (UFF). CO<sub>2</sub> adsorption in ZTF-1 was simulated in Materials Studio



using the Metropolis algorithm. The LJ interactions were evaluated using a spherical cutoff of 12.5 Å and the electrostatic interactions were calculated using the Ewald summation with a precision of  $10^{-5}$  kcal/mol. Two types of trial moves were conducted for CO<sub>2</sub> molecules, namely, translation and rotation. The number of steps in the simulation was  $2 \times 10^6$  for equilibration and  $10^7$  for production.

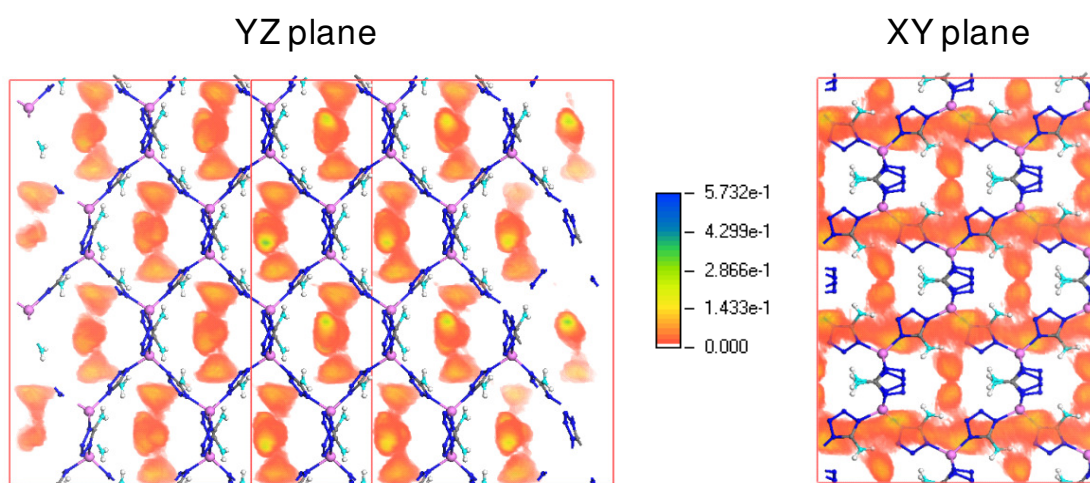
### Simulation Results and Discussion

Figure 2.11a shows the adsorption isotherm of CO<sub>2</sub> in ZTF-1 at 273 K. The simulated isotherm agrees quite well with experiment. The capacity of CO<sub>2</sub> at 100 kPa is about 5.3 mmol/g at 273 K, which is higher than in most MOFs (MOF-2, MOF-177, MOF-505, IRMOF-1, -3, -6 and -11).



**Figure 2.11:** (a) Isotherm and (b) isothermic heat for CO<sub>2</sub> adsorption in ZTF-1 at 273 K. The open symbols are from simulation and the filled symbols are from experiment. (c) Distances between CO<sub>2</sub> molecule and different N atoms and (d) radial distribution functions of CO<sub>2</sub> around N6, N7, N3 and Zn atoms in ZTF-1 at 273 K.

The high CO<sub>2</sub> capacity is attributed to the narrow pores, exposed –NH<sub>2</sub> functionality and free tetrazole nitrogen. As a consequence, there is a substantial overlap of the potential fields for CO<sub>2</sub> in the pores, and a strong interaction between the amino group and CO<sub>2</sub>. Figure 2.11b shows the calculated isosteric heat  $Q_{st}$  for CO<sub>2</sub> adsorption in ZTF-1.  $Q_{st}$  increases with increasing loading, which is similar to CO<sub>2</sub> adsorption in IRMOF-1 [2.15]. At zero coverage,  $Q_{st}$  is approximately 25.4 kJ mol<sup>-1</sup>. With increasing loading,  $Q_{st}$  increases; which is similar to CO<sub>2</sub> adsorption in IRMOF-1. The isosteric heat predicted is consistent with the high capacity observed in the experiment. The increase of  $Q_{st}$  is due to the cooperative attractive interactions between adsorbed CO<sub>2</sub> molecules. However, the magnitude of  $Q_{st}$  in ZTF-1 is much higher than in IRMOF-1. To identify the favorable binding sites for CO<sub>2</sub> in ZTF-1, we have calculated the density distributions of adsorbed CO<sub>2</sub> molecules along the YZ plane at 273 K and 100 kPa. We see that CO<sub>2</sub> molecules are primarily adsorbed in the pores along the X axis and the binding sites are mostly located in the pore centers. To better understand the nature of the binding sites, we have calculated the distances between a single CO<sub>2</sub> molecule and different N atoms in a six member adamantane ring consists of Zn atoms (Figure 2.11c and 2.13). It is observed that CO<sub>2</sub> is closer to the both –NH<sub>2</sub> nitrogen atoms (3.94 Å) and to the uncoordinated tetrazole nitrogen (3.45 Å).



**Figure 2.12:** Density distributions of adsorbed CO<sub>2</sub> molecules on (a) YZ and (b) XY planes in ZTF-1 at 273 K and 100 kPa.

The observed different distances can be further elucidated from the radial distribution functions  $g(r)$  of CO<sub>2</sub>. The  $g(r)$  was calculated by

$$g_{ij}(r) = \frac{\Delta N_{ij} V}{4\pi r^2 \Delta r N_i N_j}$$

where  $r$  is the distance between species  $i$  and  $j$ ,  $\Delta N_{ij}$  is the number of species  $j$  around  $i$  within a shell from  $r$  to  $r + \Delta r$ ,  $V$  is the volume,  $N_i$  and  $N_j$  are the numbers of species  $i$  and  $j$ . As shown in Figure 2.11d, a pronounced peak is centered at  $r = 3.4 \text{ \AA}$  in the  $g(r)$  around N6, and at  $r = 3.9 \text{ \AA}$  in the  $g(r)$  around N7. The peak of  $g(r)$  around N3 and Zn is beyond  $4.0 \text{ \AA}$ . This structural analysis reveals that CO<sub>2</sub> is more preferentially bound onto N6 atom, and then N7 atom.

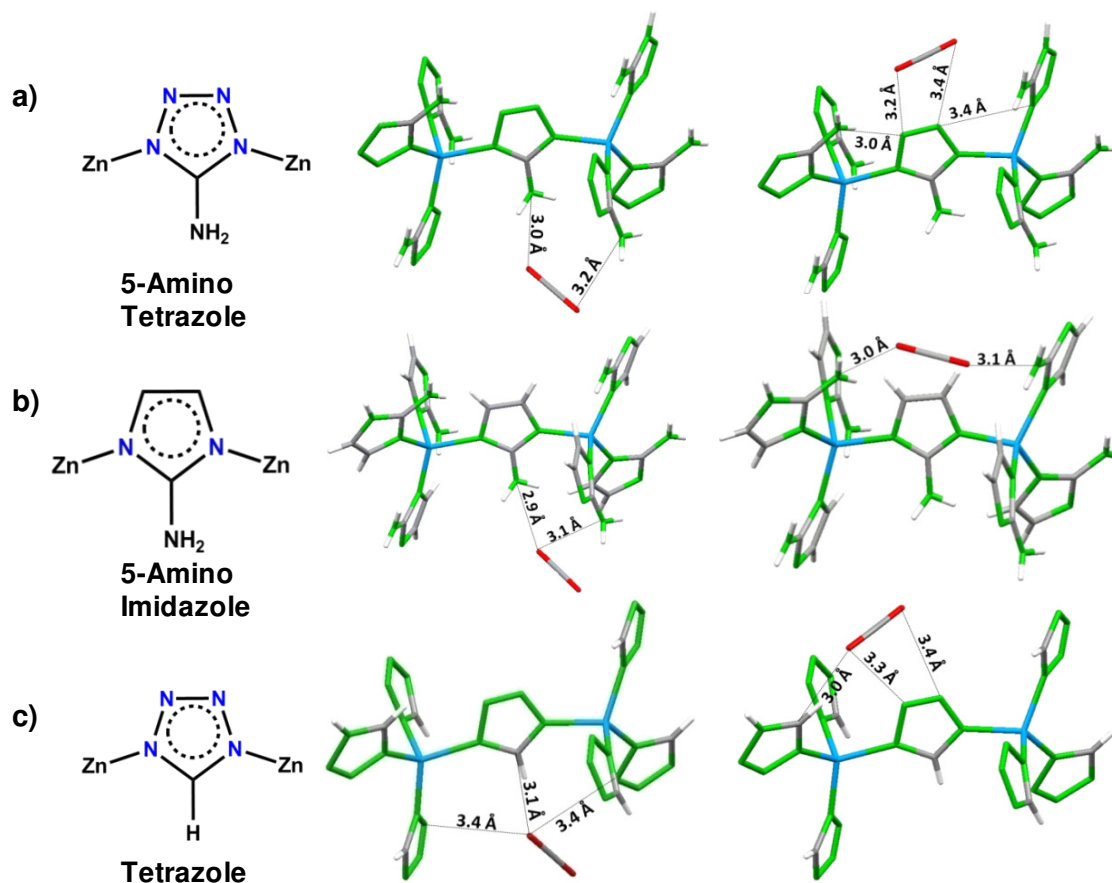


**Figure 2.13:** Calculated distances of carbon dioxide (CO<sub>2</sub>) from (a) ZTF-1 (b) ZTF-1 analogue without free tetrazole nitrogen (c) ZTF-1 analogue without amino functionality.

### 2.2.5.2 *Ab initio* calculations of Zn and Co-ZIF-68, -69 and -81

To elucidate the difference in experimentally measured adsorption isotherms of CO<sub>2</sub> in Zn- and Co-ZIFs, we calculated CO<sub>2</sub> binding energies with Zn- and Co-ZIF-68 clusters from first-principles method. Two representative clusters constructed on the basis of experimental crystallographic data, as shown in Figure 2.14a and b, were used in *ab initio* calculations.

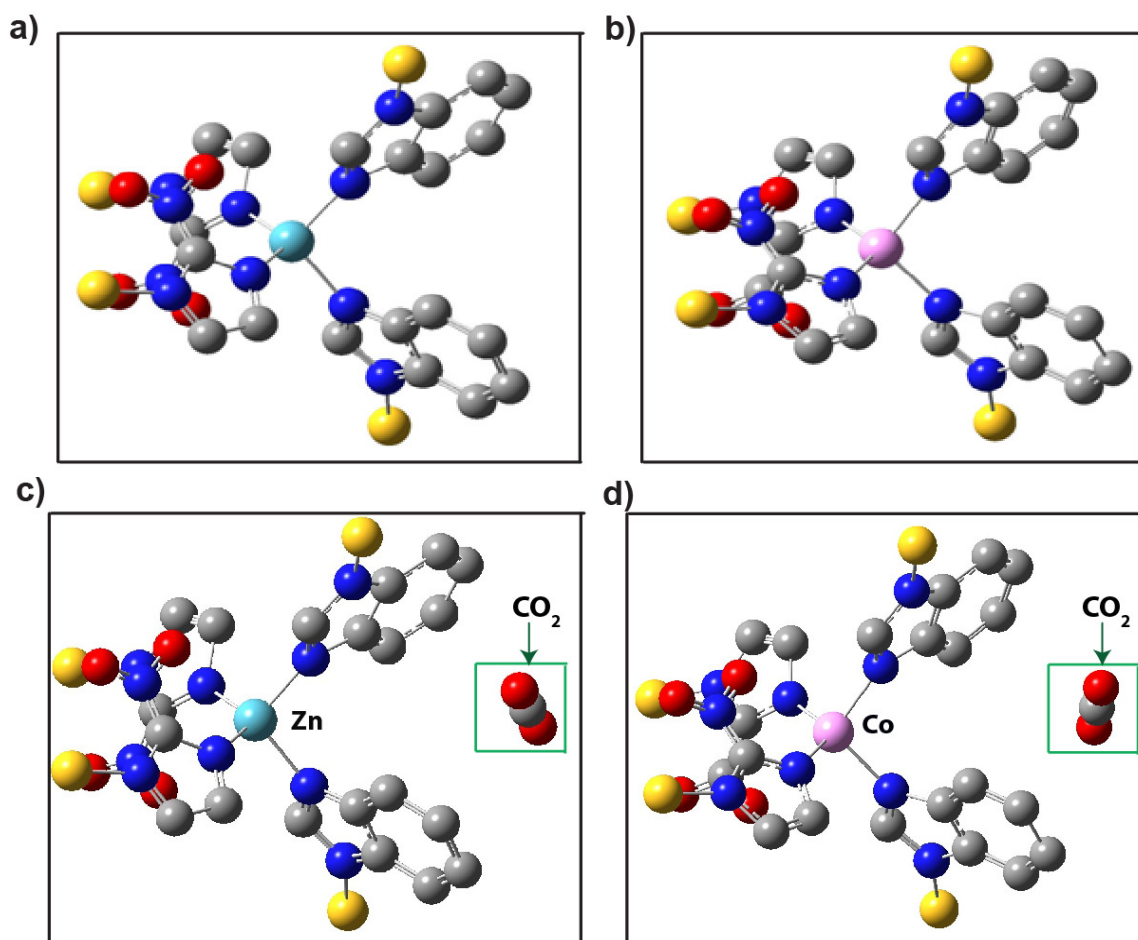


**Figure 2.14:** (a) Zn-ZIF-68 (b) Co-ZIF-68 clusters. The clusters are terminated by Li atoms (yellow); H atoms are omitted for clarity. (c) and (d) optimized CO<sub>2</sub> positions around Zn-ZIF-68 and Co-ZIF-68 clusters respectively.

For each cluster, CO<sub>2</sub> position was optimized using the Becke exchange plus the Lee-Yang-Parr functional and 6-31g(d,p) basis set; interaction energy was evaluated from the 2<sup>nd</sup> Møller-Plesset method and 6-311++g(d,p) basis set. The basis set superposition errors were

corrected by counterpoise method [2.17]. All the *ab initio* calculations were performed using Gaussian 09 [2.18]. Figure 2.14c and d illustrates the optimized CO<sub>2</sub> positions around Zn-ZIF-68 and Co-ZIF-68 clusters. The binding energies were estimated to be -16.37 and -19.89 kJ/mol around Zn- and Co-ZIF-68 clusters, respectively. This validates the above assumption that CO<sub>2</sub> has a stronger interaction with Co-ZIF compared to Zn-ZIF. The difference of binding energy (~ 3 kJ/mol) is for one cluster only and seems to be small. In crystalline structures, which contain large number of such clusters however, the difference would be significantly enhanced and lead to distinctly different adsorption isotherms as experimentally observed.

### 2.3 Conclusion

Synthesis of zeolitic MOFs with free amino decorated pores was always a challenge for researchers as the free amine group tends to coordinate with the metal, resulting into hindering its 3D structure generation. Successful synthesis and crystallization of ZTF-1, the first zeolitic MOF with *both* exposed -NH<sub>2</sub> functionality and free tetrazole nitrogen, could only become possible once we found a possible structure directing agent DMAz. ZTF-1 has high CO<sub>2</sub> capacity. This material is comparable to recently reported bioMOF-11 and outperforms other amine-functionalized MOFs and ZIFs. The CO<sub>2</sub> uptake in ZTF-1 compared to -NH<sub>2</sub> functionalised ZIF-96 is also validated as we found the location of CO<sub>2</sub> is closer to the both -NH<sub>2</sub> nitrogen atoms and to the uncoordinated tetrazole nitrogen. It is hard to quantify the exact contributions of exposed NH<sub>2</sub> functionality or free tetrazole nitrogen for the high CO<sub>2</sub> capacity of ZTF-1 but these results point toward the value of utilizing amino functionalized links and free aromatic nitrogen atoms as a building block for constructing MOFs for high and reversible CO<sub>2</sub> capture. Moreover, in this chapter we have also identified three isorecticular cobalt based hetero-linked ZIFs that share the GME topology. We have shown that, we can not only tune the pore size and the pore environment by changing the link functionality but can also replace the coordinated metal to understand the role of metals on CO<sub>2</sub> binding. The metal replacement, we have showcased in this paper, as these ZIFs do not contain an open metal site.

## 2.4 Experimental Procedures

### 2.4.1 Materials

Thionyl chloride, hydrazine hydrate, diethyl ether, benzene, and *N, N*-dimethylformamide (DMF) were purchased from Rankem chemicals. 5-amino tetrazole,  $\text{Co}(\text{NO}_3)_2 \cdot 6\text{H}_2\text{O}$ , benzimidazole, 5-chloro benzimidazole, 6-bromo benzimidazole and methanol were purchased from Sigma aldrich chemicals. 2-nitroimidazole (2-nIM) was purchased from 3B Scientific corporation. All starting materials were used without further purification. All experimental operations were performed in 5 mL glass vial inside a programmed oven for Co-nIM based zeolitic imidazolate frameworks as well as for ZTF-1 synthesis.

### 2.4.2 Synthesis of *N,N*-Dimethylformamide Azine Dihydrochloride (DMAz)

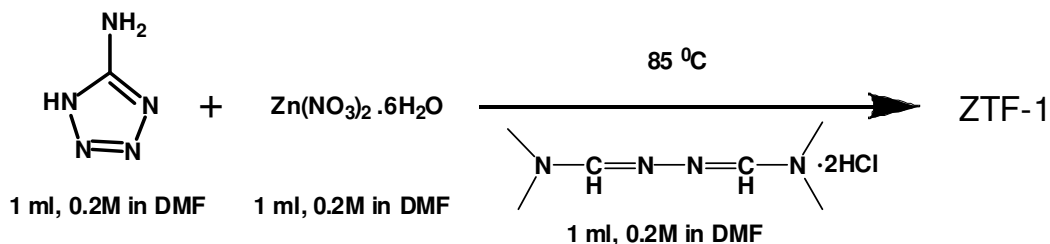
28.6 mL, 0.4 mol of Thionyl chloride ( $\text{SOCl}_2$ ) was added with stirring to DMF (150 mL) at 5 °C. After addition keep this mixture at 5 °C for 24h and then added slowly aqueous hydrazine hydrate (5 mL, 0.1 mol) in 20 mL DMF. After addition the mixture was stirred at room temperature for 48h and the white precipitate of *N, N*-dimethylformamide azine dihydrochloride was collected by filtration and washed with DMF and diethyl ether: 19.1 g; mp 251 °C.

*FTIR*: (KBr 4000-400 $\text{cm}^{-1}$ ): 3473(s), 3223 (w), 2951(w), 2848(w), 2031(m), 1715(s), 1609(m), 1507(s), 1398(w), 1287(s), 1228(m), 1137(s), 1054(s), 1019(m), 877(m), 672(s), 654(m), 530(m), 496(m).

### 2.4.3 Synthesis of ZTF-1

Our initial attempt to synthesize ZTF-1 by means of solvothermal reactions of  $\text{Zn}(\text{NO}_3)_2 \cdot 6\text{H}_2\text{O}$  and 5-aminotetrazole (5-AT,  $\text{CN}_5\text{H}_3$ ) in different molar ratio in aqueous or non aqueous media (*DMF/DEF/NMP*) resulted in the precipitation of un-reacted starting material. Usage of diverse structure directing agents (like tetra-butyl ammonium salts) also resulted into similar outcome [Table 2.5]. However after several attempts we discovered that reaction of  $\text{Zn}(\text{NO}_3)_2 \cdot 6\text{H}_2\text{O}$  (1 mL, 0.2M) with 5-AT (1 mL, 0.2M) in a *N,N'*-dimethylformamide (DMF) solution in the presence of *N,N'*-dimethylformamide-azine-dihydrochloride (DMAz) [1 mL 0.2M] at 100 °C for 72 h afforded a colorless microcrystalline material with a dodecahedron morphology. So far we are unable to understand the role of DMAz during the synthesis and crystallization of ZTF-1, as it is non-

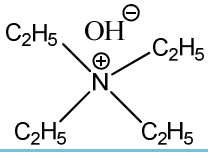
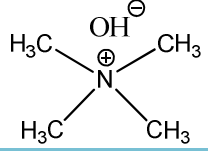
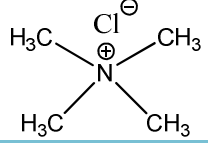
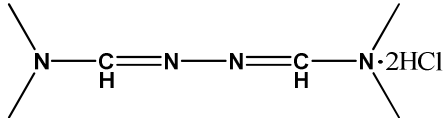
existent in the resulting crystal structure. We anticipate that, it might be acting as a structure directing agent (SDA) as it contains two tetrahedral nitrogens. The as-synthesized compound, was characterized and formulated by X-ray diffraction (XRD) studies as  $[\text{Zn}(\text{CN}_5\text{H}_2)_2] \cdot \text{DMF}$ .



**FTIR: (KBr 4000-400 $\text{cm}^{-1}$ ):** 3341(s), 3196 (m), 2806(w), 1642(s), 1567(s), 1472(m), 1449(m), 1387(w), 1307(m), 1283(m), 1163(m), 1096(s), 1008(m), 843(m), 750(m), 597(w), 489(s).

**Table 2.5:** Types of structure directing agents used for the synthesis of ZTF-1.

SL. No	Type of SDA	No Reaction	Unreacted starting materials	Crystalline ZTF-1
1		√		
2		√		
3		√		
4		√		
5			√	

6		√		
7			√	
8			√	
9				√

**No reaction** = after reaction solution is crystal clear. **Unreacted starting Material** = after reaction starting material is precipitate.

#### 2.4.4 Synthesis procedure of Co-ZIFs

**Synthesis of Co-ZIF-68 [C<sub>10</sub>H<sub>7</sub>CoN<sub>5</sub>O<sub>2</sub>, DMF]:** 1 mL 0.2(M) DMF solution of Co(NO<sub>3</sub>)<sub>2</sub>·6H<sub>2</sub>O was added to 1.5 mL 0.2(M) DMF solution of 2 nitro imidazole and 1 mL 0.2(M) DMF solution of benzimidazole in a 5 mL culture tube and heated 120 °C temperature for 24h. Plate like pink crystals were collected by filtration (75% yield by Co) and washed with DMF and dry acetone then dried in air. **FT-IR:** (KBr 4000-600 cm<sup>-1</sup>): 1670(w), 1660(m), 1461(s), 1354(s), 1273(m), 1237(s), 1171(s), 1110(m), 901 (m), 825(m), 733 (s), 647 (m).

**Elemental analysis (%) of as synthesized Co-ZIF-68. [C<sub>10</sub>H<sub>7</sub>CoN<sub>5</sub>O<sub>2</sub>, DMF]** calcd: C (43.21%), H (3.80%), N (23.26%); Found: C (43.32%), H (3.85%), N (23.02%)

**Elemental analysis (%) of vacuum dried sample of Co-ZIF-68 [C<sub>10</sub>H<sub>7</sub>CoN<sub>5</sub>O<sub>2</sub>]** calcd: C=41.67%, H=2.43 % and N=24.31%; Found: C=41.22%, H=2.45% and N=24.15%

**Synthesis of Co-ZIF-69 [C<sub>10</sub>H<sub>5</sub>Cl<sub>2</sub>CoN<sub>5</sub>O<sub>2</sub>, DMF]:** 1 mL 0.2(M) DMF solution of Co(NO<sub>3</sub>)<sub>2</sub>·6H<sub>2</sub>O was added to 1.0 mL 0.2(M) DMF solution of 2 nitro imidazole and 3 mL 0.2(M) DMF solution of 5-chlorobenzimidazole in a 5 mL culture tube and heated 120 °C temperature for 12h. pink crystals were collected by filtration (77% yield by Co) and



washed with DMF and dry acetone then dried in air. **FT-IR:** (KBr 4000-600  $\text{cm}^{-1}$ ): 1660(s), 1456(s), 1360 (s), 1283(m), 1237(m), 1156(s), 1095(s) , 1059 (m), 953 (m), 795 (s), 718(m), 647(s)  $\text{cm}^{-1}$

**Elemental analysis (%) of as synthesized Co-ZIF-69. [ $\text{C}_{10}\text{H}_5\text{Cl}_2\text{CoN}_5\text{O}_2$ . DMF]** calcd: C (36.28%), H (2.79%), N (19.53%); Found C (35.98%), H (2.67%), N (19.55%).

**Elemental analysis (%) of vacuum dried sample of Co-ZIF-69 [ $\text{C}_{10}\text{H}_5\text{Cl}_2\text{CoN}_5\text{O}_2$ ]** calcd: C (33.62%), H (1.40%), N (19.61%); Found C (33.48%), H (1.50%), N (19.55%).

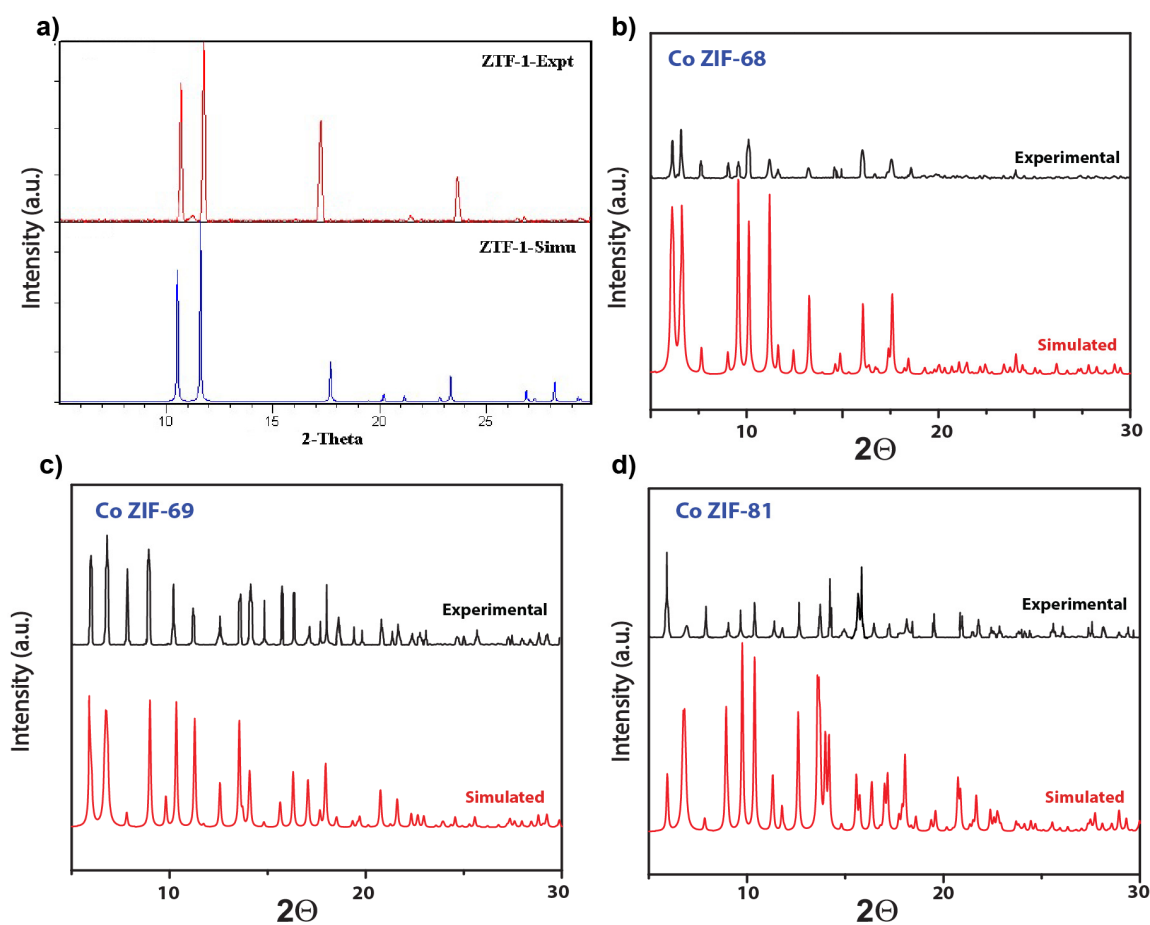


**Figure 2.15:** Comparison of the experimental PXRD pattern of as-synthesized (top) with the simulated from its single crystal structure (bottom) of (a) ZTF-1 (b) Co-ZIF-68 (c) Co-ZIF-69 and (d) Co-ZIF-81.

**Synthesis of Co-ZIF-81 [ $\text{C}_{10}\text{H}_5\text{Br}_2\text{CoN}_5\text{O}_2$ . DMF]:** 1 mL 0.2(M) DMF solution of  $\text{Co}(\text{NO}_3)_2 \cdot 6\text{H}_2\text{O}$  was added to 1.0 mL 0.2(M) DMF solution of 2 nitro imidazole and 2 mL 0.2(M) DMF solution of 5-bromobenzimidazole in a 5 mL culture tube and heated 120  $^\circ\text{C}$

temperature for 12h. pink crystals were collected by filtration (60% yield by Co) and washed with DMF and dry acetone then dried in air. **FT-IR:** (KBr 4000-600  $\text{cm}^{-1}$ ): 1644(w), 1456(s), 1349 (s), 1283(m), 1237(m), 1151(s), 1100(m), 1049 (m), 947 (m), 795 (s), 698(m), 647(s)  $\text{cm}^{-1}$ .

**Elemental analysis (%) of as synthesized Co-ZIF-81. [ $\text{C}_{10}\text{H}_5\text{Br}_2\text{CoN}_5\text{O}_2$ . DMF]** calcd: C (30.06%), H (2.31%), N (16.19%); Found C (30.15%), H (2.28%), N (16.17%).

**Elemental analysis (%) of vacuum dried sample of Co-ZIF-81 [ $\text{C}_{10}\text{H}_5\text{Br}_2\text{CoN}_5\text{O}_2$ ]** calcd: C (26.92%), H (1.12%), N (15.70%); Found C (26.88%), H (1.05%), N (15.61%).

#### 2.4.5 General methods for characterization

**(a) Powder X-Ray Diffraction (PXRD).** The PXRD patterns were collected on a Phillips PANalytical diffractometer on a Cu  $K\alpha$  radiation ( $\lambda = 1.5406 \text{ \AA}$ ), with a scan speed of  $2^\circ \text{ min}^{-1}$ . The tube voltage and amperage were set at 40 kV and 50 mA respectively. Each sample was scanned between  $5$  and  $50^\circ 2\theta$  with a step size of  $0.02^\circ$ . The instrument was previously calibrated using a silicon standard.

**(b) Thermogravimetric Analysis (TGA).** TGA was performed on a SDT Q600 TG-DTA analyzer instrument. Approximately 5 mg of the sample was added to an aluminium crucible and heated from 25 to  $800^\circ\text{C}$  under  $\text{N}_2$  atmosphere at a heating rate of  $10^\circ\text{C min}^{-1}$ .

**(c) Hot-Stage Microscopy.** Leica M-80 optical microscope with hot stage and camera attachment was used for collecting photographs.

**(d) IR Spectroscopy.** The Fourier transform (FT) infrared spectra of the MOFs were taken on a *PERKIN ELMER FT-IR SPECTRUM* (Nicolet) spectrometer. KBr samples (2 mg in 20 mg of KBr) were prepared and 10 scans were collected at  $4 \text{ cm}^{-1}$  resolution for each sample. The spectra were measured over the range of  $4000\text{-}600 \text{ cm}^{-1}$ .

**(f) Gas Adsorption.** All low-pressure gas-sorption experiments (up to 1 atm) were performed on a Quantachrome Autosorb-1 automatic volumetric instrument. Approximately 50 mg of the as-synthesized samples were immersed in dry methanol at ambient temperature for 72 h, evacuated at ambient temperature for 24 h, followed by

elevated temperature (85 °C) for 48 h. Finally the activated samples are treated for gas adsorption (H<sub>2</sub>, N<sub>2</sub> and CO<sub>2</sub>).

#### 2.4.6 X-ray Crystallography

##### General Data Collection and Refinement Procedures:

All single crystal data were collected on a Bruker SMART APEX three circle diffractometer equipped with a CCD area detector and operated at 1500 W power (50 kV, 30 mA) to generate Mo K $\alpha$  radiation ( $\lambda=0.71073$  Å). The incident X-ray beam was focused and monochromated using Bruker Excalibur Gobel mirror optics. All crystals reported in this chapter were mounted on nylon CryoLoops (Hampton Research) with Paraton-N (Hampton Research).

Initial scans of each specimen were performed to obtain preliminary unit cell parameters and to assess the mosaicity (breadth of spots between frames) of the crystal to select the required frame width for data collection. In every case frame widths of 0.5° were judged to be appropriate and full hemispheres of data were collected using the *Bruker SMART* [2.19] software suite. Following data collection, reflections were sampled from all regions of the Ewald sphere to redetermine unit cell parameters for data integration and to check for rotational twinning using *CELL\_NOW* [2.20]. No data collection was evidence for crystal decay encountered. Following exhaustive review of the collected frames the resolution of the dataset was judged. Data were integrated using Bruker *SAINT* [2.21] software with a narrow frame algorithm and a 0.400 fractional lower limit of average intensity. Data were subsequently corrected for absorption by the program *SADABS* [2.22]. The space group determinations and tests for merohedral twinning were carried out using *XPREP* [2.23]. In all cases, the highest possible space group was chosen.

All structures were solved by direct methods and refined using the *SHELXTL 97* [2.23] software suite. Atoms were located from iterative examination of difference F-maps following least squares refinements of the earlier models. Final models were refined anisotropically (if the number of data permitted) until full convergence was achieved. Hydrogen atoms were placed in calculated positions (C-H = 0.93 Å) and included as riding atoms with isotropic displacement parameters 1.2-1.5 times  $U_{eq}$  of the attached C atoms. Data were collected at 100(2) K for all the MOF presented in this paper. This lower

temperature was considered to be optimal for obtaining the best data. Electron density within void spaces has not been assigned to any guest entity but has been modeled as isolated oxygen and/or carbon atoms. The foremost errors in all the models are thought to lie in the assignment of guest electron density. All structures were examined using the *Adsym* subroutine of PLATON [2.24 and 2.25] to assure that no additional symmetry could be applied to the models. All ellipsoids in ORTEP diagrams are displayed at the 50% probability level unless noted otherwise. For all structures we note that elevated R-values are commonly encountered in MOF crystallography for the reasons expressed above by us and by other research groups. [2.26 to 2.35]

**Experimental and refinement details for ZTF-1:** A colorless prismatic crystal ( $0.20 \times 0.16 \times 0.10 \text{ mm}^3$ ) of ZTF-1 was placed in a 0.7 mm diameter nylon CryoLoops (Hampton Research) with Paraton-N (Hampton Research). The loop was mounted on a SMART APEX three circle diffractometer. A total of 7544 reflections were collected of which 3042 were unique and 2879 of these were greater than  $2\sigma(I)$ . The range of  $\theta$  was from 2.43 to 28.09°. All non-hydrogen atoms were refined anisotropically ZTF-1 contains two 5-amino tetrazole molecule in the asymmetric unit. It should be noted that other supporting characterization data (*vide infra* Section S2) are consistent with the crystal structure. Final full matrix least-squares refinement on  $F^2$  converged to  $R_1 = 0.0510$  and  $wR_2 = 0.1283$ (all data) with GoF = 1.051.

**Experimental and refinement details for Co-ZIF-68:**

A pink colored plate like crystal ( $0.31 \times 0.26 \times 0.15 \text{ mm}^3$ ) of **Co-ZIF-68** was placed in 0.7 mm diameter nylon CryoLoops (Hampton Research) with Paraton-N (Hampton Research). The loop was mounted on a Super Nova Dual source X-ray Diffractometer system (Agilent Technologies) equipped with a CCD area detector and operated at 250 W power (50 kV, 0.8 mA) to generate Mo K $\alpha$  radiation ( $\lambda = 0.71073 \text{ \AA}$ ) at 100(2) K in a liquid N<sub>2</sub> cooled stream of nitrogen. A total of 5153 reflections were collected of which 2116 were unique. The range of  $\theta$  was from 3.05 to 29.26. Analysis of the data showed negligible decay during collection. The structure was solved in the Hexagonal  $P6_3/mmc$  space group, with  $Z = 24$ , using direct methods. All non-hydrogen atoms were refined anisotropically with hydrogen atoms generated as spheres riding the coordinates of their parent atoms. We have

repeatedly collected the single crystal XRD data of Co-ZIF-68 at different temperature (100, 120, 150 K). We would like to mention that each time

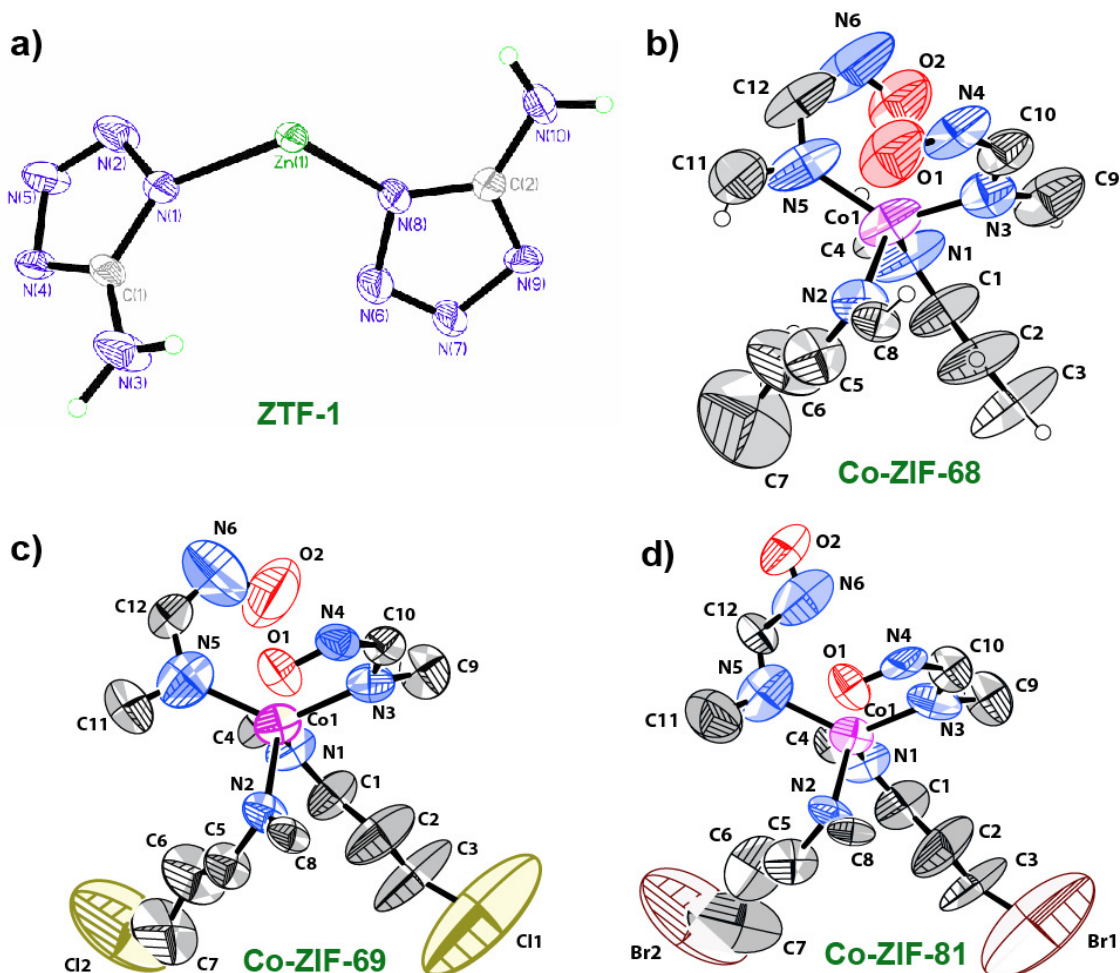


**Figure 2.16:** Asymmetric unit ORTEP diagram (50% probability) of (a) ZTF-1 (b) Co-ZIF-68 (c) Co-ZIF-69 and (d) Co-ZIF-81.

during the refinement of crystal structure we encountered electron densities within the framework cavity. However, assigning these electron densities with isolated O, N and C atoms, leads to highly distorted atoms, although the refinement become stable with decreased R factor and goodness of fit. Hence, we believe that one DMF molecule reside inside the asymmetric unit of Co-ZIF-68, however, these atoms of DMF molecule have very high thermal parameters apart from Co-ZIF frameworks with several IUCr checkcif errors. Hence we have decided to use the SQUEEZE routine to remove these unstable and highly distorted DMF molecules from the pores of Co-ZIF-68. It should be noted that

SQUEEZE structure is very stable with minimal IUCr checkcif problems, less R factor and goodness of fit. In this manuscript we have provided the SQUEEZE applied cif file of Co-ZIF-68. Final full matrix least-squares refinement on  $F^2$  converged to  $R_1 = 0.0992 (F > 2\sigma F)$  and  $wR_2 = 0.2938$  (all data) with GoF = 0.884 (CCDC 952993).

**Refine\_special\_details** We believe anisotropic distortion in the aromatic ring in Co-ZIF-68 structure appears due to static or dynamic disorder. As a result despite lowering the data collection temperature to 100 K this distortion remains persistent. There is disorder by symmetry in the structure of Co-ZIF-68.

#### **Experimental and refinement details for Co-ZIF-69:**

A colorless block like crystal ( $0.33 \times 0.23 \times 0.16 \text{ mm}^3$ ) of **Co-ZIF-69** was placed in 0.7 mm diameter nylon CryoLoops (Hampton Research) with Paraton-N (Hampton Research). The loop was mounted on a Super Nova Dual source X-ray Diffractometer system (Agilent Technologies) equipped with a CCD area detector and operated at 250 W power (50 kV, 0.8 mA) to generate Mo  $K\alpha$  radiation ( $\lambda = 0.71073 \text{ \AA}$ ) at 100(2) K in a liquid  $N_2$  cooled stream of nitrogen. A total of 5174 reflections were collected of which 2364 were unique. The range of  $\theta$  was from 3.16 to 29.17. Analysis of the data showed negligible decay during collection. The structure was solved in the Hexagonal  $P6_3/mmc$  space group, with  $Z = 24$ , using direct methods. All non-hydrogen atoms were refined anisotropically with hydrogen atoms generated as spheres riding the coordinates of their parent atoms. We have repeatedly collected the single crystal XRD data of Co-ZIF-69 at different temperature (100, 120, 150 K). We would like to mention that each time during the refinement of crystal structure we encountered electron densities within the framework cavity. However, assigning these electron densities with isolated O, N and C atoms, leads to highly distorted atoms, although the refinement become stable with decreased R factor and goodness of fit. Hence, we believe that one DMF molecule reside inside the asymmetric unit of Co-ZIF-69, however, these atoms of DMF molecule have very high thermal parameters apart from Co-ZIF-69 frameworks with several IUCr checkcif errors. Hence we have decided to use the SQUEEZE routine to remove these unstable and highly distorted DMF molecules from the pores of Co-ZIF-69. It should be noted that SQUEEZE structure is very stable with minimal IUCr checkcif problems, less R factor and goodness of fit. In this manuscript we have provided the SQUEEZE applied cif file of Co-ZIF-69. Final full matrix least-squares

refinement on  $F^2$  converged to  $R_1 = 0.0997$  ( $F > 2\sigma F$ ) and  $wR_2 = 0.2862$  (all data) with GoF = 0.979 (CCDC 952994).

### **Refine\_special\_details**

We believe anisotropic distortion in the aromatic ring in Co-ZIF-69 structure appears due to static or dynamic disorder. As a result despite lowering the data collection temperature to 100 K this distortion remains persistent. Moreover, there is disorder by symmetry in the crystal structure of Co-ZIF-69.

**NB:** There is only one Cl atom per cobalt metal center in the crystal structure Co-ZIF-69. However, due to crystallographic disorder of chlorine atom Co-ZIF-69 shows two chlorine atoms with  $\frac{1}{2}$  occupancy factor per cobalt center. Hence, the formula used ( $C_{10}H_5Cl_2CoN_5O_2$ ) in the cif and crystallographic tables is the original one, generated from crystallographically.

### **Experimental and refinement details for Co-ZIF-81:**

A colorless block like crystal ( $0.31 \times 0.26 \times 0.17 \text{ mm}^3$ ) of **Co-ZIF-81** was placed in 0.7 mm diameter nylon CryoLoops (Hampton Research) with Paraton-N (Hampton Research). The loop was mounted on a Super Nova Dual source X-ray Diffractometer system (Agilent Technologies) equipped with a CCD area detector and operated at 250 W power (50 kV, 0.8 mA) to generate Mo  $K\alpha$  radiation ( $\lambda = 0.71073 \text{ \AA}$ ) at 100(2) K in a liquid  $N_2$  cooled stream of nitrogen. A total of 4947 reflections were collected of which 1471 were unique. The range of  $\theta$  was from 3.13 to 29.14. Analysis of the data showed negligible decay during collection. The structure was solved in the Hexagonal  $P6_3/mmc$  space group, with  $Z = 24$ , using direct methods. All non-hydrogen atoms were refined anisotropically with hydrogen atoms generated as spheres riding the coordinates of their parent atoms. We have repeatedly collected the single crystal XRD data of Co-ZIF-81 at different temperature (100, 120, 150 K). We would like to mention that each time during the refinement of crystal structure we encountered electron densities within the framework cavity. However, assigning these electron densities with isolated O, N and C atoms, leads to highly distorted atoms, although the refinement become stable with decreased R factor and goodness of fit. Hence, we believe that one DMF molecule reside inside the asymmetric unit of Co-ZIF-81, however, these atoms of DMF molecule have very high thermal parameters apart from Co-

ZIF-81 frameworks with several IUCr checkcif errors. Hence we have decided to use the SQUEEZE routine to remove these unstable and highly distorted DMF molecules from the pores of Co-ZIF-81. It should be noted that SQUEEZE structure is very stable with minimal IUCr checkcif problems, less R factor and goodness of fit. In this manuscript we have provided the SQUEEZE applied cif file of Co-ZIF-81. Final full matrix least-squares refinement on  $F^2$  converged to  $R_1 = 0.0995$  ( $F > 2\sigma F$ ) and  $wR_2 = 0.2545$  (all data) with GoF = 0.702 (CCDC 952995).

### **Refine\_special\_details**

We believe anisotropic distortion in the aromatic ring in Co-ZIF-81 structure appears due to static or dynamic disorder. As a result despite lowering the data collection temperature to 100 K this distortion remains persistent. Moreover, there is disorder by symmetry in the crystal structure of Co-ZIF-81.

**NB:** There is only one Br atom per cobalt metal center in the crystal structure Co-ZIF-81. However, due to crystallographic disorder of bromine atom Co-ZIF-81 shows two bromine atoms with  $\frac{1}{2}$  occupancy factor per cobalt center. Hence, the formula used ( $C_{10}H_5Br_2CoN_5O_2$ ) in the cif and crystallographic tables is the original one, generated from crystallographic data.

**NOTE:** The results of this chapter have already been published in *Chem. Commun.*, 2011, **47**, 2011-2013 and *CrystEngComm*, 2014, **16**, 4677-4680. with the title: “Amino functionalized zeolitic tetrazolate framework (ZTF) with high capacity for storage of carbon dioxide” and “Enhancement of CO<sub>2</sub> Uptake in Iso-reticular Co based Zeolitic Imidazolate Frameworks via Metal Replacement” respectively. These publications were the results of the collaboration between the group of Dr. Rahul Banerjee and his students Tamas Panda and Pradip Pachfule from CSIR National Chemical Laboratory, Pune, India and the group of Dr. Jianwen Jiang and his students Yifei Chen and Krishna M. Gupta from CSIR National University of Singapore, Singapore. Apart from computational study major works contributed by Tamas Panda.



## CHAPTER 3

---

### ENHANCEMENT OF POROSITY IN TRIAZOLE FUNCTIONALIZED ISOMERIC MOFs BY INDUCING SIZE DEPENDENT TEMPLATE.

---

#### 3.1 Introduction:

Over the last decade, considerable efforts have been made to improve the CO<sub>2</sub> storage capacity in MOFs [3.1]. Functionalization of organic linkers is one route that is currently being explored by several groups [3.2]. Previous studies have revealed that, the presence of functional groups may reduce the pore size of MOFs. However, selecting proper functional group might lead to an improved CO<sub>2</sub> adsorption capability in the low pressure range (0-1 bar) [3.3]. We also found that, functional groups, like -NH<sub>2</sub>, -NO<sub>2</sub> and uncoordinated nitrogen, have significant role for enhancing the CO<sub>2</sub> storage capacities of MOF architectures as reported in Chapter 2. In fact, the interactions of CO<sub>2</sub> with -NH<sub>2</sub> functionalities in MOFs have been proved crystallographically [3.4]. In this regard, we attempted to synthesize a -NH<sub>2</sub> functionalized MOF by using 5-amino isophthalic acid as an organic linker, but our approach appeared unsuccessful. After several efforts, we could not able to get any expected product or crystal structures out of it. We speculate that, instead of -NH<sub>2</sub> functionality, incorporation of any nitrogen rich functional groups (viz, triazole, tetrazole etc) in the same organic linker might have profound effect on CO<sub>2</sub> storage capacity of the resulted MOF. Considering the fact, we replaced 5-amino isophthalic acid by 5-triazole isophthalic acid (5TIA) [3.5] to acquire the advantage of nitrogen rich functionality (triazole group) in MOF networks for high CO<sub>2</sub> storage. In order to achieve that, we attempted to synthesize 5TIA based MOF architectures with different transition metal salts. First successful synthesis of 5TIA and Mn(NO<sub>3</sub>)<sub>2</sub>.xH<sub>2</sub>O in presence of N,N' dimethyl formamide (DMF) solvent resulted a non porous structure Mn-5TIA-1 [Figure 3.1]. Since, this structure has negligible porosity as well as poor surface area we decided to synthesize the porous isomeric analogues of Mn-5TIA-1. We anticipated that, these porous isomers with triazole functionality might act as high CO<sub>2</sub> adsorbing material. However, several structural features such as surface area, pore size, shape and pore

functionalization have been found to play important role to design MOFs for high CO<sub>2</sub> adsorption. Thus, synthetic strategies that allow the control of the pore size and pore geometry are particularly important [3.6]. Although, porous MOFs can be synthesized using multi-dentate ligand, however, the final structural topology is highly influenced by several factors including metal–ligand ratio, pH, solvent of crystallization, temperature and often on oxidation state of the metal [3.7]. As a result, predicting the final MOF topology by using flexible ligands is even more difficult due to the possibility of existence of several structural isomers [3.8]. Therefore the design and synthesis of a particular structural isomer is still a challenging aspect of crystal engineering, [3.9] as these are governed by diverse perturbation factors, such as the conformational flexibility of ligands, influence of guest/solvent molecules and reaction conditions. Among these factors, the effect of solvent and conformational flexibility has been demonstrated by several researchers, in which different MOFs could be selectively synthesized from the same components using different solvents [3.10].

In this chapter, we have strategically synthesized three new isomeric Mn-MOFs, starting from organic linker 5-triazole isophthalic acid (5-TIA), Mn(NO<sub>3</sub>)<sub>2</sub>.xH<sub>2</sub>O and N, N' dimethyl formamide (DMF) as a solvent. First one is non porous Mn-5TIA-1(C<sub>26</sub>H<sub>24</sub>Mn<sub>2</sub>N<sub>8</sub>O<sub>10</sub>) synthesized without any template. Rest two are, Mn-5TIA-2 (C<sub>43.7</sub>H<sub>10</sub>Mn<sub>2</sub>N<sub>6</sub>O<sub>8</sub>) and Mn-5TIA-3 (C<sub>10</sub>H<sub>5</sub>MnN<sub>3</sub>O<sub>4</sub>) where porosity is systematically induced by the use of different size template [Figure 3.1]. It is interesting to note that, structural conversions from non-porous to porous MOFs due to the template effect have been observed. We have used pyrazine and 4,4'-bipyridine as a template to synthesise Mn-5TIA-2 and -3 [Figure 3.1]. The cross sectional pore apertures of the resulting Mn-MOFs are comparable to the molecular dimensions of the template (pyrazine and 4,4'-bipyridine). The periodic increased porosity in Mn-MOFs depending on the size of the template used has been further confirmed by the CO<sub>2</sub> adsorption isotherms. To the best of our knowledge this is the first report, where the porosity and CO<sub>2</sub> uptake capacity of the structural isomers is enhanced periodically due to size dependent template effect.

### 3.2 Result and Discussion:

#### 3.2.1 Structural analysis of Mn-MOFs

In the crystal structure of Mn-5TIA-1 (space group  $P2_1/c$ ) only one type of SBU [3.11] is present with two Mn(II) metal centres (Mn1 and Mn2) [Figure 3.3a]. Among these two Mn(II) metal centers, Mn1 adopts an octahedral geometry, while Mn2 is in trigonal bipyramidal coordination state. It is noteworthy that, octahedral Mn1 is coordinated to four oxygens from  $\mu_2$ -CO<sub>2</sub><sup>-</sup> functionalities of 5TIA and two DMF oxygen atoms, while trigonal bipyramidal Mn2 is coordinated to two  $\mu_2$ -CO<sub>2</sub><sup>-</sup>, one  $\mu_1$ -CO<sub>2</sub><sup>-</sup> oxygen atoms and one  $\mu_1$ -N atom (from triazolate functionality) of 5TIA ligand. In the structure of Mn-5TIA-1, octahedral Mn1 bridges to the next trigonal bipyramidal Mn2 through the  $\mu_2$ -CO<sub>2</sub><sup>-</sup> carboxyl functionalities and  $\mu_1$ -triazole group of the 5-TIA [Figure 3.3a].

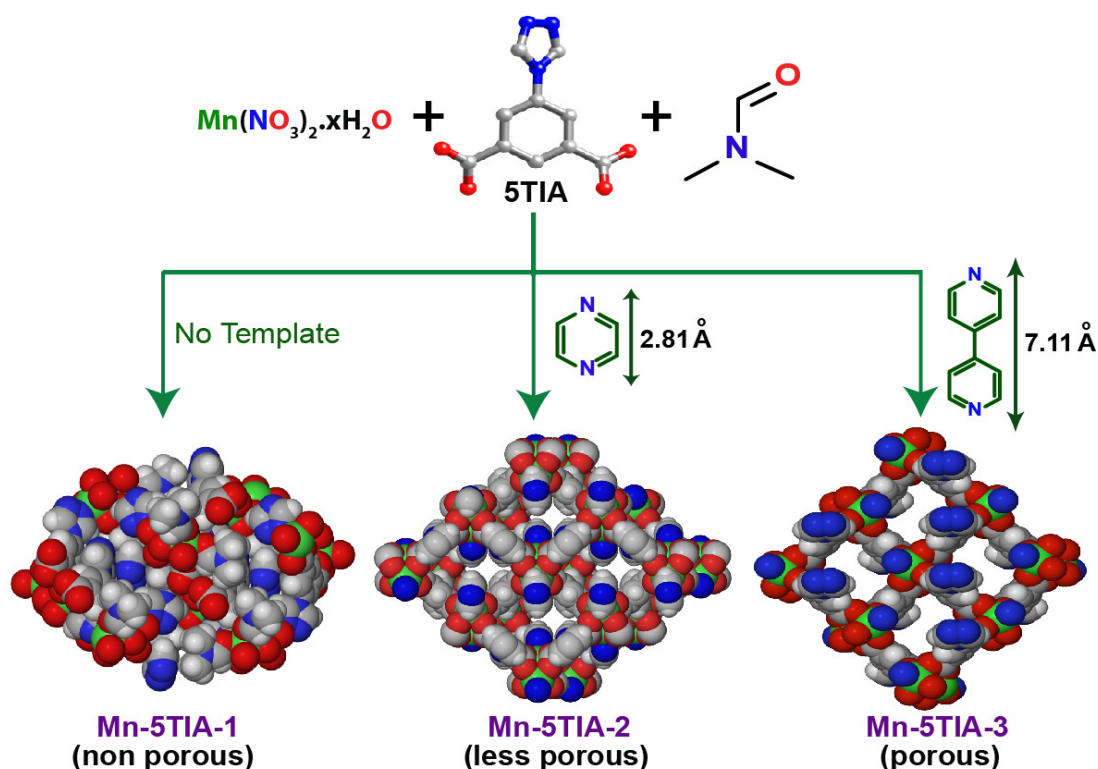


**Figure 3.1:** Synthesis of three isomeric Mn-MOFs starting from 5TIA, Mn(II) salt and DMF, shows enhancement of porosity depending on the size of templates used during synthesis. Color code: Mn (green), N (blue), O (red), C (black), H (white).

These two Mn(II) centers extend in three dimensions through the coordination of  $\mu_2$ -CO<sub>2</sub><sup>-</sup>,  $\mu_1$ -CO<sub>2</sub><sup>-</sup> oxygens and  $\mu_1$ -triazole nitrogen functionality of 5-TIA ligand [Figure 3.3a]. Mn-

5TIA-2 on the other hand, crystallizes in *Pbcn* space group. Both Mn(II) centers in the dimanganese paddlewheel SBU have almost the same coordination environments with a nearly ideal octahedral sphere ( $\tau \approx 0$ ) [3.12] enclosed by six 5-TIA ligands. Four such 5TIA ligands are coordinated to this paddlewheel unit via one of their carboxylate groups and rest of the two are coordinated via the triazolyl nitrogen functionality [Figure 3.3b]. Each paddlewheel SBU extends further in three dimensions through two bridging  $\mu_2$ -CO<sub>2</sub><sup>-</sup> carboxyl groups and one nitrogen from  $\mu_1$ -triazolyl group of each 5-TIA ligand. The structure extends extensively through *b* axis via coordination of  $\mu_2$ -CO<sub>2</sub><sup>-</sup> carboxyl group. Whereas through *a* and *c* axis, it extends through the coordination of  $\mu_2$ -CO<sub>2</sub><sup>-</sup> carboxyl group as well as  $\mu_1$ -triazolyl nitrogen functionality of 5-TIA ligand [Figure 3.3b]. In Mn-5TIA-2 the coordination of  $\mu_1$ -triazolyl nitrogen functionality to the Mn(II) metal is convergent on both sides of the dimanganese paddlewheel SBU [Figure 3.2].

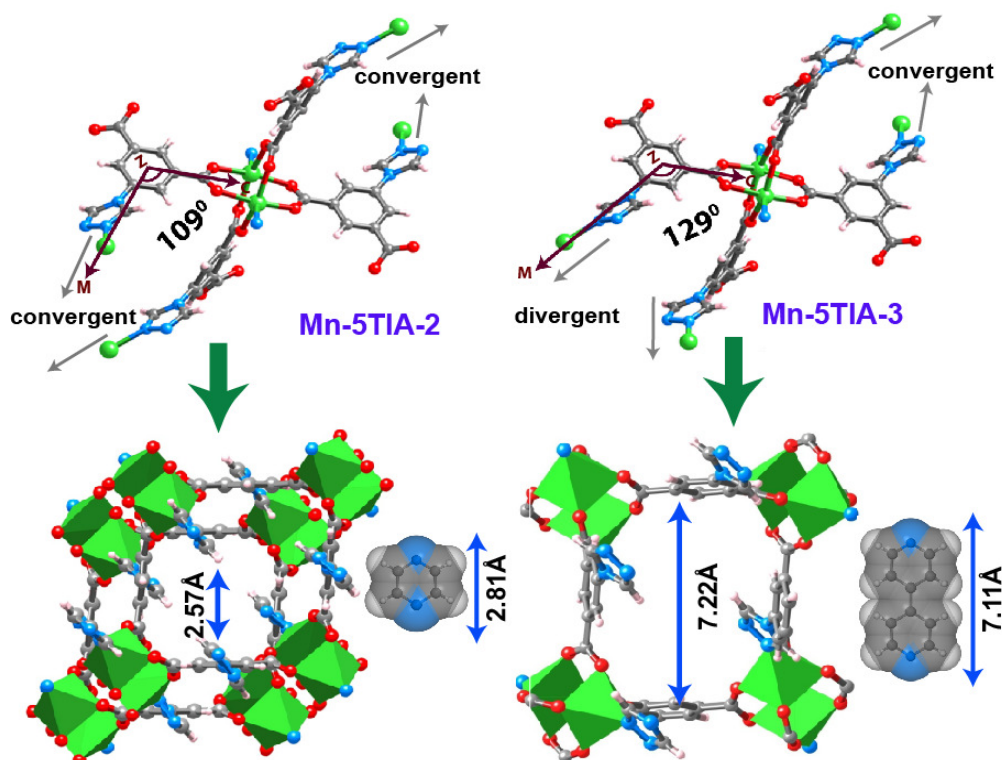


**Figure 3.2:** (a) Structural differences between Mn-5TIA-2 and -3. In Mn-5TIA-2 the N2 nitrogen of triazole ring is connected with Mn(II) but in Mn-5TIA-3 the N3 nitrogen of triazole ring is connected with Mn(II) resulting into the increase in MZC angle (Mn–centroid of benzene ring in 5-TIA–carboxylate carbon of 5-TIA) for Mn-5TIA-3 (129°) than Mn-5TIA-2 (109°). Color code: Mn (green), N (blue), O (red), C (black), H (light pink).

In the crystal structure of Mn-5TIA-3 (space group  $P2_1/c$ ) exactly similar dimanganese paddlewheel SBU like Mn-5TIA-2 [with octahedral Mn(II) metal centers] has been observed. Like Mn-5TIA-2, the structure of Mn-5TIA-3 extends in three dimensions through the two bridging  $\mu_2$ -CO<sub>2</sub><sup>-</sup> carboxyl group and  $\mu_1$ -triazolyl nitrogen from each 5-TIA ligand [Figure 3.3c]. However, unlike Mn-5TIA-2, the coordination of  $\mu_1$ -triazolyl nitrogen functionalities to the Mn (II) metal is convergent on one side and divergent on the other side of the dimanganese paddlewheel SBU [Figure 3.2]. In case of Mn-5TIA-3, twist of the triazole ring from the plane of benzene ring of 5-TIA ligand (42.5°) is lower compared to the Mn-5TIA-2 (50.9°).

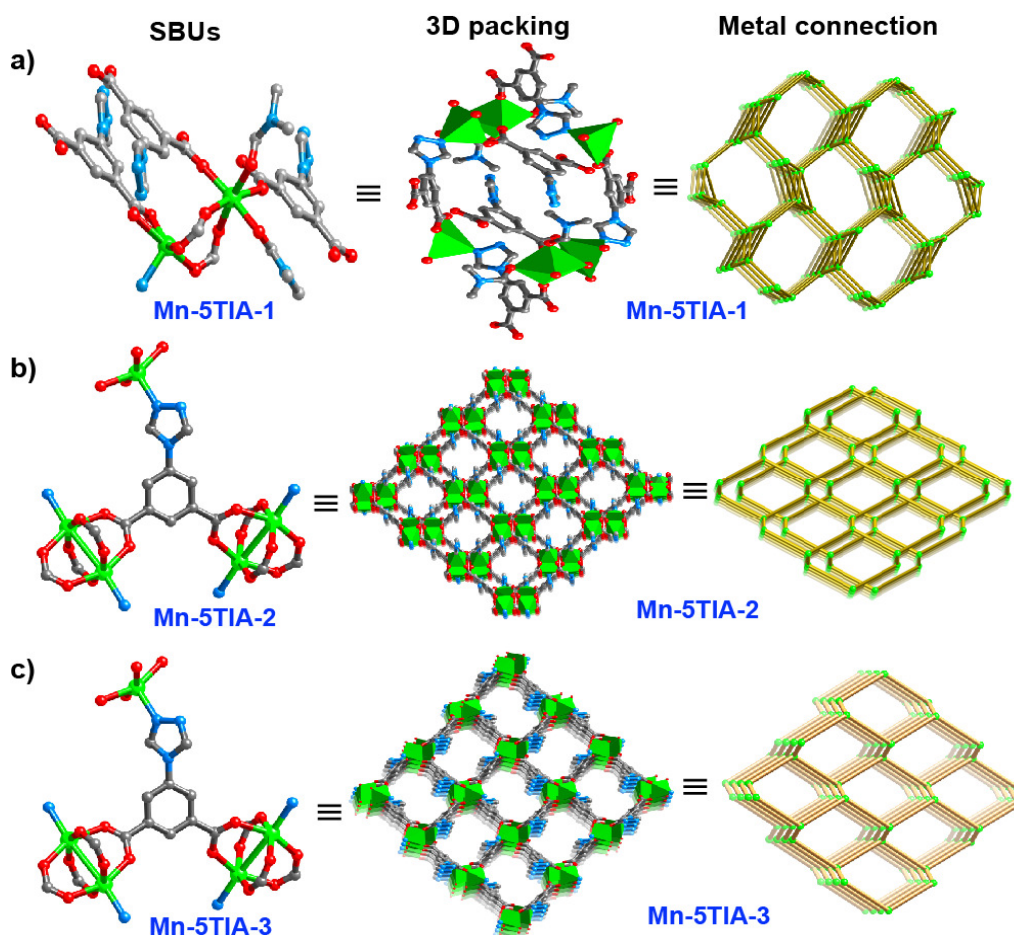


**Figure 3.3:** Coordination of 5TIA with metal SBU (left), ball and stick three dimensional packing (middle) and metal connections (right) of (a) Mn-5TIA-1 (b) Mn-5TIA-2 and (c) Mn-5TIA-3. Solvent molecules are omitted for clarity. Color code: Mn (green), N (blue), O (red), C (black), H (light pink).

Structural analysis of Mn-5TIA-1 indicates, that it is non porous in nature. Exactly similar reaction conditions yielded Mn-5TIA-2, when we used pyrazine as a co-ligand. It is noteworthy that pyrazine molecules are not coordinated to the Mn(II) metal and neither trapped as guest inside the pores of Mn-5TIA-2. However, solvent accessible voids in Mn-5TIA-2 are higher (51.6%) compared to the solvent accessible voids of Mn-5TIA-1 (0%). Analysis of the pore aperture of Mn-5TIA-2 indicates that, it has 2.56 Å pore aperture which is comparable to the length of the pyrazine molecule (2.81 Å from one nitrogen to another nitrogen of pyrazine) as shown in figure 3.2. We thought that, increase in pore aperture, which has similar dimensionality like pyrazine molecule, could be an indication of pyrazine molecules acting as template for creating higher porosity in Mn-5TIA-2. To prove this hypothesis, we replaced pyrazine with 4,4'-bipyridine and attempted similar synthetic procedure which yielded Mn-5TIA-3. Mn-5TIA-3 has higher solvent accessible void (52.5%) than Mn-5TIA-2 (51.6%). Close analysis of the crystal structure indicates the increase in the pore aperture from 2.57 Å (in Mn-5TIA-2) to 7.26 Å (in Mn-5TIA-3). It is noteworthy that the pore aperture of Mn-5TIA-3 is comparable to the molecular dimension of the 4,4'-bipyridine molecule (7.21 Å from one nitrogen to another nitrogen of 4,4'-bipyridine). Like Mn-5TIA-2, 4,4'-bipyridine molecules are not coordinated to the metal and neither trapped as guest inside the pores of Mn-5TIA-3. The formation of Mn-5TIA-2 and -3 and subsequent systematic increase of their porosity and pore aperture indicate the template effect of pyrazine and 4,4'-bipyridine during the MOF formation.

### 3.2.2 Thermal properties and X-ray powder diffraction analysis

Thermal gravimetric analysis (TGA) performed on as-synthesized Mn-5TIA-1, -2 and -3 revealed that, these compounds have high thermal stability [Figure 3.4d]. The TGA trace for as synthesized Mn-5TIA-1, -2 and -3 showed a gradual weight-loss step of 2.13% (20–200 °C), 5.28% (20–200 °C) and 7.55% (20–200 °C) respectively, corresponding to escape of guest DMF solvent molecules from the pores [Figure 3.4d]. This is followed by a sharp weight loss (290–450 °C) probably due to the decomposition of the framework. In order to confirm the phase purity of the bulk materials, powder X-ray diffraction (PXRD) experiments were carried out on all complexes. All major peaks of experimental PXRDs of Mn-5TIA-1, -2 and -3 matches well with simulated PXRDs, indicating their reasonable crystalline phase purity [Figure 3.4a, b and c]

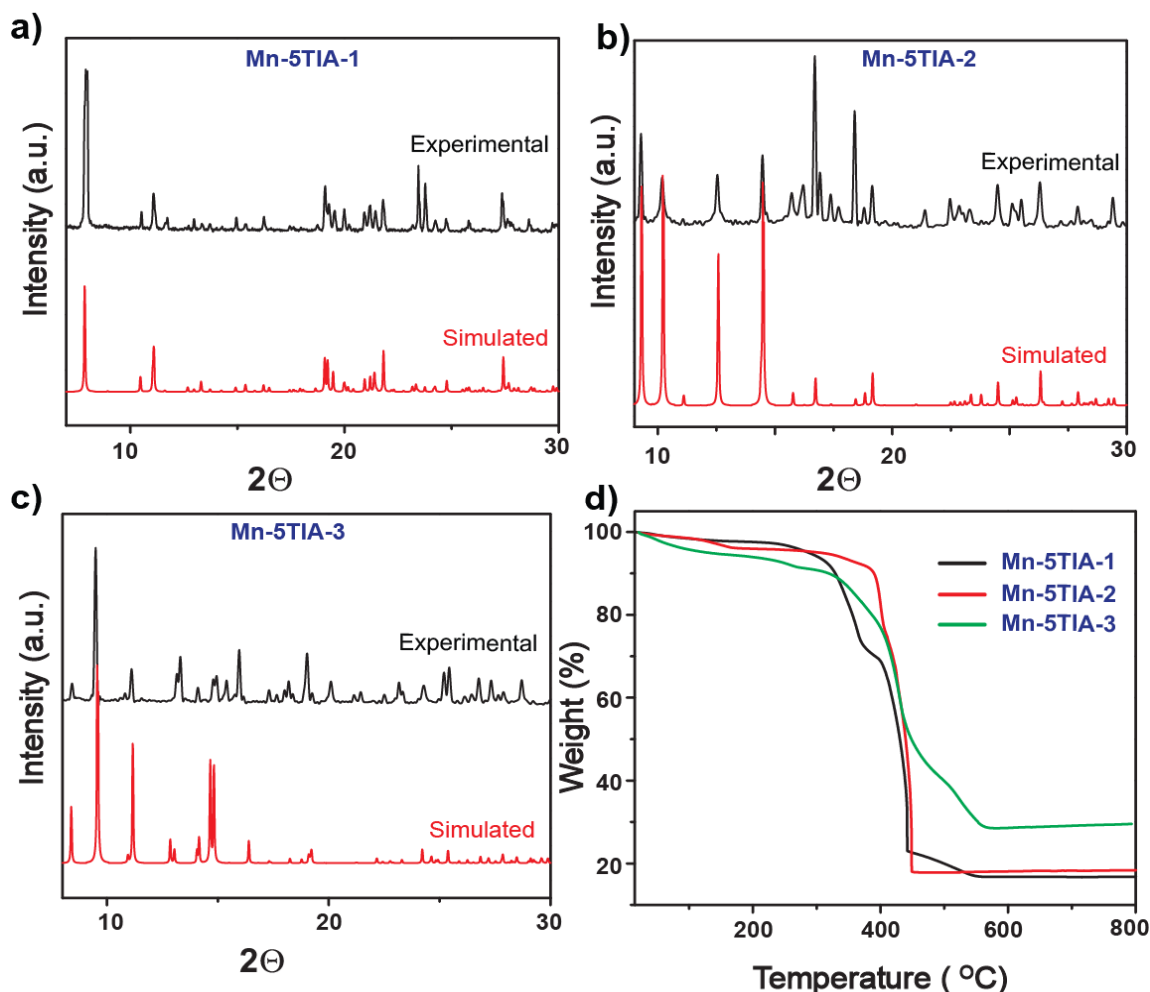


**Figure 3.4:** Comparison of the simulated (bottom) and experimental (top) PXRD patterns of (a) Mn-5TIA-1 (b) Mn-5TIA-2 and (c) Mn-5TIA-3. The framework structures of all Mn-MOFs were matches well with simulated PXRD. (d) Thermo gravimetric analysis (TGA) of Mn-5TIA-1, -2, and -3.

### 3.2.3 Gas adsorption Properties of Mn-MOFs

Template (pyrazine and 4,4'-bipyridine) induced enhancement of porosity has been observed in the Mn-MOFs reported in this chapter. From the structural analysis using PLATON [3.13] it was clear that Mn-5TIA-2 and -3 are having 51.6% and 52.5% solvent accessible void with 2.57 Å and 7.22 Å pore aperture respectively. High solvent accessible void and pore sizes comparable to the kinetic diameter of N<sub>2</sub> (3.65 Å) and CO<sub>2</sub> (3.40 Å) prompted us to analyze the N<sub>2</sub> and CO<sub>2</sub> adsorption properties of these two MOFs. Prior to gas sorption experiments, guest DMF solvent molecules are removed by solvent exchange



(1:1 mixture of DCM: MeOH) followed by thermal activation at an optimized temperature of 110 °C, for 48 h. We could not get the N<sub>2</sub> adsorption in Mn-5TIA-2 and Mn-5TIA-3, as the kinetic diameter of N<sub>2</sub> (3.6 Å) is higher than the cross sectional pore aperture of all these Mn-MOFs (Mn-5TIA-2, 2.57 × 2.57 Å and Mn-5TIA-3, 2.8 × 7.22 Å). But the CO<sub>2</sub> adsorption isotherms for these MOFs analyzed at 298 K are completely reversible. A possible reason for the selective CO<sub>2</sub> adsorption over N<sub>2</sub> could be due to the quadrupole interactions of N<sub>2</sub> with the electrostatic field gradients near the pore surface, which subsequently block other molecules to enter the pores. Whereas at 298 K such type of quadrupole interactions are overcome by the thermal energy in case of CO<sub>2</sub> adsorption. The CO<sub>2</sub> adsorption isotherm in Mn-5TIA-1 shows 2 cc/g CO<sub>2</sub> adsorption, as it is non-porous in nature. Mn-5TIA-2 shows 9.85 cc/g CO<sub>2</sub> adsorption at the same conditions [Figure 3.5a]. Whereas, CO<sub>2</sub> adsorption of Mn-5TIA-3 increases to 37.45 cc/g as pressure reaches to 1 bar [Figure 3.5a]. The reason for higher CO<sub>2</sub> adsorption in Mn-5TIA-3 (compare to Mn-5TIA-1 and -2) is the high solvent accessible void (52.5%) along with larger pore aperture (7.216 Å).

We also collected the H<sub>2</sub> adsorption data on the activated samples of Mn-5TIA-1, -2 and -3 at 77 K and 1 bar pressure [Figure 3.5b]. As expected, Mn-5TIA-1 is non-porous to H<sub>2</sub> like other gas molecules. But Mn-5TIA-2 having comparable pore radius with kinetic diameter of H<sub>2</sub> molecule (2.89 Å) shows 23.44 cc/g of H<sub>2</sub> uptake. Also Mn-5TIA-3 having larger pores in Mn-MOFs series shows 49.57 cc/g H<sub>2</sub> uptake at 77 K as pressure approaches to 1 bar [Figure 3.5b]. These H<sub>2</sub> uptakes are well justified with the increasing pore size from Mn-5TIA-1 to Mn-5TIA-3. Since, CO<sub>2</sub>/CH<sub>4</sub> separation is very important to industrial process, we have examined the CH<sub>4</sub> adsorption behavior for Mn-5TIA-2 and -3 at 298 K and 1 bar pressure [Figure 3.5c]. At aforementioned conditions, activation samples of Mn-5TIA-2 and Mn-5TIA-3 could adsorb 1.05 cc/g and 1.87 cc/g of CH<sub>4</sub> as pressure approaches to 1 bar. This uptake is completely reversible but as compared to CO<sub>2</sub> uptake it is very less [Figure 3.5c].

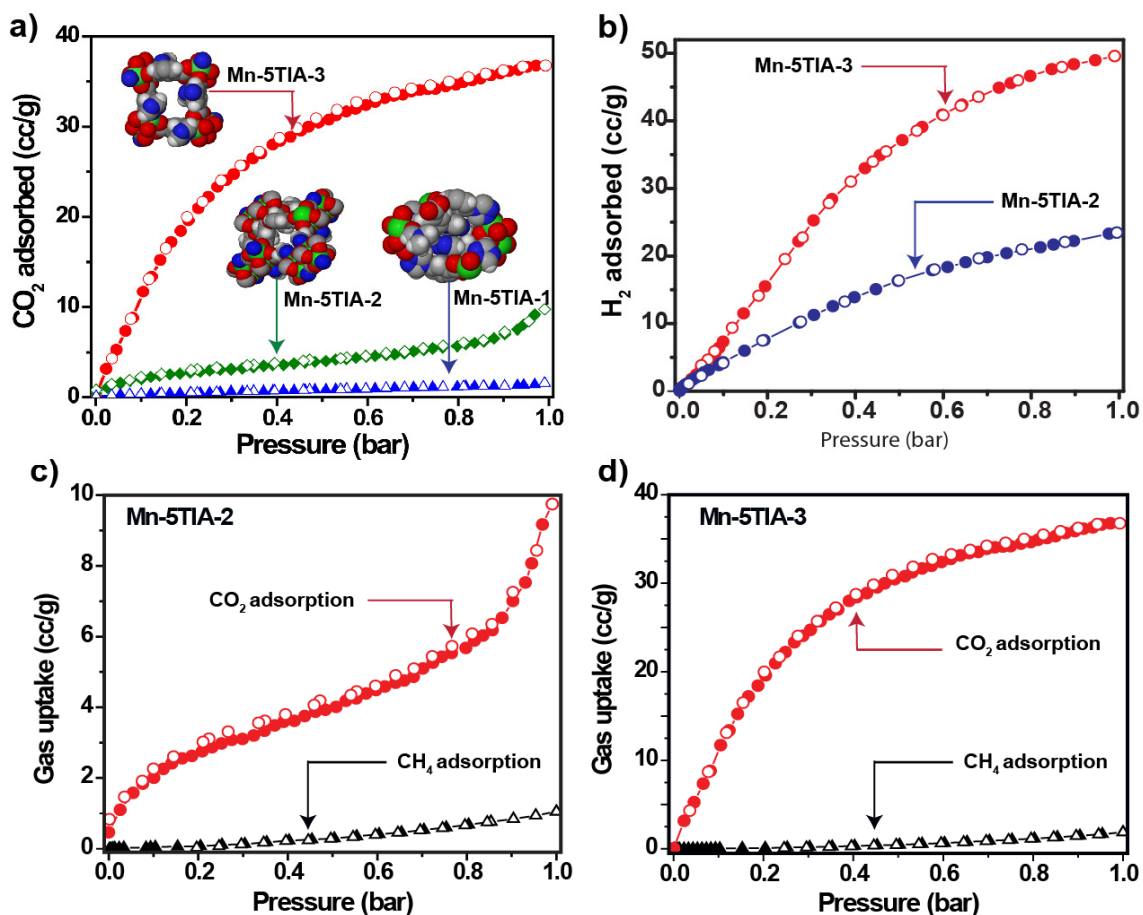


**Figure 3.5:** Gas adsorption isotherms of Mn-5TIA-1, -2 and -3, (a) CO<sub>2</sub> adsorption isotherms for all Mn-MOFs, showing increase in CO<sub>2</sub> uptake from Mn-5TIA-1 to Mn-5TIA-3. (b) H<sub>2</sub> adsorption isotherms of Mn-MOFs at 77 K. (c) and (d) Comparison of CO<sub>2</sub> and CH<sub>4</sub> gas-sorption isotherms for Mn-5TIA-2 and -3 measured at 298 K respectively. Open and filled symbol represents adsorption and desorption, respectively.

### 3.3 Conclusion:

In conclusion, we have synthesized three new Mn-MOFs using predesigned 5TIA ligand with transition metal Mn(II). First time we discovered that in structural isomers porosity can be controlled by controlling the size of template. Mn-TIA-1 is nonporous as no template has been used during its synthesis. Mn-5TIA-2 has 2.56 Å pore aperture which is comparable to the length of the pyrazine molecule. Similarly, the pore aperture of Mn-5TIA-3 is comparable to the molecular dimension of the 4,4'-bipyridine molecule. This increment in porosity in these Mn-MOFs depending on the size of the template used has been further validated by the CO<sub>2</sub> adsorption isotherms. Non porous Mn-5TIA-1 showed 2

cc/g CO<sub>2</sub> uptake, whereas Mn-5TIA-2 and porous Mn-5TIA-3 is showing 9.85 cc/g and 37.45 cc/g CO<sub>2</sub> adsorption, respectively. Although, the CO<sub>2</sub> uptake property is not promising here but we believe this strategy of enhancement of porosity by using template will open up a new avenues in the research of MOF for gas adsorption.

### 3.4 Experimental Procedures:

#### 3.4.1 Materials

Thionyl chloride, hydrazine hydrate, diethyl ether, benzene, and *N, N*-dimethylformamide (DMF) were purchased from Rankem chemicals. 5-amino isophthalic acid was purchased from the Aldrich Chemicals. All starting materials were used without further purification. All experimental operations were performed in 5 mL glass vial inside a programmed oven for synthesis.

#### 3.4.2 Synthesis procedure of Mn-MOFs

**Synthesis of Mn-5TIA-1 [Mn(5-TIA)(DMF)]:** 1.0 mL of 5-TIA (0.20M) solution in *N,N*-dimethylformamide (DMF) was taken in a 5 mL vial. 0.5 mL of Mn(NO<sub>3</sub>)<sub>2</sub> • xH<sub>2</sub>O solution (0.20 M) in DMF was added to this solution. The vial was capped and heated to 85 °C for 72 h. The mother liquor was decanted and the Rectangular golden color crystals were filtered off, washed with DMF. The unreacted ligand can be removed by washing in DMF (3 mL, 4 times) as 5-TIA is highly soluble in DMF and afterwards resulting MOF was dried in air (10 min). [**Yield:** 70 %, 0.0130 g depending on Mn(NO<sub>3</sub>)<sub>2</sub> • xH<sub>2</sub>O]. **FT-IR:** 3448(m, br), 2929(w), 2867(w), 1652(s), 1505(w), 1383(s), 1250(m), 1092(s), 780(m), 708(m), 656(m) cm<sup>-1</sup>.

**Elemental analysis (%) of of evacuated Mn-5TIA-1** Found (%) C= 44.42, H= 3.37, N= 15.82; Calc. (%) C= 43.46, H= 3.36, N= 15.59.

**Synthesis of Mn-5TIA-2 [Mn(5-TIA)]:** 1.0 mL of 5-TIA (0.20M) solution in *N,N*-dimethyl formamide (DMF) was taken in a 5 mL vial. 0.5 mL of Mn(NO<sub>3</sub>)<sub>2</sub> • xH<sub>2</sub>O solution (0.20 M) in DMF and 0.5 mL of pyrazine solution (0.20 M) in DMF was added to this solution. The vial was capped and heated to 85 °C for 72 h. The mother liquor was decanted and the square yellow color crystals were filtered off, washed with DMF) and dried in air (10 min). [**Yield:** 74%, 0.0074 g depending on Mn(NO<sub>3</sub>)<sub>2</sub> • xH<sub>2</sub>O]. **FT-IR:** (KBr 4000-600 cm<sup>-1</sup>): 2980(m), 2308(m), 1654(s), 1367(s), 1091(m), 774(m), 711(m), cm<sup>-1</sup>.

**Elemental analysis (%) of evacuated Mn-5TIA-2:** Found (%) C= 40.83, H= 1.77, N= 14.828; Calc. (%) C= 41.98, H= 1.76, N= 14.68.

**Synthesis of Mn-5TIA-3 [Mn(5-TIA)]:** 1.0 mL of 5-TIA (0.20M) solution in *N,N*-dimethyl formamide (DMF) was taken in a 5 mL vial. 0.5 mL of Mn(NO<sub>3</sub>)<sub>2</sub> • 3H<sub>2</sub>O solution (0.20 M) in DMF and 0.5 mL of 4, 4' bipyridine solution (0.20 M) in DMF was added to this solution. The vial was capped and heated to 85 °C for 72 h. The mother liquor was decanted and the rectangular colorless crystals were filtered off, washed with DMF) and dried in air (10 min). [**Yield:** 74%, 0.0074 g depending on Mn(NO<sub>3</sub>)<sub>2</sub> • xH<sub>2</sub>O]. **FT-IR:** (KBr 4000-600 cm<sup>-1</sup>): 3524(m br), 2929(m), 1654(s), 1052(w), 1384(s), 1254(m), 1091(s), 776(w), 712(w), 658(s), cm<sup>-1</sup>.

**Element analysis of evacuated Mn-5TIA-3:** Found (%) C= 40.82, H= 1.77, N= 14.924; Calc. (%) C= 41.98, H= 1.76, N= 14.68.

### 3.4.3 General methods for characterization

**(a) Powder X-Ray Diffraction (PXRD).** The PXRD patterns were collected on a Phillips PANalytical diffractometer on a Cu K $\alpha$  radiation ( $\lambda = 1.5406 \text{ \AA}$ ), with a scan speed of 2° min<sup>-1</sup>. The tube voltage and amperage were set at 40 kV and 50 mA respectively. Each sample was scanned between 5 and 50° 2 $\theta$  with a step size of 0.02°. The instrument was previously calibrated using a silicon standard.

**(b) Thermogravimetric Analysis (TGA)** TGA was performed on a SDT Q600 TG-DTA analyzer instrument. Approximately 5 mg of the sample was added to an aluminium crucible and heated from 25 to 800 °C under N<sub>2</sub> atmosphere at heating rate of 10 °C min<sup>-1</sup>.

**(c) Hot-Stage Microscopy.** Leica M-80 optical microscope with hot stage and camera attachment was used for collecting photographs.

**(d) IR Spectroscopy.** The Fourier transform (FT) infrared spectra of the MOFs were taken on a *PERKIN ELMER FT-IR SPECTRUM* (Nicolet) spectrometer. KBr samples (2 mg in 20 mg of KBr) were prepared and 10 scans were collected at 4 cm<sup>-1</sup> resolution for each sample. The spectra were measured over the range of 4000-400 cm<sup>-1</sup>

**(f) Gas Adsorption.** All low-pressure gas-sorption experiments (up to 1 atm) were performed on a Quantachrome Autosorb-1 automatic volumetric instrument. Approximately 50 mg of the The as-synthesized samples were immersed in dry methanol at

ambient temperature for 72 h, evacuated at ambient temperature for 24 h, followed by elevated temperature (85 °C) for 48 h. Finally the activated samples are treated for gas adsorption (H<sub>2</sub>, CH<sub>4</sub> and CO<sub>2</sub>).

#### 3.4.4 X-ray Crystallography

##### General Data Collection and Refinement Procedures:

All single crystal data were collected on a Bruker SMART APEX three circle diffractometer equipped with a CCD area detector and operated at 1500 W power (50 kV, 30 mA) to generate Mo K $\alpha$  radiation ( $\lambda=0.71073$  Å). The incident X-ray beam was focused and monochromated using Bruker Excalibur Gobel mirror optics. All crystals reported in this chapter were mounted on nylon CryoLoops (Hampton Research) with Paraton-N (Hampton Research).

Initial scans of each specimen were performed to obtain preliminary unit cell parameters and to assess the mosaicity (breadth of spots between frames) of the crystal to select the required frame width for data collection. In every case frame widths of 0.5° were judged to be appropriate and full hemispheres of data were collected using the *Bruker SMART* [2.19] software suite. Following data collection, reflections were sampled from all regions of the Ewald sphere to redetermine unit cell parameters for data integration and to check for rotational twinning using *CELL\_NOW* [2.20]. In no data collection was evidence for crystal decay encountered. Following exhaustive review of the collected frames the resolution of the dataset was judged. Data were integrated using *Bruker SAINT* [2.21] software with a narrow frame algorithm and a 0.400 fractional lower limit of average intensity. Data were subsequently corrected for absorption by the program *SADABS* [2.22]. The space group determinations and tests for merohedral twinning were carried out using *XPREP* [2.22]. In all cases, the highest possible space group was chosen.

All structures were solved by direct methods and refined using the *SHELXTL 97* [2.23] software suite. Atoms were located from iterative examination of difference F-maps following least squares refinements of the earlier models. Final models were refined anisotropically (if the number of data permitted) until full convergence was achieved. Hydrogen atoms were placed in calculated positions (C-H = 0.93 Å) and included as riding atoms with isotropic displacement parameters 1.2-1.5 times  $U_{eq}$  of the attached C atoms.

Data were collected at 293(2) K for Mn-5TIA-2 MOF and 190(2) K for Mn-5TIA-1 and -3 MOFs presented in this paper. This lower temperature was considered to be optimal for obtaining the best data. Electron density within void spaces has not been assigned to any guest entity but has been modeled as isolated oxygen and/or carbon atoms. The foremost errors in all the models are thought to lie in the assignment of guest electron density. All structures were examined using the *Adsym* subroutine of PLATON [2.24] to assure that no additional symmetry could be applied to the models. All ellipsoids in ORTEP diagrams are displayed at the 50% probability level unless noted otherwise. For all structures we note that elevated R-values are commonly encountered in MOF crystallography for the reasons expressed above by us and by other research groups. [2.25–2.35]

**Experimental and refinement details for Mn-5TIA-1:** A colorless type crystal ( $0.20 \times 0.16 \times 0.12 \text{ mm}^3$ ) of Mn-5TIA-1 was mounted on 0.7 mm diameter nylon CryoLoops (Hampton Research) with Paraton-N (Hampton Research). The loop was mounted on a *SMART APEX* three circle diffractometer equipped with a CCD area detector (Bruker Systems Inc., 1999a) and operated at 1500 W power (50 kV, 30 mA) to generate Mo  $K\alpha$  radiation ( $\lambda = 0.71073 \text{ \AA}$ ). The incident X-ray beam was focused and monochromated using Bruker Excalibur Gobel mirror optics. A total of 32862 reflections were collected of which 6794 were unique and 6116 of these were greater than  $2\sigma(I)$ . The range of  $\theta$  was from  $1.85\text{--}28.27^\circ$ . Analysis of the data showed negligible decay during collection. The structure was solved in monoclinic  $P2_1/c$  space group, with  $Z = 4$ , using direct methods. All non-hydrogen atoms were refined anisotropically. Mn-5TIA-1 contains two 5-amino isophthalic acid molecule in the asymmetric unit. It should be noted that other supporting characterization data are consistent with the crystal structure. Final full matrix least-squares refinement on  $F^2$  converged to  $R_1 = 0.0462$  and  $wR_2 = 0.1024$  (all data) with GOF = 1.157.

**Experimental and refinement details for Mn-5TIA-2:**

A colorless type crystal ( $0.20 \times 0.16 \times 0.12 \text{ mm}^3$ ) of Mn-5TIA-2 was mounted on 0.7 mm diameter nylon CryoLoops (Hampton Research) with Paraton-N (Hampton Research). The loop was mounted on a *SMART APEX* three circle diffractometer equipped with a CCD area detector (Bruker Systems Inc., 1999a) and operated at 1500 W power (50 kV, 30 mA) to generate Mo  $K\alpha$  radiation ( $\lambda = 0.71073 \text{ \AA}$ ). The incident X-ray beam was focused and

monochromated using Bruker Excalibur Gobel mirror optics. A total of 9625 reflections were collected of which 3380 were unique and 2380 of these were greater than  $2\sigma(I)$ .

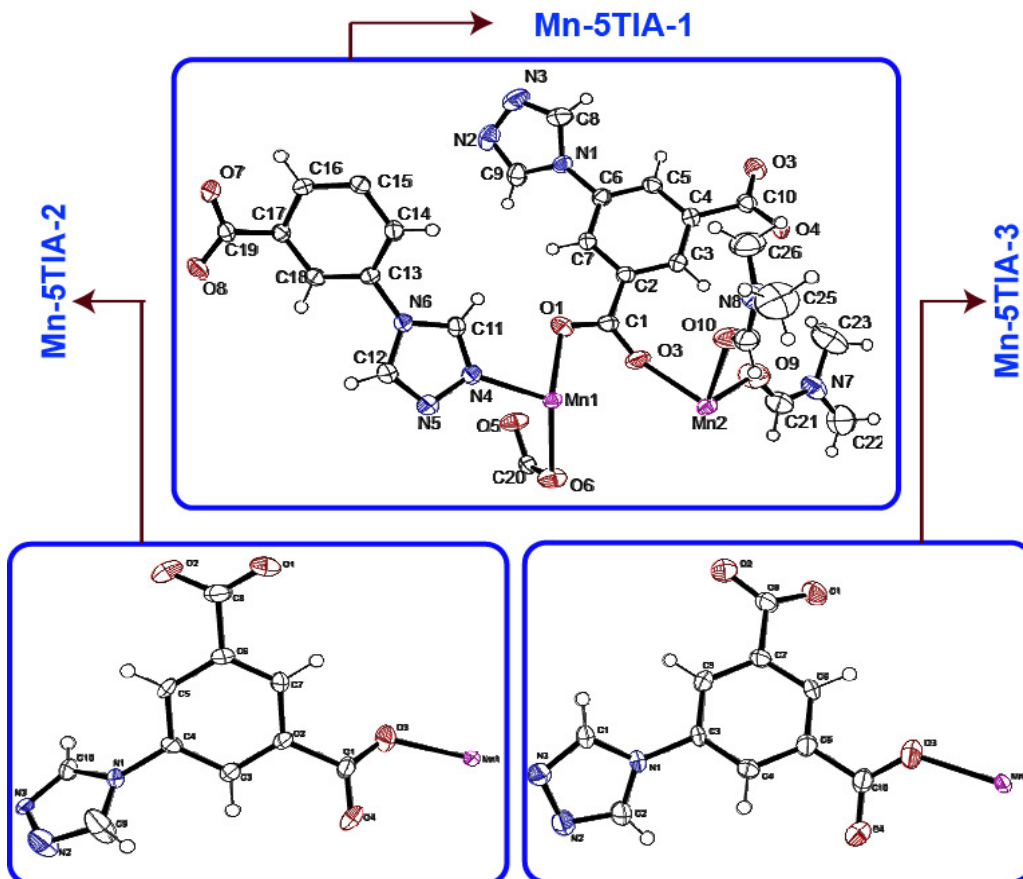


**Figure 3.6:** Asymmetric unit ORTEP diagrams (50% probability) of Mn-5TIA-1, -2 and -3.

The range of  $\theta$  was from  $2.89\text{--}25.00^\circ$ . Analysis of the data showed negligible decay during collection. The structure was solved in orthorhombic  $Pbcn$  space group, with  $Z = 4$ , using direct methods. All non-hydrogen atoms were refined anisotropically. Mn-5TIA-2 contains one 5-amino isophthalic acid molecule in the asymmetric unit.

The attempts made to model the guests (solvent molecules) did not lead to identification of guest entities in these structures due to the limited periodicity of the solvent molecules in the crystals. Since the solvent is neither bonded to the framework nor tightly packed into the voids, solvent disorder can be expected for the MOF structures. Thus, electron density within void spaces which could not be assigned to any definite guest entity was modeled as isolated carbon or oxygen atoms, and the foremost errors in all the models lie with the

assignment of guest electron density. To assess the correctness of the atomic positions in the framework, the application of the SQUEEZE routine of A. Spek has been performed. However, atomic co-ordinates for the “non-SQUEEZE” structures are also presented. It should be noted that the precision of this model is low; however, the structure is reported to demonstrate the nature of the framework of Mn-5TIA-2. Other supporting characterization data (*vide infra* Materials and Methods) agree with the structure. Final full matrix least-squares refinement on  $F^2$  converged to  $R_1 = 0.0862$  and  $wR_2 = 0.2761$  (all data) with GOF = 1.147.

### **Experimental and refinement details for Mn-5TIA-3:**

A colorless type crystal ( $0.20 \times 0.16 \times 0.12 \text{ mm}^3$ ) of Mn-5TIA-3 was mounted on 0.7 mm diameter nylon CryoLoops (Hampton Research) with Paraton-N (Hampton Research). The loop was mounted on a *SMART APEX* three circle diffractometer equipped with a CCD area detector (Bruker Systems Inc., 1999a) and operated at 1500 W power (50 kV, 30 mA) to generate Mo  $K_\alpha$  radiation ( $\lambda=0.71073 \text{ \AA}$ ). The incident X-ray beam was focused and monochromated using Bruker Excalibur Gobel mirror optics. A total of 20465 reflections were collected of which 4436 were unique and 3554 of these were greater than  $2\sigma(I)$ . The range of  $\theta$  was from  $1.93 - 28.26^\circ$ . Analysis of the data showed negligible decay during collection. The structure was solved in monoclinic  $P2_1/c$  space group, with  $Z = 4$ , using direct methods. All non-hydrogen atoms were refined anisotropically. Mn-5TIA-3 contains one 5-amino isophthalic acid molecule in the asymmetric unit. It should be noted that other supporting characterization data are consistent with the crystal structure. Final full matrix least-squares refinement on  $F^2$  converged to  $R_1 = 0.0642$  and  $wR_2 = 0.15991$  (all data) with GOF = 0.997.

**NOTE:** The results of this chapter have already been published in *Chem. Commun.*, 2011, **47**, 7674-7676. with the title: “*Template induced structural isomerism and enhancement of porosity in manganese(II) based metal-organic frameworks (Mn-MOFs)*”. These publications were the results from the group of Dr. Rahul Banerjee and his students Tamas Panda and Pradip Pachfule from CSIR National Chemical Laboratory, Pune, India. Major works are contributed by Tamas Panda with the instrumental facilities of CSIR National Chemical Laboratory.



## CHAPTER 4

---

### SELF ASSEMBLED ONE DIMENSIONAL FUNCTIONALIZED METAL ORGANIC NANOTUBES (MONTs) FOR HYDROUS PROTON CONDUCTION

---

#### 4.1 Introduction:

Proton-conducting materials are prime important component of fuel cells [1.39]. The beneficial aspects of the fuel cell have prompted many researchers to look for materials that can transport protons efficiently, as the facile proton conduction appears to be at the heart of the fuel-cell technology [1.40]. Recently, metal-organic frameworks (MOFs), showed their potential as a proton conductor due to their tunability of pore sizes, shapes, and different functionalities [3.2]. In Section 1.8, the overview of new types of proton-conducting MOFs and their unique proton-conduction properties are discussed. In general, promises for proton conduction in MOFs have been classified in two categories: *water assisted proton-conducting MOFs operating below 100 °C* and *anhydrous proton conductors operating above 100 °C*. Although several attempts like incorporation of water channel and doping of organic molecules (imidazole, triazole etc.) inside the pores have been implemented to get higher proton conductivity in MOFs. However, it is clearly visible that applications of MOFs as proton conductors have not been explored as broadly as gas storage properties [1.43a and b]. Extensive amount of research is still necessary to explore the potential of MOFs as promising proton conducting materials for fuel cell application. As a part of our investigation (from earlier chapter) on the study of functionalization in MOFs, we have chosen 5TIA as organic linker considering the effect of triazole functionalization might enhance the CO<sub>2</sub> uptake. In order to investigate this ideology, we have tried to synthesize various MOFs with the same linker 5TIA. In this chapter, we report two isostructural self assembled and functionalized metal organic nanotubes MONTs, In-5TIA [In(C<sub>10</sub>O<sub>4</sub>N<sub>3</sub>H<sub>5</sub>)<sub>2</sub>(C<sub>2</sub>H<sub>8</sub>N)(H<sub>2</sub>O)] and Cd-5TIA [Cd(C<sub>10</sub>O<sub>4</sub>N<sub>3</sub>H<sub>5</sub>)<sub>2</sub>(C<sub>2</sub>H<sub>8</sub>N)<sub>2</sub>(H<sub>2</sub>O)] have been synthesized using In(III) and Cd(II) ions as

metal center with 5-triazole isophthalic acid (5-TIA) as organic building block. We would like to mention that, although there have been several reports of MOFs with diverse architecture, still discrete metal organic nanotubular structures are extremely rare [4.1]. Only a handful of literature reports are available where self assembled metal organic nanotubes (MONTs) has been constructed using capping agents (like, ethylene diamine, phenanthroline) or secondary linkers (like, 4,4' bipyridine, iodine) [4.2]. However most of these reports reveal only the structural details of the MONTs without showcasing any fundamental application. Moreover, most of the MONTs reported in literature are interconnected by metal ions [4.3] leaving only one or two examples of self assembled hydrogen bonded MONTs.

Both In-5TIA and Cd-5TIA consists of one dimensional single walled self assembled nanotubes with 7.8 and 8.2 Å inner dimensions and outer dimension of 26.6 and 27.4 Å, respectively. These MONTs are held together by weak C-H...O hydrogen bonding [4.4] to form the self assembled architectures. Initially, we analyzed the N<sub>2</sub> adsorption isotherm of these two MONTs. However, owing to their one dimensional structure In-5TIA and Cd-5TIA MONTs do not show any gas adsorption despite their decent pore aperture of 7.8 and 8.2 Å respectively. Structural investigation reveals that both these structures consist (CH<sub>3</sub>)<sub>2</sub>NH<sub>2</sub><sup>+</sup> cations, trapped inside the frameworks. As mentioned in section 1.8.1.2, various cation molecules [NH<sub>4</sub><sup>+</sup>, (CH<sub>3</sub>)<sub>2</sub>NH<sub>2</sub><sup>+</sup>, (C<sub>2</sub>H<sub>5</sub>)<sub>2</sub>NH<sub>2</sub><sup>+</sup> etc.] trapped inside the MOFs could be useful for proton conduction under hydrous condition. Since these MONTs have cationic (CH<sub>3</sub>)<sub>2</sub>NH<sub>2</sub><sup>+</sup> inside these nanotubes, we decided to measure their proton conductivities under hydrous condition. It is noteworthy that, Cd-5TIA and In-5TIA MONTs shows high proton conductivity of  $3.61 \times 10^{-3} \text{ Scm}^{-1}$  and  $5.35 \times 10^{-5} \text{ Scm}^{-1}$  at ambient temperature (301 K) and 98% relative humidity (RH). We have also collected the proton conductivity data of the literature reported self assembled Indium isophthalic acid based MONT (In-IA) [4.5] to systematically study the proton conduction pathways in these MONTs. To the best of our knowledge, In-5TIA and Cd-5TIA are the first example of self assembled functionalized (MONTs) which shows application like proton conductivity.

## 4.2 Result and discussion:

### 4.2.1 Structural analysis of In-IA, In-5TIA and Cd-5TIA

Isophthalate building blocks are well-known for synthesis of isolated nanocubes [4.6a-b] and nanoballs [4.6c-d]. Among these, Metal Organic Polyhedras (MOPs), [4.7] are the well known example of isolated nanoballs constructed from isophthalic acid. Self assembled MONT architecture has already been reported [4.5] with isophthalic acid as the organic building unit and In(III) as metal center with small inner dimension (4.8 Å) (Figure 4.1a). One would assume that the angle between two carboxylate groups of isophthalate scaffold (115°) favors the formation of the nanotubular architecture. This motivated us to choose 5TIA as the organic ligand which posses the specific geometry as well as functionalization of the outer core to achieve these large functionalized nanotubular architectures (Figure 4.1b). 5TIA offers triazole moiety on the five positions of isophthalate scaffold which could hold these nanotubes in close proximity via hydrogen bonding and create functionalization on the outer wall of these nanotubes. Single-crystal X-ray diffraction analysis reveals that both In-5TIA and Cd-5TIA are isostructural and crystallizes in the tetragonal space group  $P4/n$ . The asymmetric unit of In-5TIA consists of one octahedral In (III) ion and two 5TIA molecules. Each In (III) SBU is coordinated to eight oxygens from four  $\mu_1$ -CO<sub>2</sub><sup>-</sup> functionalities and each carboxylate group of 5TIA chelates to one In (III) site (Figure 4.2a). Each 5TIA ligand is coordinated to two different In(III) ions with In–5TIA–In angle of 126° ( for Cd-5TIA, Cd–5TIA–Cd angle is 124.7°) . It is noteworthy that, the triazole moiety of 5-TIA is not coordinated to any In(III) / Cd(II) metal center. These types of M (CO<sub>2</sub>)<sub>4</sub> type of SBU could be found in some In(III) based MOFs [4.8] but it is very rare among Cd(II) based MOFs. In the crystal structure of In-5TIA each In(III) SBU extends through *a* and *b* axis to form a metallomacrocycle where four In(III) ions are linked by four 5TIA via  $\mu_1$ -CO<sub>2</sub><sup>-</sup> carboxyl groups to generate a [In<sub>4</sub>(5TIA)<sub>4</sub>] square grid with In-In distance being 9.7 Å (for Cd-5TIA, Cd-Cd distance being 9.9 Å). These [In<sub>4</sub>(5TIA)<sub>4</sub>] squares are infinitely connected to  $\mu_1$ -CO<sub>2</sub><sup>-</sup> functionalities of 5TIA ligands along the *c* axis to produce a 1D nano channel containing [In<sub>8</sub>(5TIA)<sub>12</sub>] boxes (Figure 4.2c). The top view of the open-ended, hollow nanotube indicates that it is an undulated tetranuclear [In<sub>4</sub>(5TIA)<sub>4</sub>] metallamacrocycle with a very unusual 32-membered ring (32MR) consisting of four In(III) atoms and four 5TIA ligands (4 In, 20 C, and 8 O) with S<sub>4</sub> symmetry, where

all the triazole moiety of 5TIA molecules are pointed to the periphery of the MONT (Figure 4.2d). The interior and exterior wall cross sectional diameter of these nanotubes of In-5TIA is 7.8 and 26.6 Å whereas for Cd-5TIA, it is 8.2 and 27.4 Å respectively. These independent MONTs are further self assembled to produce an interesting 3D supramolecular aggregate along bc plane where triazole functionality of one MONT is interdigitated to another MONT and vice versa (Figure 4.2d).

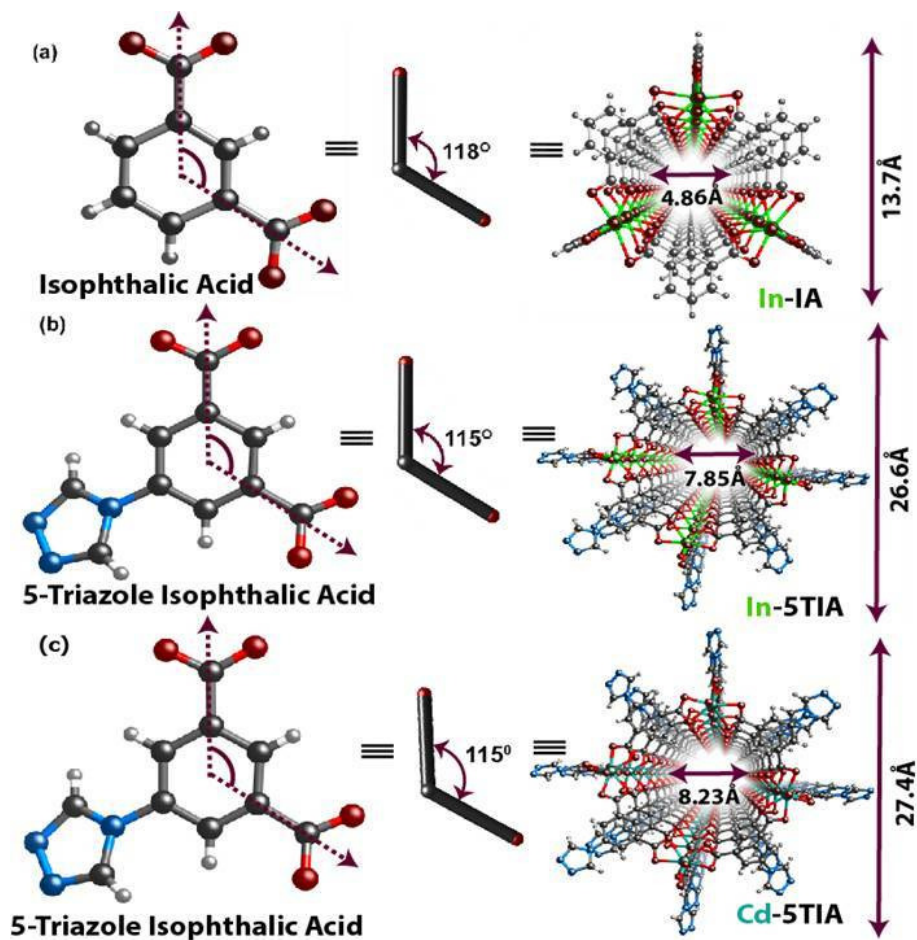


**Figure 4.1:** Structures of In-IA and In-5TIA MONTs: a) Schematic view IA ligand, showing the angle  $118^\circ$  between two carboxylic acid moiety and forms three centered MONT with In(III). (b) and (c) Schematic view of functionalized 5-TIA ligand, showing the angle  $115^\circ$  between two carboxylic acid moiety and forms four centered MONT with In(III) and Cd(II) respectively. Color code: In (green), Cd (light blue), N (blue), O (red), C (gray) and H (white).

The C-H...O hydrogen bonding [ $D=3.645(7)$  Å,  $d=2.811(5)$  Å,  $\theta=150.0^\circ(3)$ ] between triazole carbon bound hydrogen and metal [In(III) or Cd(II)] coordinated carboxylate oxygen holds these self assembled MONTs, which rules out the possibility of

interpenetration among In-5TIA ring through tube to tube cohesion. The extra-framework volumes per unit cell for In-5TIA and Cd-5TIA are approximately 48.8 and 50.6 %, respectively, calculated using PLATON [4.9]. A side view of these frameworks reveals another tetragonal channel opening with effective dimensions of  $7.8 \times 8.5 \text{ \AA}$  along the bc plane for In-5TIA whereas for Cd-5TIA it is  $6.7 \times 8.4 \text{ \AA}$  (Figure 4.2e). The whole framework of In-5TIA and Cd-5TIA bears negative charge due to the coordination of each metal [In(III) or Cd(II)] atom to the four carboxylate ligands. It is noteworthy that each SBU of In-5TIA contains one negative charge whereas each SBU of Cd-5TIA contains two negative charges. However, after careful investigation of these two isostructural MOFs, we propose that, single negative charge of In-5TIA SBU were balanced by one dimethyl ammonium cation. Whereas in Cd-5TIA, two negative charges at SBU was neutralized by two dimethyl ammonium cations. These cations were heavily disordered and confirmed by the elemental analysis of In-5TIA and Cd-5TIA. (See Experimental section).

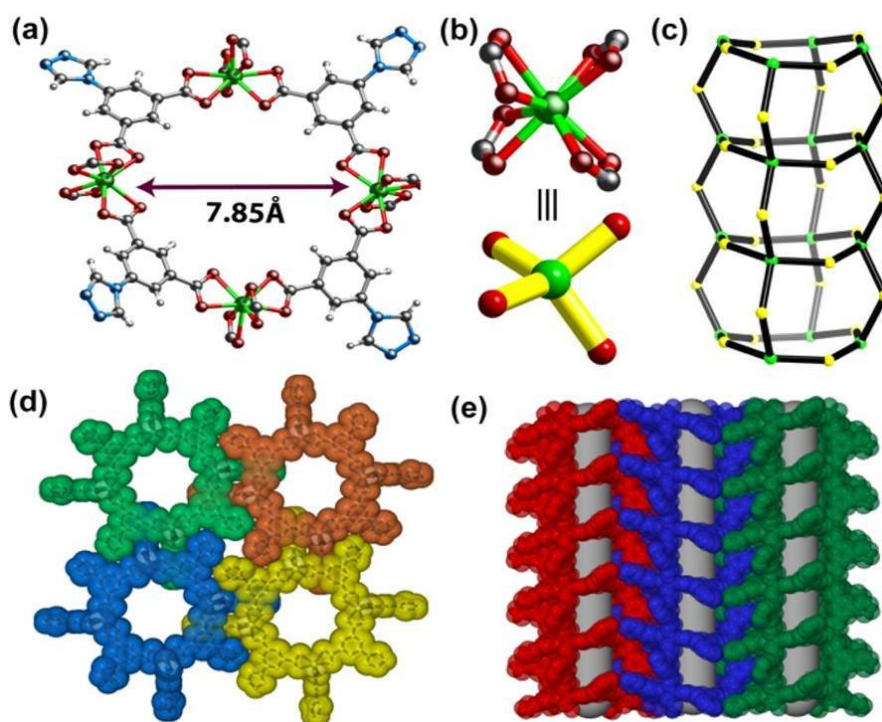


**Figure 4.2:** (a) The cross sectional view of In-5TIA MONTs. (b) Self assembled MONTs are arranged in three dimensional manners. (c) Simplified view of a eight-connected Indium center, yellow stick indicates each  $\mu_1\text{-CO}_2^-$  carboxyl group connected with octahedral In(III) node (d) Side view of the simplified nanotube structure (e) packing view of three different self assembled MONTs.

**Charge mismatch of In-5TIA and Cd-5TIA:**

During the refinement of In-5TIA and Cd-5TIA X-ray data, we encountered an electron density within the framework cavity and also one more electron density near the SBU of Cd-5TIA. Structural investigation of In-5TIA SBU reveals that one In (III) metal center with tri-positive charges coordinated to eight  $\mu_1$ -CO<sub>2</sub><sup>-</sup> oxygens from four 5TIA links creating an extra negative charge associated with each In(III) metal center. A cation should be present to balance the negative charge in the SBU. On the contrary, Cd-5TIA SBU contains one Cd(II) metal center with di-positive charges get coordinated with eight  $\mu_1$ -CO<sub>2</sub><sup>-</sup> oxygens from four 5TIA link creating extra double negative charge associated with each Cd(II) metal center. Hence a single cation in the SBU of In-5TIA and double cations in the SBU of Cd-5TIA should be present to balance the negative charge in the SBU. Upon careful investigation of the crystal structure of both these MONTs, we have found heavily disordered dimethyl ammonium cation within the framework cavity. Hence, we believe that one dimethyl ammonium cation is balancing the extra negative charge of In-5TIA SBU, whereas two dimethyl ammonium cations are balancing the extra negative charge of Cd-5TIA SBU. To prove the correctness of the electron density within these frameworks, the SQUEEZE routine has been applied. It should be noted that SQUEEZE structures does not contain any disordered dimethyl ammonium cations within the framework cavity of both In-5TIA and Cd-5TIA. So from the crystal structures of both In-5TIA and Cd-5TIA, we anticipate that the molecular formula of In-5TIA and Cd-5TIA could be In(C<sub>10</sub>O<sub>4</sub>N<sub>3</sub>H<sub>5</sub>)<sub>2</sub>(C<sub>2</sub>H<sub>8</sub>N) and Cd(C<sub>10</sub>O<sub>4</sub>N<sub>3</sub>H<sub>5</sub>)<sub>2</sub>(C<sub>2</sub>H<sub>8</sub>N)<sub>2</sub>, respectively as we were unable to locate any solvent molecule inside the framework. Also the experimental elemental analysis (CHN) of as-synthesized In-5TIA and Cd-5TIA matches well with the calculated CHN data from the aforementioned molecular formula. The calculated CHN percentage of In-5TIA (including dimethyl ammonium cation) was found to be, C=42.3%, H=2.9% and N=15.7%, in accordance with experimental elemental analysis data (C=42.2%, H=3.0% and N=15.6%) and support the dimethyl ammonium cation contain In-5TIA crystal structure. Similarly for as-synthesized Cd-5TIA, we have also done the elemental analysis and found the percentage of C=42.3%, H=4.01% and N=16.12% is also in accordance with calculated CHN percentage of dimethyl ammonium cation contained Cd-5TIA (C=42.7%, H=3.9% and N=16.8%). For representation we have provided SQUEEZE structure. It should be

noted that SQUEEZE structures does not contain any disordered dimethyl ammonium cations within the framework cavity of both In-5TIA and Cd-5TIA.

#### 4.2.2 Thermal properties and X-ray powder diffraction analysis:

Thermal gravimetric analysis (TGA) revealed that both In-5TIA and Cd-5TIA retains its stability at temperature as high as 150 °C (Figure 4.3), which was further confirmed by *in situ* variable temperature single crystal X-Ray data.

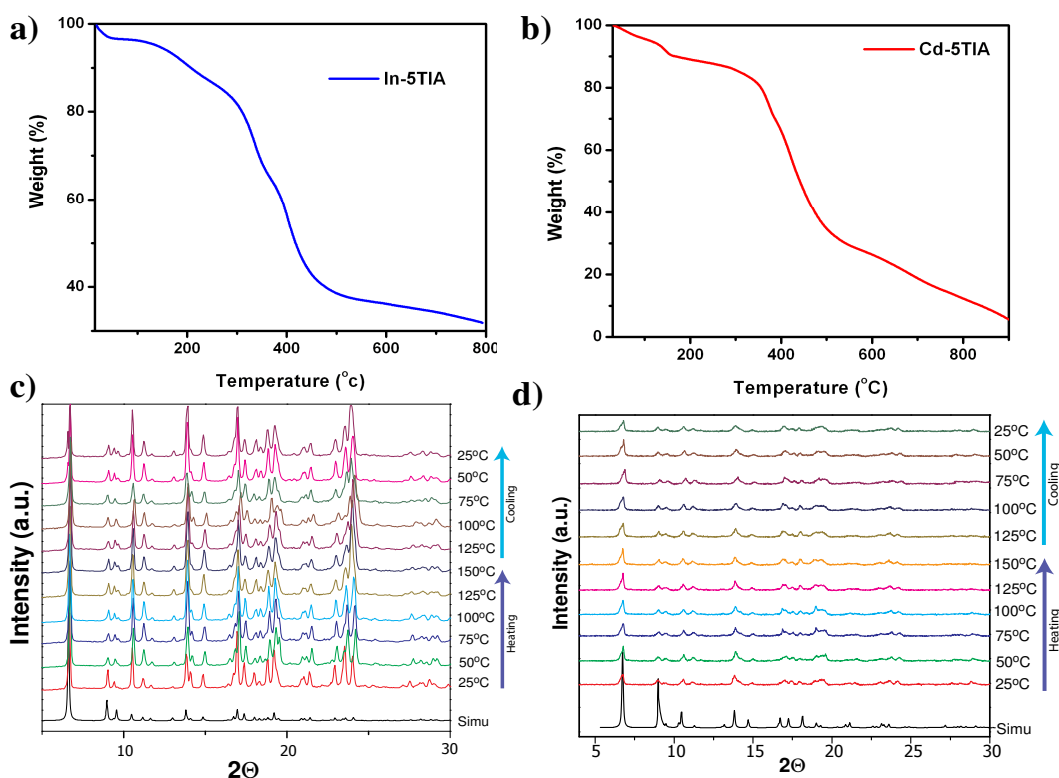


**Figure 4.3:** Thermal gravimetric analysis (TGA) data of (a) In-5TIA and (b) Cd-5TIA. Variable temperature powder Xray diffraction VTPXRD data of (c) In-5TIA and (d) Cd-5TIA comparison with the simulated one clearly indicates its high crystallinity as well as thermal stability at broad temperature range (25 °C to 150 °C).

In order to confirm the phase purity of the bulk materials, powder X-ray diffraction (PXRD) experiments were carried out on In-5TIA and Cd-5TIA. All major peaks of experimental PXRDs of In-5TIA and Cd-5TIA matches well with simulated PXRDs, indicating their reasonable crystalline phase purity (Figures 4.3 and 4.12). Variable temperature powder X-Ray diffraction data (VTPXRD) performed on as-synthesized In-

5TIA and Cd-5TIA (from 25 °C to 150 °C) further confirms their stability and crystallinity at elevated temperatures (Figure 4.3c and 4.3d).

### 4.2.3 Proton Conductivity Measurement:

**4.2.3.1 Methods and plots:** Proton conductivity was measured by a quasi-two-probe method, with a Solatron 1287 Electrochemical Interface with 1255B frequency response analyzer. As synthesized samples of In-5TIA and Cd-5TIA were pelletized under hydraulic pellet pressure with 0.5 mm and 0.6 mm thickness and 6.5 mm diameter under humidified condition for 24 hours and then subject to analysis for proton conduction. The resistances were calculated from the semicircle of the Nyquist plots. The activation energy values were obtained from the slope by least square fitting of the straight line. If the data points are  $(x_1, y_1)$ ,  $(x_2, y_2)$ , .....,  $(x_n, y_n)$  where  $x$  is the independent variable and  $y$  is the dependent variable. The fitting curve  $f(x)$  has the deviation (error)  $d$  from each data point, i.e.,  $d_1 = y_1 - f(x_1)$ ,  $d_2 = y_2 - f(x_2)$ , ...,  $d_n = y_n - f(x_n)$ . According to the method of least squares, the best fitting curve has the properties:

$$\Pi = d_1^2 + d_2^2 + \dots + d_n^2 = \sum_{i=1}^n d_i^2 = \sum_{i=1}^n [y_i - f(x_i)]^2 = \text{a minimum}$$

**N.B.** From the semicircle we got the resistance **R**

(Ohm). Now, from diameter  $r$  (mm) and thickness  $A$  (mm) proton conductivity ( $\sigma$ ) value can be calculated by the following equation,

$$\sigma = A / (R \times \pi r^2) \text{ Scm}^{-1}$$

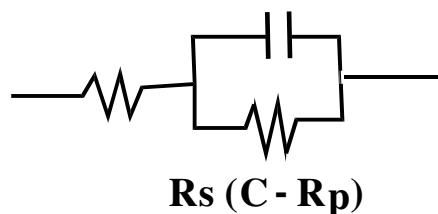


**Figure 4.4:** Equivalent circuit model representation of the Nyquist plot.



For high-temperature proton conductivity measurements, the pellets were inserted within a humidification chamber, which was encircled with a controlled heating coil attached with an automated temperature controller. The heat flow within the temperature controller was controlled by a dimerstat accordingly. The temperature of the chamber was measured by an infrared temperature sensor attachment, having a sensing accuracy of  $\pm 0.5$  °C.

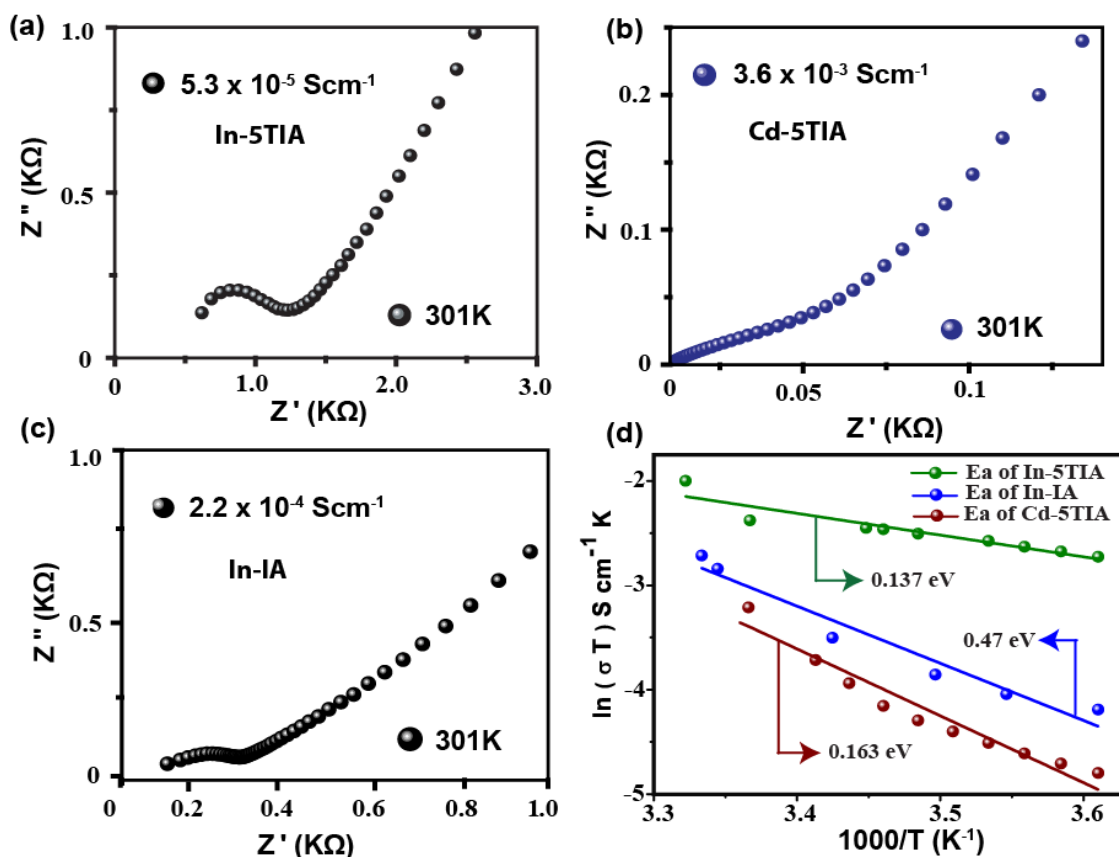


**Figure 4.5:** Nyquist plots of (a) In-5TIA MONT (b) Cd-5TIA MONT and (c) In-IA MONT at 31 °C under 98% RH (b) Arrhenius plots of activation energy for In-5TIA, Cd-5TIA and In-IA MONTs.

For low-temperature proton conductivity measurements, the pellets were inserted within a humidification chamber, which was encircled with a water circulation coil attached with a chiller integrated with an automated temperature controller. The heat flow within the chamber was controlled by the chiller accordingly. The temperature of the chamber was measured by an infrared temperature sensor attachment, having a sensing accuracy of  $\pm 0.5$  °C.

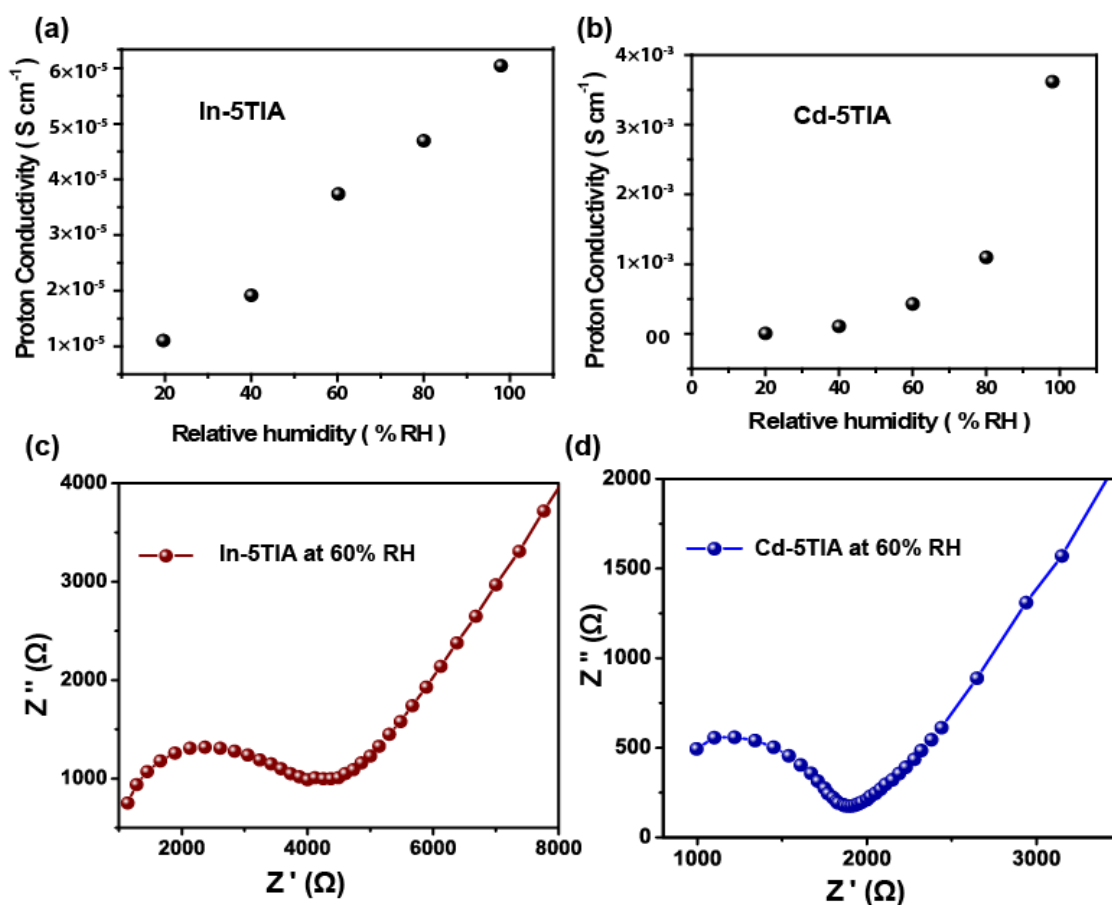


**Figure 4.6:** Proton conductivity vs humidity plot of (a) In-5TIA and (b) Cd-5TIA, shows that at lesser humidity decrease in proton conductivity values. Proton conductivity plots of (c) In-5TIA and (b) Cd-5TIA, at 60% RH shows decrease in proton conductivity values.

#### 4.2.3.2 Proton Conductivity Measurements of all MONTs:

The proton conductivity values were measured for In-5TIA and Cd-5TIA as  $5.35 \times 10^{-5} \text{ Scm}^{-1}$  and  $3.61 \times 10^{-3} \text{ Scm}^{-1}$ , respectively at ambient temperature (301 K) with 98% RH (Figure 4.5a and b). The conductivities were determined from the semicircle in the Nyquist plots, as shown in Figure 4.5. These values are highly humidity-dependent and dropped from  $5.35 \times 10^{-5} \text{ Scm}^{-1}$  and  $3.61 \times 10^{-3} \text{ Scm}^{-1}$  at 98% RH to  $1.25 \times 10^{-5} \text{ Scm}^{-1}$  and  $3.14 \times 10^{-3} \text{ Scm}^{-1}$  at 20% RH, respectively for In-5TIA and Cd-5TIA at 301 K (Figure 4.6), which indicates gradual decrease in proton conductivity upon decreasing humidification and establishes the role of water in proton conduction. The proton conductivity vs humidity and /or temperature plots clearly shows that Cd-5TIA is much more humidity and temperature sensitive than In-5TIA.

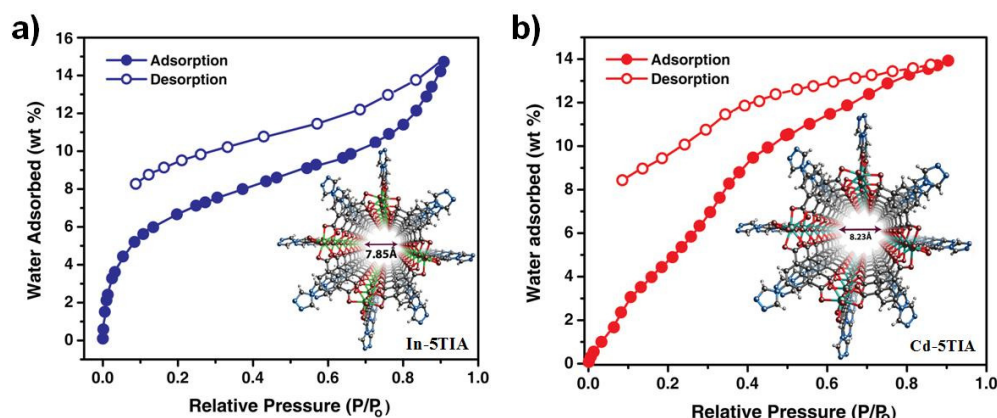


**Figure 4.7:** Water vapour adsorption plot at 298 K and 1 bar pressure for (a) In-5TIA and (b) Cd-5TIA. Filled circle represents adsorption and empty circle represents desorption.

We believe that, loosely bound water molecules due to humidification and dimethyl ammonium cations play a pivotal role in drastic difference in proton conductivity in these materials. At 298 K and 1 bar pressure, the water vapor uptake of In-5TIA and Cd-5TIA is 15 wt% and 14 wt% respectively (Figure 4.7). Interestingly, proton conductivity of Cd-5TIA is far more humidity sensitive than In-5TIA, evident from sharp drop in proton conductivity upon lesser humidification (from 98% RH to 60% RH) (Figure 4.6). This humidity sensitive proton conductivity behavior of Cd-5TIA is similar to  $(\text{NH}_4)_2(\text{adp})[\text{Zn}_2(\text{ox})_3] \cdot 3\text{H}_2\text{O}$  ( $8 \times 10^{-3} \text{ Scm}^{-1}$  at 98% RH while  $6 \times 10^{-6} \text{ Scm}^{-1}$  at 298 K 70% RH) [1.44e]. Worth mentioning, In-5TIA has only one dimethyl ammonium cation whereas Cd-5TIA has two dimethyl ammonium cations per SBU, providing enhanced hydrophilic environment within the nanotubular channel in case of Cd-5TIA. This phenomenon justifies the high proton conductivity of Cd-5TIA ( $3.61 \times 10^{-3} \text{ Scm}^{-1}$ ) compared to In-5TIA ( $5.35 \times 10^{-5} \text{ Scm}^{-1}$ ). Also, ramping the sample results in dislocation of the adsorbed water molecules, showing lower proton conductivity at elevated temperature (Figure 4.8b and 8d).

**Table 4.1:** Comparison of Proton Conductivity Values of Cd-5TIA and In-5TIA with other proton conducting MOF (based on the literature report within August 2012):

SL.No.	MOFs and CPs	Proton conductivity ( $\text{Scm}^{-1}$ )	Ea (eV)	Conditions	Reference
1	$(\text{NH}_4)_2(\text{adp})[\text{Zn}_2(\text{ox})_3] \cdot 3\text{H}_2\text{O}$	$8 \times 10^{-3}$	0.63	25 °C and 98%	1.44e

				RH	
<b>2</b>	Cd-5TIA	$3.6 \times 10^{-3}$	0.163	28 °C and 98% RH	This report
<b>3</b>	1D Ferrous Oxalate Dihydrate	$1.3 \times 10^{-3}$	0.37	25 °C and 98% RH	1.44c
<b>4</b>	$(\text{NH}_4)_4[\text{MnCr}_2(\text{ox})_6]_3 \cdot 4\text{H}_2\text{O}$	$1.1 \times 10^{-3}$	0.23	25 °C and 98% RH	1.44o
<b>5</b>	Cucurbit[6]uril (CB[6])	$1.1 \times 10^{-3}$	0.39	25 °C and 98% RH	1.44d
<b>6</b>	$\{\beta\text{-PCMOF2}(\text{Tz})_{0.45}\}$	$5 \times 10^{-4}$	0.51	150 °C	1.45b
<b>7</b>	$\text{Mg}_2(\text{dobdc})_3 \cdot 0.35\text{LiO}i\text{Pr}_3 \cdot 0.25\text{LiBF}_4 \cdot \text{EC3} \cdot \text{DEC}$	$3.1 \times 10^{-4}$	0.14	27 °C	1.44p
<b>8</b>	$\{\text{NH}(\text{prol})_3\}[\text{MIICrIII}(\text{ox})_3]$ (MII) = MnII, FeII, CoII	$1 \times 10^{-4}$		25 °C and 75% RH	1.44n
<b>9</b>	$(\text{H}_5\text{C}_2)_2(\text{dtoa}) \text{Cu}$	$1 \times 10^{-4}$		25 °C and 80% RH	1.44i
<b>10</b>	In-5TIA	$5.35 \times 10^{-5}$	0.137	28 °C and 98% RH	This report
<b>11</b>	$[\text{Zn}(\text{l-LcI})(\text{Cl})](\text{H}_2\text{O})_2$	$4.45 \times 10^{-5}$	0.34	28 °C and 98% RH	1.44l
<b>12</b>	PCMOF-3	$3.5 \times 10^{-5}$	0.17	25 °C and 98% RH	1.44b
<b>13</b>	$[\text{MIL-53}(\text{Fe})-(\text{COOH})_2]$	$2.0 \times 10^{-6}$	0.21	25 °C and 98% RH	1.44a

In-5TIA outperforms MIL-53 based MOFs ( $10^{-6}$ - $10^{-7} \text{ Scm}^{-1}$ ) [1.44a] and PCMOF-3 ( $3.5 \times 10^{-5} \text{ Scm}^{-1}$ ) [1.44b], whereas Cd-5TIA outperforms Ferrous oxalate dehydrate ( $1.3 \times 10^{-3} \text{ Scm}^{-1}$ ) [1.44c] and cucurbituril ( $1.3 \times 10^{-3} \text{ Scm}^{-1}$ ) [1.44d], although it posses lower proton conductivity value than  $(\text{NH}_4)_2(\text{adp})[\text{Zn}_2(\text{ox})_3] \cdot 3\text{H}_2\text{O}$  ( $8 \times 10^{-3} \text{ Scm}^{-1}$ ) [1.44e] at 298 K (Table 4.1).

High temperature proton conducting MOFs are extremely rare, where imidazole [1.45a] or triazole [1.45b] is the proton carrier. Contrary to other proton conducting MOFs, In-5TIA and Cd-5TIA shows proton conductivity in wide range of temperatures, from 277 K ( $2.8 \times 10^{-5} \text{ Scm}^{-1}$  for In-5TIA and  $3 \times 10^{-5} \text{ Scm}^{-1}$  for Cd-5TIA) to 368 K ( $2.7 \times 10^{-5} \text{ Scm}^{-1}$  for In-5TIA and  $1.2 \times 10^{-5} \text{ Scm}^{-1}$  for Cd-5TIA) (Figure 4.9 and Table 4.3), proving their potential for working in various applications. For In-5TIA, proton conductivity value increases from 277 K to 312 K, and then decreases steadily upto 368 K whereas for Cd-5TIA proton conductivity increases from 277 K to 301 K and then decreases upto 368 K (Figure 4.8,

Table 4.2 and 4.3). However, we acknowledge that both In-5TIA and Cd-5TIA show proton conductivity till 368 K. It is noteworthy that, In-5TIA and Cd-5TIA shows decrease in proton conductivity at lower temperatures than 301 K (Figure 4.8). To further compare the proton conducting efficiency of In-5TIA and Cd-5TIA, we have collected the proton conductivity data of the literature reported MONT architecture (In-IA) (Figure 4.8e and 8f), which reveals that In-IA and In-5TIA has comparable proton conductivity ( $5.35 \times 10^{-5} \text{ Scm}^{-1}$  for In-5TIA and  $2.20 \times 10^{-4} \text{ Scm}^{-1}$  for In-IA, respectively at 301 K and 98% RH) as both material contain one dimethyl ammonium cation per SBU within the framework. Accordingly, Cd-5TIA shows higher proton conduction ( $3.61 \times 10^{-3} \text{ Scm}^{-1}$  at 301 K and 98% RH) than In-5TIA and In-IA as Cd-5TIA possess two dimethyl ammonium cations per SBU inside the framework.

**Table 4.2:** Low temperatures Proton Conductivities of In-5TIA and Cd-5TIA:

Sr. no	In-5TIA		Cd-5TIA	
	Temperature (K)	Proton conductivity value (98% RH) ( $\text{Scm}^{-1}$ )	Temperature (K)	Proton conductivity value (98% RH) ( $\text{Scm}^{-1}$ )
1	277	$2.81 \times 10^{-5}$	277	$2.98 \times 10^{-5}$
2	279	$2.93 \times 10^{-5}$	279	$3.24 \times 10^{-5}$
3	281	$3.05 \times 10^{-5}$	281	$3.54 \times 10^{-5}$
4	283	$3.2 \times 10^{-5}$	283	$3.89 \times 10^{-5}$
5	287	$3.38 \times 10^{-5}$	285	$4.3 \times 10^{-5}$
6	289	$3.5 \times 10^{-5}$	287	$4.76 \times 10^{-5}$
7	290	$3.54 \times 10^{-5}$	289	$5.43 \times 10^{-5}$
8	297	$3.72 \times 10^{-5}$	291	$6.7 \times 10^{-5}$
9	301	$5.35 \times 10^{-5}$	293	$8.3 \times 10^{-5}$
10	—	—	297	$1.5 \times 10^{-4}$
11	—	—	301	$3.61 \times 10^{-3}$

**Table 4.3:** High temperatures Proton Conductivities of In-5TIA and Cd-5TIA:

Serial no	In-5TIA		Cd-5TIA	
	Temperature (K)	Proton conductivity value (98% RH) ( $\text{Scm}^{-1}$ )	Temperature (K)	Proton conductivity value (98% RH) ( $\text{Scm}^{-1}$ )
1	305	$9.12 \times 10^{-5}$	306	$1.6 \times 10^{-4}$
2	312	$3.85 \times 10^{-4}$	311	$8.46 \times 10^{-5}$
3	333	$6.72 \times 10^{-5}$	316	$6.11 \times 10^{-5}$
4	343	$4.87 \times 10^{-5}$	321	$4.75 \times 10^{-5}$
5	348	$4.56 \times 10^{-5}$	326	$3.8 \times 10^{-5}$
6	358	$3.0 \times 10^{-5}$	331	$3.18 \times 10^{-5}$
7	368	$2.7 \times 10^{-5}$	336	$2.71 \times 10^{-5}$
8	—	—	341	$2.47 \times 10^{-5}$
9	—	—	346	$2.12 \times 10^{-5}$
10	—	—	351	$1.80 \times 10^{-5}$
11	—	—	356	$1.63 \times 10^{-5}$
12	—	—	368	$1.148 \times 10^{-5}$

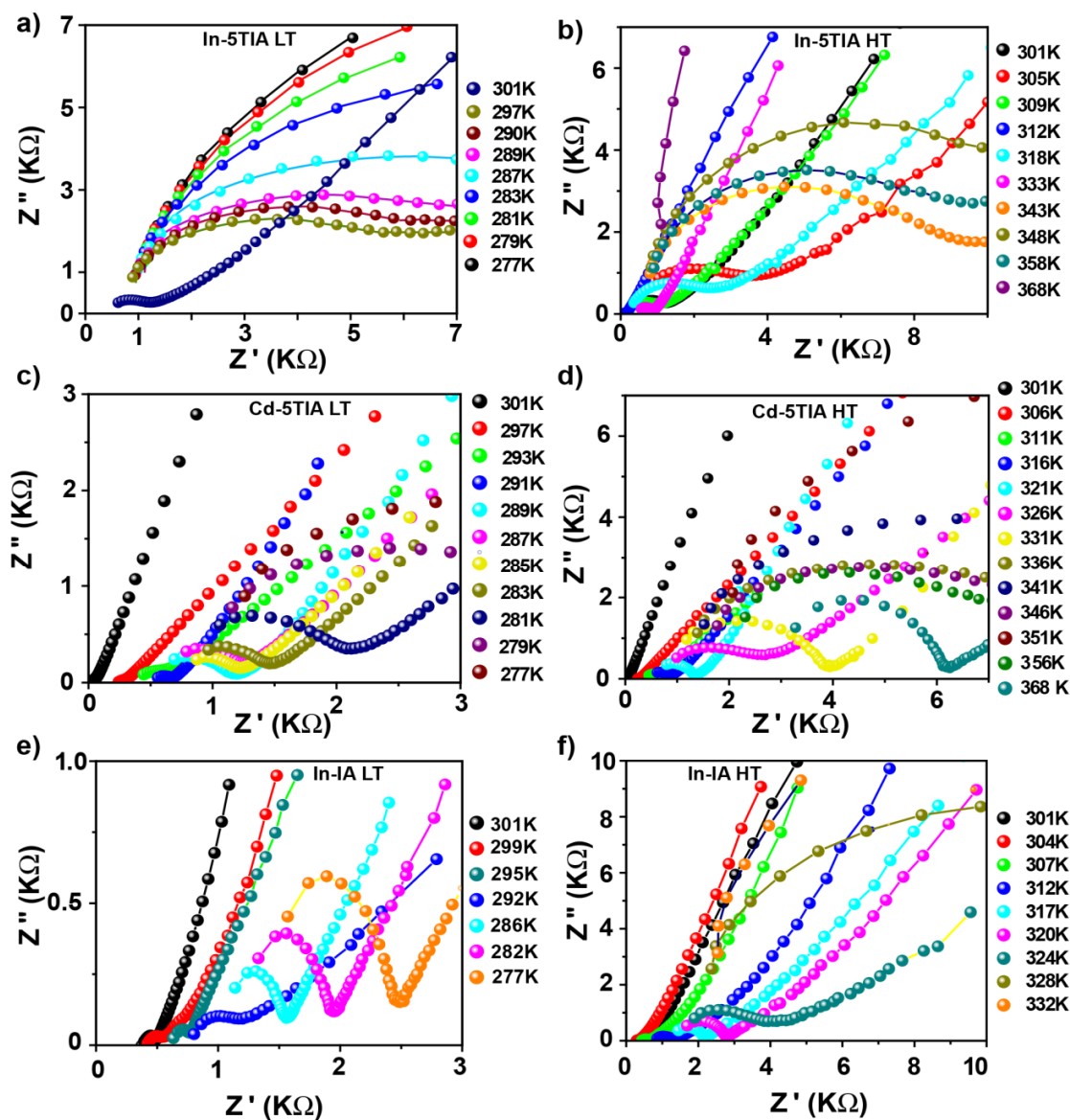


**Figure 4.8:** Proton conductivity plots of (a) In-5TIA at lower temperature, (b) In-5TIA at elevated temperature, (c) Cd-5TIA at lower temperature, (d) Cd-5TIA at elevated temperature, (e) In-IA at lower temperature and (f) In-IA at elevated temperature.

#### 4.2.3.3 Possible Mechanism for proton conduction in In-5TIA and Cd-5TIA:

To account for the high proton conductivity of In-5TIA and Cd-5TIA, we speculate a possible mechanism for proton hopping within the 1D tubular channels. Firstly, water molecules were adsorbed during humidification of as-synthesized sample by strong hydrogen bonding with dimethyl ammonium cations, triazole nitrogens and In(III) bound



carboxylate moieties within the hollow tubular cavity (Figure 4.9 and 4.10). The proton from dimethyl ammonium cation was transferred to In(III) bound carboxylate moiety,

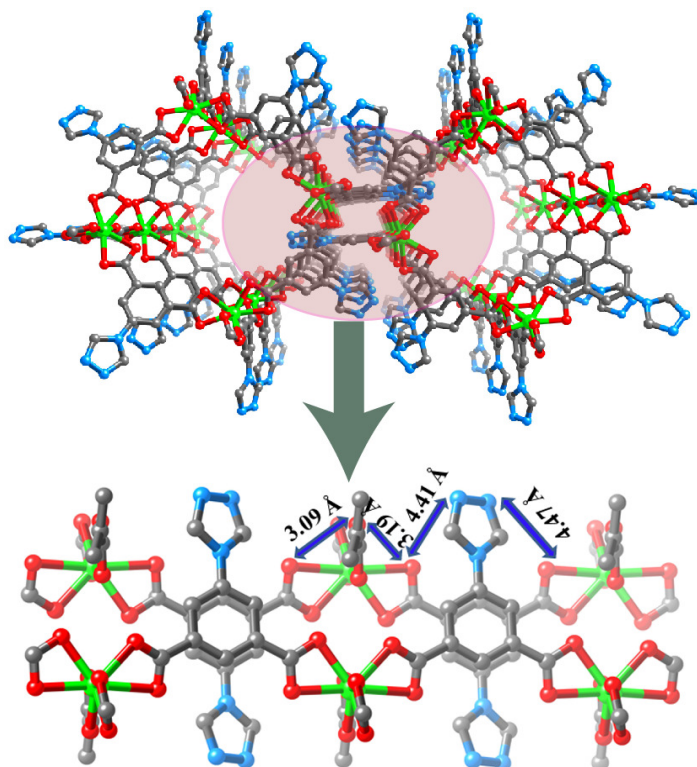


**Figure 4.9:** Schematic view of stacking triazole incorporated in the one dimensional nanotube which is the key factor for proton conduction.

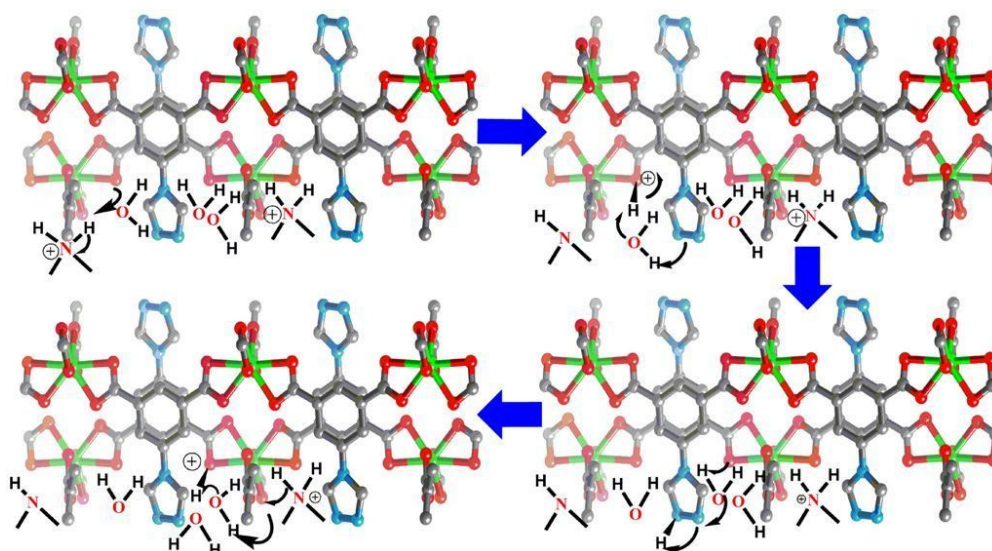


**Figure 4.10:** Possible scheme of Grotthuss proton hopping mechanism of In and Cd-5TIA.



then hopped to next triazole nitrogen via adsorbed water molecule. Again it gets transferred to next In(III) bound carboxylate moiety via another adsorbed water molecule. Finally, this proton moved to adjacent In(III) bound carboxylate moieties and the hopping goes on within these MONTs (Figure 4.10).

#### 4.2.3.4 Activation Energy Value:

In-5TIA and Cd-5TIA show considerably lower activation energy value than In-IA (0.137 eV for In-5TIA and 0.163 eV for Cd-5TIA whereas 0.47 eV for In-IA). Thus, proton conductivities in In-5TIA and Cd-5TIA follow mainly Grotthuss proton hopping mechanism [4.10] whereas proton conductivity of In-IA follows chiefly vehicular mechanism, which hint at the role of triazole moiety for providing proton conducting pathways in In-5TIA and Cd-5TIA

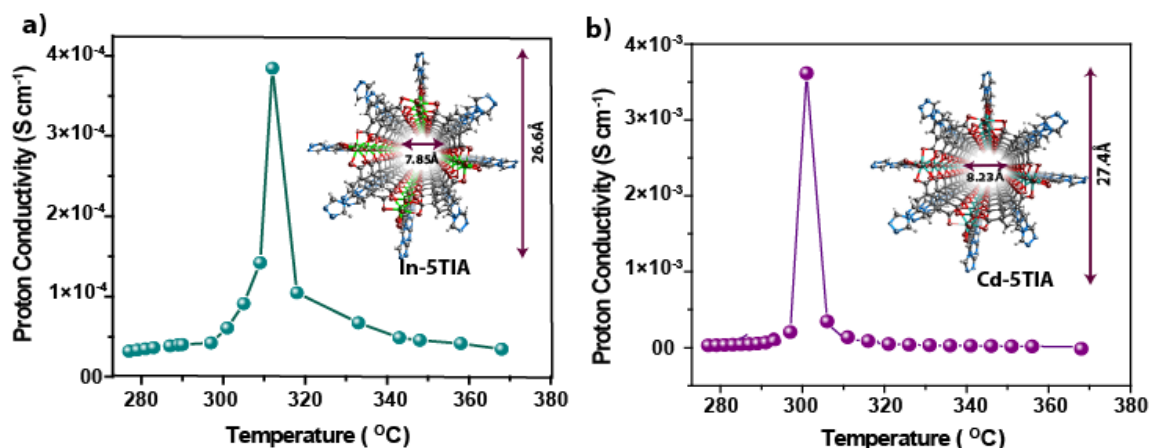


**Figure 4.11:** Proton conductivity vs temperature plot of (a) In-5TIA and (b) Cd-5TIA with increasing temperature.

and hence the advantages of functionalization of the framework. Activation energy value of In-5TIA (0.137 eV) (Figure 4.11) is comparable to nafion based membrane electrolytes (0.22 eV), [4.11] and lowest activation value reported till date for MOF based proton conducting materials. Cd-5TIA also posses low activation energy value of 0.163 eV (Figure 4.11).

#### 4.3 Conclusion:

In conclusion, we report two isostructural single-walled functionalized metal–organic nanotubes (MONTs) by using 5TIA as single organic building block and In(III) or Cd(II) as

metal node. These large MONTs are held together by hydrogen bonding interactions, leading to unique supramolecular nanotubular arrays. In this work, 5TIA serves dual purpose, to construct nanotubular architecture using single organic precursor linked with In(III) or Cd(II) node, as well as functionalize the pore wall with triazole moieties. The triazole decorated pores along with dimethyl ammonium cation and Cd(II) or In(III) bound carboxylate moiety provide an unique pathway for proton conduction under humid condition, showing noticeably high proton conductivity values ( $3.61 \times 10^{-3}$  to  $1.15 \times 10^{-5}$   $\text{Scm}^{-1}$  for Cd-5TIA and  $5.35 \times 10^{-5}$  to  $2.7 \times 10^{-5}$   $\text{Scm}^{-1}$  for In-5TIA) across a wide range of temperature (301 K to 368 K) and 98% relative humidity. Moreover, proton conductivity shown by Cd-5TIA ( $3.61 \times 10^{-3}$   $\text{Scm}^{-1}$  at 301 K) stands at high position among the proton conducting MOFs reported till date. We have also studied and compared the proton conductivity of the literature reported MONT architecture (In-IA). We expect that, this finding will lead to many new applications previously unrealized in nanotube based porous materials.

#### **4.4 Experimental Procedures:**

##### **4.4.1 Materials:**

Thionyl chloride, hydrazine hydrate, diethyl ether, benzene, and N,N'-dimethylformamide (DMF), benzene were purchased from Rankem chemicals. 5-amino isophthalic acid was purchased from the Aldrich Chemicals. All starting materials were used without further purification. All experimental operations were performed in air.

##### **4.4.2 Synthesis of 5-triazole isophthalic acid:**

###### **Synthesis of N,N'-Dimethylformamide Azine Dihydrochloride (DMAz):**

28.6 mL, 0.4 mol of Thionyl chloride ( $\text{SOCl}_2$ ) was added with stirring to DMF (150 mL) at  $5^\circ\text{C}$ . After addition keep this mixture at  $5^\circ\text{C}$  for 24h and then added slowly aqueous hydrazine hydrate (5 mL, 0.1 mol) in 20 mL DMF. After addition the mixture was stirred at room temperature for 48h and the white precipitate of N, N'-dimethylformamide azine dihydrochloride was collected by filtration and washed with DMF and diethyl ether: 19.1 g; mp  $251^\circ\text{C}$ .

**FT-IR:** (KBr 4000-600  $\text{cm}^{-1}$ ): 3473(s), 3223 (w), 2951(w), 2848(w), 2031(m), 1715(s), 1609(m), 1507(s), 1398(w), 1287(s), 1228(m), 1137(s), 1054(s), 1019(m), 877(m), 672(s), 654(m), 530(m), 496(m).

#### Synthesis of 5-Triazole Isophthalic Acid:

Refluxing a mixture of N, N'-dimethylformamide azine dihydrochloride (4.0 g, 1.866 mmol) and 5-amino isophthalic acid (3.38 g, 1.866 mmol) in 50 mL benzene (Benzene is *carcinogenic*; reaction should be conducted in a fume hood) for 8h gave whitish solid. The solid was filtered and washed with ethanol (2 × 15 mL) and Diethyl ether (1 × 17 mL); yield: 2.38 g (68%).

**FT-IR:** (KBr 4000-600  $\text{cm}^{-1}$ ): 3119(m), 2906 (w), 2552(w), 1699(s), 1519(s), 1448(m), 1268(m), 11224(m), 1143(m), 1095(s), 889(m), 755(s), 665(s).

#### 4.4.3 Synthesis of In-5TIA and Cd-5TIA:

**In-5TIA [ $\text{In}(\text{C}_{10}\text{O}_4\text{N}_3\text{H}_5)_2(\text{C}_2\text{H}_8\text{N})(\text{H}_2\text{O})$ ]:** 0.25 mmol of 5-TIA (0.058 g) and 0.06 mmol of  $\text{In}(\text{NO}_3)_3 \cdot 3\text{H}_2\text{O}$  (0.023 g) was taken in a 15 mL scintillation vial. A mixture of 2.5 mL of N,N'-diethylformamide (DEF) and 1 mL of DMF was added and sonicated for 30 minutes, then transferred to a pre-heated oven at 120 °C for 96 hours. Rod shaped crystals of In-5TIA ( $\text{C}_{20}\text{H}_6\text{InN}_6\text{O}_8$ ) was filtered, washed repeatedly with DMF and ethanol and air dried for 20 mins (yield~ 37%).

**FT-IR:** (KBr 4000-600  $\text{cm}^{-1}$ ): 3122(w), 2736(w, br), 1571(s), 1469(w), 1362(s), 1252(m), 188(s), 1054(m), 1019(w), 869(s, br), 779 (s), 732 (s), 636 (m)  $\text{cm}^{-1}$ .

**Elemental analysis (%)** calcd: C=41.25, H=3.12, N=15.30; found: C= 41.17, H=2.28, N=15.12

**Cd-5TIA [ $\text{Cd}(\text{C}_{10}\text{O}_4\text{N}_3\text{H}_5)_2(\text{C}_2\text{H}_8\text{N})_2(\text{H}_2\text{O})$ ]:** 3.0 mL of 5-TIA (0.20M) solution in N,N'-dimethylformamide (DMF) was taken in a 5 mL culture tube 0.5 mL of  $\text{Cd}(\text{NO}_3)_2 \cdot 4\text{H}_2\text{O}$  solution (0.20 M) in DMF was added to this solution. The culture tube was capped and heated to 120 °C for 96 h. The mother liquor was decanted and the rod like colorless crystals were filtered off, washed with DMF. The unreacted ligand can be removed by washing in DMF (3 mL, 4 times) as 5-TIA is highly soluble in DMF and afterwards

resulting MOF was dried in air (10 min). [Yield: 70%, 0.0130 g depending on  $\text{Cd}(\text{NO}_3)_2 \cdot 4\text{H}_2\text{O}$ ].

**FT-IR:** (KBr 4000-600  $\text{cm}^{-1}$ ): 1568(s), 1472(w), 1368(s), 1246(m), 1164(w), 1109(s), 1047(m), 1013(w), 869(br), 793(s), 732(s), 650 (m)  $\text{cm}^{-1}$ .

**Element analysis (%)** calcd: C= 42.10, H= 4.1, N= 16.37; Found: C= 42.34, H= 3.91, N= 16.11.

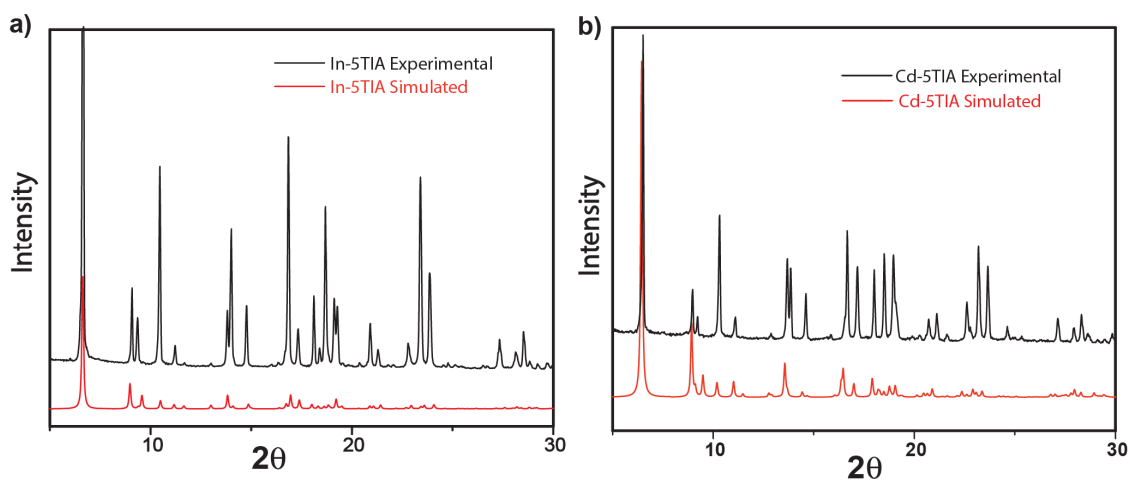


**Figure 4.12:** Comparison of the experimental PXRD pattern of as-synthesized (a) In-5TIA (top) and (b) Cd-5TIA (top) with the one simulated from its single crystal structure (bottom).

#### 4.4.4 General methods for characterization:

**(a) Powder X-Ray Diffraction (PXRD):** The PXRD patterns were collected on a Phillips PANalytical diffractometer on a  $\text{Cu K}\alpha$  radiation ( $\lambda = 1.5406 \text{ \AA}$ ), with a scan speed of  $2^\circ \text{ min}^{-1}$ . The tube voltage and amperage were set at 40 kV and 50 mA respectively. Each sample was scanned between  $5$  and  $50^\circ 2\theta$  with a step size of  $0.02^\circ$ . The instrument was previously calibrated using a silicon standard.

**(b) Thermogravimetric Analysis (TGA):** TGA was performed on a SDT Q600 TG-DTA analyzer instrument. Approximately 5 mg of the sample was added to an aluminium crucible and heated from  $25$  to  $800^\circ \text{C}$  under  $\text{N}_2$  atmosphere at a heating rate of  $10^\circ \text{C min}^{-1}$ .

**(c) Hot-Stage Microscopy:** Leica M-80 optical microscope with hot stage and camera attachment was used for collecting photographs.

**(d) IR Spectroscopy:** The Fourier transform (FT) infrared spectra of the MOFs were taken on a *PERKIN ELMER FT-IR SPECTRUM* (Nicolet) spectrometer. KBr samples (2 mg in 20 mg of KBr) were prepared and 10 scans were collected at  $4\text{ cm}^{-1}$  resolution for each sample. The spectra were measured over the range of  $4000\text{-}400\text{ cm}^{-1}$

**(e) Proton Conductivity:** Proton conductivity data were measured in a quasi-two-probe method, with a Solartron 1287 Electrochemical Interface with frequency response analyzer.

**(f) Water Adsorption:** All low-pressure water adsorption experiments (up to 1 bar) were performed on a BELSORP-max volumetric instrument. Approximately 50 mg of the sample was activated after solvent exchange by the use of activation chamber. The activated sample was loaded inside the glass bulb of water adsorption instrument and measured the capacity.

#### 4.4.5 X-ray Crystallography:

##### 4.4.5.1 General Data Collection and Refinement Procedures:

Single crystal data were collected on Bruker SMART APEX three circle diffractometer equipped with a CCD area detector and operated at 1500 W power (50 kV, 30 mA) to generate Mo  $K_{\alpha}$  radiation ( $\lambda=0.71073\text{ \AA}$ ). The incident X-ray beam was focused and monochromated using Bruker Excalibur Gobel mirror optics. Crystals of all MOFs reported in the paper was mounted on nylon CryoLoop (Hampton Research) with Paraton-N (Hampton Research). Initial scans of each specimen were performed to obtain preliminary unit cell parameters and to assess the mosaicity (breadth of spots between frames) of the crystal to select the required frame width for data collection. In every case frame widths of  $0.5^{\circ}$  were judged to be appropriate and full hemispheres of data were collected using the *Bruker SMART* [2.19] software suite. Following data collection, reflections were sampled from all regions of the Ewald sphere to redetermine unit cell parameters for data integration and to check for rotational twinning using *CELL\_NOW* [2.20]. In no data collection was evidence for crystal decay encountered. Following exhaustive review of the collected frames the resolution of the dataset was judged. Data were integrated using Bruker *SAINT* [2.21] software with a narrow frame algorithm and a 0.400 fractional lower limit of average intensity. Data were subsequently corrected for absorption by the program *SADABS* [2.22].

The space group determinations and tests for merohedral twinning were carried out using *XPREP*. In these cases, the highest possible space group was chosen.

Structures were solved by direct methods and refined using the *SHELXTL 97* [2.23] software suite. Atoms were located from iterative examination of difference F-maps following least squares refinements of the earlier models. Final model was refined anisotropically (if the number of data permitted) until full convergence was achieved. Hydrogen atoms were placed in calculated positions ( $C-H = 0.93 \text{ \AA}$ ) and included as riding atoms with isotropic displacement parameters 1.2-1.5 times  $U_{eq}$  of the attached C atoms. In some cases modeling of electron density within the voids of the frameworks did not lead to identification of recognizable solvent molecules in these structures, probably due to the highly disordered contents of the large pores in the frameworks. Highly porous crystals that contain solvent-filled pores often yield raw data where observed strong (high intensity) scattering becomes limited to  $\sim 1.0 \text{ \AA}$  at best, with higher resolution data present at low intensity. A common strategy for improving X-ray data, increasing the exposure time of the crystal to X-rays, did not improve the quality of the high angle data in these cases, as the intensity from low angle data saturated the detector and minimal improvement in the high angle data was achieved. Additionally, diffuse scattering from the highly disordered solvent within the void spaces of the framework and from the capillary to mount the crystal contributes to the background and the 'washing out' of the weaker data. The only optimal crystals suitable for analysis were generally small and weakly diffracting. Unfortunately, larger crystals, which would usually improve the quality of the data, presented a lowered degree of crystallinity and attempts to optimize the crystal growing conditions for large high-quality specimens have not yet been fruitful. Single Crystal X-ray Diffraction data for In-5TIA and Cd-5TIA was collected at 293(2) K. Electron density within void spaces has not been assigned to any guest entity but has been modeled as isolated oxygen and/or carbon atoms. The foremost errors in all the models are thought to lie in the assignment of guest electron density. Structures were examined using the *ADDSYM* subroutine of *PLATON* [2.24] to assure that no additional symmetry could be applied to the models. All ellipsoids in *ORTEP* diagrams are displayed at the 50% probability level unless noted otherwise. For these structures we noted that elevated R-values are commonly encountered

in MOF crystallography for the reasons expressed above by some research groups [2.25-2.35]. CCDC 845047- 845048.

#### 4.4.5.2 Experimental and Refinement Details for In-5TIA:

A colorless plate type crystal ( $0.20 \times 0.16 \times 0.10 \text{ mm}^3$ ) of In-5TIA was mounted on 0.7 mm diameter nylon CryoLoops (Hampton Research) with Paraton-N (Hampton Research). The loop was mounted on a *SMART APEX* three circle diffractometer equipped with a CCD area detector (Bruker Systems Inc., 1999a) and operated at 1500 W power (50 kV, 30 mA) to generate Mo  $K_{\alpha}$  radiation ( $\lambda=0.71073 \text{ \AA}$ ). The incident X-ray beam was focused and monochromated using Bruker Excalibur Gobel mirror optics. A total of 41933 reflections were collected of which 8329 were unique and 6118 of these were greater than  $2\sigma(I)$ . The range of  $\theta$  was from 3.69 to 28.09°. Analysis of the data showed negligible decay during collection. The structure was solved in the tetragonal  $P4/n$  space group, with  $Z = 8$ , using direct methods. Atoms C10, C19, C20, N4, N5 and N6 were refined isotropically. All other non-hydrogen atoms were refined anisotropically. Modeling of electron density within the voids of the frameworks did not lead to identification of solvent molecules in all structures due to the lowered resolution of the data. The attempts made to model the solvent molecules did not lead to identification it in all structures due to the limited periodicity of the solvent molecules in the crystals. Since the solvent is free in the framework this can be expected for the MOF structures. However, very high displacement parameters, high esd's and partial occupancy due to the disorder make it impossible to determine accurate positions for these solvent molecules. Thus, electron density within void spaces which could not be assigned to any definite guest entity was modeled as isolated carbon and oxygen atoms, and the foremost errors in all the models lies with assignment of guest electron density. To prove the correctness of the atomic positions in the framework the application of the SQUEEZE routine of A. Spek has been performed. The unit cell of In-5TIA SQUEEZE structure contains 2 units of 5TIA and one Indium ion. Final full matrix least-squares refinement on  $F^2$  converged to  $R_1 = 0.0778$  ( $F > 2\sigma F$ ) and  $wR_2 = 0.2224$  (all data) with GOF = 1.099. It should be noted that other supporting characterization data (CHN, EDAX) are consistent with the crystal structure. CCDC 845048.

#### 4.4.5.3 Experimental and Refinement Details for Cd-5TIA:

A pink plate type crystal ( $0.24 \times 0.15 \times 0.12 \text{ mm}^3$ ) of Cd-5TIA was mounted on 0.7 mm diameter nylon CryoLoops (Hampton Research) with Paraton-N (Hampton Research). The loop was mounted on a *SMART APEX* three circle diffractometer equipped with a CCD area detector (Bruker Systems Inc., 1999a) and operated at 1500 W power (50 kV, 30 mA) to generate Mo  $K_\alpha$  radiation ( $\lambda=0.71073 \text{ \AA}$ ). The incident X-ray beam was focused and monochromated using Bruker Excalibur Gobel mirror optics. A total of 35539 reflections were collected of which 8874 were unique and 5876 of these were greater than  $2\sigma(I)$ . The range of  $\theta$  was from 3.61 to 28.11°. Analysis of the data showed negligible decay during collection. The structure was solved in the tetragonal  $P4/n$  space group, with  $Z = 8$ , using direct methods. All other non-hydrogen atoms were refined anisotropically. Modeling of electron density within the voids of the frameworks did not lead to identification of solvent molecules in all structures due to the lowered resolution of the data. The attempts made to model the solvent molecules did not lead to identification it in all structures due to the limited periodicity of the solvent molecules in the crystals. Since the solvent is free in the framework this can be expected for the MOF structures. However, very high displacement parameters, high esd's and partial occupancy due to the disorder make it impossible to determine accurate positions for these solvent molecules. Thus, electron density within void spaces which could not be assigned to any definite guest entity was modeled as isolated carbon and oxygen atoms, and the foremost errors in all the models lies with assignment of guest electron density. To prove the correctness of the atomic positions in the framework the application of the SQUEEZE routine of A. Spek has been performed. The unit cell of Cd-5TIA contains 2 units of 5-TIA and per Cadmium ion. Final full matrix least-squares refinement on  $F^2$  converged to  $R_1 = 0.0927$  ( $F > 2\sigma F$ ) and  $wR_2 = 0.2739$  (all data) with GOF = 1.088. It should be noted that other supporting characterization data (CHN, EDAX) are consistent with the SQUEEZE crystal structure. CCDC 845047.



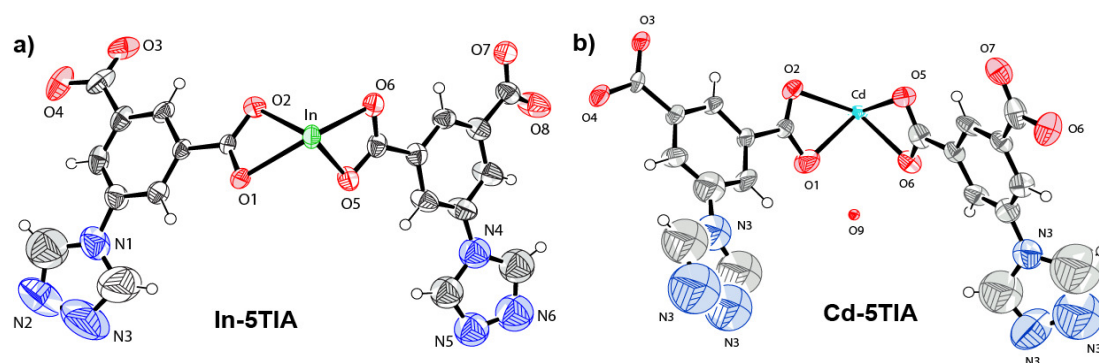


**Figure 4.13:** ORTEP diagram of the asymmetric unit of (a) In-5TIA and (b) Cd-5TIA.

**NOTE:** The results of this chapter have already been published in *Chem. Commun.*, 2012, **48**, 5464-5466 with the title: “Self-assembled one dimensional functionalized metal organic nanotubes (MONTs) for proton conduction.” These publications were the results from the group of Dr. Rahul Banerjee and his students Tamas Panda and Tanay Kundu from CSIR National Chemical Laboratory, Pune, India. Major works are contributed by Tamas Panda with the help of Tanay Kundu and instrumental facilities of CSIR National Chemical Laboratory.

## CHAPTER 5

---

# STRUCTURAL ISOMERISM LEADING TO ANHYDROUS PROTON CONDUCTIVITY IN INDIUM (III) ISOPHTHALIC ACID BASED FRAMEWORKS

---

### 5.1 Introduction:

As discussed in earlier chapters and section 1.6.3, most of the proton conducting MOFs reported in literatures works at low temperatures under hydrous conditions. It is interesting to note that, despite the disadvantages (high cost, lack of performance at high temperature etc.), nafion [5.1] is still the most extensively used commercial proton conducting material under fuel cells. However, it is necessary to develop an anhydrous proton-conductor capable of perform in an intermediate temperature region (100 °C to 200 °C) which is important in fuel cell [1.40]. Since water molecules cannot be used as a proton carrier, hence the synthesis of an anhydrous materials proton conductor is much more difficult. It has been observed that, organic heterocycles like imidazolium (pKa: 6.9) and pyrazolium (pKa: 2.6) have been proposed as proton transfer agents due to their fast proton transfer behaviour and amphiprotic nature, analogous to that of water. Few attempts such as incorporation of heterocycles (imidazole, triazole, histamine) inside the confined channels of MOFs have been implemented for anhydrous proton conduction. However, inherent anhydrous proton conduction inside the MOF architectures without doping any other heterocycles is extremely rare. Moreover, it is clear that, the development of new anhydrous proton-conducting MOFs is still in infancy. Therefore, more fundamental research is necessary to understand the issues of anhydrous proton conduction in MOFs. In our previous attempts, we found that, In(III), Cd(II) and triazole functionalized metal organic nanotubular (MONT) architectures (In-5TIA and Cd-5TIA MONTs) shows proton conduction under hydrous condition [5.2]. However, detailed structural investigation of these MONTs show that trapped  $[(\text{CH}_3)_2\text{NH}_2]^+$  cations acts as a trigger for hydrous proton conduction. We thought that, instead of using triazole functionalized isophthalic acid

(5TIA) as organic linker, if we use only isophthalic acid that might enhance the proton conduction among the resulting MOFs due to less steric hindrance. In this regard, we present two In(III) based isomeric MOFs (In-IA-2D-1 and -2), synthesized by using isophthalic acid (IA) as the organic linker under solvothermal condition (Figure 5.1). These In(III) isophthalate based MOFs adopt two dimensional architecture and exhibit proton conductivity. Proton conductivity shown by In-IA-2D-1 and -2 are  $3.4 \times 10^{-3}$  and  $4.2 \times 10^{-4}$   $\text{Scm}^{-1}$  at 27 °C with 98% RH respectively. Interestingly, In-IA-2D-2 shows proton conductivity in anhydrous conditions [ $2.6 \times 10^{-5}$   $\text{Scm}^{-1}$  at 25 °C and  $1.18 \times 10^{-5}$   $\text{Scm}^{-1}$  at 90 °C] as well. Moreover, proton conductivity of In-IA-2D-1 ( $3.4 \times 10^{-3}$   $\text{Scm}^{-1}$  at ambient temperature and 98% RH) stands at high position among the proton conducting MOFs reported in the literature.

## 5.2 Result and Discussion:

### 5.2.1 Structural analysis of In-IA-2D-1 and In-IA-2D-2

In (III) carboxylate based MOFs have well known tendency to create anionic frameworks. [5.3] In order to neutralize these anionic structures different types of cations get trapped inside the system. In our previous work, we have observed that anionic In(III)-5 triazole isophthalic acid (In-5TIA) based MOFs have been neutralized by  $[(\text{CH}_3)_2\text{NH}_2]^+$  cations inside the framework. [5.2] These  $[(\text{CH}_3)_2\text{NH}_2]^+$  cations act as a proton carrier and favour proton conductivity at 98% RH. Like 5TIA, isophthalic acid (IA) also forms anionic frameworks with In(III) metal. However, only one In-IA based MOF, In-IA-1D, that contains  $[(\text{CH}_3)_2\text{NH}_2]^+$  cations inside the porous framework, has been reported in the literature. In-IA-1D adopts one dimensional hydrogen bonded channel structure, [5.4] and can conduct protons due to the presence of  $[(\text{CH}_3)_2\text{NH}_2]^+$  cations inside the framework. [5.2] However,  $[(\text{CH}_3)_2\text{NH}_2]^+$  cations, in In-IA-1D, are located within the void between the channels and have very limited freedom to facilitate the proton transport. Hence, we decided to investigate whether the ease of carrier ion mobility {in this case  $[(\text{CH}_3)_2\text{NH}_2]^+$ }, as well as openness of the framework can enhance the proton conductivity in In(III)-IA based MOFs. In order to achieve this, we attempted to synthesize the 2D and 3D isomers of In-IA based MOFs containing  $[(\text{CH}_3)_2\text{NH}_2]^+$  cations. However, we could only synthesize two 2D isomers [In-IA-2D-1 and -2] for which we measured the proton conductivity.

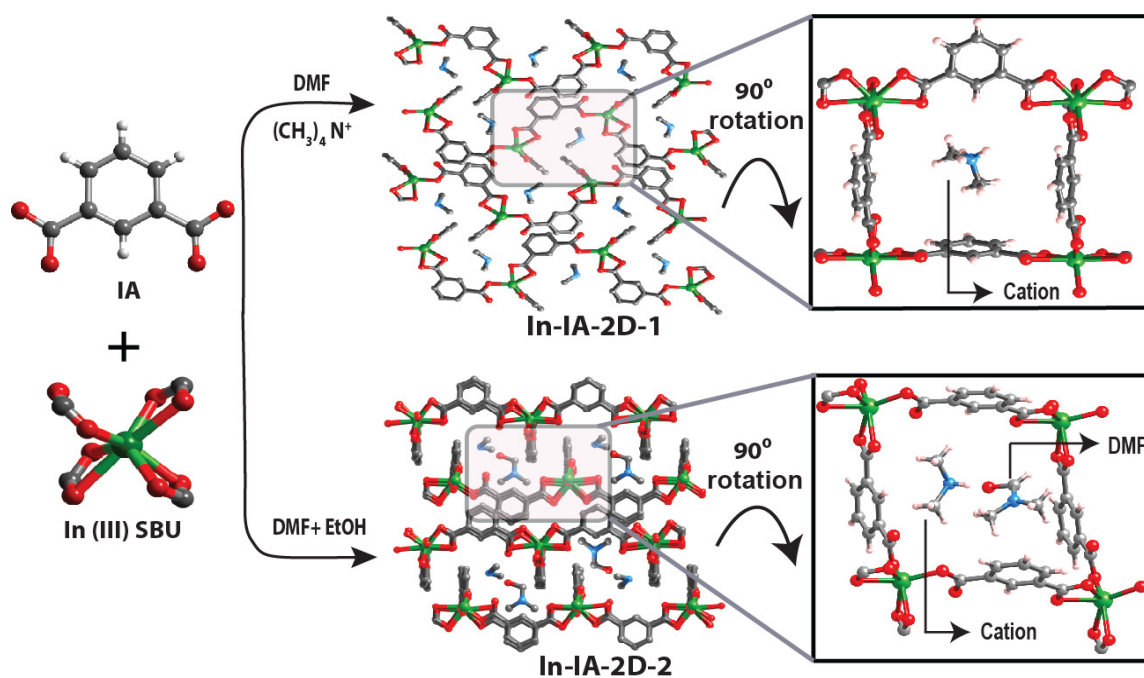


**Figure 5.1.** Schematic representation of isophthalic acid (IA) moiety and In(III)(CO<sub>2</sub><sup>-</sup>)<sub>4</sub> SBU. Two dimensional (2D) structure of In-IA-2D-1 and -2, indicating [(CH<sub>3</sub>)<sub>2</sub>NH<sub>2</sub>]<sup>+</sup> cations inside In-IA-2D-1 framework, and [(CH<sub>3</sub>)<sub>2</sub>NH<sub>2</sub>]<sup>+</sup> cations as well as DMF molecules inside the In-IA-2D-2 framework. (Note: Zoomed in figures have been rotated 90° for clarity).

In the crystal structure of In-IA-2D-1 and -2 have similar secondary building units (SBU). Each In (III) centre in In-IA-2D-1 and -2 is coordinated to seven oxygen atoms from four carboxylate functionalities to form a tetrahedral In(III) SBU (Figure 5.1). Detailed structural investigation of In-IA-2D-1 and -2 reveals that, one In(III) metal center with tri-positive [+3] charge is coordinated to six  $\mu_1^c$ -CO<sub>2</sub><sup>-</sup> [-3] and one  $\mu_1^t$ -CO<sub>2</sub><sup>-</sup> [-1] oxygens from four IA links, thus creating an extra negative charge [-1] associated with each In(III) metal center. This extra negative charge is neutralized by one [(CH<sub>3</sub>)<sub>2</sub>NH<sub>2</sub>]<sup>+</sup> cation per In(III) metal center inside these frameworks. In-IA-2D-1 contains guest H<sub>2</sub>O and [(CH<sub>3</sub>)<sub>2</sub>NH<sub>2</sub>]<sup>+</sup> cations, whereas In-IA-2D-2 contains [(CH<sub>3</sub>)<sub>2</sub>NH<sub>2</sub>]<sup>+</sup> cations and solvent (DMF) molecules inside the framework (Figure 5.2). In the extended structure of In-IA-2D-1 and -2, In(III) SBUs are connected to each other *via* IA linkers to form a 1D coordination network along the *a* axis. Adjacent one dimensional network in In-IA-2D-1 are bridged *via* IA moieties to form a 2D layer structure along the crystallographic *ab* plane. Similar 2D layer structures have been observed along the *bc* plane in In-IA-2D-2. These two dimensional layers in In-IA-2D-1 and -2 prefer to interdigitate. Interestingly, this interdigitation creates  $\pi$ - $\pi$

stacking among the phenyl rings of isophthalic acid moieties of adjacent 2D layer in In-IA-2D-2 (Figure 5.1). Similar  $\pi$ - $\pi$  stacking has not been observed in In-IA-2D-1 despite the high degree of interdigitation. Moreover, in In-IA-2D-2, the coordination of the carboxylate functionality to the In(III) metal is *cisoid* on either sides of the In (III) SBU but in In-IA-2D-1 the coordination of the carboxylate functionality to the In(III) metal is *transoid* on one side and *cisoid* on other side of the In(III) SBU (Figure 5.2).

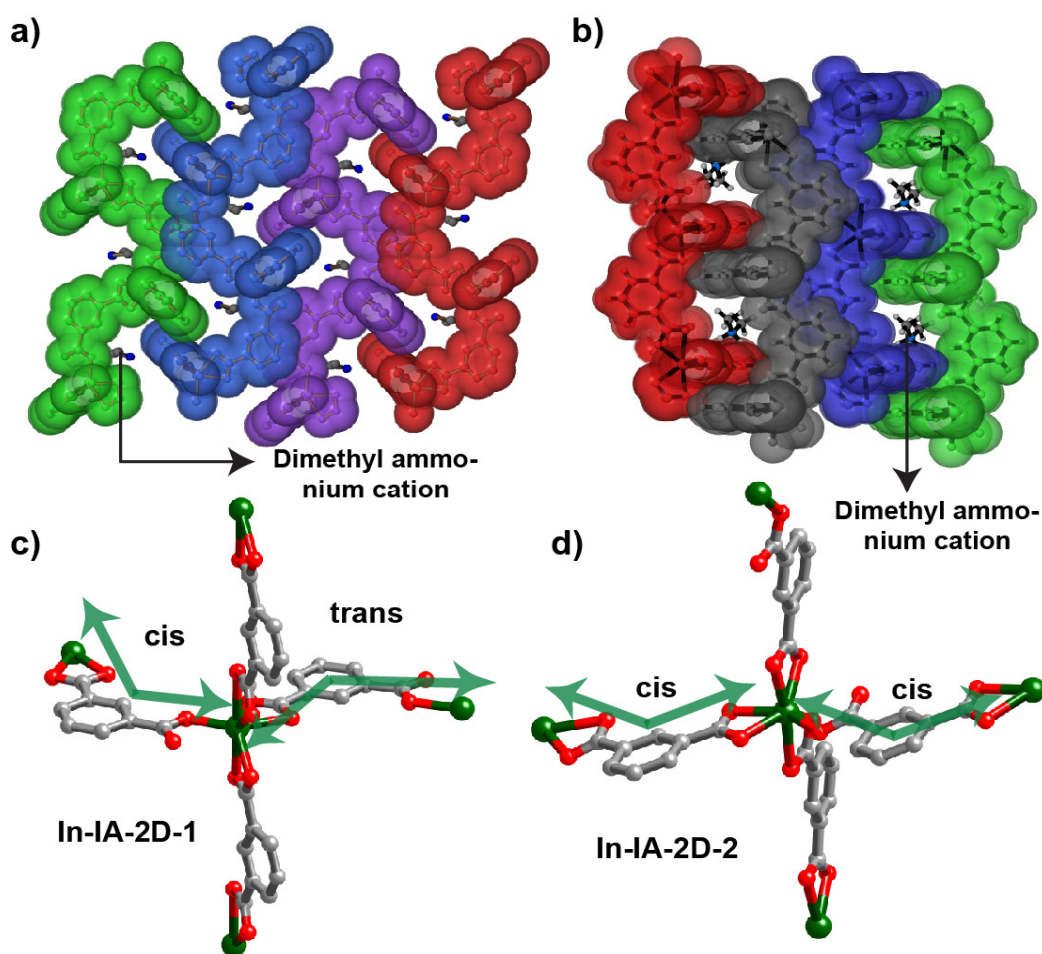


**Figure 5.2.** Three dimensional packing orientations of (a) In-IA-2D-1 and (b) In-IA-2D-2 MOFs. Each 2D layer clarified by different color. (c) and (d) structural difference of In-IA-2D-1 and -2.

### 5.2.2 Thermal properties and X-ray powder diffraction analysis:

TGA performed on as-synthesized In-IA-2D-1 and -2 MOFs revealed that these compounds have high thermal stability. TGA trace for as synthesized In-IA-2D-1 and -2 MOF show a stepwise weight-loss of 3% (30–200 °C) and 4% (30–105 °C) respectively, correspond to

escape of guest molecules from the lattice (Figure 5.3d). For In-IA-2D-1 we observed a flat plateau from 200–370 °C which confirms the stability of the framework. A sharp weight loss in the range of 370–440 °C for In-IA-2D-1 is probably due to the decomposition of the framework.

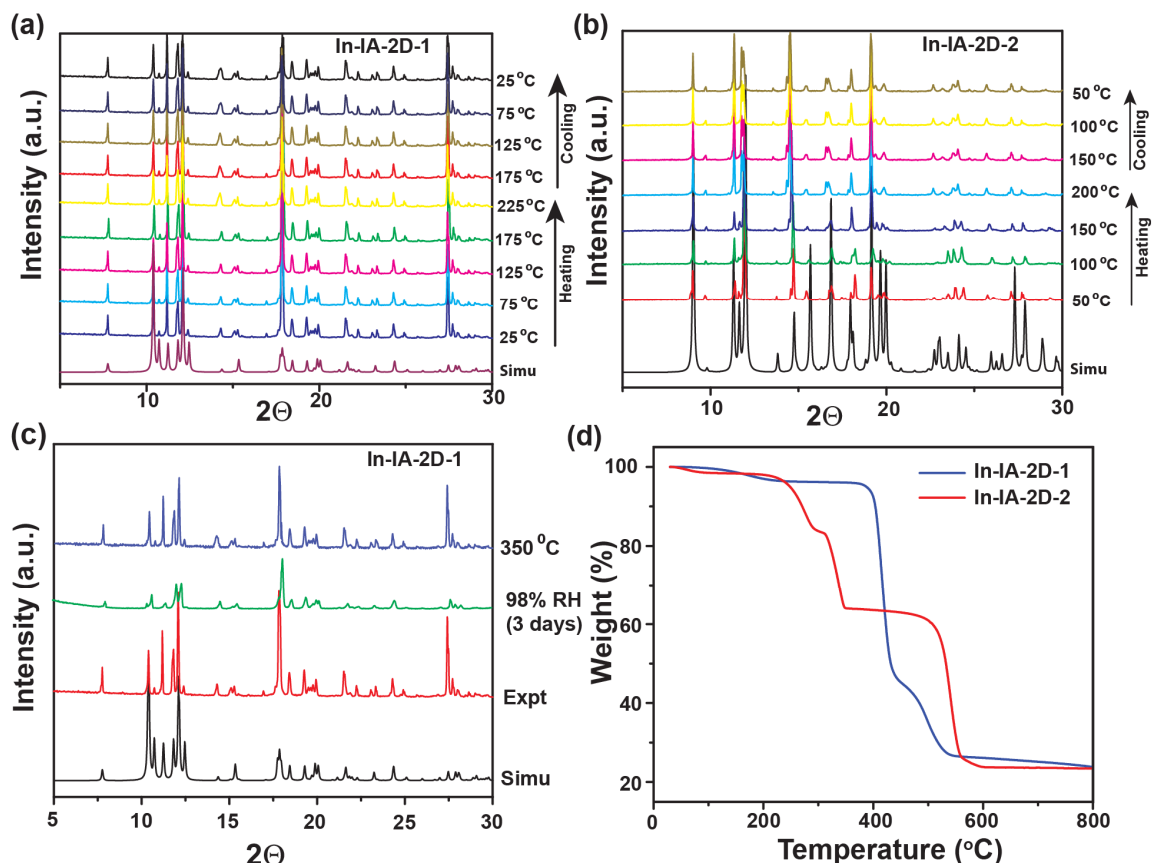


**Figure 5.3.** Variable temperature powder X-ray diffraction (VTPXRD) data of (a) In-IA-2D-1 and (b) In-IA-2D-2 comparison with the simulated one clearly indicates its high crystallinity as well as thermal stability at broad temperature range (25 °C to 200 °C). (c) PXRD analysis of as synthesized (Expt), humidified (under 98% RH for 3 days) and preheated at 350 °C of In-IA-2D-1 in comparison with the simulated (d) Thermal gravimetric analysis (TGA) data of In-IA-2D-1 and In-IA-2D-2.

For In-IA-2D-2, on the other hand, a sharp weight loss has been observed from 220–350 °C due to the loss of  $[(\text{CH}_3)_2\text{NH}_2]^+$  cations. To prove this phenomenon, we have performed the elemental analysis (CHN) of preheated (350 °C) In-IA-2D-2 samples. The % of elements found: C (44.08%), H (1.85%), N (0.01%), confirms the absence of N atoms in preheated (350 °C) In-IA-2D-2 samples. Hence, it matches with the molecular formula of  $\{\text{In}(\text{IA})_2$



$\text{H}^+$ ] [ Calc: C (43.35%), H (1.89%), N (0%)] indicates the absence of  $[(\text{CH}_3)_2\text{NH}_2]^+$  cations from the framework. After that, a stable framework of In-IA-2D-2 is obtained at higher temperature (350–460 °C) followed by sharp weight loss (460–600 °C) due to the decomposition of the framework. *In Situ* VTPXRD performed on as-synthesized In-IA-2D-1 and -2 (from 25 °C to 200 °C) further confirms their stability and crystallinity at elevated temperatures (Figure 5.3a and 5.3b).

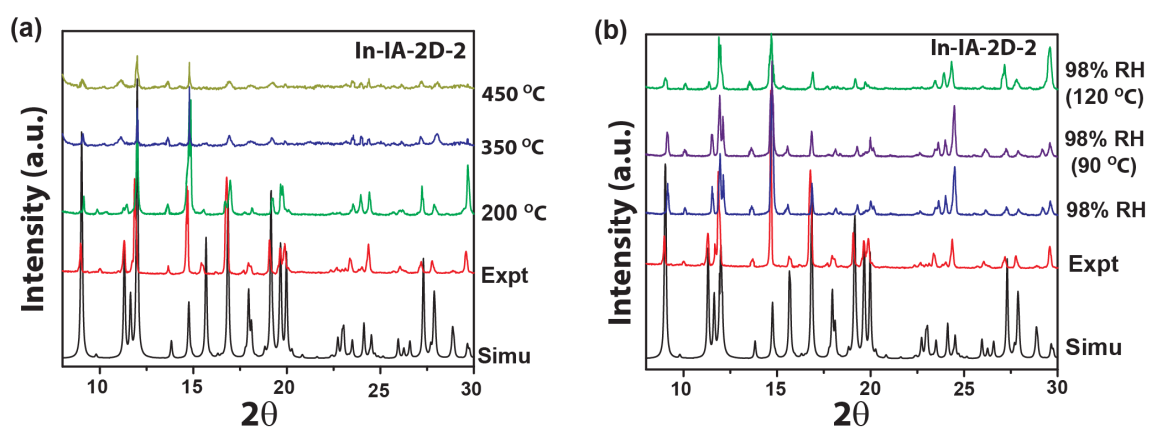


**Figure 5.4.** Powder X-ray diffraction analysis of (a) as synthesized (Expt) and pre heated (200 °C and 350 °C) samples of In-IA-2D-2 in comparison with the simulated one and (b) In-IA-2D-2 as synthesized (Expt), 98% Relative humidified condition and 98% RH then heated to 90 °C and 120 °C of In-Ia 2D-2. All these case it is clearly indicates its high crystallinity, purity as well as stability at long time humidified condition.

The architectural stability of In-IA-2D-1 and -2 at very high temperature has been confirmed by PXRD pattern agreement between simulated and preheated In-IA-2D-1 and -2 crystals at 350 °C and 450 °C respectively (Figure 5.3c and 5.4a). We have also collected the *in situ* variable temperature single crystal X ray diffraction (VTSCXRD) data of In-IA-2D-2 at different temperatures (35 °C, 55 °C, 65 °C, 75 °C, 85 °C and 95 °C) to monitor the mobility of the solvent DMF molecules at higher temperature (Figure 5.19). VTSCXRD data of In-IA-2D-2 reveals that, after 90 °C, the electron density of the DMF molecules decrease significantly, which indicates the loss of DMF molecules from the lattice. This phenomenon correlates with the TGA data (discussed earlier) as well as anhydrous proton conductivity data (discussed later) of In-IA-2D-2 (Figure 5.12). To prove the higher temperature stability we took three batches of In-IA-2D-2 samples and separately heated

200 °C, 350 °C and 450 °C in a furnace for 2 hours followed by cooling up to room temperature. PXRD pattern of these three samples indicates its crystallinity and framework stability at higher temperatures (Figure 5.4). It is also clear that after removal of  $[(\text{CH}_3)_2\text{NH}_2]^+$  cations at 450 °C, the parent framework of In-IA-2D-2 is quite stable.

### 5.2.3 Proton Conductivity

#### 5.2.3.1 Methods and plots:

Proton conductivity was measured in Solartron instrument. As synthesized samples of In-IA-2D-1 and -2 were pelletized of 0.6 mm and 1.25 mm thickness, with 6.5 mm diameter under humidified condition for 24 hours and then subject to analysis for proton conduction. The resistances were calculated from the semicircle of the Nyquist plots. The activation energy values were obtained from the slope by least square fitting of the straight line. If the data points are  $(x_1, y_1)$ ,  $(x_2, y_2)$ , .....,  $(x_n, y_n)$  where  $x$  is the independent variable and  $y$  is the dependent variable. The fitting curve  $f(x)$  has the deviation (error)  $d$  from each data point, i.e.,  $d_1 = y_1 - f(x_1)$ ,  $d_2 = y_2 - f(x_2)$ , ...,  $d_n = y_n - f(x_n)$ . According to the method of least squares, the best fitting curve has the properties:

$$\Pi = d_1^2 + d_2^2 + \dots + d_n^2 = \sum_{i=1}^n d_i^2 = \sum_{i=1}^n [y_i - f(x_i)]^2 = \text{a minimum}$$

**N.B.** From the semicircle we got the resistance  $R$  (Ohm). Now, from diameter  $r$  (mm) and thickness  $A$  (mm) proton conductivity ( $\sigma$ ) value can be calculated by the following equation,

$$\sigma = A / (R \times \pi r^2) \text{ Scm}^{-1}$$

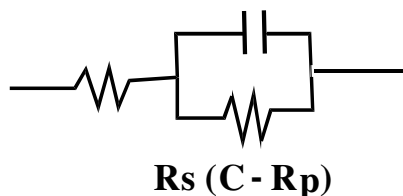


**Figure 5.5.** Equivalent circuit model representation of the Nyquist plot.



For high-temperature proton conductivity measurements, the pellets were inserted within a humidification chamber, which was encircled with a controlled heating coil attached with an automated temperature controller. The heat flow within the temperature controller was controlled by a dimerstat accordingly. The temperature of the chamber was measured by an infrared temperature sensor attachment, having a sensing accuracy of  $\pm 0.5$  °C. The pellets were inserted within a humidification chamber for low-temperature proton conductivity measurements which was encircled with a water circulation coil attached with a chiller integrated with an automated temperature controller. The heat flow within the chamber was controlled by the chiller accordingly. The temperature of the chamber was measured by an infrared temperature sensor attachment, having a sensing accuracy of  $\pm 0.5$  °C.

### 5.2.3.2 Proton Conductivity Measurements of In-IA-2D-1 and -2:

In our previous contribution [5.2], we observed that the  $[(\text{CH}_3)_2\text{NH}_2]^+$  cation based In-IA-1D framework can conduct protons under 98% RH [ $2.2 \times 10^{-4} \text{ Scm}^{-1}$ ].

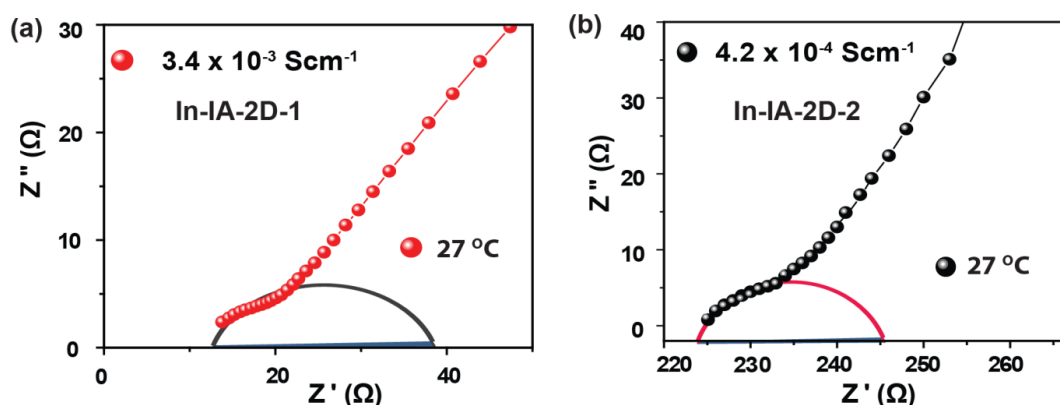


**Figure 5.6.** (a) Nyquist plot of In-IA-2D-1 at 27 °C in 98% RH (b) Nyquist plot of In-IA-2D-2 at 27 °C in 98% RH.

Since In-IA-2D-1 and -2 has carrier mediated  $[(\text{CH}_3)_2\text{NH}_2]^+$  cations inside the framework, we decided to study the proton conductivity of all these MOFs. Proton conductivity values measured for In-IA-2D-1 and -2 are  $3.4 \times 10^{-3}$  and  $4.2 \times 10^{-4} \text{ Scm}^{-1}$  respectively at ambient temperature (27 °C) with 98% RH. The conductivities were determined from the diameter of the pellet and resistance from the Nyquist plots, as shown in Figure 5.6. Proton conductivity values of these MOFs [In-IA-2D-1 and -2] are highly humidity dependent and dropped from  $3.5 \times 10^{-3}$  and  $4.2 \times 10^{-4} \text{ Scm}^{-1}$  (at 98% RH) to  $2.1 \times 10^{-5}$  and  $6.7 \times 10^{-5} \text{ Scm}^{-1}$

(at 60% RH), respectively at ambient temperature (Figure 5.7). The high temperature proton conductivity of these MOFs was also measured (Figure 5.8). In-IA-2D-1 shows proton conductivity till 65 °C [ $9.3 \times 10^{-6} \text{ Scm}^{-1}$ ] at 98% RH (Figure 5.8b and Table 5.2). In-IA-2D-2, on the other hand, shows proton conductivity up to 120 °C [ $1.6 \times 10^{-5} \text{ Scm}^{-1}$ ] under humidification

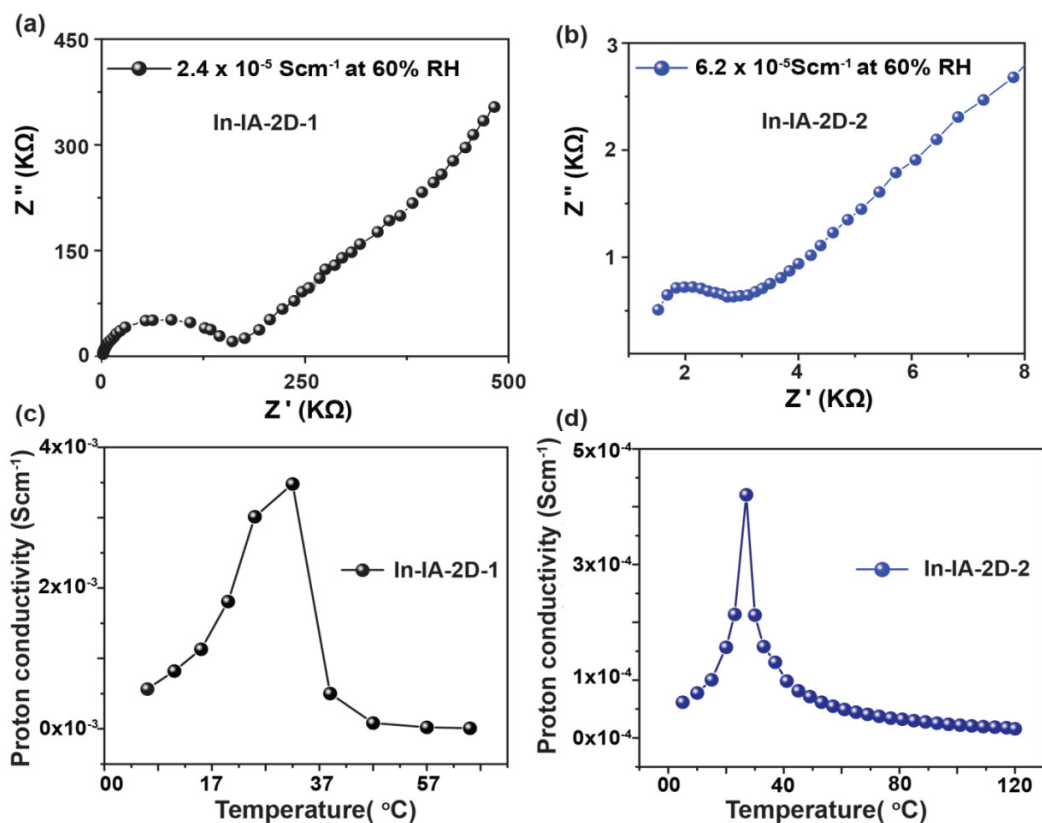


**Figure 5.7.** Proton conductivity plots at lesser humidity (60% RH) of (a) In-IA-2D-1 showing decrease in proton conductivity values  $2.4 \times 10^{-5} \text{ Scm}^{-1}$  and (b) In-IA-2D-2 showing decrease in proton conductivity values  $6.2 \times 10^{-5} \text{ Scm}^{-1}$ . Proton conductivity vs. temperature plots of (c) In-IA-2D-1 and (d) In-IA-2D-2 under 98% RH.

(Figure 5.8d and Table 5.2) which is a rare phenomenon among the proton conducting MOFs. TGA profile of In-IA-2D-2 signifies that the solvent DMF molecule leaves the framework at 90 °C. We assume that, at high temperature (>90 °C) and under humidified condition (98% RH) water molecules replace the DMF molecules due to the high water vapour pressure inside the humidification chamber and occupy the void space of In-IA-2D-2. This could be the possible reason for high temperature (120 °C) proton conductivity of In-IA-2D-2. For In-IA-2D-1 proton conductivity increases from 4 °C to 27 °C and then

decreases upto 65 °C. On the other hand, for In-IA-2D-2, proton conductivity value increases from 4 °C to 28 °C, and then decreases steadily upto 120 °C. The proton conductivity values of In-IA-2D-2 outperforms MIL-53 based MOFs ( $10^{-6}$ - $10^{-7}$   $\text{Scm}^{-1}$ ) [1.44a] and PCMOF-3 ( $3.5 \times 10^{-5}$   $\text{Scm}^{-1}$ ), [1.44b] whereas In-IA-2D-1 outperforms ferrous oxalate dihydrate ( $1.3 \times 10^{-3}$   $\text{Scm}^{-1}$ ) [1.44c] and cucurbituril ( $1.3 \times 10^{-3}$   $\text{Scm}^{-1}$ ) [1.44d], although it posses lower proton conductivity value than  $(\text{NH}_4)_2(\text{adp})[\text{Zn}_2(\text{ox})_3].3\text{H}_2\text{O}$  ( $8 \times 10^{-3}$   $\text{Scm}^{-1}$ ) [1.44e] at 25 °C and 98% RH (Table 5.3). High degree of resemblance of PXRD pattern between simulated and moisture treated In-IA-2D-1 and -2 MOFs confirms the stability of the framework at 98% RH even at high temperature (Figure 5.3c and 5.4b).

**Table 5.1:** Low temperatures proton conductivities of In-IA-2D-1 and -2 :

Serial no	In-IA-2D-1		In-IA-2D-2	
	Temperature (°C)	Proton conductivity value (98% RH) [ $\text{Scm}^{-1}$ ]	Temperature (°C)	Proton conductivity value (98% RH) [ $\text{Scm}^{-1}$ ]
1	5	$5.65 \times 10^{-4}$	5	$6.19 \times 10^{-5}$
2	10	$8.22 \times 10^{-4}$	10	$7.78 \times 10^{-5}$
3	15	$1.13 \times 10^{-3}$	15	$1.00 \times 10^{-4}$
4	20	$1.81 \times 10^{-3}$	20	$1.56 \times 10^{-4}$
5	25	$3.01 \times 10^{-3}$	23	$2.13 \times 10^{-4}$
6	27	$3.37 \times 10^{-3}$	27	$4.20 \times 10^{-4}$
7	32	$3.48 \times 10^{-3}$	30	$2.12 \times 10^{-4}$

**Table 5.2:** High temperatures proton conductivities of In-IA-2D-1 and -2 :

Sr. no	In-IA-2D-1		In-IA-2D-2	
	Temperature (°C)	Proton conductivity value (98% RH) [ $\text{Scm}^{-1}$ ]	Temperature (°C)	Proton conductivity value (98% RH) [ $\text{Scm}^{-1}$ ]
1	32	$3.48 \times 10^{-3}$	33	$1.58 \times 10^{-4}$
2	39	$5.02 \times 10^{-4}$	41	$9.8 \times 10^{-5}$
3	47	$8.3 \times 10^{-5}$	49	$7.16 \times 10^{-5}$
4	57	$2.13 \times 10^{-5}$	57	$5.49 \times 10^{-5}$
5	65	$9.33 \times 10^{-6}$	65	$4.46 \times 10^{-5}$
6	—	—	73	$3.73 \times 10^{-5}$
7	—	—	81	$3.24 \times 10^{-5}$
8	—	—	89	$2.77 \times 10^{-5}$

9	—	—	97	$2.38 \times 10^{-5}$
10	—	—	105	$2.08 \times 10^{-5}$
11	—	—	113	$1.87 \times 10^{-5}$
12	—	—	120	$1.59 \times 10^{-5}$

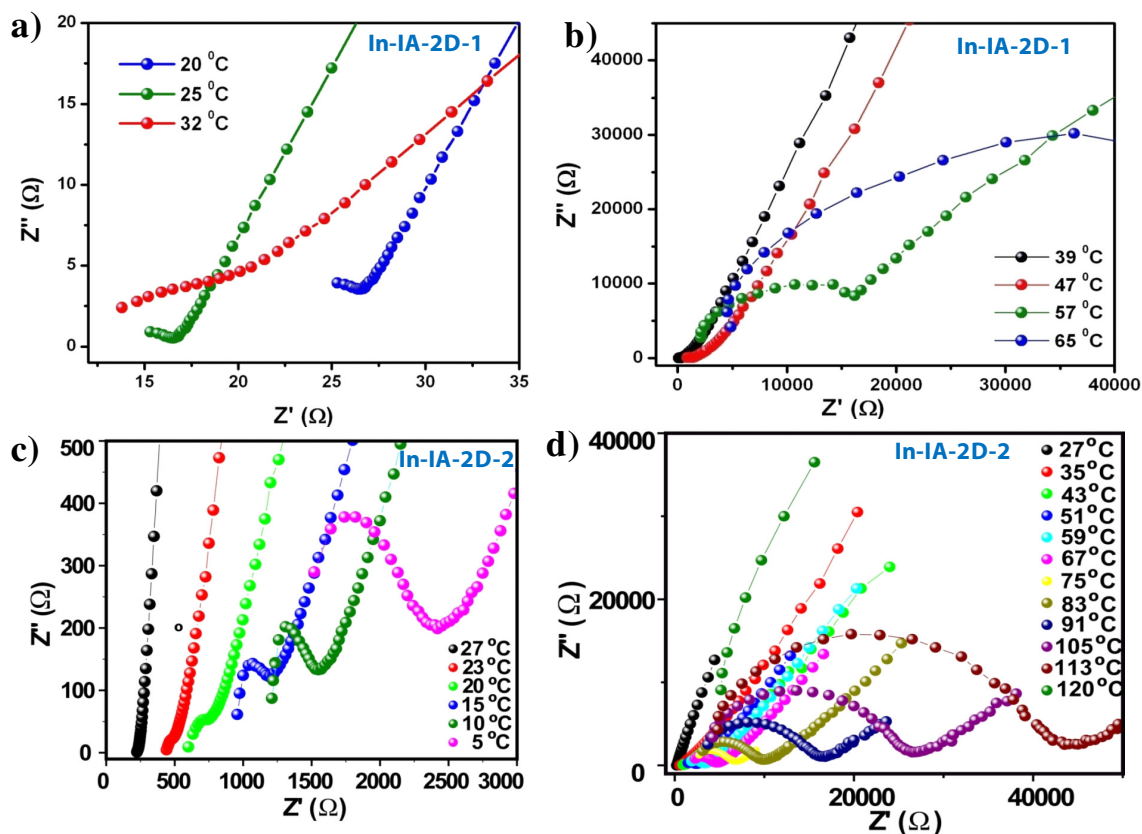


**Figure 5.8.** Proton conductivity plots of In-IA-2D-1 at (a) lower temperature and (b) higher temperature under 98% RH showing decrease in proton conductivity. Proton conductivity plots of In-IA-2D-2 at (c) lower temperatures and (d) elevated temperatures under 98% RH.

A possible reason behind these diverse proton conductivities among In-IA based MOFs could be found in the crystal structure. In In-IA-2D-1 framework, solvent H<sub>2</sub>O and [(CH<sub>3</sub>)<sub>2</sub>NH<sub>2</sub>]<sup>+</sup> cations together facilitate the proton conductivity under humidified condition. However, In-IA-2D-2 contains [(CH<sub>3</sub>)<sub>2</sub>NH<sub>2</sub>]<sup>+</sup> cations as well as DMF molecules inside the framework. Hence, approachability of water molecules to [(CH<sub>3</sub>)<sub>2</sub>NH<sub>2</sub>]<sup>+</sup> cations become restricted under humidified condition. As a result, In-IA-2D-2 shows less proton conductivity ( $4.2 \times 10^{-4} \text{ Scm}^{-1}$ ) than In-IA-2D-1 ( $3.4 \times 10^{-3} \text{ Scm}^{-1}$ ) at 27 °C under 98% RH despite of adopting a similar 2D network structure. To understand the role of [(CH<sub>3</sub>)<sub>2</sub>NH<sub>2</sub>]<sup>+</sup>

cations for conduction, we have performed humidified proton conductivity study on In-IA-2D-2 sample preheated at 350 °C. Sample of In-IA-2D-2 preheated at 350 °C does not show any proton conductivity (at 98% RH), presumably due to loss of carrier dimethyl ammonium cations leaving bare proton to the framework. Low temperature proton conductivity measurement reveals that activation energy of 0.61 and 0.48 eV for In-IA-2D-1 and -2, respectively under 98% RH (Figure 5.7). Hence, we assume that proton conduction of In-IA-2D-1 and -2 follow the Grotthuss mechanism along with some other process such as the direct diffusion of additional protons with water molecules or  $[(\text{CH}_3)_2\text{NH}_2]^+$  cations molecules (vehicle mechanism) [5.7].

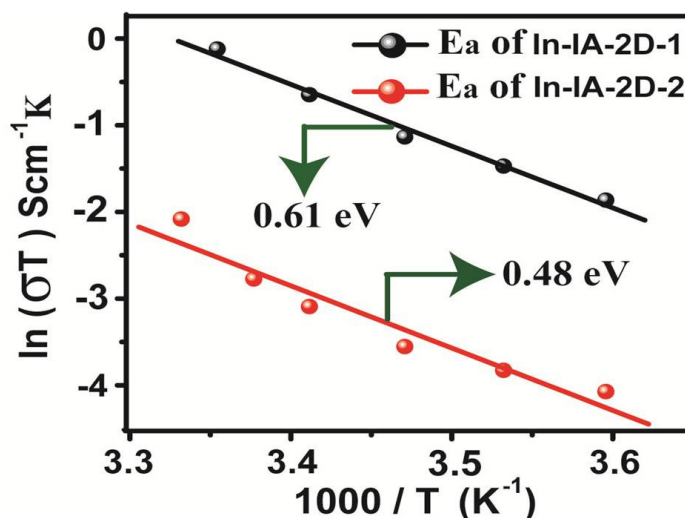


**Figure 5.9.** Arrhenius plot of activation energy (under 98% RH) for In-IA-2D-1 and -2 MOFs.

**Table 5.3:** Comparison of hydrous proton conductivity values of In-IA-2D-1 and In-IA-2D-2 with other proton conducting MOFs:

SL. No.	MOFs and CPs	Proton conductivity (Scm <sup>-1</sup> )	Ea (eV)	Conditions	Reference
1	(NH <sub>4</sub> ) <sub>2</sub> (adp)[Zn <sub>2</sub> (ox) <sub>3</sub> ]. 3H <sub>2</sub> O	8 × 10 <sup>-3</sup>	0.63	25 °C and 98% RH	4.4e
2	Cd-5TIA	3.6 × 10 <sup>-3</sup>	0.163	28 °C and 98% RH	5.6a
3	In-IA-2D-1	3.48 × 10 <sup>-3</sup>	0.61	32 °C and 98% RH	This report
4	1D Ferrous Oxalate Dihydrate	1.3 × 10 <sup>-3</sup>	0.37	25 °C and 98% RH	4.4c
5	(NH <sub>4</sub> ) <sub>4</sub> [MnCr <sub>2</sub> (ox) <sub>6</sub> ] <sub>3</sub> .4H <sub>2</sub> O.	1.1 × 10 <sup>-3</sup>	0.23	25 °C and 98% RH	4.4o
6	Cucurbit[6]uril (CB[6])	1.1 × 10 <sup>-3</sup>	0.39	25 °C and 98% RH	4.4d

7	( $\beta$ -PCMOF2(Tz) <sub>0.45</sub> )	$5 \times 10^{-4}$	0.51	150 °C	4.5b
8	In-IA-2D-2	$4.2 \times 10^{-4}$	0.48	32 °C and 98% RH	This report
9	Mg <sub>2</sub> (dobdc) <sub>3</sub> -0.35LiO <sub>i</sub> Pr <sub>3</sub> . 0.25LiBF <sub>4</sub> . EC3. DEC	$3.1 \times 10^{-4}$	0.14	27 °C	4.4p
10	{NH(prol) <sub>3</sub> }[MIIICrIII(ox) <sub>3</sub> ] (MII) =MnII, FeII, CoII)	$1 \times 10^{-4}$		25 °C and 75% RH	4.4n
11	(H <sub>3</sub> C <sub>2</sub> ) <sub>2</sub> (dtoa) Cu	$1 \times 10^{-4}$		25 °C and 80% RH	4.4i
12	In-5TIA	$5.35 \times 10^{-5}$	0.137	28 °C and 98% RH	5.6a
13	[Zn(l-L <sub>Cl</sub> )(Cl)](H <sub>2</sub> O) <sub>2</sub>	$4.45 \times 10^{-5}$	0.34	28 °C and 98% RH	4.4l
14	PCMOF-3	$3.5 \times 10^{-5}$	0.17	25 °C and 98% RH	4.4b
15	[MIL-53(Fe)-(COOH) <sub>2</sub> ]	$2.0 \times 10^{-6}$	0.21	25 °C and 98% RH	4.4a

### 5.2.3.3 Water adsorption study:

Since, In-IA-2D-1 and -2 shows proton conductivity under hydrous condition. Hence, it is necessary to evaluate the amount of water vapor adsorb for these materials at standard temperature 273K and 1 bar pressure (abbreviated as STP). In this manner, 110 mg of as synthesized In-IA-2D-1 has been taken and dried at room temperature upto 4 hours and treated for water adsorption. The uptake capability of In-IA-2D-1 are 2.9 wt% at

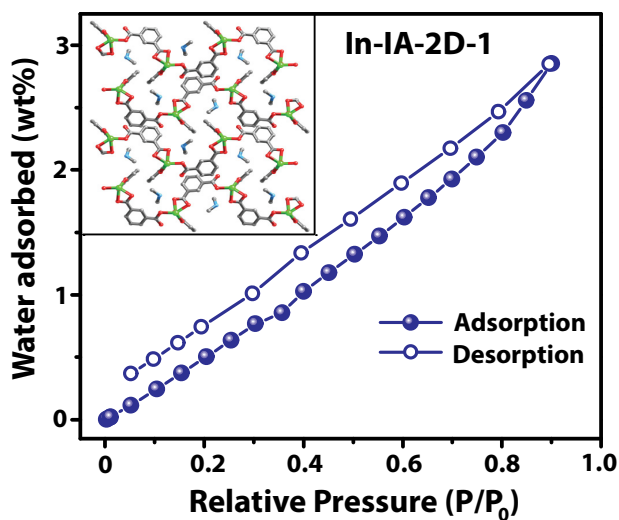
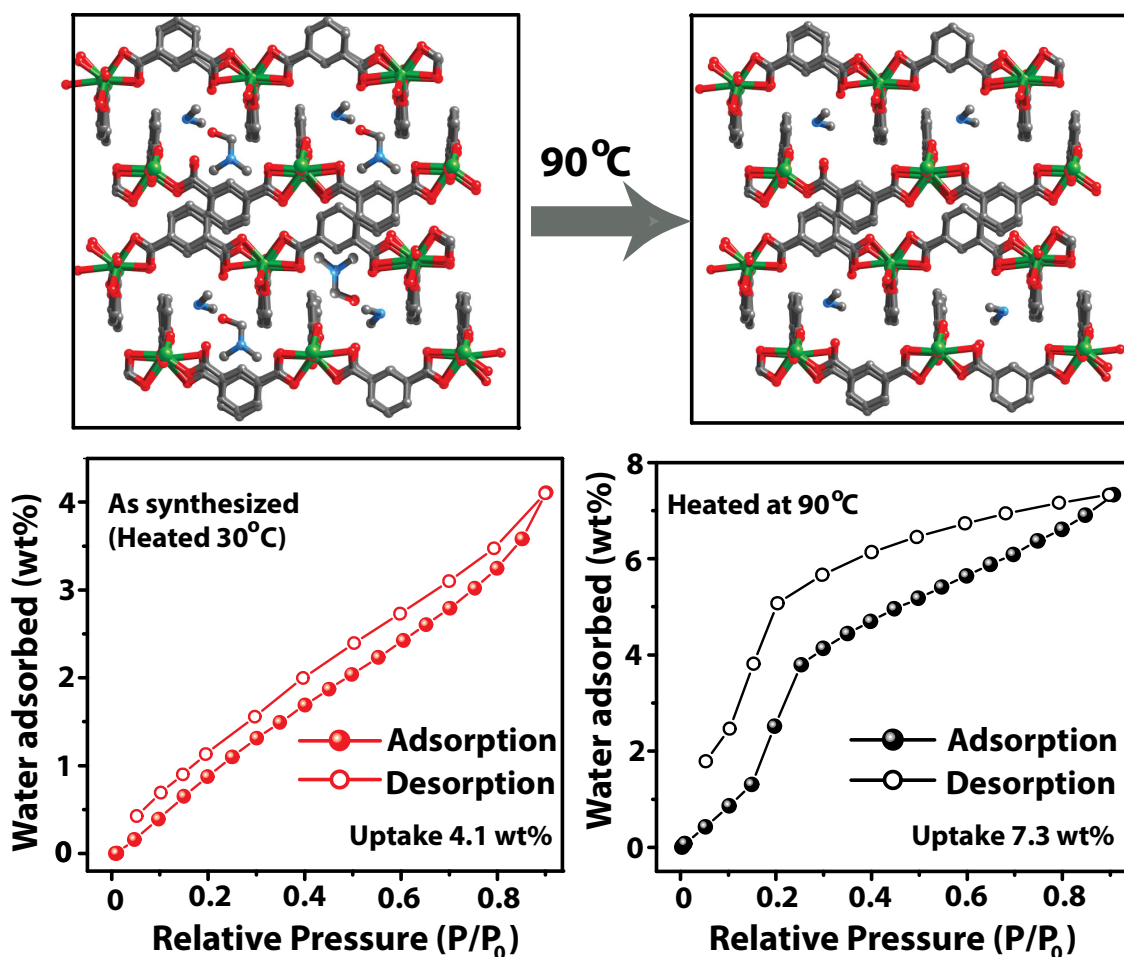


Figure 5.10. Water vapor adsorption of In-IA-2D-1 at STP.

STP. Similarly, as synthesized In-IA-2D-2, 110 mg of sample was taken and dried at room temperature upto 4 hrs. sample was used for water vapor adsorption measurement. The result shows that In-IA-2D-2 takes up 4.1 wt% water vapor at STP. For our interest, another fresh batch of as synthesized sample of In-IA-2D-2 (110 mg) was heated at 90 °C for 4 hours followed by evacuation and then measured for water vapor adsorption.

Preheated In-IA-2D-2 takes up 7.3 wt% water vapor at STP. The reason behind this high uptake could be the removal of the DMF molecules from In-IA-2D-2 framework at 90 °C under evacuation. We have also calculated the number of water molecules inside the void space of In-IA-2D-1 and -2 by using the water adsorption study.



**Figure 5.11.** Schematic representation of increasing hydrophilicity of In-IA-2D-2 via DMF removal at 90 °C, confirmed by water vapor adsorption experiment at STP.

**Calculation of water content molecular formula at 98% RH of In-IA-2D-1 and In-IA-2D-2:** For In-IA-2D-1, 2.85 wt% H<sub>2</sub>O uptake =  $2.85 \times \text{MW of In-IA-2D-1} / 100 = 2.85 \times 489.14 / 100 = 13.94 \text{ cc H}_2\text{O}$ . Hence, number of water molecules for In-IA-2D-1 =  $13.94 / 18 = 0.78$ . For In-IA-2D-2, 4.1 wt% of H<sub>2</sub>O =  $4.1 \times \text{MW of In-IA-2D-2} / 100 = 4.1 \times 562.23 / 100 = 23.05 \text{ cc H}_2\text{O}$ . Hence, number of H<sub>2</sub>O molecule for In-IA-2D-2 =  $23.05 / 18 = 1.3$



We have also calculated the possible chemical formula of both these MOFs at 98% RH. As per our calculations  $\sim 1.3$  water molecules per asymmetric unit of In-IA-2D-1 and  $\sim 0.78$  water molecules per asymmetric unit of In-IA-2D-2 are absorbed within the pores. Hence, the molecular formula at 98% RH of these MOFs are  $[\text{In}(\text{IA})_2 \{(\text{CH}_3)_2\text{NH}_2\}] \cdot 0.78\text{H}_2\text{O}$  and  $[\text{In}(\text{IA})_2 \{(\text{CH}_3)_2\text{NH}_2\}(\text{DMF})] \cdot 3\text{H}_2\text{O}$ , respectively for In-IA-2D-1 and -2.

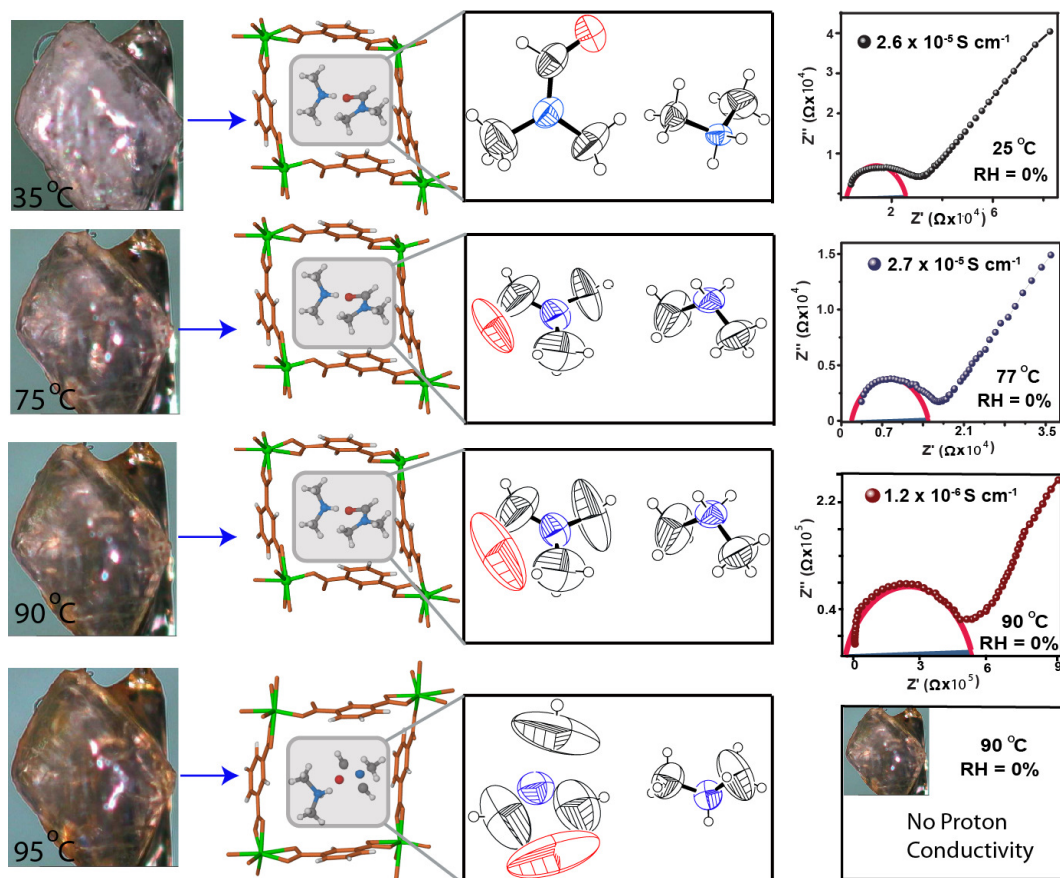


**Figure 5.12.** In situ variable temperature single crystal XRD structures and anhydrous proton conductivity plot of In-IA-2D-2 at 25, 90 and 95 °C. Electron density of DMF resides in the cavity dispersed considerably at temperatures beyond 90 °C.

#### 5.2.3.4 Anhydrous proton conduction in In-IA-2D-2:

The “anhydrous condition” mentioned for the proton conductivity in In-IA-2D-2 refers to perfectly anhydrous system both from sample as well as proton conductivity chamber point of view. The sample holder was held in a dry condition in  $\text{N}_2$  containing chamber with occasional flushing of dry  $\text{N}_2$  to ensure complete humid free environment throughout the



measurements. The reproducibility of the entire process were confirmed by repeated experiments. In-IA-2D-2 shows proton conductivity at ambient (25 °C) as well as high temperatures (90 °C) under anhydrous conditions due to the presence of  $[(\text{CH}_3)_2\text{NH}_2]^+$  cations and high boiling DMF solvent molecules as proton carriers (boiling point of DMF 154 °C).

**Table 5.4:** Anhydrous proton conductivity values of In-IA-2D-2 at different temperatures:

In-IA-2D-2 (anhydrous condition)		
Serial. no	Temperature (°C)	Proton conductivity value (Anhydrous Condition) [ $\text{Scm}^{-1}$ ]
1	25	$2.61 \times 10^{-5}$
2	40	$2.56 \times 10^{-5}$
3	55	$2.12 \times 10^{-5}$
4	60	$2.51 \times 10^{-5}$
5	77	$2.72 \times 10^{-5}$
6	80	$1.37 \times 10^{-5}$
7	90	$1.18 \times 10^{-5}$

**Table 5.5:** Comparison of anhydrous proton conductivity values of In-IA-2D-2 with other proton conducting MOFs:

SL.No.	MOFs and CPs	Protonconductivity ( $\text{Scm}^{-1}$ )	Ea (eV)	Conditions	Reference
1	$[\beta\text{-PCMOF2}(\text{Tz})_{0.45}]$	$5 \times 10^{-4}$	0.51	150 °C	4.5b
2	$[\{\text{Zn}(\text{HPO}_4)(\text{H}_2\text{PO}_4)_2\}(\text{ImH}_2)_2]$	$2.6 \times 10^{-4}$	0.47	130 °C	4.5d
3	$[\text{Al}(\text{OH})(\text{ndc})]_n \supset \text{His}$	$2.1 \times 10^{-4}$	0.25	150 °C	4.5c
4	$[\text{Zn}(\text{H}_2\text{PO}_4)_2(\text{TzH})_2]_n$	$1.2 \times 10^{-4}$	0.6	150 °C	4.5e
5	Al-PCP $\subset$ Imdz	$2.2 \times 10^{-5}$	0.6	120 °C	4.5a
6	In-IA-2D-2	$1.2 \times 10^{-5}$	0.61	90 °C	<i>This report</i>

Proton conductivity of In-IA-2D-2 is  $2.6 \times 10^{-5} \text{ Scm}^{-1}$  at 25 °C,  $2.7 \times 10^{-5} \text{ Scm}^{-1}$  at 77 °C and  $1.18 \times 10^{-5} \text{ Scm}^{-1}$  at 90 °C under anhydrous conditions (Figure 5.12). We speculate that, under anhydrous condition DMF molecules and  $[(\text{CH}_3)_2\text{NH}_2]^+$  cations both facilitate the proton transport (up to 90 °C) in In-IA-2D-2 framework (Figure 5.12 and 5.15). However, beyond 90 °C, DMF molecules leave the framework which is confirmed by the TGA and

VTSCXRD (Figure 5.3b and 5.19). This results in the non-conducting (proton) behaviour of In-IA-2D-2 beyond 90 °C under anhydrous conditions (Figure 5.12). Interestingly, the anhydrous proton conductivity of In-IA-2D-2 at room temperature (27 °C) outperforms Al-PCPC=Imdz ( $5.5 \times 10^{-8} \text{ Scm}^{-1}$  at 25 °C) and  $\beta$ -PCMOF2 (H<sub>2</sub>O)<sub>0.5</sub> ( $5.0 \times 10^{-6} \text{ Scm}^{-1}$  at 30 °C).

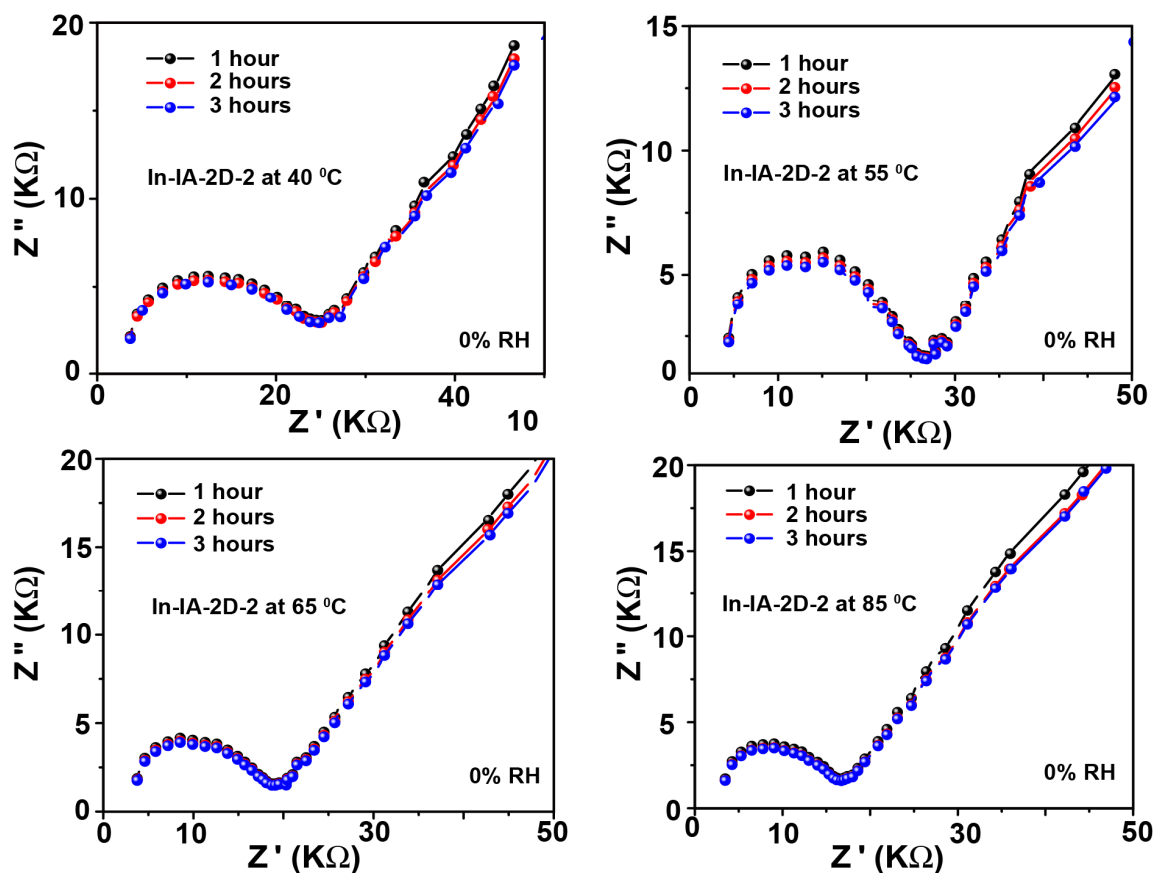


**Figure 5.13.** Anhydrous proton conductivity plots of In-IA-2D-2 at different temperatures (40, 55, 65 85 °C) for 1, 2 and 4 hrs respectively.

At higher temperature (90 °C) In-IA-2D-2 shows comparable proton conductivity value ( $1.2 \times 10^{-5} \text{ Scm}^{-1}$  at 90 °C) like Al-PCPC=Imdz ( $2.2 \times 10^{-5} \text{ Scm}^{-1}$  at 120 °C), [1.45a] but less proton conductivity value than  $\beta$ -PCMOF2 (Tz)<sub>0.45</sub> ( $5 \times 10^{-4} \text{ Scm}^{-1}$  at 150 °C), [1.45b]  $\{[\text{Zn}(\text{HPO}_4)(\text{H}_2\text{PO}_4)_2](\text{ImH}_2)_2\}$  ( $2.6 \times 10^{-4} \text{ Scm}^{-1}$  at 130 °C), [1.45d]  $[\text{Al}(\text{OH})(\text{ndc})_n]\text{His}$  ( $2.1 \times 10^{-4} \text{ Scm}^{-1}$  at 150 °C) [1.45c] and  $[\text{Zn}(\text{H}_2\text{PO}_4)_2(\text{TzH})_2]_n$  ( $1.2 \times 10^{-4} \text{ Scm}^{-1}$  at 150 °C) [1.45e] [Table 5.4] under anhydrous medium. It is interesting to note that, anhydrous proton conductivity of In-IA-2D-2 remains constant over a wide range of temperature (2.6

$\times 10^{-5} \text{ Scm}^{-1}$  at 25 °C and  $1.15 \times 10^{-5} \text{ Scm}^{-1}$  at 90 °C) compared to other anhydrous proton conducting materials like  $\{\text{Zn}(\text{HPO}_4)(\text{H}_2\text{PO}_4)_2\}(\text{ImH}_2)_2$ , [ $3.3 \times 10^{-8} \text{ Scm}^{-1}$  at 25 °C to  $2.6 \times 10^{-4} \text{ Scm}^{-1}$  at 130 °C], Al-PCP $\subset$  Imdz, [ $5.5 \times 10^{-8} \text{ Scm}^{-1}$  at 25 °C to  $2.2 \times 10^{-5} \text{ Scm}^{-1}$  at 120 °C] and like  $\beta$ -PCMOF2 (Tz) $_{0.45}$ , [ $9.5 \times 10^{-7} \text{ Scm}^{-1}$  at 25 °C to  $5 \times 10^{-4} \text{ Scm}^{-1}$  at 150 °C]. To prove the durability of anhydrous proton conduction in In-IA-2D-2, we have measured time dependent performance for 1 hr, 2 hrs and 4 hrs. It is interesting to note that anhydrous proton conductivity of In-IA-2D-2 at different temperatures (40, 55, 65 85 °C) are pretty stable up to 4 hours.

### 5.2.3.5 Anhydrous proton conduction Mechanism:

The anhydrous proton conduction of In-IA-2D-2 is due to the presence of inherent  $(\text{CH}_3)_2\text{NH}_2^+$  cations and DMF molecules inside the crystal structure. Figure 5.14 shows the close proximity (small hopping distance) of  $(\text{CH}_3)_2\text{NH}_2^+$  cations and DMF molecules which facilitated the proton conduction pathway through the channel of In-IA-2D-2 network.

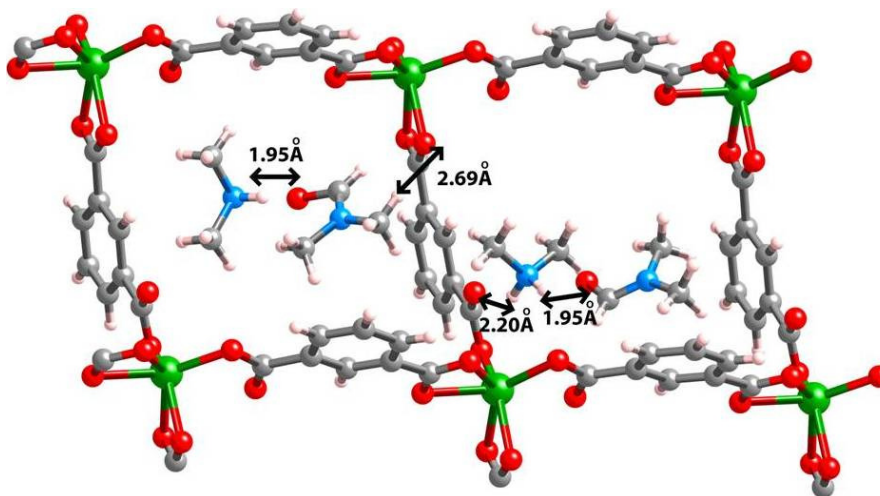


**Figure 5.14.** Intermolecular distance between proton hopping sites in the crystal structure of In-IA-2D-2.

The conduction mechanism of In-IA-2D-2 pictorially discussed at Figure 5.15. It should be noted that proton of  $(\text{CH}_3)_2\text{NH}_2^+$  cations take the initiation by passing one proton to adjacent oxygen of DMF molecules. Alternatively, the extra proton of DMF molecules was transferred to the framework oxygen of carboxylate moiety and finally passes the proton to

another  $(\text{CH}_3)_2\text{NH}_2^+$  cation. It is interesting to note that, anhydrous proton conduction occurs due to the low hopping distances among the conducting sites which is well maintained inside the structural networks of In-IA-2D-2.

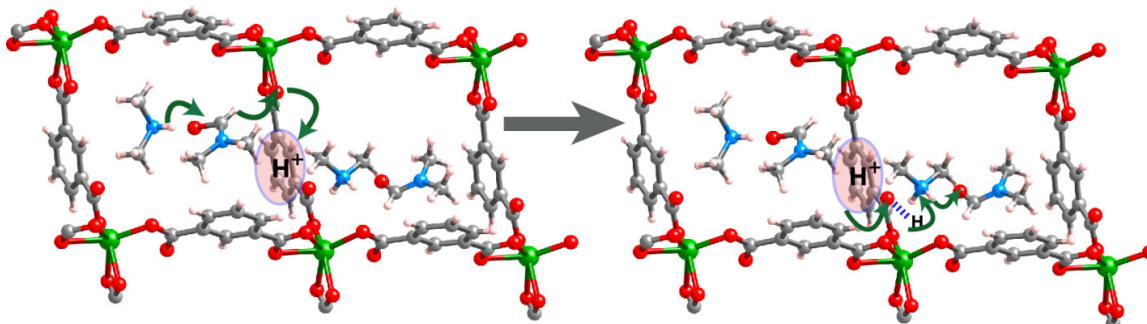


**Figure 5.15.** Schematic representation and possible proton hopping mechanism of In-IA-2D-2 MOF under anhydrous condition. The arrows indicate the possible movement of the  $\text{H}^+$  ion.

### 5.3 Conclusions

In conclusion, we have successfully synthesized two isomeric 2D MOFs, In-IA-2D-1 and In-IA-2D-2, by using IA as the organic building block and In(III) as the metal node. This In-IA based isomeric MOFs exhibit significant difference in proton conductivity owing to their structural variation. In-IA-2D-1 shows high proton conductivity of  $3.4 \times 10^{-3} \text{ Scm}^{-1}$  at ambient temperature ( $27^\circ\text{C}$ ) and 98% RH due to the large available void space filled with  $\text{H}_2\text{O}$  molecules enhances the proton transport. Although In-IA-2D-2 shows a proton conductivity lower than In-IA-2D-1 under humid conditions, it shows proton conductivity in anhydrous condition. Research on the conduction properties of MOF is still at its infancy and there are many fundamental aspects that need to be clarified. However, we believe that these results will encourage researchers to explore new materials that can substitute the conventional conductive polymers.

### 5.4 Experimental Procedures:

**5.4.1 Materials:** Isophthalic acid and N, N'-dimethylformamide (DMF) were purchased from Rankem chemicals.  $\text{In}(\text{NO}_3)_3 \cdot x\text{H}_2\text{O}$  as a metal salt and tetra methyl ammonium chloride were purchased from the Aldrich Chemicals. All starting materials were used without further purification. All experimental operations were performed in air.

### 5.4.2 Synthesis of In-IA-2D-1 and In-IA-2D-2:

**In-IA-2D-1** ( $C_{18}H_{16}InNO_8$ ): In the synthesis of In-IA-2D-1 ( $C_{18}H_{16}InNO_8$ ), we used isophthalic acid (IA) as organic linker and  $In(NO_3)_3 \cdot xH_2O$  as a metal salt. Solvothermal reaction between 1.0 mmol of IA (0.170 g), 1.00 mmol of tetra methyl ammonium chloride (0.1096 g) and 0.3 mmol of  $In(NO_3)_3 \cdot xH_2O$  (0.102 g) in presence of 5 ml N,N'-dimethylformamide (DMF) solution at 120 °C for 96 hours yielded rod shaped crystals of In-IA-2D-1 MOF. **IR (KBr,  $cm^{-1}$ ):** 2977 (w), 2307(w), 2172 (w), 1679 (w), 1610 (m), 1550(m), 1486(w), 1374(d,s), 1163(w), 1069(w), 992(w), 852(w), 793(w), 739(s), 657(m),  $cm^{-1}$ . **Elemental Analysis:** Calculated – C (44.83%), H (4.12%), N (4.98%); Found – C(44.75%), H (4.21%), N (5.08%).

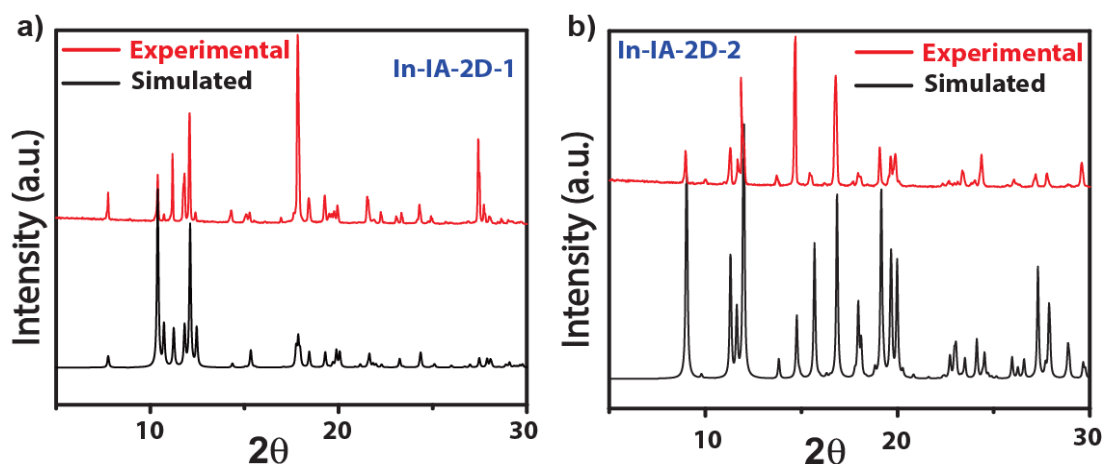


**Figure 5.16.** Comparison of the experimental PXRD pattern of (a) as-synthesized In-IA-2D-1 (top) with the simulated one from its single crystal structure (bottom) and (b) as-synthesized In-IA-2D-1 (top) with the simulated one from its single crystal structure (bottom).

**In-IA-2D-2** ( $C_{21}H_{23}InN_2O_9$ ): 0.3 mmol of IA (0.049 g) and 0.1 mmol of  $In(NO_3)_3 \cdot 3H_2O$  (0.031 g) was taken in a 15 ml scintillation vial. A mixture of 2 ml of DMF and 1ml of  $H_2O$  was added and sonicated for 30 minutes, then transferred to a pre-heated oven at 90 °C for 126 hours. Cube shaped crystals of In-IA-2D-2 ( $C_{21}H_{23}InN_2O_9$ ) was filtered washed repeatedly with DMF and  $H_2O$  and air dried for 20 minutes (yield~ 77%). **IR (KBr,  $cm^{-1}$ ):** 2319(w), 1668(m), 1610(m), 1526(s), 1350(d, s), 1163(w), 1080(m), 1022 (w), 928 (w), 840 (m), 746(s), 657(m). **Elemental Analysis:** Calculated- C (34.37%), H (3.90%), N (7.29%); Found C (34.35%), H (3.92%), N (7.25%).

### 5.4.3 General methods for characterization

**(a) Powder X-Ray Diffraction (PXRD).** The PXRD patterns were collected on a Phillips PANalytical diffractometer on a Cu K $\alpha$  radiation ( $\lambda = 1.5406 \text{ \AA}$ ), with a scan speed of  $2^\circ \text{ min}^{-1}$ . The tube voltage and amperage were set at 40 kV and 50 mA respectively. Each sample was scanned between  $5$  and  $50^\circ 2\theta$  with a step size of  $0.02^\circ$ . The instrument was previously calibrated using a silicon standard.

**(b) Thermogravimetric Analysis (TGA).** TGA was performed on a SDT Q600 TG-DTA analyzer instrument. Approximately 5 mg of the sample was added to a platinum crucible and heated from  $25$  to  $800^\circ \text{C}$  under  $\text{N}_2$  atmosphere at a heating rate of  $10^\circ \text{C min}^{-1}$ .

**(c) Hot-Stage Microscopy.** Leica M-80 optical microscope with hot stage and camera attachment was used for collecting photographs.

**(d) IR Spectroscopy.** The Fourier transform (FT) infrared spectra of the MOFs were taken on a *PERKIN ELMER FT-IR SPECTRUM* (Nicolet) spectrometer. KBr samples (2 mg in 20 mg of KBr) were prepared and 10 scans were collected at  $4 \text{ cm}^{-1}$  resolution for each sample. The spectra were measured over the range of  $4000\text{-}400 \text{ cm}^{-1}$ .

**(e) Proton Conductivity.** Proton conductivity data were measured in a quasi-two-probe method, with a Solartron 1287 Electrochemical Interface with frequency response analyzer.

**(f) Water Adsorption.** All low-pressure water adsorption experiments (up to 1 bar) were performed on a BELSORP-max volumetric instrument. Approximately 50 mg of the sample was activated after solvent exchange by the use of activation chamber. The activated sample was loaded inside the glass bulb of water adsorption instrument and measured the capacity.

### 5.4.4 X-ray Crystallography

#### 5.4.4.1 General Data Collection and Refinement Procedures:

Datas were collected on a Super Nova Dual source X-ray Diffractometer system (Agilent Technologies) equipped with a CCD area detector and operated at 250 W (50 kV, 0.8 mA) to generate Mo K $\alpha$  radiation ( $\lambda = 0.71073 \text{ \AA}$ ) and Cu K $\alpha$  radiation ( $\lambda = 1.54178 \text{ \AA}$ ). The crystal reported in this paper was mounted on Nylon CryoLoops (Hampton Research) with Paraton-N (Hampton Research). Initial scans of each specimen were performed to obtain

preliminary unit cell parameters and to assess the mosaicity (breadth of spots between frames) of the crystal to select the required frame width for data collection. CrysAlis<sup>Pro</sup> [5.8] program software suite to carry out was used overlapping  $\phi$  and  $\omega$  scans at detector ( $2\theta$  settings ( $2\theta = 28$ ). Following data collection, reflections were sampled from all regions of the Ewald sphere to redetermine unit cell parameters for data integration. In no data collection was evidence for crystal decay encountered. Following exhaustive review of collected frames the resolution of the dataset was judged. Data were integrated using CrysAlis<sup>Pro</sup> software with a narrow frame algorithm. Data were subsequently corrected for absorption by the program SCALE3 ABSPACK [5.9] scaling algorithm.

These structures were solved by direct method and refined using the SHELXTL 97 [2.23] software suite. Atoms were located from iterative examination of difference F-maps following least squares refinements of the earlier models. Final model was refined anisotropically (if the number of data permitted) until full convergence was achieved. Hydrogen atoms were placed in calculated positions (C-H = 0.93 Å) and included as riding atoms with isotropic displacement parameters 1.2-1.5 times  $U_{eq}$  of the attached C atoms. Data were collected at 100(2) K for the MOF presented in this paper. This lower temperature was considered to be optimal for obtaining the best data. The structure was examined using the Addsym subroutine of PLATON [2.25] to assure that no additional symmetry could be applied to the models. The ellipsoids in ORTEP diagrams are displayed at the 50% probability level unless noted otherwise. For all structures we note that elevated R-values are commonly encountered in MOF crystallography for the reasons expressed above by us and by other research groups [2.26-2.35]. Crystallographic data (excluding structure factors) for the structures are reported in this paper have been deposited in CCDC as deposition No. CCDC 932278 – 932280. Copies of the data can be obtained, free of charge, on application to the CCDC, 12 Union Road, Cambridge CB2 1EZ, U.K. [fax: þ 44 (1223) 336 033; e-mail: deposit@ccdc.cam.ac.uk].

#### 5.4.4.2 Experimental and Refinement Details for In-IA-2D-1:

A colorless plate like crystal ( $0.35 \times 0.28 \times 0.16 \text{ mm}^3$ ) of **In-IA-2D-1** was placed in 0.7 mm diameter nylon CryoLoops (Hampton Research) with Paraton-N (Hampton Research). The loop was mounted on a Super Nova Dual source X-ray Diffractometer system (Agilent

Technologies) equipped with a CCD area detector and operated at 250 W power (50 kV, 0.8 mA) to generate Mo K $\alpha$  radiation ( $\lambda = 0.71073 \text{ \AA}$ ) at 100(2) K in a liquid N<sub>2</sub> cooled stream of nitrogen. A total of 15548 reflections were collected of which 7034 were unique. The range of  $\theta$  was from 3.29 to 29.15. Analysis of the data showed negligible decay during collection. The structure was solved in the orthorhombic  $Pna2_1$  space group, with  $Z = 4$ , using direct methods. All non-hydrogen atoms were refined anisotropically with hydrogen atoms generated as spheres riding the coordinates of their parent atoms. We have repeatedly collected the single crystal XRD data of In-IA-2D-1 at different temperature (90, 120, 150K). We would like to mention

that each time during the refinement of crystal structure we encountered two electron densities within the framework cavity apart from dimethyl ammonium cation. However, assigning these electron densities with isolated O atoms, leads to highly distorted O atoms, although the refinement become stable with decreased R factor and goodness of fit. Hence, we believe that

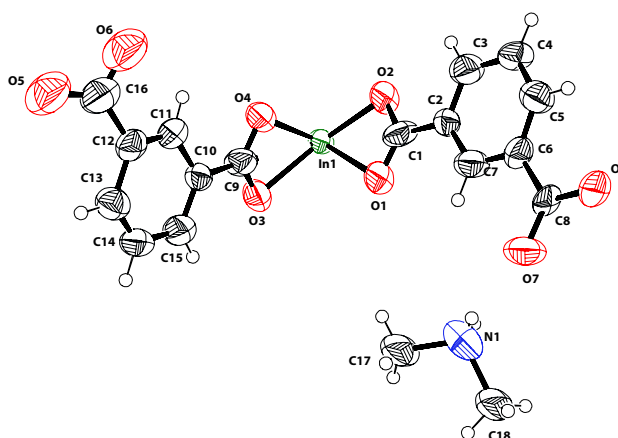


**Figure 5.17.** ORTEP diagram (50% probability) of the asymmetric unit of In-IA-2D-1.

two water molecules reside inside the asymmetric unit of In-IA-2D-1, however, the O atoms of water molecules have very high thermal parameters apart from In-IA and  $(\text{CH}_3)_2\text{NH}_2$  cations with several IUCr checkcif errors. Hence we have decided to use the SQUEEZE routine to remove these unstable and highly distorted water molecules from the pores of In-IA-2D-1. It should be noted that SQUEEZE structure is very stable with minimal IUCr checkcif problems, less R factor and goodness of fit. In this manuscript we have provided the SQUEEZE applied cif file of In-IA-2D-1. Final full matrix least-squares refinement on  $F^2$  converged to  $R_1 = 0.0725$  ( $F > 2\sigma F$ ) and  $wR_2 = 0.2213$  (all data) with GOF = 1.132. [CCDC 932278].

**Refine\_special\_details:** We believe this distortion in the benzene ring in In-IA-2D-1 structure appears due to possible merohedral or pseudo-merohedral twinning not due to a static or dynamic disorder. As a result despite lowering the data collection temperature to



110 K this distortion remains persistent. A close look of the .res file will show that the structure contains a twinning with a BASF parameter 0.545. This indicates a 50/50 twinning in the crystal lattice. In order to overcome this distortion we have used 8 EADP and 3 FLAT commands in the .res file.

#### 5.4.4.3 Experimental and Refinement Details for In-IA-2D-2:

A colorless block like crystal ( $0.35 \times 0.27 \times 0.15 \text{ mm}^3$ ) of **In-IA-2D-2** was placed in 0.7 mm diameter nylon CryoLoops (Hampton Research) with Paraton-N (Hampton Research).

The loop was mounted on a Super Nova Dual source X-ray Diffractometer system (Agilent Technologies) equipped with a CCD area detector and operated at 250 W power (50 kV, 0.8 mA) to generate Cu K $\alpha$  radiation ( $\lambda = 1.54178 \text{ \AA}$ ) at 100(2) K in a liquid N<sub>2</sub> cooled stream of nitrogen. A total of 8741

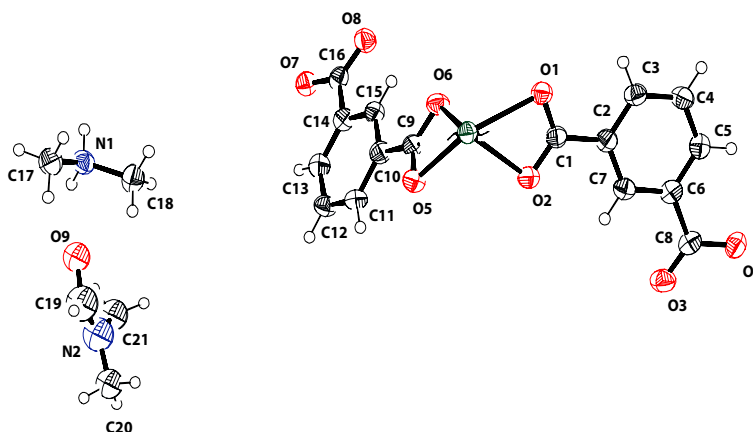


**Figure 5.18.** ORTEP diagram (50% probability) of the asymmetric unit of In-IA-2D-2 MOF

reflections were collected of which 4027 were unique. The range of  $\theta$  was from 4.50 to 70.72. Analysis of the data showed negligible decay during collection. The structure was solved in the Monoclinic  $P2_1/c$  space group, with  $Z = 4$ , using direct methods. All non-hydrogen atoms were refined anisotropically with hydrogen atoms generated as spheres riding the coordinates of their parent atoms. Final full matrix least-squares refinement on  $F^2$  converged to  $R_1 = 0.0684$  ( $F > 2\sigma F$ ) and  $wR_2 = 0.1826$  (all data) with GOF = 0.993. [CCDC 932279]

#### Refine\_special\_details:

The solvent DMF molecule has been refined as isotropic due to large anisotropic displacement of N atom of DMF molecule even after several refinements.

## Variable temperature single crystal X-ray (VTSCXRD) of In-IA-2D-2 :

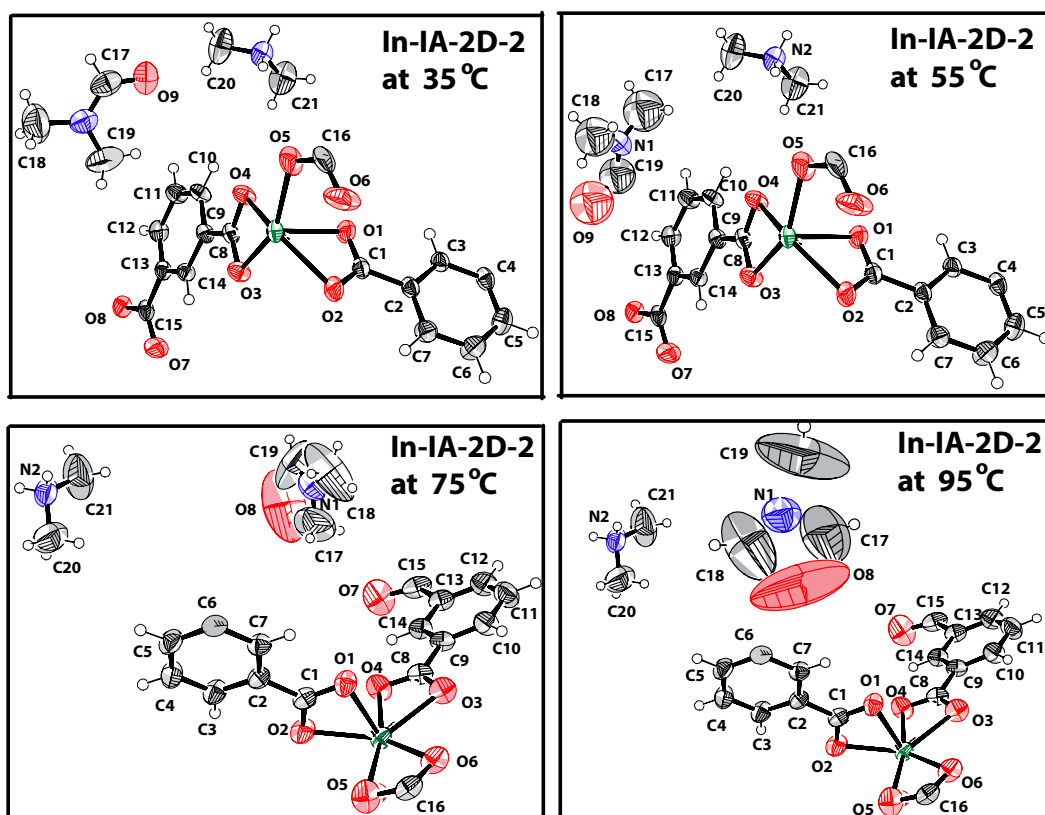


**Figure 5.19.** ORTEP diagrams (50 % probability) of In-IA-2D-2 single crystal X-ray data at variable temperature (35, 55, 75 and 95 °C).

**NOTE:** The results of this chapter have already been published in *Chem. Commun.*, 2013, **49**, 6197-6199. with the title: “Structural Isomerism Leading to Variable Proton Conductivity in Indium (III) Isophthalic Acid based Framework.” These publications were the results from the group of Dr. Rahul Banerjee and his students Tamas Panda and Tanay Kundu from CSIR National Chemical Laboratory, Pune, India. Major works are contributed by Tamas Panda with the help of the instrumental facilities of CSIR National Chemical Laboratory.

## CHAPTER 6

---

### CONCLUSION OF ALL CHAPTERS AND FUTURE DIRECTION

---

#### 6.1 Conclusion:

In this dissertation, the applications of MOFs have been emphasized on high CO<sub>2</sub> storage capacity and proton conduction capability. A series of MOFs/ZIFs have been synthesized and characterized successfully for such applications.

The conclusion of chapter 2 is divided into two parts. First part, describes the synthesis and isolation of a three dimensional amino functionalized zeolitic tetrazolate framework (ZTF-1) where only N1 and N4 are coordinated to metal centers. This is the first report of a -NH<sub>2</sub> functionalized MOF among different metal imidazoles / triazoles / tetrazoles where M-TET-M angle is close to 145°. ZTF-1 adopts diamond (**dia**) topology and shows high CO<sub>2</sub> (273 K) and H<sub>2</sub> (77 K) uptake due to the presence of free -NH<sub>2</sub> group as well as uncoordinated tetrazolate nitrogens. We have also found the exact location of the CO<sub>2</sub> by GCMC calculation. It is very challenging to find out the exact contributions of exposed -NH<sub>2</sub> functionality or free tetrazole nitrogens for the high CO<sub>2</sub> capacity of ZTF-1 but these results shows the value of utilizing -NH<sub>2</sub> functionalized links as well as free aromatic nitrogen atoms as building block for constructing MOFs for high and reversible CO<sub>2</sub> capture. In the second part, we have demonstrated the effects of metal replacement (from Zn to Co) on CO<sub>2</sub> gas adsorption properties in a series of isostructural zeolitic imidazolate frameworks (ZIFs). These Co-ZIFs [Co-ZIF-68, -69, -81] feature the same structural topology as well as a range of functionality and finely varied pore metrics. Although CO<sub>2</sub> adsorption study (computational and experimental) on open metal sites have been demonstrated in MOFs. However, there are very limited reports, where combined experimental and theoretical approach has been spotlighted on isostructural MOFs/ZIFs contains different metals with saturated coordination center. Co-ZIF-68, -69 and -81 show

high CO<sub>2</sub> (273 K) uptake (124, 115 and 96 cc/g respectively) and stands at high position among the MOFs with high CO<sub>2</sub> capture capability. These Co-ZIFs shows high CO<sub>2</sub> (273 K / 298 K) uptake (33 to 60%) compare to their isostructural Zn based analogues (Zn-ZIF-68, -69 and -81) due to the replacement of the metal center. Moreover, *Ab initio* calculations of Co-ZIF-68, and Zn-ZIF-68, highlights that CO<sub>2</sub> has a stronger interaction with Co-ZIF compared to Zn-ZIF, which is in well agreement with experimental data.

In chapter 2, we have reported three new Mn-MOFs using predesigned 5-TIA ligand with transition metal Mn(II). This is the first report which describes the usage of template (like pyrazine and 4,4'-bipyridine) for systematic and controlled enhancement of the porosity. We have prepared nonporous to microporous MOFs from the same reactants by increasing the size of the template (pyrazine and 4,4'-bipyridine). This is the first report where the porosity of the structural isomers in MOFs is enhanced due to size dependent template effect. The cross sectional pore aperture of the resulting Mn-MOFs are comparable to the molecular dimensions of the template (pyrazine and 4,4'-bipyridine). The increased porosity in MOFs depending on the size of the template used has been further confirmed by the CO<sub>2</sub> adsorption isotherms.

In chapter 3, we have reported two isostructural self assembled functionalized Metal Organic Nanotubes. These MONTs (Cd-5TIA and In-5TIA) are held together by weak C-H...O hydrogen bonding to form the self assembled architecture. These are the first example of self assembled functionalized metal organic nanotubes (MONTs) which shows application like proton conductivity. Proton conductivity shown by Cd-5TIA ( $3.61 \times 10^{-3} \text{ Scm}^{-1}$  at 301 K) stands at high position among the proton conducting MOFs reported till date. Not only that, In-5TIA and Cd-5TIA shows high proton conductivity ( $5.35 \times 10^{-5}$  to  $2.7 \times 10^{-5} \text{ Scm}^{-1}$  for In-5TIA and  $3.61 \times 10^{-3}$  to  $1.15 \times 10^{-5} \text{ Scm}^{-1}$  for Cd-5TIA) across a wide range of temperature (301 K to 368 K). In-5TIA shows significantly low activation value (0.137 eV) compared to nafion based membrane electrolytes (0.22 eV), and lowest activation value reported till date for MOF based proton conducting materials. We have also studied and compared the proton conductivity of the literature reported MONT architecture (In-IA).

In chapter 4, we have reported two isomeric 2D MOFs, In-IA-2D-1 and In-IA-2D-2, by using IA as the organic building block and In(III) as the metal node. These isomeric

MOFs exhibit significant difference in proton conductivity owing to their structural variation. Interestingly, In-IA-2D-2 MOF shows the proton conduction ( $2.6 \times 10^{-5} \text{ Scm}^{-1}$  to  $1.18 \times 10^{-5} \text{ Scm}^{-1}$ ) at wide range of temperature (25 to  $90^\circ \text{C}$ ) at anhydrous conditions as well as ( $4.2 \times 10^{-4}$  to  $1.6 \times 10^{-5} \text{ Scm}^{-1}$ ) under humidified condition (25 to  $120^\circ \text{C}$ ). Proton conductivity shown by In-IA-2D-1 (a structural isomer of In-IA-2D-2) under humidification ( $3.4 \times 10^{-3} \text{ Scm}^{-1}$  at  $27^\circ \text{C}$ ) stands at high position among the proton conducting MOFs reported till date. We believe, the high proton conduction of In-IA-2D-2 due to the large available space, which facilitates the higher proton transport.

## 6.2 Future direction:

### Plan-1: Design and Synthesis of amino ( $-\text{NH}_2$ ) Functionalized Zeolitic Tetrazolate Frameworks with various zeolitic topology.

The aim of our future plan implies extensive study and synthesis of zeolitic amino functionalized ( $\text{NH}_2$ -ZMOFs) MOFs which selectively adsorbed  $\text{CO}_2$  at low pressures. In our previous report (chapter 2), first time we could isolate zeolitic tetrazolate framework (ZTF-1) with diamondoid topology and exhibits high  $\text{CO}_2$  uptake (120 cc/gm at 1 bar pressure). ZTF-1 contains the organic building block 5-amino tetrazole coordinated with Zn metal atom. We proved that, high  $\text{CO}_2$  uptake of ZTF-1 is not only for amino functionalization but also for free tetrazolate nitrogens. Taking up this opportunity, we realize that if we can make ZTFs with different zeolitic topologies with

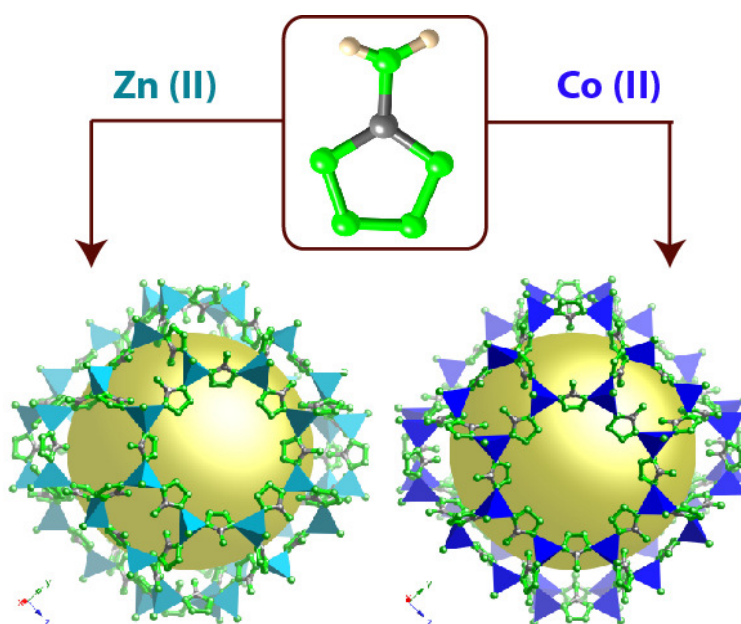


**Figure 6.1.** RHO topology of 5-amino tetrazole with Zn(II) and Co(II) metal could be the suitable candidates for high  $\text{CO}_2$  uptake.

large pore size (e.g., GME, RHO, FAU topology) would be the suitable materials for high CO<sub>2</sub> uptake. Figure 6.1 is the proposed structure of highly porous RHO topological ZIF will be synthesized from 5-amino tetrazole (5-AT) with different metal center [Zn(II) and Co(II)]. High surface area, free amino groups as well as uncoordinated tetrazolate nitrogens are exposed inside the pores and may therefore increase the material's affinity for enhanced CO<sub>2</sub> adsorption, including high uptake and high selectivity.

### Plan-2: Induction of polar functionality in zeolitic tetrazolate Frameworks.

As described in chapter 2 the use of various metals (nodes) and ligands (rods) under a wide variety of reaction conditions have produced diverse MOF structures that have shown great promise in a range of applications especially CO<sub>2</sub> storage and sequestration. Despite impressive progress in the area of ZIFs, it remains a significant challenge to introduce proper polar functionality inside the ZIF lattice which could enhance the CO<sub>2</sub> uptake incredibly at low pressure.

Recent literatures of MOFs with polar functional groups increases the interaction of CO<sub>2</sub> in many fold compared to non functionalized counterpart [3.2]. In this regards, we would like to incorporate different polar functional groups such as -F, -Cl, -NO<sub>2</sub> and -OH inside the

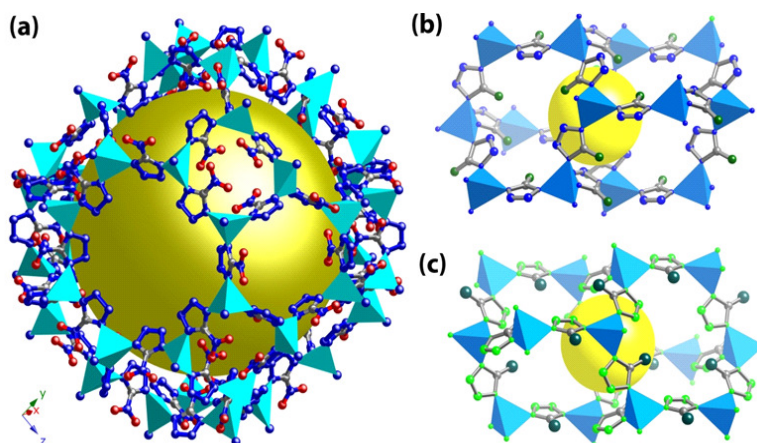


**Figure 6.2.** Induction of polar functionality in ZTF (a) 5-nitro tetrazole based zeolitic MOF (b) and (c) Incorporation of polar functional group -F and -Cl in 5 position of tetrazole moiety could enhance the high CO<sub>2</sub> uptake.

zeolitic tetrazolate structures. For this purpose, we have chosen tetrazolate ligand as report of such kind of structure is very less and functionalized the 5- position of tetrazole with mentioned polar groups. As a result, after the formation of MOF free tetrazole nitrogens as well as polar functional groups at 5- position of tetrazole moieties will interact strongly with CO<sub>2</sub> (Figure 6.2).

**Plan-3: Phosphoric acid doped benzimidazole based stable covalent organic frameworks (COFs) and porous organic frameworks (POFs) for high proton conduction.**

The objective of this plan is to design and synthesis of benzimidazole based COFs and POFs which can show very high proton conductivity at hydrous and anhydrous condition. Earlier studies [6.1] revealed that, phosphoric acid ( $\text{H}_3\text{PO}_4$ ) doped polybenzimidazole polymers (PBI) have great potential for higher proton conduction at temperatures as high as  $200\text{ }^\circ\text{C}$  without humidification. The proton conduction of these polymers have initiated by doped  $\text{H}_3\text{PO}_4$  molecules which form a salt by protonation of the imine N group of imidazole ring (6.1a) and creates proton hopping channel through the polymer backbone.

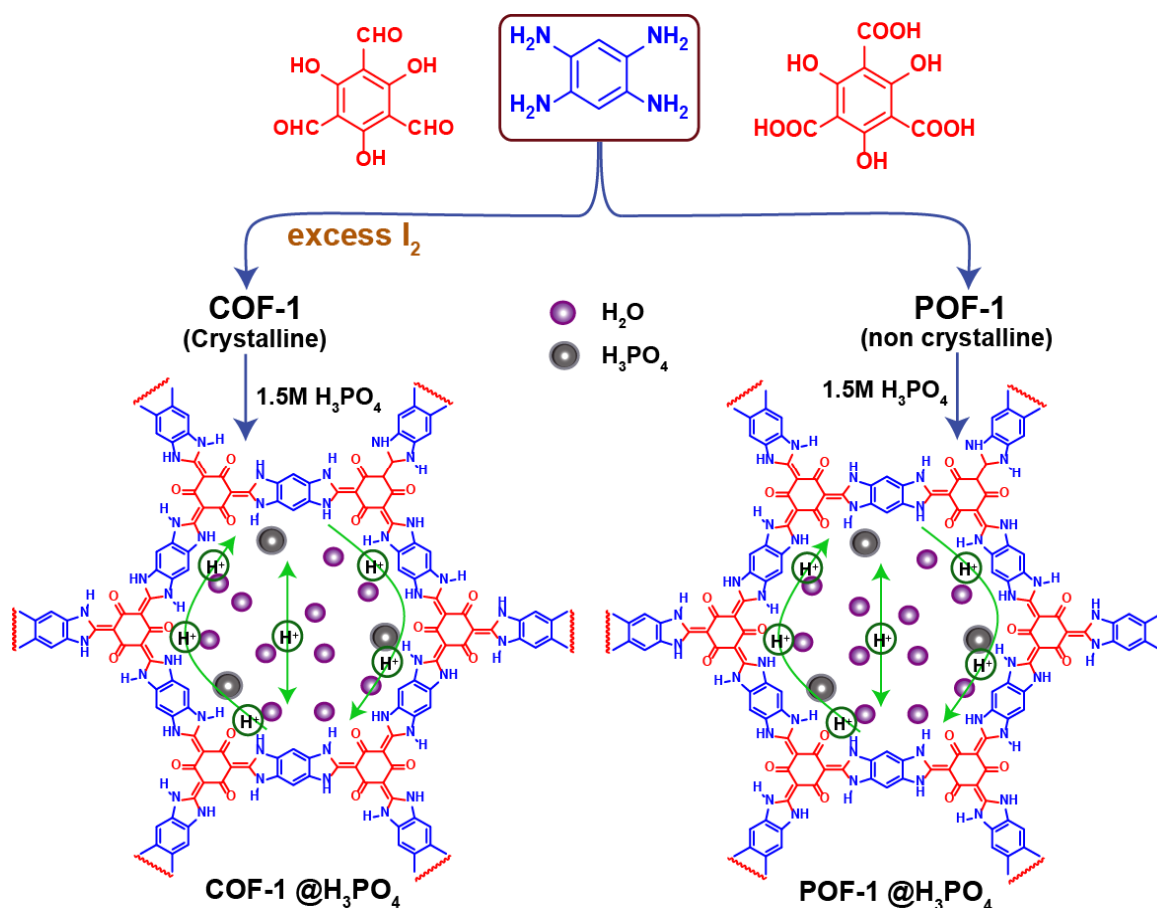


**Figure 6.3.** Scheme of synthesis and proposed proton conduction mechanism in phosphoric acid doped benzimidazole based covalent organic frameworks.

Keep these things in perspective, our approach focused on the synthesis of stable COFs and POFs which will have repeating benzimidazole units in the framework backbones as such units have proton anchoring sites. Moreover, long range periodicity, tailorable porosity, regular arrangement of voids and dynamic behaviour of COF and POFs are especially beneficial for their use as proton conductors compare to PBI based polymers. However, the major obstacles of COFs and POFs have the lack of stability in acidic, alkaline as well as in aqueous solutions. Recent report from our group reveals that, the stability of these materials can be overcome via irreversible enol to keto tautomerization, which enhances the chemical stability [6.2]. Taking the advantages of these materials we propose the synthesis of COF-1 and POF-1 by using the organic linkers 1,2,4,5-benzenetetramine with 1,3,5-triformyl phloroglucinol and 1,3,5-tricarboxy phloroglucinol respectively. Both COF-1 and POF-1 will be chemically stable due to enol to keto tautomerization which is established earlier. After that,  $H_3PO_4$  doping in COF-1 and POF-1 will lead to immobilization of the acid within the porous frameworks that probably enhance the proton conduction in both the hydrous and anhydrous state (Figure 6.3).

**Plan-4: Salt inclusion in hydrophobic covalent organic frameworks (COFs) for hydroxide ion ( $OH^-$ ) conductivity.**

Recently, hydroxide ion conductors have received a great deal of interest as electrolytes for alkaline fuel cells that can operate without precious-metal catalysts (platinum). In general, hydroxide ion conduction at ambient temperature requires  $OH^-$  ion carriers and conducting pathways created by hydrogen bonded networks, [6.3] similar like proton conduction. Future prospective in porous materials vessel should rely on the synthesized COFs that could conduct  $OH^-$  ions based on “salt inclusion into alkaline stable COFs”. For this purpose two fundamental requirements are necessary (1) an alkaline stable porous COF as a host and (2) the counter cations of  $OH^-$  ions having an affinity to adsorb in the frameworks must be employed. In this regard, we are proposing the synthesis of two stable COFs named as TpPA-2 and TpPA-3 [6.2a] as the host frameworks, which is highly stable for Lewis bases due to the hydrophobic pore surface in presence of a methyl and ethyl groups. Syntheses of these COFs will be done by the Schiff base reactions of 1,3,5-



triformylphloroglucinol (**Tp**) with 2,5-dimethyl-*p*-phenylenediamine (**Pa-2**) and 2,5-diethyl-*p*-phenylenediamine (**Pa-3**), respectively, in 1:1 mesitylene/dioxane. The ligand tetrabutyl ammonium hydroxide salt,  $\text{NBu}_4\text{OH}$  (Bu =n-butyl), was selected as the included salt. We believe, the hydrophobic nature of n-butyl groups will interact with hydrophobic frameworks of TpPA-2 and TpPA-3 and leaves  $\text{OH}^-$  ions free for conduction (Figure 6.4).

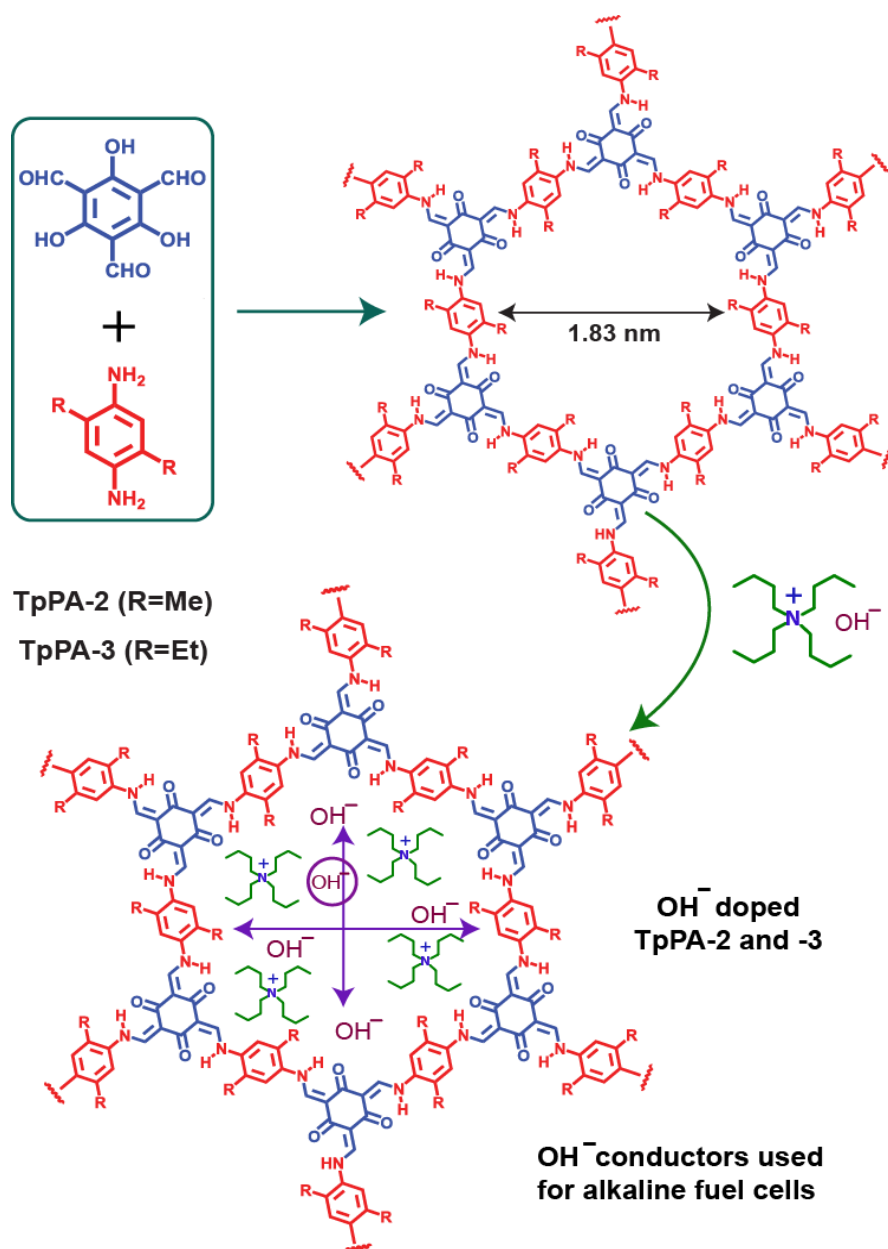


**Figure 6.4.** Scheme of synthesis and structures of stable COFs loaded with n-tetrabutylammonium hydroxide ( $\text{NBu}_4\text{OH}$ ) salts inside the pore surface. Hydrophobic interaction between  $\text{NBu}_4^+$  cations and COF frameworks leaves  $\text{OH}^-$  ions free for conduction.

## REFERENCES

## CHAPTER 1

- [1.1] (a) M. E. Davis, *Nature*, 2002, **417**, 813. (b) Y. Ma, W. Tong, H. Zhou, S. L. Suib, *Micropor Mesopor Mat*, 2000, **37**, 243.
- [1.2] (a) A. Corma, *Chem. Rev.*, 1997, **97**, 2373. (b) F. Schüth and W. Schmidt, *Adv. Mater.* 2002, **9**, 629.
- [1.3] (a) M. Eddaoudi, D. B. Moler, H. Li, B. Chen, T. M. Reinecke, M. O’Keeffe, O. M. Yaghi, *Acc. Chem. Res.*, 2001, **34**, 319. (b) C. Janiak, *Angew. Chem., Int. Ed. Engl.*, 1997, **36**, 1431. (c) A. J. Blake, N. R. Champness, P. Hubberstey, W.-S. Li, M. A. Withersby, M. Schroder, *Coord. Chem. Rev.*, 1999, **183**, 117. (d) B. Kesanli, Y. Cui, M. Smith, E. Bittner, B. Bockrath, W. Lin, *Angew. Chem., Int. Ed.*, 2005, **44**, 72. (e) S. Kitagawa, R. Kitaura, S. -I. Noro, *Angew. Chem., Int. Ed.*, 2004, **43**, 2334. (f) G. Ferey, *Chem. Soc. Rev.*, 2008, **37**, 191. (g) B. Chen, S. Xiang, G. Qian, *Acc. Chem. Res.*, 2010, **43**, 1115. (h) L. Ma, C. Abney, W. Lin, *Chem. Soc. Rev.*, 2009, **38**, 124. (i) Z. G. Gu, Y. P. Cai, H. C. Fang, Z. Y. Zhou, P. K. Thallapally, J. A. Tian, J. Liu, G. J. Exarhos, *Chem. Commun.*, 2010, **46**, 5373. (j) B. Chen, M. Eddaoudi, S. T. Hyde, M. O’Keeffe, O. M. Yaghi, *Science*, 2001, **291**, 1021. (k) P. Pachfule, Y. Chen, J. Jiang, R. Banerjee *J. Mater. Chem.*, 2011, **21**, 17737. (l) J. W. Yoon, S. H. Jhung, Y. K. Hwang, S. M. Humphrey, P. T. Wood, J. -S. Chang, *Adv. Mater.*, 2007, **19**, 1830. (m) K. L. Mulfort, O. K. Farha, C. D. Malliakas, M. G. Kanatzidis and J. T. Hupp, *Chem. Eur. J.*, 2010, **16**, 276. (n) H. -S. Choi, M. P. Suh, *Angew. Chem.*, 2009, **121**, 6997. (o) X. Gu, Z.-H. Lu, Q. Xu, *Chem. Commun* 2010, **46**, 7400. (p) S. -T. Zheng, J. T. Bu, Y. Li, T. Wu, F. Zuo, P. Feng, X. Bu. *J. Am. Chem. Soc.*, 2010, **132**, 17062. (q) J. An, N. L. Rosi, *J. Am. Chem. Soc.*, 2010, **132**, 5578. (r) A. G. Wong-Foy, O. Lebel, A. J. Matzger, *J. Am. Chem. Soc.*, 2007, **129**, 15740. (s) H. Chun, D. N. Dybtsev, H. Kim, K. Kim, *Chem. Eur. J.*, 2005, **11**, 3521. (t) J. Rowsell, A. Millward, K. Park, O. Yaghi *J. Am. Chem. Soc.*, 2004, **126**, 5666.
- [1.4] (a) H. Furukawa, K. E. Cordova, M. O’Keeffe, O. M. Yaghi, *Science*, 2013, **341**, 6149. (b) R. J. Kupplera, D. J. Timmons, Q. -R. Fanga, J. -R. Lia, T. A. Makala, M. D. Younga, D. Yuana, D. Zhaoa, W. Zhuanga, H. -C. Zhou. *Coord. Chem. Rev.*,

- 2009, **253**, 3042. (c) A. Morozan, F. Jaouen, *Energy Environ. Sci.*, 2012, **5**, 9269.
- (d) A. U. Czaja, N. Trukhan, U. Müller, *Chem. Soc. Rev.*, 2009, **38**, 1284. (e) U. Mueller, M. Schubert, F. Teich, H. Puetter, K. Schierle-Arndt and J. Pastré *J. Mater. Chem.*, 2006, **16**, 626.
- [1.5] (a) N. Stock, S. Biswas *Chem. Rev.*, 2012, **112**, 933. (b) C. Dey, T. Kundu, B. P. Biswal, A. Mallick and R. Banerjee, *Acta Cryst.*, 2014, **B70**, 3.
- [1.6] (a) B. Sakintuna and Y. Yürüm *Ind. Eng. Chem. Res.*, 2005, **44**, 2893. (b) Y. Tao, H. Kanoh, L. Abrams, K. Kaneko, *Chem. Rev.*, 2006, **106**, 896.
- [1.7] (a) M. O’Keeffe, M. A. Peskov, S. J. Ramsden, O. M. Yaghi, *Acc. Chem. Res.*, 2008, 41, 1782. (b) M. O’Keeffe, O. M. Yaghi, *Chem. Rev.*, 2012, **112**, 675. (c) N. W. Ockwig, O. D.-Friedrichs, M. O’Keeffe, O. M. Yaghi, *Acc. Chem. Res.*, 2005, **38**, 176. (d) D. J. Tranchemontagne, Z. Ni, M. O’Keeffe, O. M. Yaghi, *Angew. Chem. Int. Ed.*, 2008, **47**, 5136.
- [1.8] H. Li, M. Eddaoudi, M. O’Keeffe, O. M. Yaghi. *Nature*, 1999, **402**, 276.
- [1.9] (a) L. J. Murray, M. Dincă, J. R. Long, *Chem. Soc. Rev.*, 2009, **38**, 1294 (b) Y. Tao, H. Kanoh, L. Abrams, K. Kaneko, *Chem. Rev.*, 2006, **106**, 896.
- [1.10] (a) M. P. Suh, H. J. Park, T. K. Prasad, D. -W. Lim, *Chem. Rev.*, 2012, **1128**, 782. (b) D. J. Collinsa, H. -C. Zhou, *J. Mater. Chem.*, 2007, **17**, 3154.
- [1.11] (a) N.L. Rosi, J. Eckert, M. Eddaoudi, D.T. Vodak, J. Kim, M. O’Keeffe, O.M. Yaghi, *Science*, 2003, **300**, 1127. (b) Y. Yan, X. Lin, S. Yang, A. J. Blake, A. Dailly, N. R. Champness, P. Hubberstey and M. Schröder *Chem. Commun.*, 2009, 1025. (c) O. K. Farha, A. O. Yazaydin, I. Eryazici, C. D. Malliakas, B. G. Hauser, M. G. Kanatzidis, S. T. Nguyen, R. Q. Snurr, J. T. Hupp, *Nat. Chem.*, 2010, **2**, 944. (d) H. Furukawa, N. Ko, Y. B. Go, N. Aratani, S. B. Choi, E. Choi, A. O. Yazaydin, R. Q. Snurr, M. O’Keeffe, J. Kim, O. M. Yaghi, *Science*, 2010, **329**, 424.
- [1.12] (a) S. Noro, S. Kitagawa, M. Kondo, K. Seki, *Angew. Chem. Int. Ed. Engl.*, 2000, **39**, 2082.
- [1.13] (a) H. K. Chae, D. Y. Siberio-Perez, J. Kim, Y. Go, M. Eddaoudi, A. J. Matzger, M. O’Keeffe and O. M. Yaghi, *Nature*, 2004, **427**, 523.
- [1.14] (a) J. Y. Lee, O. K. Farha, J. Roberts, K. A. Scheidt, S. T. Nguyen, J. T. Hupp, *Chem. Soc. Rev.*, 2009, **38**, 1450. (b) M. Zhao, S. Ou, C. -D. Wu *Acc. Chem. Res.*,

- 2014, **47**, 1199. (c) J. Gascon, A. Corma, F. Kapteijn, F. X. L. Xamena, *ACS Catal.*, 2014, **4**, 361.
- [1.15] (a) S. Hasegawa, S. Horike, R. Matsuda, S. Furukawa, K. Mochizuki, Y. Kinoshita, S. Kitagawa, *J. Am. Chem. Soc.*, 2007, **129**, 2607. (b) J. Gascon, U. Aktay, M. D. Hernandez-Alonso, G. P. M. van Klink, F. Kapteijn, *J. Catal.*, 2009, **261**, 75. (c) D.-Y. Hong, Y. K. Hwang, C. Serre, G. Férey, J.-S. Chang, *Adv. Funct. Mater.*, 2009, **19**, 1537. (d) A. Dhakshinamoorthy, M. Alvaro, Y. K. Hwang, Y. K. Seo, A. Corma, H. Garcia, *Dalton Trans.*, 2011, **40**, 10719. (e) F. Vermoortele, M. Vandichel, B. Van de Voorde, R. Ameloot, M. Waroquier, V. Van Speybroeck, D. E. De Vos, *Angew. Chem. Int. Ed.*, 2012, **51**, 4887. (f) M.-H. Xie, X. -L. Yang, C. Zou, C. -D. Wu, A. *Inorg. Chem.*, 2011, **50**, 5318. (g) M. Fujita, Y. J. Kwon, S. Washizu, K. Ogura, *J. Am. Chem. Soc.*, 1994, **116**, 1151. (h) D. Dang, P. Wu, C. He, Z. Xie, C. Duan, *J. Am. Chem. Soc.*, 2010, **132**, 14321. (i) T. Sawaki, T. Dewa, Y. Aoyama, *J. Am. Chem. Soc.*, 1998, **120**, 8539. (j) T. Sawaki, T. Dewa, Y. Aoyama, *J. Am. Chem. Soc.*, 1998, **120**, 8539. (k) N. B. Pathan, A. M. Rahatgaonkar, M. S. Chorghade, *Catal. Commun.*, 2011, **12**, 1170. (l) N. T. S. Phan, K. K. A. Le, T. D. Phan, *Appl. Catal. A.*, 2010, **382**, 246. (m) J. M. Roberts, B. M. Fini, A. A. Sarjeant, O. K. Farha, J. T. Hupp, K. A. Scheidt, *J. Am. Chem. Soc.*, 2012, **134**, 3334. (n) Y. Huang, Z. Zheng, T. Liu, J. Lü, Z. Lin, H. Li, R. Cao, *Catal. Commun.*, 2011, **14**, 27. (o) T. Osako, Y. Uozumi, *Heterocycles* 2010, **80**, 505. (p) B. Xiao, H. Hou, Y. Fan, *J. Organomet. Chem.*, 2007, **692**, 2014. (p) K. K. Tanabe, S. M. Cohen, *Inorg. Chem.*, 2010, **49**, 6766. (q) F. Gándara, A. García-Cortés, C. Cascales, B. Gómez-Lor, E. Gutiérrez-Puebla, M. Iglesias, A. Monge, N. Snejko, *Inorg. Chem.*, 2007, **46**, 3475. (r) S. Proch, J. Herrmannsdörfer, R. Kempe, C. Kern, A. Jess, L. Seyfarth, J. Senker, *Chemistry*, 2008, **14**, 8204. (s) H. L. Jiang, B. Liu, T. Akita, M. Haruta, H. Sakurai, Q. Xu, *J. Am. Chem. Soc.*, 2009, **131**, 11302. (t) Y. Li, L. Xie, Y. Li, J. Zheng, X. Li, *Chemistry*, 2009, **15**, 8951. (u) Y. K. Park, S. B. Choi, H. J. Nam, D. Y. Jung, H. C. Ahn, K. Choi, H. Furukawa, J. Kim, *Chem. Commun.*, 2010, **46**, 3086. (v) B. Gomez-Lor, E. Gutiérrez-Puebla, M. Iglesias, M. A. Monge, C. Ruiz-Valero, N. Snejko, *Inorg. Chem.*, 2002, **41**, 2429.

- [1.16] (a) R. E. Dickinson, R. J. Cicerone *Nature* 1986, **319**, 109. (b) M. R. Allen, D. J. Frame, C. Huntingford, C. D. Jones, J. A. Lowe, M. Meinshausen, N. Meinshausen. *Nature* 2009, **458**, 1163.
- [1.17] (a) M. R.M. Abu-Zahraa, J. P.M. Niederer, P. H.M. Feron, G. F. Versteeg *Int. J. Green Gas Cont.*, 2007, **1**, 135. (b) J. D. Figueroa, T. Fout, S. Plasynski, H. McIlvried, R. D. Srivastava. *Int. J. Green Gas Cont.*, 2008, **2**, 9. (c) T. Lewis, M. Faubel, B. Winter, J. C. Hemminger, *Angew. Chem. Int. Ed.*, 2011, **50**, 1.
- [1.18] (a) E. Kintisch, *Science*, 2007, **317**, 184. (b) H. Herzog, E. Drake, E. Adams, *CO<sub>2</sub> Capture, Reuse, and Storage Technologies for Mitigating Global Climate Change*; Report No. DE-AF22-96PC01257; U.S. Department of Energy: Washington, D.C., 1997. (c) D. Reichle, et al. *Carbon Sequestration Research and Development*; Department of Energy: Washington, D.C. 1999, Chapter 2. (d) E. J. Granite, H. W. Pennline, *Ind. Eng. Chem. Res.*, 2002, **41**, 5470.
- [1.19] J. D. Figueroa, T. Fout, S. Plasynski, H. McIlvried, R. D. Srivastava, *Int. J. Greenhouse Gas Control*, 2008, **2**, 9.
- [1.20] D. Aaron, C. Tsouris, *Sep. Sci. Technol.*, 2005, **40**, 321.
- [1.21] (a) R. S. Franchi, P. J. E. Harlick, A. Harlick, *Ind. Eng. Chem. Res.*, 2005, **44**, 8007. (b) S. Cavenati, C. A. Grande, A. E. Rodrigues, *J. Chem. Eng. Data*, 2004, **49**, 1095.
- [1.22] (a) P. Misaelides, *Sep. Sci. Technol.*, 2011, **144**, 15. (b) T. Kyotani, *Carbon*, 2000, **38**, 269.
- [1.23] A. R. Millward, O. M. Yaghi. *J. Am. Chem. Soc.*, 2005, **127**, 17998.
- [1.24] (a) M. Xue, Y. Liu, R. M. Schaffino, S. Xiang, X. Zhao, G. -S. Zhu, S. -L. Qiu, B. Chen, *Inorg. Chem.*, 2009, **48**, 4649. (b) P. D. C. Dietzel, V. Besikiotis, R. Blom, *J. Mater. Chem.*, 2009, **19**, 7362. (c) Z. R. Herm, J. A. Swisher, B. Smit, R. Krishna, J. R. Long, *J. Am. Chem. Soc.*, 2011, **133**, 5664. (d) J. A. Botas, G. Calleja, M. Sanchez, M. G. Orcajo, *Langmuir*, 2010, **26**, 5300. (e) J. -S. Choi, W. -J. Son, J. Kim, W.-S. Ahn, *Microporous Mesoporous Mater.* 2008, **116**, 727. (f) K. Gedrich, I. Senkovska, N. Klein, U. Stoeck, A. Henschel, M. R. Lohe, I. A. Baburin, U. Mueller, S. Kaskel, *Angew. Chem., Int. Ed.*, 2010, **49**, 8489. (g) D. -W. Jung, D. -A. Yang, J. Kim, W. -S. Ahn, *Dalton Trans.*, 2010, **39**, 2883. (h) D. Yuan, D. Zhao, D. Sun, H. -C. Zhou, *Angew. Chem., Int. Ed.*, 2010, **49**, 5357. (i) P. L. Llewellyn, S.

- Bourrelly, C. Serre, A. Vimont, M. Daturi, L. Hamon, G. D. Weireld, J. -S. Chang, D. -Y. Hong, Y. K. Hwang, S. H. Jung, G. Ferey, *Langmuir*, 2008, **24**, 7245. (j) Z. Zhang, S. Huang, S. Xian, H. Xi, Z. Li, *Energy Fuels*, 2011, **25**, 835. (k) P. D. C. Dietzel, V. Besikiotis, R. Blom, *J. Mater. Chem.*, 2009, **19**, 7362. (l) B. Mu, P. M. Schoenecker, K. S. Walton, *J. Phys. Chem. C.*, 2010, **114**, 6464. (m) C. Tan, S. Yang, N. R. Champness, X. Lin, A. J. Blake, W. Lewis, M. Schroder *Chem. Commun.* 2011, **47**, 4487. (n) Y. K. Park, S. B. Choi, H. Kim, K. Kim, B.-H. Won, K. Choi, J. -S. Choi, W. -S. Ahn, N. Won, S. Kim, D. H. Jung, S. -H. Choi, G. -H. Kim, S. -S. Cha, Y. H. Jhon, J. K. Yang, J. Kim, *Angew. Chem., Int. Ed.*, 2007, **46**, 8230. (o) J. Moellmer, A. Moeller, F. Driesbach, R. Glaeser, R. Staudt, *Microporous Mesoporous Mater.* 2011, **138**, 140. (p) L. Hamon, E. Jolimaitre, G. D. Pirngruber, *Ind. Eng. Chem.Res.*, 2010, **49**, 7497. (q) Z. Liang, M. Marshall, A. L. Chaffee, *Energy Procedia*, 2009, **1**, 1265. (r) Z. Liang, M. Marshall, A. L. Chaffee, *Energy Fuels*, 2009, **23**, 2785. (s) Z. Liang, M. Marshall, A. L. Chaffee, *Microporous Mesoporous Mater.* 2010, **132**, 305. (t) S. K. Nune, P. K. Thallapally, A. Dohnalkova, C. Wang, J. Liu, G. J. Exarhos, *Chem. Commun.* 2010, **46**, 4878. (u) S. Bourrelly, P. L. Llewellyn, C. Serre, F. Millange, T. Loiseau, G. Ferey, *J. Am. Chem. Soc.*, 2005, **127**, 13519. (v) S. Couck, J. F. M. Denayer, G. V. Baron, T. Remy, J. Gascon, F. Kapteijn, *J. Am. Chem. Soc.*, 2009, **131**, 6326. (w) H. J. Park, M. P. Suh, *Chem. Commun.* 2010, **46**, 610. (x) I. Senkovska, F. Hoffmann, M. Froba, J. Getzschmann, W. Bohlmann, S. Kaskel, *Microporous Mesoporous Mater.* 2009, **122**, 93. (y) P. Chowdhury, C. Bikkina, S.J. Gumma, *Phys. Chem. C.*, 2009, **113**, 6616. (z) S. Galli, N. Masciocchi, G. Tagliabue, A. Sironi, J. A. R. Navarro, J. M. Salas, L. Mendez-Li~nan, M. Domingo, M. Perez-Mendoza, E. Barea, *Chem.Eur. j.*, 2008, **14**, 9890.
- [1.25] K. Sumida, D. L. Rogow, J. A. Mason, T. M. McDonald, E. D. Bloch, Z. R. Herm, T. -H. Bae, J. R. Long, *Chem. Rev.*, 2012, **112**, 724.
- [1.26] (a) Z. Bao, L. Yu, Q. Ren, X. Lu, S. J. Deng, *Colloid Interface Sci.* 2011, **353**, 549. (b) A. O. Yazaydin, R. Q. Snurr, T.-H. Park, K. Koh, J. Liu, M. D. LeVan, A. I. Benin, P. Jakubczak, M. Lanuza, D. B. Galloway, J. L. Low, R. R. *J. Am. Chem. Soc.*, 2009, **131**, 18198. (c) J. A. Mason, K. Sumida, Z. R. Herm, R. Krishna, J. R.

- Long, *Energy Environ. Sci.*, 2011, **4**, 3030. (d) D. Britt, H. Furukawa, B. Wang, T. G. Glover and O. M. Yaghi, *Proc Natl Acad Sci USA* 2009, **106**, 20637. (e) S. R. Caskey, A. G. Wong-Foy, A. J. Matzger, *J. Am. Chem. Soc.*, 2008, **130**, 10870. (f) A. O. Yazaydin, A. I. Benin, S. A. Faheem, P. Jakubczak, J. L. Low, R. Willis, R. R. Q. Snurr, *Chem. Mater.*, 2009, **21**, 1425. (g) J. Liu, Y. Wang, A. I. Benin, P. Jakubczak, R. R. Willis, M. D. LeVan, *Langmuir*, 2010, **26**, 14301. (h) P. D. C. Dietzel, R. E. Johnsen, H. Fjellvag, S. Bordiga, E. Groppo, S. Chavan, R. Blom, *Chem. Commun.*, 2008, 5125 (i) P. Aprea, D. Caputo, N. Gargiulo, F. Iucolano, F. Pepe, *J. Chem. Eng. Data*, 2010, **55**, 3655 (j) P. Chowdhury, C. Bikkina, D. Meister, F. Dreisbach, S. Gumma, *Microporous Mesoporous Mater.* 2009, **117**, 406. (k) J. Liu, Y. Wang, A. I. Benin, P. Jakubczak, R. R. Willis, M. D. LeVan, *Langmuir*, 2010, **26**, 14301. (l) D. Farrusseng, C. Daniel, C. Gaudillère, U. Ravon, Y. Schuurman, C. Mirodatos, D. Dubbeldam, H. Frost, R. Q. Snurr, *Langmuir*, 2009, **25**, 7383. (m) J. Kim, S. -T. Yang, S. B. Choi, J. Sim, J. Kim, W. -S. Ahn, *J. Mater. Chem.*, 2011, **21**, 3070. (n) T. M. McDonald, D. M. D'Alessandro, R. Krishna, J. R. Long. *Chem. Sci.*, 2011, **2**, 2022. (o) J. An, S. J. Geib, N. Rosi, *J. Am. Chem. Soc.*, 2009, **132**, 38. (p) A. Demessence, D. M. D'Alessandro, M. L. Foo, J. R. Long, *J. Am. Chem. Soc.*, 2009, **131**, 8784. (q) R. Vaidhyanathan, S. S. Iremonger, K. W. Dawson, G. K. H. Shimizu, *Chem. Commun.* 2009, 5230. (r) B. Arstad, H. Fjellvåg, K. O. Kongshaug, O. Swang, R. Blom, *Adsorption*, 2008, **14**, 755. (s) T. K. Prasad, D. H. Hong, M. P. Suh, *Chem. Eur. J.*, 2010, **16**, 14043. (t) K. Sumida, S. Horike, S. S. Kaye, Z. R. Herm, W. L. Queen, C. M. Brown, F. Grandjean, G. J. Long, A. Dailly, J. R. Long, *Chem. Sci.*, 2010, **1**, 184. (u) J. Kim, S. -T. Yang, S. B. Choi, J. Sim, J. Kim, W. -S. Ahn. *J. Mater. Chem.*, 2011, **21**, 3070. (v) H. Kanoh, A. Kondo, H. Noguchi, H. Kajiro, A. Tohdoh, Y. Hattori, W. -C. Xu, M. Inoue, T. Sugiura, K. Morita, H. Tanaka, T. Ohba, K. J. Kaneko, *Colloid Interface Sci.*, 2009, **334**, 1. (w) O. K. Farha, C. D. Malliakas, M.G. Kanatzidis, J. T. Hupp *J. Am. Chem. Soc.*, 2010, **132**, 950. (x) Y. -S. Bae, O. K. Farha, J. T. Hupp, R. Q. Snurr, *J. Mater. Chem.*, 2009, **19**, 2131. (y) Y. -S. Bae, O. K. Farha, A. M. Spokoyny, C. A. Mirkin, J. T. Hupp, R. Q. Snurr. *Chem. Commun.*, 2008, 4135

- [1.27] (a) Material with high CO<sub>2</sub> should poses high adsorption enthalpy like Mg-MOF-74 (47 kJ/mol) and high CO<sub>2</sub> uptake like MOF-177 (761.6 cc/gm) at 42 bar and 298K. C. Lastoskie, *Science*, 2010, **330**, 595. (b) D. Yu, A. O. Yazaydin, J. R. Lane, P. D. C. Dietzel, *Chem. Sci.*, 2013, **4**, 3544.
- [1.28] S. S. -Y. Chui, S. M. -F. Lo, J. Charmant, A. G. Orpen, I. D. Williams, *Science*, 1999, **283**, 1148.
- [1.29] (a) Y. F. Chen, A. Nalaparaju, M. Eddaoudi, J. W. Jiang, *Langmuir*, 2012, **28**, 3903. (b) R. Babarao, J. W. Jiang, *Ind Eng Chem Res.* 2010, **50**, 62.
- [1.30] Q. Xu , D. Liu, Q. Yang , C. Zhong, J. Mi *J. Mater. Chem.*, 2010, **20**, 706.
- [1.31] (a) Y. -S. Bae, B.G. Hauser, O. K. Farha, J. T Hupp, R. Q. Snurr, *Micropor Mesopor Mat.*, 2011, **141**, 231. (b) O. K. Farha, Y.-S. Bae, B.G. Hauser, A. M. Spokoyny, R.Q. Snurr, C. Mirkin, J. T. Hupp. *Chem. Commun.*, 2010, **46**, 1056.
- [1.32] (a) B. Arstad, R. Blom, O. Swang, *J. Phys. Chem. A*, 2007, **111**, 1222. (b) E. F. da Silva and H. F. Svendsen, *Int. J. Greenhouse Gas Control*, 2007, **1**, 151.
- [1.33] (a) R. Vaidhyanathan, S. S. Iremonger, G. K. H. Shimizu, P. G. Boyd, S. Alavi, T. K. Woo, *Science*, 2010, **330**, 650.
- [1.34] T. M. McDonald, W. R. Lee, J. A. Mason, B. M. Wiers, C. S. Hong, J. R. Long, *J. Am. Chem. Soc.*, 2012, **134**, 7056.
- [1.35] (a) J. An, S. J. Geib, N. L. Rosi, *J. Am. Chem. Soc.*, 2010, **132**, 38. (b) T. K. Prasad, D. H. Hong, M. P. Suh, *Chem. Eur. J.*, 2010, **16**, 14043. (c) S. -S. Chen, M. Chen, S. Takamizawa, P. Wang, G. -C. Lv, W. -Y. Sun, *Chem. Commun.*, 2011, **47**, 4902. (d) F. Debatin, A. Thomas, A. Kelling, N. Hedin, Z. Bacsik, I. Senkovska, S. Kaskel, M. Junginger, H. Muller, U. Schilde, C. Jager, A. Friedrich, H. -J. Holdt, *Angew. Chem., Int. Ed.*, 2010, **49**, 1258. (e) G. Beobide, W. -G. Wang, O. Castillo, A. Luque, P. Roman, G. Tagliabue, S. Galli, J. A. R. Navarro, *Inorg. Chem.*, 2008, **47**, 5267.
- [1.36] D. Aaron, C. Tsouris, *Sep. Sci. Technol.*, 2005, **40**, 321.
- [1.37] (a) K. S. Park, N. Zheng, A. -P. Côté, J. Y. Choi, R. Huang, F. J. Uribe-Romo, H. K. Chae, M. O’Keeffe, O. M. Yaghi, *Proc. Natl. Acad. Sci., U.S.A.*, 2006, 10310186 (b) X. -C. Huang, Y. -Y. Lin, J. -P. Zhang, X. -M. Chen, *Angew. Chem., Int. Ed.*, 2006, **45**, 1557. (c) R. Banerjee, A. Phan, B. Wang, C. Knobler, H. Furukawa, M.



- O’Keeffe, O. M. Yaghi, *Science*, 2008, **319**, 939. (d) R. Banerjee, H. Furukawa, D. Britt, C. Knobler, M. O’Keeffe, O. M. Yaghi, *J. Am. Chem. Soc.*, 2009, **131**, 3875. (e) B. Wang, A. P. Côté, H. Furukawa, M. O’Keeffe, O. M. Yaghi, *Nature*, 2008, **453**, 207. (f) A. J. Cairns, J. A. Perman, L. Wojtas, V. Ch. Kravtsov, M. H. Alkordi, M. Eddaoudi, M. J. Zaworotko, *J. Am. Chem. Soc.*, 2008, **130**, 1560.
- [1.38] U.S. Department of Energy, U.S. Energy Information Administration: International Energy Outlook 2013 (Report: DOE/EIA-0484(2013)), 2013.
- [1.39] (a) Boyle, Godfrey. *Renewable energy*. OXFORD university press, 2004. (b) Johansson, Thomas B., and Laurie Burnham, eds. *Renewable energy: sources for fuels and electricity*. Island Press, 1993.
- [1.40] (a) G. W. Crabtree, M. S. Dresselhaus, *MRSBull.* 2008, **33**, 421. (b) S. Hamrock and M. Yandrasits, *Polym. Rev.*, 2006, **46**, 219.
- [1.41] (a) K. -D. Kreuer, *Chem. Mater.*, 1996, **8**, 610. (b) K. -D. Kreuer, *J. Membr. Sci.*, 2001, **185**, 29. (c) K. D. Kreuer, S. J. Paddison, E. Spohr, M. Schuster, *Chem. Rev.*, 2004, **104**, 4637. (c) B., Atilla. *Int. J. Hydrogen Energ*, 2005, **30**, 1181. (d) Y. Shao, G. Yin, Z. Wang, Y. Gao, *J. Power Sources*, 2007, **167**, 235.
- [1.42] (a) K. A. Mauritz, R. B. Moore, *Chem. Rev.*, 2004, **104**, 4535. (b) G. Alberti, R. Narducci, M. Sganappa, *J. Power Source*, 2008, **178**, 575. (c) G. Alberti, R. Narducci, *Fuel Cells*, 2009, **9**, 410. (d) K. A. Mauritz and R. B. Moore, *Chem. Rev.*, 2004, **104**, 4535.
- [1.43] (a) G. K. H. Shimizu, J. M. Taylor, S. Kim, *Science*, 2013, **341**, 354. (b) S. Horike, D. Umeyama, S. Kitagawa, *Acc. Chem. Res.*, 2013, **46**, 2376. (c) N. Agmon *Chem. Phys. Lett.* 1995, **5**, 456. (d) H. Arribart, Y. Piffard, *Solid State Commun*, 1983, **45**, 571. (e) K. D. Kreuer, A. Rabenau, W. Weppner, *Angew. Chem., Int. Ed. Engl.*, 1982, **21**, 208.
- [1.44] (a) A. Shigematsu, T. Yamada, H. Kitagawa, *J. Am. Chem. Soc.*, 2011, **133**, 2034. (b) J. M. Taylor, R. K. Mah, I. L. Moudrakovski, C. I. Ratcliffe, R. Vaidyanathan, G. K. H. Shimizu, *J. Am. Chem. Soc.*, 2010, **132**, 14055. (c) T. Yamada, M. Sadakiyo, H. Kitagawa, *J. Am. Chem. Soc.*, 2009, **131**, 3144. (d) M. Yoon, K. Suh, H. Kim, Y. Kim, N. Selvapalam, K. Kim, *Angew. Chem. Int. Ed.*, 2011, **50**, 7870. (e) M. Sadakiyo, T. Yamada, H. Kitagawa, *J. Am. Chem. Soc.*, 2009, **131**, 9906. (f)

- V. G. Ponomareva, K. A. Kovalenko, A. P. Chupakhin, D. N. Dybtsev, E. S. Shutova, V. P. Fedin, *J. Am. Chem. Soc.*, 2012, **134**, 15640. (g) S. Kanda, K. Yamashita, K. Ohkawa, *Bull. Chem. Soc. Jpn.*, 1979, **52**, 3296. (h) T. Yamada, S. Morikawa, H. Kitagawa, *Bull. Chem. Soc. Jpn.*, 2010, **83**, 42. (i) S. Kim, K. W. Dawson, B. S. Gelfand, J. M. Taylor, G. K. H. Shimizu, *J. Am. Chem. Soc.*, 2013, **135**, 963. (j) S. C. Sahoo, T. Kundu, R. Banerjee. *J. Am. Chem. Soc.*, 2011, **133**, 17950. (k) S. Sen, N. N. Nair, T. Yamada, H. Kitagawa, P. K. Bharadwaj, *J. Am. Chem. Soc.*, 2012, **134**, 19432. (l) C. Dey, T. Kundu, R. Banerjee. *Chem. Commun.*, 2012, **48**, 266. (m) H. Okawa, A. Shigematsu, M. Sadakiyo, T. Miyagawa, K. Yoneda, M. Obha, H. Kitagawa, *J. Am. Chem. Soc.*, 2009, **131**, 13516. (n) E. Pardo, C. Train, G. Gontard, K. Boubekour, O. Fabelo, H. Liu, B. Dkhil, F. Lloret, K. Nakagawa, H. Tokoro, S. Ohkoshi, M. Verdaguer, *J. Am. Chem. Soc.*, 2011, **133**, 15328. (o) B. M. Wiers, M. -L. Foo, N. P. Balsara, J. R. Long, *J. Am. Chem. Soc.*, 2011, **133**, 14522. (p) M. Sadakiyo, H. Okawa, A. Shigematsu, M. Obha, T. Yamada, H. Kitagawa, *J. Am. Chem. Soc.*, 2012, **134**, 5472. (q) C. Serre, F. Millange, C. Thouvenot, M. Nogus, G. Marsolier, D. Lour, G. Frey, *J. Am. Chem. Soc.*, 2002, **124**, 13519. (r) A. Shigematsu, T. Yamada, H. Kitagawa, *J. Am. Chem. Soc.*, 2011, **133**, 2034. (s) T. Kundu, S. C. Sahoo, R. Banerjee. *Chem. Commun.*, 2012, **48**, 4998. (t) V. G. Ponomareva, K. A. Kovalenko, A. P. Chupakhin, D. N. Dybtsev, E. S. Shutova, V. P. Fedin, *J. Am. Chem. Soc.*, 2012, **134**, 15640.
- [1.45] a) S. Bureekaew, S. Horike, M. Higuchi, M. Mizuno, T. Kawamura, D. Tanaka, N. Yanai, S. Kitagawa, *Nat. Mater.*, 2009, **8**, 831. (b) J. A. Hurd, R. Vaidhyanathan, V. Thangadurai, C. I. Ratcliffe, I. L. Moudrakovski, G. K. Shimizu, *Nat. Chem.*, 2009, **1**, 705. (c) D. Umeyama, S. Horike, M. Inukai, Y. Hijikata, S. Kitagawa, *Angew. Chem., Int. Ed.*, 2011, **50**, 11706. (d) S. Horike, D. Umeyama, M. Inukai, T. Itakura, S. Kitagawa, *J. Am. Chem. Soc.*, 2012, **134**, 7612. (e) D. Umeyama, S. Horike, M. Inukai, T. Itakura, S. Kitagawa, *J. Am. Chem. Soc.*, 2012, **134**, 12780.
- [1.46] (a) K. D. Kreuer, S. J. Paddison, E. Spohr, M. Schuster, *Chem. Rev.*, 2004, **104**, 4637. (b) M. F. H. Schuster, W. H. Meyer, *Annu. Rev. Mater. Res.*, 2003, **33**, 233. (c) P. Jannasch, *Curr. Opin. Colloid Interface Sci.*, 2003, **8**, 96.

- [1.47] (a) G. Alberti, U. Constantino, M. Casciola, R. Vivani, A. Peraio, *Solid State Ionics*, 1991, **46**, 61. (b) K. D. Kreuer, A. Fuchs, M. Ise, M. Spaeth, J. Maier, *Electrochim. Acta*, 1998, **43**, 1281. (c) W. Munch, K. D. Kreuer, W. Silvestri, J. Maier, G. Seifert, *Solid State Ionics*, 2001, **145**, 437.
- [1.48] (a) S. C. Sahoo, T. Kundu, R. Banerjee. *J. Am. Chem. Soc.*, 2011, **133**, 17950. (b) J. M. Taylor, R. K. Mah, I. L. Moudrakovski, C. I. Ratcliffe, R. Vaidhyanathan, G. K. H. Shimizu, *J. Am. Chem. Soc.*, 2010, **132**, 14055.
- [1.49] (a) A. Comotti, S. Bracco, P. Sozzani, S. Horike, R. Matsuda, J. Chen, M. Takata, Y. Kubota, S. Kitagawa, *J. Am. Chem. Soc.*, 2008, **130**, 13664. (b) T. Loiseau, C. Serre, C. Huguenard, G. Fink, F. Taulelle, M. Henry, T. Bataille, G. Férey, *Chem. Eur. J.*, 2004, **10**, 1373.

## CHAPTER 2

- [2.1] <http://www.iza-structure.org/databases/>; Reticular Chemistry Structure Resource (RCSR), <http://rcsr.anu.edu.au/home>; M. O’Keeffe, B. G. Hyde, *Crystal Structures I. Patterns and Symmetry*; Mineralogical Society of America: Washington, DC, 1996. [2.2] (a) J. C. Jansen, in *Introduction to Zeolite Science and Practice*; A. van Bekkum, P. A. Jacobs, E. M. Flanigen, J. C. Jansen, Eds. Elsevier: Amsterdam, 2001. (b) C. Baerlocher, W. M. Meier, D. H. Olson, *Atlas of Zeolite Framework Types*, Elsevier: Amsterdam, 2001.
- [2.3] O. D.-Friedrichs, M. D. Foster, M. O’Keeffe, D. M. Proserpio, M. Treacy, O. M. Yaghi, *J. Solid State Chem.*, 2005, **178**, 2533.
- [2.4] Diamond has also been described as the underlying topology of a MOF structure that actually has low crystallographic symmetry (reference 1.7a)
- [2.5] M. O’Keeffe, B. G. Hyde, *Crystal Structures I. Patterns and Symmetry* Mineralogical Society of America: Washington, DC, 1996.
- [2.6] (a) G. R. Desiraju, *Chem. Commun.*, 2005, **24**, 2995. (b) G. R. Desiraju, *Acc. Chem. Res.*, 2002, **35**, 565. (c) J. Elguero, *Angew. Chem. Int. Ed.*, 2001, **40**, 799.
- [2.7] (a) A. Sayari, Y. Belmabkhout, *J. Am. Chem. Soc.*, 2010, **132**, 6312 (b) W. Morris, B. Leung, H. Furukawa, O. K. Yaghi, N. He, H. Hayashi, Y. Houndonougbo, M. Asta, B. B. Laird, O. M. Yaghi, *J. Am. Chem. Soc.*, 2010, **132**, 11006.

- [2.8] A. Samanta, T. Furuta, J. Li, *J. Chem. Phys.*, 2006, **125**
- [2.9] O. S. Smart, J. G. Neduvellil, X. Wang, B. A. Wallace, M. S. P. Sansom, *J. Mol. Graphics Model.*, 1996, **14**, 354.
- [2.10] Materials Studio, v., Accelrys: San Diego, 2007.
- [2.11] A. Hirotsu, K. Mizukami, R. Miura, H. Takaba, T. Miya, A. Fahmi, A. Stirling, M. Kubo, A. Miyamoto, *Appl. Surf. Sci.*, 1997, **120**, 81.
- [2.12] A. K. Rappe, C. J. Casewit, K. S. Colwell, W. A. Goddard, W. M. Skiff, *J. Am. Chem. Soc.*, 1992, **114**, 10024.
- [2.13] G. Garberoglio, A. I. Skoulidas, J. K. Johnson, *J. Phys. Chem. B.*, 2005, **109**, 13094.
- [2.14] A. I. Skoulidas, D. S. Sholl, *J. Phys. Chem. B.*, 2005, **109**, 15760.
- [2.15] R. Babarao, Z. Q. Hu, J. W. Jiang, S. Chempath, S. I. Sandler, *Langmuir*, 2007, **23**, 659.
- [2.16] R. Babarao, J. W. Jiang, *Langmuir*, 2008, **24**, 6270.
- [2.17] S. F. Boys and F. Bernardi, *Mol. Phys.*, 1970, **19**, 553.
- [2.18] M. J. Frisch, G. W. Trucks, H. B. Schlegel, G. E. Scuseria, M. A. Robb, J. R. Cheeseman, V. G. Zakrzewski, J. A. Montgomery, R. E. Stratmann, J. C. Burant, S. Dapprich, J. M. Millam, A. D. Daniels, K. N. Kudin, M. C. Strain, O. Farkas, J. Tomasi, V. Barone, M. Cossi, R. Cammi, B. Mennucci, C. Pomelli, C. Adamo, S. Clifford, J. Ochterski, G. A. Petersson, P. Y. Ayala, Q. Cui, K. Morokuma, D. K. Malick, A.D. Rabuck, K. Raghavachari, J. B. Foresman, J. Cioslowski, J. V. Ortiz, B. B. Stefanov, G. Liu, A. Liashenko, P. Piskorz, I. Komaromi, R. Gomperts, R. L. Martin, D. J. Fox, T. Keith, M. A. Al-Laham, C. Y. Peng, A. Nanayakkara, C. Gonzalez, M. Challacombe, P. M. W. Gill, B. G. Johnson, W. Chen, M. W. Wong, J. L. Andres, M. Head-Gordon, E. S. Replogle and J. A. Pople, *Gaussian 09*, Revision D.01 ed. Gaussian Inc., Wallingford CT, **2009**.
- [2.19] Bruker (2005). *APEX2*. Version 5.053. Bruker AXS Inc., Madison, Wisconsin, USA.
- [2.20] Sheldrick, G. M. (2004). *CELL\_NOW*. University of Göttingen, Germany. Steiner, Th. (1998). *Acta Cryst.* B54, 456–463.
- [2.21] Bruker (2004). *SAINT-Plus* (Version 7.03). Bruker AXS Inc., Madison, Wisconsin, USA.

- [2.22] Sheldrick, G. M. (2002). *SADABS* (Version 2.03) and *TWINABS* (Version 1.02). University of Göttingen, Germany.
- [2.23] Sheldrick, G. M. (1997). *SHELXS '97* and *SHELXL '97*. University of Göttingen, Germany.
- [2.24] WINGX version 1.80.04. Louis Farrugia, University of Glasgow.
- [2.25] A. L. Spek (2005) *PLATON, A Multipurpose Crystallographic Tool*, Utrecht University, Utrecht, The Netherlands.
- [2.26] L. A. Dakin, P. C. Ong, J. S. Panek, R. J. Staples, and P. Stavropoulos, *Organometallics*, 2000, **19**, 2896.
- [2.27] S. Noro, R. Kitaura, M. Kondo, S. Kitagawa, T. Ishii, H. Matsuzaka, and M. Yamashita, *J. Am. Chem. Soc.*, 2002, **124**, 2568.
- [2.28] M. Eddaoudi, J. Kim, D. Vodak, A. Sudik, J. Wachter, M. O'Keeffe, and O. M. Yaghi, *Proc. Natl. Acad. Sci.*, USA, 2002, **99**, 4900.
- [2.29] R. A. Heintz, H. Zhao, X. Ouyang, G. Grandinetti, J. Cowen, and K. R. Dunbar, *Inorg. Chem.*, 1999, **38**, 144.
- [2.30] K. Biradha, Y. Hongo, and M. Fujita, *Angew. Chem. Int. Ed.* 2000, **39**, 3843.
- [2.31] P. Grosshans, A. Jouaiti, M. W. Hosseini, and N. Kyritsakas, *New J. Chem.*, (Nouv. J. Chim.) 2003, **27**, 793.
- [2.32] N. Takeda, K. Umemoto, K. Yamaguchi, and M. Fujita, *Nature (London)* 1999, **398**, 794.
- [2.33] M. Eddaoudi, J. Kim, N. Rosi, D. Vodak, J. Wachter, M. O'Keeffe, and O. M. Yaghi, *Science*, 2002, **295**, 469.
- [2.34] B. Kesanli, Y. Cui, M. R. Smith, E. W. Bittner, B. C. Bockrath, and W. Lin, *Angew. Chem. Int. Ed.*, 2005, **44**, 72.
- [2.35] F. A. Cotton, C. Lin, and C. A. Murillo, *Inorg. Chem.*, 2001, **40**, 478.

## CHAPTER 3

- [3.1] (a) K. Sumida, D. L. Rogow, J. A. Mason, T. M. McDonald, E. D. Bloch, Z. R. Herm, T.-H. Bae, J. R. Long, *Chem. Rev.*, 2012, **112**, 724. (b) T. Li, J. E. Sullivan, N. L. Rosi, *J. Am. Chem. Soc.*, 2013, **135**, 9984. (c) J. An, O. K. Farha, J. T. Hupp, E. Pohl, J. I. Yeh, N. L. Rosi, *Nat. Commun.*, 2012, **3**, 604. (d) L. J. Barbour, *Chem. Commun.*, 2006, **11**, 1163. (e) A. W. Thornton, K. M. Nairn, J. M. Hill, A. J. Hill, M. R. Hill *J. Am. Chem. Soc.*, 2009, **131**, 10662. (f) Y. Liu, Z. U. Wang, H. C. Zhou, *Greenhouse Gas Sci Technol.* 2012, **2**, 239.
- [3.2] (a) X. Lin, I. Telepeni, A. J. Blake, A. Dailly, C. M. Brown, J. M. Simmons, M. Zoppi, G. S. Walker, K. M. Thomas, T. J. Mays, P. Hubberstey, N. R. Champness, M. Schroder, *J. Am. Chem. Soc.*, 2009, **131**, 2159. (b) E. Neofotistou, C. D. Malliakas, P. N. Trikalitis, *Chem. Eur. J.*, 2009, **15**, 4523. (c) C. Zlotea, D. Phanon, M. Mazaj, D. Heurtaux, V. Guillern, C. Serre, P. Horcajada, T. Devic, E. Magnier, F. Cuevas, G. Ferey, P. L. Llewellyn, M. Latroche, *Dalton Transactions*, 2011, **40**, 4879. (d) P. Pachfule, Y. Chen, S. C. Sahoo, J. Jiang, R. Banerjee, *Chem. Mater.*, 2011, **23**, 2908. (e) K. L. Mulfort, J. T. Hupp, *J. Am. Chem. Soc.*, 2007, **129**, 9604. (f) K. L. Mulfort, O. K. Farha, C. L. Stern, A. A. Sarjeant, J. T. Hupp, *J. Am. Chem. Soc.*, 2009, **131**, 3866. (g) T. Gadzikwa, B. -S. Zhang, J. T. Hupp, J. G. Nguyen, *Chem. Commun.*, 2008, 3672. (h) J. L. C. Rowsell, O. M. Yaghi, *J. Am. Chem. Soc.*, 2006, **128**, 1304. (i) H. Deng, C. J. Doonan, H. Furukawa, R. B. Ferreira, J. Towne, C. B. Knobler, B. Wang, O. M. Yaghi, *Science*, 2010, **327**, 846. (j) D. Yuan, W. Lu, D. Zhao, H. -C. Zhou, *Adv. Mater.*, 2011, **23**, 3723. (k) J. Yang, A. Grzech, F. M. Mulder, T.J. Dingemans, *Chem. Commun.*, 2011, **47**, 5244.
- [3.3] (a) T. Li, J. E. Sullivan, N. L. Rosi, *J. Am. Chem. Soc.*, 2013, **135**, 9984. (b) J. An, O. K. Farha, J. T. Hupp, E. Pohl, J. I. Yeh, N. L. Rosi, *Nat. Commun.*, 2012, **3**, 604. (c) L. J. Barbour, *Chem. Commun.*, 2006, **11**, 1163. (d) R. Vaidhyanathan, S. S. Iremonger, K.W. Dawson, G. K. H. Shimizu, *Chem. Commun.*, 2009, 5230. (e) S. R. Caskey, A. G. Wong-Foy, A. J. Matzger, *J. Am. Chem. Soc.*, 2008, **130**, 10870. (f) B. Chen, N. W. Ockwig, A. R. Millward, D. S. Contreras, O. M. Yaghi, *Angew. Chem., Int. Ed.*, 2005, **44**, 4745. (g) T. M. McDonald, W. R. Lee, J. A. Mason, B. M. Wiers, C. S. Hong, J. R. Long *J. Am. Chem. Soc.*, 2012, **134**, 7056.

- [3.4] (a) T. Panda, P. Pachfule, Y. Chen, J. Jiang, R. Banerjee. *Chem. Commun.*, 2011, **47**, 2011. (b) T. Panda, K.gupta, J. Jiang, R. Banerjee. *CrystEngComm*, 2014., **DOI:** 10.1039/ C3CE42075B. (c) R. Vaidhyanathan, S. S. Iremonger, G. K. H. Shimizu, P. G. Boyd, S. Alavi, T. K. Woo. *Science*, 2010, **330**, 650.
- [3.5] D. Lässig, J. Lincke, H. Krautscheid, *Tetrahedron Lett.*, 2010, **51**, 653.
- [3.6] (a) M. Radha Kishan, T. Jian, P. K. Thallapally, C. A. Fernandez, S. J. Dalgarno, J. E. Warren, B. P. McGraila, J. L. Atwood, *Chem. Commun.*, 2010, **46**, 538. (b) H. -L. Jiang, Y. Tatsu, Z. -H. Lu, Q. Xu, *J. Am. Chem. Soc.*, 2010, **132**, 5586.
- [3.7] (a) O. M. Yaghi, M. O’Keeffe, N. W. Ockwig, H. K. Chae, M. Eddaoudi, J. Kim, *Nature*, 2003, **423**, 705. (b) S. Chen, J. Zhang, T. Wu, P. Feng, X. Bu, *J. Am. Chem. Soc.*, 2009, **131**, 16027. (c) L. Ma and W. Lin, *J. Am. Chem. Soc.*, 2008, **130**, 13834. (d) S. K. Ghosh, G. Savitha, P. K. Bharadwaj, *Inorg. Chem.*, 2004, **43**, 5495. (e) P. Mahata, A. Sundaresan, S. Natarajan. *Chem. Commun.*, 2007, **43**, 4471.
- [3.8] (a) S. Ma, D. Sun, M. Ambrogio, J. A. Fillinger, S. Parkin, H. -C. Zhou, *J. Am. Chem. Soc.*, 2007, **129**, 1858. (b) D. Zhao, D. J. Timmons, D. Yuan, H. -C. Zhou, *Acc. Chem. Res.*, 2011, **44**, 123.
- [3.9] (a) G. R. Desiraju, *Acc. Chem. Res.*, 2002, **35**, 565. (b) G. R. Desiraju, *Chem. Commun.*, 2005, 2995. (c) G. R. Desiraju, *CrystEngComm.*, 2003, **5**, 466. (d) P. Vishweshwar, R. Thaimattam, M. Jaskólski, G. R. Desiraju, *Chem. Commun.*, 2002, 1830.
- [3.10] (a) M. Eddaoudi, H. Li, O. M. Yaghi, *J. Am. Chem. Soc.*, 2000, **122**, 1391. (b) K. E. deKrafft, Z. Xie, G. Cao, S. Tran, L. Ma, O. Z. Zhou, W. Lin, *Angew. Chem. Int. Ed.*, 2009, **48**, 9901.
- [3.11] (a) F. Nouar, J. F. Eubank, T. Bousquet, L. Wojtas, M. J. Zaworotko, M. Eddaoudi, *J. Am. Chem. Soc.*, 2008, **130**, 1833. (b) S. Xiang, W. Zhou, J. M. Gallegos, Y. Liu, B. Chen, *J. Am. Chem. Soc.*, 2009, **131**, 12415. (c) D. J. Tranchemontagne, J. L. Mendoza-Cortes, M. O’Keefe, O. M. Yaghi, *Chem. Soc. Rev.*, 2009, **38**, 1257. (d) M. O’Keefe, M. Eddaoudi, H. Li, T. M. Reineke, O. M. Yaghi, *J. Solid State Chem.*, 2000, **152**, 3. (e) M. O’Keefe, B. G. Hyde, *Crystal Structures I. Patterns and Symmetry*; Mineralogical Society of America: Washington, DC, 1996.

- [3.12] A. W. Addison, T. N. Rao, J. Reedijk, J. V. Rijn and G. C. Verschoor, *J. Chem. Soc., Dalton Trans.*, 1984, 1349.
- [3.13] A. L. Spek (2005) PLATON, *A Multipurpose Crystallographic Tool*, Utrecht University, Utrecht, The Netherlands, 2007, **46**, 5046.

## CHAPTER 4

- [4.1] (a) X. C. Huang, W. Luo, Y. F. Shen, X. J. Lin, D. Li, *Chem. Commun.*, 2008, 3995. (b) A. L. Pickering, G. Seeber, D. L. Long, L. Cronin, *Chem. Commun.*, 2004, 136. (c) Z. Fei, D. Zhao, T. J. Geldbach, R. Scopelliti, P. J. Dyson, S. Antonijevic, G. Bodenhausen, *Angew. Chem. Int. Ed.*, 2005, **44**, 5720. (d) Q. -R. Fang, G. -S. Zhu, Z. Jin, Y. -Y. Ji, J. -W. Ye, M. Xue, H. Yang, Y. Wang, S. -L. Qiu, *Angew. Chem. Int. Ed.*, 2007, **46**, 6638.
- [4.2] (a) K. Otsubo, Y. Wakabayashi, J. Ohara, S. Yamamoto, H. Matsuzaki, H. Okamoto, K. Nitta, T. Uruga, H. Kitagawa, *Nat. Mater.* 2011, **10**, 291. (b) F. Dai, H. He, D. Sun, *J. Am. Chem. Soc.*, 2008, **130**, 14064. (c) L. Li, J. Luo, S. Wang, Z. Sun, T. Chen, M. Hong, *Cryst. Growth Des.*, 2011, **11**, 3744.
- [4.3] (a) P. Thanasekaran, T. T. Luo, C. H. Lee, K. L. Lu, *J. Mater. Chem.*, 2011, **21**, 13140. (b) T. T. Luo, H. C. Wu, Y. C. Jao, S. M. Huang, T. W. Tseng, Y. S. Wen, G.-H. Lee, S.-M. Peng, K. L. Lu, *Angew. Chem.*, 2009, **48**, 9461. (c) S. -N. Wang, H. Xing, Y. -Z. Li, J. Bai, M. Scheer, Y. Pan, X. -Z. You, *Chem. Commun.*, 2007, 2293. (d) Z. -Z. Lu, R. Zhang, Y. -Z. Li, Z. -J. Guo, H. -G. Zheng, *J. Am. Chem. Soc.*, 2011, **133**, 4172.
- [4.4] G. R. Desiraju, *Chem. Commun.*, 2005, 2995.
- [4.5] F. Bu and S. -J. Xiao, *CrystEngComm.*, 2010, **12**, 3385.
- [4.6] (a) M. H. Alkordi, J. A. Brant, L. Wojtas, V. C. Kravtsov, A. J. Cairns, M. Eddaoudi, *J. Am. Chem. Soc.*, 2009, **131**, 17753. (b) S. Sato, Y. Ishido, M. Fujita, *J. Am. Chem. Soc.*, 2009, **131**, 6064. (c) B. Moulton, J. J. Lu, A. Mondal, M. J. Zaworotko, *Chem. Commun.*, 2001, 863. (d) Dan Zhao, D. Yuan, R. Krishna, J. M. van Baten, H. C. Zhou, *Chem. Commun.*, 2010, **46**, 7352.



- [4.7] (a) T. Tsuruoka, S. Furukawa, Y. Takashima, K. Yoshida, S. Isoda, S. Kitagawa, *Angew. Chem. Int. Ed.*, 2009, **48**, 4739. (b) M. Jung, H. Kim, K. Baek and K. Kim, *Angew. Chem. Int. Ed.*, 2008, **47**, 5755.
- [4.8] (a) J. Sun, L. Weng, Y. Zhou, J. Chen, Z. Chen, Z. Liu, D. Zhao, *Angew. Chem., Int. Ed.*, 2002, **41**, 4471. (b) S. Chen, J. Zhang, T. Wu, P. Feng, X. Bu, *J. Am. Chem. Soc.*, 2009, **31**, 16027.
- [4.9] A. L. Spek (2005) *PLATON, A Multipurpose Crystallographic Tool*, Utrecht University, Utrecht, The Netherlands, 2007, **46**, 5046.
- [4.10] "Proton Conductors: Solids, Membranes and Gels-Materials and Devices": P. Colomban in *Chemistry of Solid State Materials, Vol. 2*, Cambridge University Press, Cambridge, U.K., 1992.
- [4.11] N. G. Hainovsky, Y. T. Pavlukhin and E. F. Hairetdinov, *Solid State Ionics*, 1986, **20**, 249.

## CHAPTER 5

- [5.1] (a) K. A. Mauritz, R. B. Moore, *Chem. Rev.*, 2004, **104**, 4535. (b) G. Alberti, R. Narducci, M. Sganappa, *J. Power Source*, 2008, **178**, 575. (c) G. Alberti, R. Narducci, *Fuel Cells*, 2009, **9**, 410.
- [5.2] (a) T. Panda, T. Kundu, R. Banerjee, *Chem. Commun.*, 2012, **48**, 5464.
- [5.3] (a) J. Sun, L. Weng, Y. Zhou, J. Chen, Z. Chen, Z. Liu, D. Zhao, *Angew. Chem., Int. Ed.*, 2002, **41**, 4471. (b) S. Chen, J. Zhang, T. Wu, P. Feng, X. Bu, *J. Am. Chem. Soc.*, 2009, **131**, 16027.
- [5.4] F. Bu, S. -J. Xiao, *CrystEngComm.*, 2010, **12**, 3385.
- [5.5] (a) B. C. H. Steele, A. Heinzl, *Nature*, 2001, **414**, 345. (b) E. Fabbri, D. Pergolesi, E. Traversa, *Chem. Soc. Rev.*, 2010, **39**, 4355.
- [5.6] M. Yoon, K. Suh, S. Natarajan, K. Kim *Angew. Chem., Int. Ed.*, 2013, **52**, 2688.
- [5.7] K. D. Kreuer, A. Rabenau, W. Weppner, *Angew. Chem., Int. Ed.*, Engl. 1982, **21**, 208.
- [5.8] CrysAlisPro, Version 1.171.33.66; Oxford Diffraction Ltd.: Abingdon, U.K., 2010.

- [5.9] G. M. Sheldrick, (1997). SHELXS '97 and SHELXL '97. University of Göttingen, Germany.

## CHAPTER 6

- [6.1] (a) J. Antonio, A. Eduardo, M. Sanchez, P. G. -Romero, *Chem. Soc. Rev.*, 2010, **39**, 3210. (b) R. B. Gupta, 2008. *Hydrogen fuel: production, transport, and storage*. CRC Press.
- [6.2] (a) S. Kandambeth, A. Mallick, B. Lukose, M. Mane, T. Heine, R. Banerjee, *J. Am. Chem. Soc.*, 2012, **134**, 19524. (b) B. P. Biswal, S. Chandra, S. Kandambeth, B. Lukose, T. Heine, R. Banerjee, *J. Am. Chem. Soc.*, 2013, **135**, 5328. (c) S. Chandra, S. Kandambeth, B. P. Biswal, B. Lukose, S. M. Kunjir, M. Chaudhary, R. Babarao, T. Heine, R. Banerjee, *J. Am. Chem. Soc.*, 2013, **135**, 17853.
- [6.3] (a) J. Antonio, A. Eduardo, M. Sanchez, P. G. -Romero, *J. Am. Chem. Soc.*, 2014, **136**, 1702. (b) J. Pan, C. Chen, L. Zhuang, J. Lu. *Acc. Chem. Res.*, 2012, **45**, 473.

## APPENDIX 1

**Table 1.** Crystallographic details of the compounds discussed in this thesis.

Crystal description	Chapter 2			
	ZTF-1	Co-ZIF-68	Co-ZIF-69	Co-ZIF-81
Chemical Formula	C <sub>5</sub> H <sub>10</sub> N <sub>11</sub> OZn	C <sub>10</sub> H <sub>7</sub> CoN <sub>5</sub> O <sub>2</sub>	C <sub>10</sub> H <sub>5</sub> Cl <sub>2</sub> CoN <sub>5</sub> O <sub>2</sub>	C <sub>10</sub> H <sub>5</sub> Br <sub>2</sub> CoN <sub>5</sub> O <sub>2</sub>
Formula weight	305.61	288.14	357.02	445.92
Crystal system	Monoclinic	Hexagonal	Hexagonal	Hexagonal
Space group	<i>Cc</i>	<i>P6<sub>3</sub>/mmc</i>	<i>P6<sub>3</sub>/mmc</i>	<i>P6<sub>3</sub>/mmc</i>
<i>a</i> (Å)	13.330(3)	26.674(2)	26.113(2)	25.9949(12)
<i>b</i> (Å)	15.327(3)	26.674(2)	26.113(2)	25.9949(12)
<i>c</i> (Å)	8.7796(17)	18.4694(20)	19.6459(14)	19.7757(11)
<i>α</i> (°)	90	90	90	90
<i>β</i> (°)	131.20(2)	90	90	90
<i>γ</i> (°)	90	120	120	120
Vol (Å <sup>3</sup> )	1349.7(5)	11380.5(19)	11601.2(16)	11572.9(10)
<i>D</i> <sub>calcd</sub> (g/cm <sup>3</sup> )	1.504	1.009	1.226	1.536
<i>μ</i> (mm <sup>-1</sup> )	1.829	0.905	1.168	5.038
<i>θ</i> range (°)	2.43–28.09	3.05–29.26	3.16–29.17	3.13–29.14
<i>Z</i>	4	24	24	24
range <i>h</i>	–17 to +17	–26 to +36	–34 to +31	–19 to +35
range <i>k</i>	–20 to +19	–32 to +36	–35 to +35	–20 to +35
range <i>l</i>	–11 to +11	–25 to +25	–21 to +25	–18 to +27
Reflns collected	7544	5133	5174	4947
Independent	3042	2116	2364	1471
<i>T</i> (K)	293(2)	100(2)	100(2)	100(2)
<i>R</i> 1	0.0510	0.0992	0.0997	0.0995
<i>wR</i> 2	0.1283	0.2938	0.2862	0.2545
GOF	1.051	0.884	0.979	0.702
CCDC No.	779031	952993	952994	952995

Table 1. Continued...

<i>Crystal description</i>	<i>Chapter 3</i>		
	<b>Mn-5TIA-1</b>	<b>Mn-5TIA-2</b>	<b>Mn-5TIA-3</b>
Chemical Formula	C <sub>26</sub> H <sub>24</sub> Mn <sub>2</sub> N <sub>8</sub> O <sub>10</sub>	C <sub>43.7</sub> H <sub>10</sub> Mn <sub>2</sub> N <sub>6</sub> O <sub>8</sub>	C <sub>10</sub> H <sub>5</sub> MnN <sub>3</sub> O <sub>4</sub>
Formula weight	718.41	856.86	286.11
Crystal system	Monoclinic	Orthorhombic	Monoclinic
Space group	<i>P2<sub>1</sub>/c</i>	<i>Pbcn</i>	<i>P2<sub>1</sub>/c</i>
<i>a</i> (Å)	10.7892(4)	12.2862(4)	11.214(11)
<i>b</i> (Å)	13.641(2)	14.9471(4)	12.585(13)
<i>c</i> (Å)	19.851(3)	20.8959(5)	14.447(15)
<i>α</i> (°)	90	90	90
<i>β</i> (°)	95.049(2)	90	110.125(15)
<i>γ</i> (°)	90	90	90
Vol (Å <sup>3</sup> )	2910.2(7)	3837.39(19)	1914(3)
D <sub>calcd</sub> (g/cm <sup>3</sup> )	1.640	1.483	0.993
<i>μ</i> (mm <sup>-1</sup> )	0.940	0.722	0.695
<i>θ</i> range (°)	1.85–28.27	2.89–25.00	1.93–28.26
<i>Z</i>	4	4	4
range <i>h</i>	–13 to +13	–8 to +14	–14 to +14
range <i>k</i>	–18 to +17	–17 to +11	–16 to +15
range <i>l</i>	–25 to +25	–24 to +12	–18 to +18
Reflns collected	32862	9625	20465
Independent reflns	6794	3380	4436
<i>T</i> (K)	190(2)	293(2)	190 (2)
<i>R</i> 1	0.0462	0.0862	0.0642
<i>wR</i> 2	0.1024	0.2761	0.1599
GOF	1.157	1.147	0.997
CCDC No.	822130	822131	822132

Table 1. Continued...

Crystal description	Chapter 4		Chapter 5	
	In-5TIA	Cd-5TIA	In-IA-2D-1	In-IA-2D-2
Chemical Formula	C <sub>20</sub> H <sub>10</sub> InN <sub>6</sub> O <sub>8</sub>	C <sub>20</sub> H <sub>10</sub> Cd N <sub>6</sub> O <sub>8.5</sub>	C <sub>16</sub> H <sub>8</sub> InO <sub>8</sub> .C <sub>2</sub> H <sub>8</sub> N	C <sub>16</sub> H <sub>8</sub> InO <sub>8</sub> , C <sub>3</sub> H <sub>7</sub> NO, C <sub>2</sub> H <sub>8</sub> N
Formula weight	577.16	582.74	489.14	562.23
Crystal system	Tetragonal	Tetragonal	Orthorhombic	Monoclinic
Space group	<i>P4/n</i>	<i>P4/n</i>	<i>Pna2</i> <sub>1</sub>	<i>P2</i> <sub>1</sub> / <i>c</i>
<i>a</i> (Å)	26.6386(5)	27.429(5)	15.8408(4)	11.9876(3)
<i>b</i> (Å)	26.6386(5)	27.429(5)	16.5349(3)	13.0329(4)
<i>c</i> (Å)	9.8419(3)	9.897(5)	9.94883(14)	18.3012(6)
$\alpha$ (°)	90	90	90	90
$\beta$ (°)	90	90	90	125.260(2)
$\gamma$ (°)	90	90	90	90
Vol (Å <sup>3</sup> )	6984.0(3)	7446(4)	2605.86(8)	2334.70(12)
<i>D</i> <sub>calcd</sub> (g/cm <sup>3</sup> )	1.098	1.040	1.247	1.600
$\mu$ (mm <sup>-1</sup> )	0.715	0.624	0.940	8.564
$\theta$ range (°)	3.69–28.09	3.61–28.11	3.29–29.15	4.50–70.72
<i>Z</i>	8	8	4	4
range <i>h</i>	–33to +33	–33 to +32	–21 to +21	–14 to +8
range <i>k</i>	–34 to +33	–36 to +37	–22 to +22	–15 to +15
range <i>l</i>	–12 to +13	–12 to +12	–13 to +13	–17 to +22
Reflns collected	41933	35539	15548	8741
Independent	8329	8874	4794	4027
<i>T</i> (K)	293(2)	239(2)	100(2)	100(2)
<i>R</i> 1	0.0778	0.0927	0.0725	0.0684
<i>wR</i> 2	0.2224	0.2739	0.2213	0.1826
GOF	1.099	1.088	1.132	0.993
CCDC No.	845048	845047	932278	932279

### **ABOUT THE AUTHOR**

Tamas Kumar Panda, son of Manoranjan Panda and Usha Rani Panda, was born in Contai, Purba Medinipore district, West Bengal, India, in 1984. He received his secondary and higher secondary education from Heria Sivaprasad Institution, Contai. He completed his B.Sc. from Bajkul milani Mahavidyalaya, Contai. After the completion of his B.Sc. he joined Department of Chemistry, Guru Ghasidas University, Bilaspur, Chattisgarh to pursue his M.Sc. He joined Department of Physical chemistry, CSIR NCL, Pune to pursue his Ph.D. degree in June 2009. He was awarded research fellowship by Council of Scientific and Industrial Research (JRF and SRF) for 2009-2014. He has received best research scholar and best high impact paper award from CSIR NCL Pune.

## List of Publications

1. **Tamas Panda**, Tanay Kundu and Rahul Banerjee "Structural Isomerism Leading to Variable Proton Conductivity in Indium (III) Isophthalic Acid based Framework" *Chem. Commun.*, 2013, **49**, 6197-6199.
2. **Tamas Panda**, Krishna M. Gupta, Jianwen Jiang and Rahul Banerjee "Enhancement of CO<sub>2</sub> Uptake in Iso-reticular Co based Zeolitic Imidazolate Frameworks via metal replacement" *CrystEngComm*, 2014. DOI : 10.1039/C3CE42075B.
3. **Tamas Panda**, Tanay Kundu and Rahul Banerjee "Self Assembled One Dimensional Functionalized Metal Organic Nanotube for Proton Conduction" *Chem. Commun.*, 2012, **48**, 5464-5466.
4. **Tamas Panda**, Pradip Pachfule, Yifei Chen, Jianwen Jiang and Rahul Banerjee "Amino functionalized zeolitic tetrazolate framework (ZTF) with high capacity for storage of carbon dioxide" *Chem. Commun.*, 2011, **47**, 2011–2013.
5. **Tamas Panda**, Pradip Pachfule and Rahul Banerjee "Template induced structural isomerism and enhancement of porosity in manganese (II) based metal–organic frameworks (Mn-MOFs)" *Chem. Commun.*, 2011, **48**, 11868–11870.
6. Bishnuprasad Biswal, **Tamas Panda** and Rahul Banerjee "Solution Mediated Phase Transformation (RHO to SOD) in Porous Co-Imidazolate based Zeolitic Framework With High Water Stability" *Chem. Commun.*, 2012, **48**, 5464-5466.
7. Chakadola Panda, Munmun Ghosh, **Tamas Panda**, Rahul Banerjee and Sayam Sen Gupta "Fe(III) complex of biuret-amide based macrocyclic ligand as peroxidase enzyme mimic" *Chem. Commun.*, 2011, **47**, 8016-8018.
8. Arijit Mallick, Eva-Maria Schön, **Tamas Panda**, K. Sreenivas, David Díaz Díaz and Rahul Banerjee "Fine-Tuning the Balance between Crystallization and Gelation and Enhancement of CO<sub>2</sub> Uptake on Functionalized Calcium Based MOFs and Metallogels" *J. Mater. Chem.*, 2012, **22**, 14951-14963.
9. Pradip Pachfule, Chandan Dey, **Tamas Panda** and Rahul Banerjee "Synthesis and structural comparisons of five new fluorinated metal organic frameworks (F-MOFs)" *CrystEngComm*, 2010, **12**, 1600–1609.
10. Pradip Pachfule, **Tamas Panda**, Chandan Dey and Rahul Banerjee "Structural diversity in a series of metal–organic frameworks (MOFs) composed of divalent transition metals, 4,4'-bipyridine and a flexible carboxylic acid" *CrystEngComm*, 2010, **12**, 2381–2389.

11. Pradip Pachfule, Chandan Dey, **Tamas Panda**, Kumar Vanka and Rahul Banerjee  
“Structural Diversity in Partially Fluorinated Metal Organic Frameworks (F-MOFs)  
Composed of Divalent Transition Metals, 1,10-Phenanthroline, and Fluorinated Carboxylic  
Acid” *Cryst. Growth Des.*, 2010, **10**, 1351–1363.
12. **Tamas Panda**, Rahul Banerjee “High Charge Carrier Mobility in two Dimensional Indium  
(III) Isophthalic Acid based Frameworks. *Proc. Indian Natn. Sci. Acad.* DOI:  
10.1007/s40010014-0152-6.